CENTRAL LIBRARY

SCHOLARLY ARTICLES

A CURRENT AWARENESS BULLETIN OF ARTICLES BY FACULTY, STUDENTS AND ALUMNI

~ *SEPTEMBER 2013* ~

DELHI TECHNOLOGICAL UNIVERSITY

(FORMERLY *DELHI COLLEGE OF ENGINEERING)*

GOVT. OF N.C.T. OF DELHI

SHAHBAD DAULATPUR, MAIN BAWANA ROAD

DELHI 110042

PREFACE

This is the Ninth Issue of Current Awareness Bulletin for the year 2013, started by Delhi Technological University Library. The aim of the bulletin is to compile, preserve and disseminate information published by the Faculty, Students and Alumni for mutual benefits. The bulletin also aims to propagate the intellectual contribution of DTU as a whole to the academia. It contains information resources available in the internet in the form of articles, reports, presentation published in international journals, websites, etc. by the faculty and students of Delhi Technological University in the field of science and technology. The publication of Faculty and Students, which are not covered in this bulletin, may be because of the reason that the full text either was not accessible or could not be searched by the search engine used by the library for this purpose. To make the bulletin more comprehensive, the learned faculty and Students may provide their uncovered publication to the library either through email or in CD, etc.

This issue contains the information published during September 2013. The arrangement of the contents is alphabetical wise starting from A-Z. The Full text of the article, which is either subscribed by the University or available in the web, is provided in this Bulletin.

CONTENTS

9. Quantifying uncertainty in measurement of mercury in suspended particulate matter by cold vapor technique using atomic absorption spectrometry with hydride generator Nahar Singh, ****Tarushee Ahuja,*** Department of Applied Chemistry, Email: tarushi_sai@yahoo.co.in, Vijay Narain Ojha, Daya Soni, S Swarupa Tripathy, Ivo Leito

10. Spectrophotometric Determination of Pt (II) and Pd (II) in Environmental Samples Collected from Highly Polluted Areas of Delhi Region of India ****Pushpa Ratre*** and ****Devendra Kumar***, Department of Applied Chemistry and Polymer Technology

11. Spectrophotometric Determination of Trace Amounts of Samarium in Environmental Samples ****Pushpa Ratre*** and ****Devendra Kumar***, Department of Applied Chemistry and Polymer Technology

12. Synthesis of Chain Extended Lactic Acid/Polypropylene Glycol Co-polymer ****Vimal Kumar, *Anshu Dev*** and ****A.P. Gupta***, Department of Applied Chemistry and Polymer Technology

 # Pro-Vice Chancellor

*** Faculty**

A Generalized ANN model for Analyzing and Synthesizing Rectangular, Circular and Triangular Microstrip Antennas

Taimoor Khan* and Asok De
Department of Electronics Engineering, Delhi Technological University,
Delhi-110 042, India, **E-mail:** ktaimoor@gmail.com

Abstract- Artificial neural networks have been used with microstrip antennas as fast computational technique for different performance parameters since last one decade. Different neural models have been proposed for calculating different performance parameters of microstrip antennas, respectively. Recently, the concept of creating generalized neural approach for computing different performance parameters has become motivating in microstrip antennas. This paper illustrates a generalized neural approach for analyzing and synthesizing the rectangular, circular and triangular MSAs, simultaneously. Thus, total seven performance parameters of three different MSAs are computed using generalized neural approach as such a method is rarely available in the open literature even for computing more than three performance parameters, simultaneously. The results thus obtained are in very good agreement to the measured results available in the referenced literature for all seven cases.

Index Term- **Different computing parameters, microstrip antennas, several radiating patches, generalized approach and RBF neural networks.**

I. INTRODUCTION

Low profile, conformable to planar and non-planar surfaces, most economical, mechanically robust, light weight, easy mount-ability etc. are the key features of the microstrip antennas (MSAs). Because of these fascinating features, the MSAs are being widely used in many communication applications [1]. Since the MSA operates only in the vicinity of the resonance frequency, hence it needs to be calculated accurately for analyzing the microstrip antennas. Similarly, for designing the MSAs, the physical dimensions must also be calculated precisely. Several classical methods [2-14] have been used for computing the resonance frequencies of rectangular MSAs [2-5], resonance frequencies of circular MSAs [6-12] and resonance frequencies of triangular MSAs [13-14].These methods can broadly be categorized as analytical methods and numerical methods. The analytical methods provide a good spontaneous explanation for the operation of MSAs. These methods are based on the physical assumptions for simplifying the radiation mechanism of the MSAs and are not suitable for many microstrip structures where the thickness of the substrate is not very thin. On the other hand, the numerical methods provide accurate results but only at the cost of huge mathematical burden in the form of complex integral equations. The choice of test functions and path integrations appears to be more critical without initial assumptions in the final stage of the numerical results. Also, these methods require a new solution even for a minor alteration in the geometry. Thus, the requirement for having a new solution for every small alteration in the geometry as well as the problems associated with the thickness of the substrates in analytical methods lead to complexities and processing cost.

In recent years, the artificial neural networks (ANNs) have acquired tremendous utilization in microwave communications [15-18] and especially, in analyzing and synthesizing the MSAs [19-26] due to their ability and adaptability to learn, generalization, smaller information requirement, fast real-time operation, and ease of implementation features [15]. The ANN model is trained using measured, calculated and/or simulated patterns. The aim of the training process is to minimize error between reference and actual outputs of the ANN model. Once the model is trained for a specified error, it returns the results for every minor change in the geometry both for electrically thin and thick MSAs within a fraction of a second. For analyzing the MSAs, several neural models [19-22] have been reported for calculating the resonance frequencies of rectangular MSAs [19], the resonance frequencies of circular MSAs [20] and the resonance frequencies of triangular MSAs [21], respectively. The side-lengths of the equilateral triangular MSAs have also been computed using neural networks by Gopalakrishnan and Gunasekaran for synthesizing purpose [22]. Thus, the neural methods [19-22] have been used for computing a single parameter (i.e. the resonance frequency or physical dimension) of the same MSAs, respectively.

Recently, the concept for creating generalized neural models has obtained popularity for computing different performance parameters simultaneously [23-26].The generalized approach is being widely used in antenna computer-aided design (CAD) programs because of instantly predicting different performance parameters simultaneously and accurately. Firstly, it has been introduced by Guney et al. [23] for computing the resonance frequencies of rectangular, circular and triangular MSAs, simultaneously. For validation purpose they have used standard experimental/measured results available in the literature [2-14]. In this work, they have obtained the equivalent patch dimensions for the circular and triangular MSAs by equating the patch area of the circular and triangular MSAs to that of equivalent rectangular MSAs before applying training to the neural

model. But the results thus computed do not have a very good agreement to their measured results. Guney and Sarikaya [24-25] have improved the performance of this generalized approach by introducing two different methods, respectively; one is based on adaptive neural network-based fuzzy inference system (ANFIS) method [24] and another based on concurrent neuro-fuzzy system (CNFS) method [25]. Both in ANFIS and CNFS methods, although a very good convergence has been obtained between the computed results and the measured results but these methods are still based on creating equivalent area. Turker et al. [26] have also proposed a generalized neural model for analyzing and synthesizing the rectangular MSAs, simultaneously and they have used the same measured results [2-5] for validation purpose. The synthesis of the problem has been defined as the forward-side and analysis as the reverse-side of the model. They have obtained the desired parameters (e.g. resonance frequency or geometric dimensions) of the rectangular MSAs at the output of the generalized model by inputting their corresponding parameters (i.e. geometric dimensions, fundamental mode, thickness and relative permittivity of the chosen substrate for computing the resonance frequency). Hence, Turker et al. [26] have computed three different parameters i.e. resonance frequency, width and length of rectangular MSAs, simultaneously using a generalized neural model whereas in ANFIS [23] and CNFS [24] methods the three computed parameters have been mentioned as the resonance frequency of rectangular MSAs, resonance frequency of circular MSAs and the resonance frequency of triangular MSAs. Thus the neural models [23-25] are based on the approach to calculate equivalent area whereas the model suggested by Turker et al. [26] is based on making switching between forward-and reverse-side prior to calculating the desired parameter. For computing different parameters, simultaneously in a common neural approach, sometimes it becomes undesirable and time consuming to the antenna designer when instant answer is required. These problems have recently been resolved by the authors in their works [27-28] by making equal dimensionality in the input patterns before applying training. Using this concept, they have successfully computed different performance parameters of triangular MSAs [27] and circular MSAs [28], respectively. In the proposed work, they have extended the generalized neural approach in analyzing and synthesizing the rectangular, circular and triangular MSAs, simultaneously as such an approach has not been attempted by anyone in the referenced literature.

II. MICROSTRIP ANTENNAS; CONVENTIONAL APPROACH

The microstrip antenna, in its simplest configuration consists of a radiating conductive patch on one side of a dielectric substrate of relative permittivity, 'ε_r' and of thickness, 'h' having a ground plane on the other side [1]. The side-view of the MSA with different radiating patches is shown in Fig. 1. In Fig. 1(b) RMSA corresponds to a rectangular MSA of physical dimensions, 'W_r' and 'L_r', CMSA to a circular MSA of radius, 'R_c' and TMSA to an equilateral triangular MSA of side-length, 'S_t'.

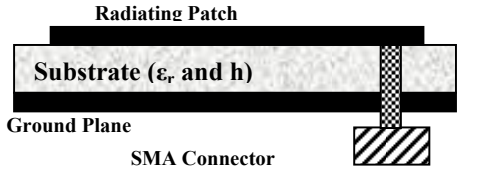

(a) Side-view

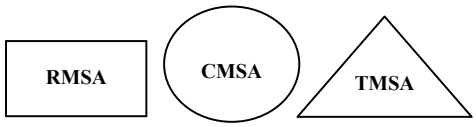

(b) Different Radiating Patches

Fig. 1 Geometry of microstrip antenna

The resonance frequency, 'f_r' of the rectangular MSA using cavity model is evaluated [1] as:

$$f_r = \frac{c}{2\sqrt{\varepsilon_e}}\sqrt{\left\{\left(\frac{m}{L_e}\right)^2 + \left(\frac{n}{W_e}\right)^2\right\}} \quad (1)$$

Where 'c' is the velocity of electromagnetic waves in free space, 'ε_e' is effective relative permittivity of the substrate, integers 'm' and n' represent the mode of propagation. 'L_e' and 'W_e' are the effective dimensions of the rectangular MSA.

For fundamental mode TM_{10}, equation (1) reduces to

$$f_r = \frac{c}{2\sqrt{\varepsilon_e}\,L_e} \quad (2)$$

The effective length, 'L_e' is defined as:

$$L_e = L_r + 2\Delta L_r \quad (3)$$

The effects of non-uniform medium and the fringing fields at each end of the patch are explained by the effective relative permittivity, 'ε_e' and the edge extension, 'ΔL_r' being the effective length to which the fields fringe at each end of the patch. The following expression of the effective relative permittivity proposed by Schneider [29] and edge-extension by Hammerstad [30] can be used in equations 2 and 3:

$$\varepsilon_e = \frac{\varepsilon_r + 1}{2} + \frac{\varepsilon_r - 1}{2}\left[1 + 10\frac{h}{W_r}\right]^{-1/2} \quad (4)$$

$$\Delta L_r = 0.412\,h\,\frac{(\varepsilon_e + 0.3)\left(\frac{W_r}{h} + 0.264\right)}{(\varepsilon_e - 0.258)\left(\frac{W_r}{h} + 0.813\right)} \quad (5)$$

For analyzing the rectangular MSA, the resonance frequency, 'f_r' can be determined from the given six input parameters; 'W_r', 'L_r', 'ε_r', 'h', 'm' and 'n' as discussed in equations (1)-(5).

The resonance frequency, 'f_c' of the circular MSA for TM_{mn} mode is given [6] as:

$$f_c = \frac{x'_{mn}}{2\pi R_e \sqrt{\mu_0 \varepsilon_0 \varepsilon_r}} = \frac{x'_{mn} c}{2\pi R_e \sqrt{\varepsilon_r}} \tag{6}$$

Where 'x'_{mn}' represents the n^{th} zero of the derivative of the Bessel function of order 'm'. 'c' represents the velocity of electromagnetic waves in free space. For the dominant mode (integer $m=1$ and integer $n=1$), x'_{11} =1.84118.

The effective value of the radius can be used [31] as:

$$R_e = R_{crcl}\left[1 + \frac{2h}{\pi R_{crcl} \varepsilon_r}\left(\ln\left(\frac{\pi R_{crcl}}{2h}\right) + 1.7726\right)\right]^{1/2} \tag{7}$$

Thus, the resonance frequency, 'f_c' of the circular MSAs can be easily determined for the given values of radius, 'R_c', relative permittivity, 'ε_r' and thickness, 'h' of substrate and mode of propagation, 'm' and 'n'. Thus, it depends on five input parameters; 'R_C', 'ε_r', 'h', 'm' and 'n'.

The resonance frequency, 'f_t' of the equilateral triangular MSA is given [32] as:

$$f_t = \frac{2c}{3S_e \sqrt{\varepsilon_e}}\left[m^2 + mn + n^2\right]^{1/2} \tag{8}$$

Where 'c' is the velocity of electromagnetic waves in free space, 'S_e' is the effective side-length of the patch, 'ε_e' is the effective relative permittivity and integer 'm' and integer 'n' represents the mode of propagation. The effective side-length, 'S_e' suggested by Helszain and James [32] and the effective relative permittivity, 'ε_e' by Bahl and Bhartia can be used [1] as:

$$S_e = S_t + \frac{h}{\sqrt{\varepsilon_e}} \tag{9}$$

$$\varepsilon_e = \frac{1}{2}(\varepsilon_r + 1) + \frac{1}{4}(\varepsilon_r - 1)\left(1 + \frac{12\,h}{S_t}\right)^{-1/2} \tag{10}$$

Thus, if the side-length, 'S_t', relative permittivity, 'ε_r' and thickness, 'h' of the substrate and mode of propagation, 'm' and 'n', are given, then the resonance frequency of triangular MSAs can be determined easily. Again for analyzing the triangular MSA, this resonance frequency, 'f_t' can be determined for the given five input parameters; 'S_t', 'ε_r', 'h', 'm' and 'n'.

From the discussion made in equations (1)-(10), it is concluded that if the geometric dimensions, relative permittivity, dielectric thickness and mode of propagation are given then the resonance frequency can be calculated easily. Keeping this concept in mind, total 81 patterns (46 for resonance frequency of rectangular MSAs, 20 for resonance frequency of circular MSAs and 15 for resonance frequency of triangular MSAs) are obtained from the literature [2-14]. The patterns for rectangular MSAs are attained from the works of Chang et al. [2], Carver [3] and Kara [4 and 5], for circular MSAs from Dahele and Lee [6 and 7], Carver [8], Antoszkiewicz and Shafai [9], Howell [10], Itoh and Mittra [11] and Abboud et al [12] and for triangular MSAs these patterns are acquired from the works of Chen et al. [13] and Dahele and Lee [14]. These 81 theoretical/experimental patterns for rectangular, circular and triangular MSAs are mentioned in Tables 1 and are used in training and testing of the proposed ANN model.

As the microstrip antenna (MSA) has narrow bandwidth and operates only in the vicinity of the resonance frequency, the choice of geometric dimensions giving specific resonance is also important. The rectangular, circular and triangular shapes of MSAs are the most popular shapes. Equations sets (1)-(5), (6)-(7), (8)-(10) can also be rearranged for synthesizing the rectangular, circular and triangular MSAs, respectively. Hence, for synthesizing the rectangular MSAs, the geometric dimensions ('W_r' and 'L_r') can be computed from the given five input parameters; 'f_r', 'ε_r', 'h', 'm' and 'n'. For synthesizing the circular MSAs, its radius 'R_c' can be estimated from the given five input parameters; 'f_c' 'ε_r' 'h' 'm' and 'n'. Similarly, for synthesizing the triangular MSAs, the side-length can also be computed if the five input parameters; 'f_t', 'ε_r', 'h', 'm' and 'n' are given. This concept is applied for creating the patterns required for synthesizing these three MSAs. Total 127 patterns (46 each for width and length of rectangular MSAs, 20 for radius of circular MSAs and 15 for side-length of triangular MSAs) are created and are shown in Table 2. These 208 patterns (81 analysis patterns + 127 synthesis patterns), are used for training and testing of the ANN model to be discussed in Section III.

III. PROPOSED ANN MODELING

In today's highly integrated world, when solutions to problems are cross-disciplinary in nature, artificial neural networks (ANNs) promise to become powerful techniques for obtaining solutions to problems quickly and accurately. The ANNs are massively distributed parallel processors that have a natural propensity for storing experiential knowledge and making it available for use. It resembles the brain since knowledge is acquired by the neural networks through learning process, and inter-neuron connection strengths are used to store this knowledge. Neural networks learn by known examples of a problem to acquire knowledge about it. Once ANN trains successfully, it can be put to effective use in solving 'unknown' or 'untrained' instances of the problem [15]. Multi-layered perceptron (MLP) and radial basis function

(RBF) neural networks have primarily been used in computing different parameters of the MSAs [19-26]. A radial basis function (RBF) neural networks consists of three-layers in which each layer is having entirely different roles. The input layer is made-up of source nodes which connect the networks to its outside environment. The input layer does not accomplish any process but simply buffers the data. The hidden layer applies a Gaussian transformation from the input space to the hidden space [33]. The output layer is linear, supplying the response of the networks to the patterns applied at the input layer. As far as training of the neural networks is concerned, the RBF neural networks are much faster than the multi-layers perceptron (MLP) neural networks. It is so because the learning process in RBF neural networks has two stages and both the stages are made more efficient by using appropriate learning algorithms [33]. This is the prime reason of using RBF neural networks instead of MLP neural networks in present work. There are three common steps followed in applying RBF neural networks on any arbitrary problem. Firstly, the training patterns are generated, then the structural configuration of hidden layer neurons is selected in the second step and finally, in the third step the weights are optimized by using training algorithm. The trained neural model is then tested on the remaining arbitrary sets of samples not included in the

Table 1: Experimental Results for Analyzing Rectangular, Circular and Triangular MSAs

Analysis of Rectangular MSAs [2-5]								**Analysis of Circular MSAs [6-12]**						
S. No.	**6-Dimensional** Input parameters						f_r (GHz)	**S. No.**	**5-Dimensional** Input Parameters					f_c (GHz)
	W_r (cm)	L_r(cm)	h (cm)	ε_r	m	n			R_c(cm)	h (cm)	ε_r	m	n	
1.	5.7000	3.8000	0.3175	2.3300	1	0	2.3100	1.	0.7400	0.1588	2.6500	1	1	6.6340
2.	4.5500	3.0500	0.3175	2.3300	1	0	2.8900	2.	0.7700	0.2350	4.5500	1	1	4.9450
3.	2.9500	1.9500	0.3175	2.3300	1	0	4.2400	3.	0.8200	0.1588	2.6500	1	1	6.0740
4.	1.9500	1.3000	0.3175	2.3300	1	0	5.8400	4.	0.9600	0.1588	2.6500	1	1	5.2240
5.	1.7000	1.1000	0.3175	2.3300	1	0	6.8000	5.	1.0400	0.2350	4.5500	1	1	3.7500
6.	1.4000	0.9000	0.3175	2.3300	1	0	7.7000	6.	1.0700	0.1588	2.6500	1	1	4.7230
7.	1.2000	0.8000	0.3175	2.3300	1	0	8.2700	7.	1.1500	0.1588	2.6500	1	1	4.4250
8.	1.0500	0.7000	0.3175	2.3300	1	0	9.1400	8.	1.2700	0.0794	2.5900	1	1	4.0700
9.	1.7000	1.1000	0.9525	2.3300	1	0	4.7300	9.	2.0000	0.2350	4.5500	1	1	2.0030
10.	1.7000	1.1000	0.1524	2.3300	1	0	7.8700	10.	2.9900	0.2350	4.5500	1	1	1.3600
11.	4.1000	4.1400	0.1524	2.5000	1	0	2.2280	11.	3.4930	0.1588	2.5000	1	1	1.5700
12.	6.8580	4.1400	0.1524	2.5000	1	0	2.2000	12.	3.4930	0.3175	2.5000	1	1	1.5100
13.	10.800	4.1400	0.1524	2.5000	1	0	2.1810	13.	3.8000	0.1524	2.4900	1	1	1.4430
14.	0.8500	1.2900	0.0170	2.2200	1	0	7.7400	14.	3.9750	0.2350	4.5500	1	1	1.0300
15.	0.7900	1.1850	0.0170	2.2200	1	0	8.4500	15.	4.8500	0.3180	2.5200	1	1	1.0990
16.	2.0000	2.5000	0.0790	2.2200	1	0	3.9700	16.	4.9500	0.2350	4.5500	1	1	0.8250
17.	1.0630	1.1830	0.0790	2.5500	1	0	7.7300	17.	5.0000	0.1590	2.3200	1	1	1.1280
18.	0.9100	1.0000	0.1270	10.200	1	0	4.6000	18.	6.8000	0.0800	2.3200	1	1	0.8350
19.	1.7200	1.8600	0.1570	2.3300	1	0	5.0600	19.	6.8000	0.1590	2.3200	1	1	0.8290
20.	1.8100	1.9600	0.1570	2.3300	1	0	4.8050	20.	6.8000	0.3180	2.3200	1	1	0.8150
21.	1.2700	1.3500	0.1630	2.5500	1	0	6.5600	**Analysis of Triangular MSAs [13-14]**						
22.	1.5000	1.6210	0.1630	2.5500	1	0	5.6000	**S. No.**	**5-Dimensional** Input Parameters					f_t (GHz)
23.	1.3370	1.4120	0.2000	2.5500	1	0	6.2000		S_t (cm)	h (cm)	ε_r	m	n	
24.	1.1200	1.2000	0.2420	2.5500	1	0	7.0500	1.	4.1000	0.0700	10.5000	1	0	1.5190
25.	1.4030	1.4850	0.2520	2.5500	1	0	5.8000	2.	4.1000	0.0700	10.5000	1	1	2.6370
26.	1.5300	1.6300	0.3000	2.5000	1	0	5.2700	3.	4.1000	0.0700	10.5000	2	0	2.9950
27.	0.9050	1.0180	0.3000	2.5000	1	0	7.9900	4.	4.1000	0.0700	10.5000	2	1	3.9730
28.	1.1700	1.2800	0.3000	2.5000	1	0	6.5700	5.	4.1000	0.0700	10.5000	3	0	4.4390
29.	1.3750	1.5800	0.4760	2.5500	1	0	5.1000	6.	8.7000	0.0780	2.3200	1	0	1.4890
30.	0.7760	1.0800	0.3300	2.5500	1	0	8.0000	7.	8.7000	0.0780	2.3200	1	1	2.5960
31.	0.7900	1.2550	0.4000	2.5500	1	0	7.1340	8.	8.7000	0.0780	2.3200	2	0	2.9690
32.	0.9870	1.4500	0.4500	2.5500	1	0	6.0700	9.	8.7000	0.0780	2.3200	2	1	3.9680
33.	1.0000	1.5200	0.4760	2.5500	1	0	5.8200	10.	8.7000	0.0780	2.3200	3	0	4.4430
34.	0.8140	1.4400	0.4760	2.5500	1	0	6.3800	11.	10.0000	0.1590	2.3200	1	0	1.2800
35.	0.7900	1.6200	0.5500	2.5500	1	0	5.9900	12.	10.0000	0.1590	2.3200	1	1	2.2420
36.	1.2000	1.9700	0.6260	2.5500	1	0	4.6600	13.	10.0000	0.1590	2.3200	2	0	2.5500
37.	0.7830	2.3000	0.8540	2.5500	1	0	4.6000	14.	10.0000	0.1590	2.3200	2	1	3.4000
38.	1.2560	2.7560	0.9520	2.5500	1	0	3.5800	15.	10.0000	0.1590	2.3200	3	0	3.8240
39.	0.9740	2.6200	0.9520	2.5500	1	0	3.9800							
40.	1.0200	2.6400	0.9520	2.5500	1	0	3.9000							
41.	0.8830	2.6760	1.0000	2.5500	1	0	3.9800							
42.	0.7770	2.8350	1.1000	2.5500	1	0	3.9000							
43.	0.9200	3.1300	1.2000	2.5500	1	0	3.4700							
44.	1.0300	3.3800	1.2810	2.5500	1	0	3.2000							
45.	1.2650	3.5000	1.2810	2.5500	1	0	2.9800							
46.	1.0800	3.4000	1.2810	2.5500	1	0	3.1500							

Table 2: Experimental Results for Synthesizing Rectangular, Circular and Triangular MSAs

Synthesis of Rectangular MSAs								Synthesis of Circular MSAs						
S. No.	5-Dimensional Input parameters					W_r (cm)	L_r (cm)	S. No.	5-Dimensional Input Parameters					R_c (cm)
	fr (GHz)	h (cm)	ε_r	m	n				f_c (GHz)	h (cm)	ε_r	m	n	
1	2.3100	0.3175	2.3300	1	0	5.7000	3.8000	1	6.6340	0.1588	2.6500	1	1	0.7400
2	2.8900	0.3175	2.3300	1	0	4.5500	3.0500	2	4.9450	0.2350	4.5500	1	1	0.7700
3	4.2400	0.3175	2.3300	1	0	2.9500	1.9500	3	6.0740	0.1588	2.6500	1	1	0.8200
4	5.8400	0.3175	2.3300	1	0	1.9500	1.3000	4	5.2240	0.1588	2.6500	1	1	0.9600
5	6.8000	0.3175	2.3300	1	0	1.7000	1.1000	5	3.7500	0.2350	4.5500	1	1	1.0400
6	7.7000	0.3175	2.3300	1	0	1.4000	0.9000	6	4.7230	0.1588	2.6500	1	1	1.0700
7	8.2700	0.3175	2.3300	1	0	1.2000	0.8000	7	4.4250	0.1588	2.6500	1	1	1.1500
8	9.1400	0.3175	2.3300	1	0	1.0500	0.7000	8	4.0700	0.0794	2.5900	1	1	1.2700
9	4.7300	0.9525	2.3300	1	0	1.7000	1.1000	9	2.0030	0.2350	4.5500	1	1	2.0000
10	7.8700	0.1524	2.3300	1	0	1.7000	1.1000	10	1.3600	0.2350	4.5500	1	1	2.9900
11	2.2280	0.1524	2.5000	1	0	4.1000	4.1400	11	1.5700	0.1588	2.5000	1	1	3.4930
12	2.2000	0.1524	2.5000	1	0	6.8580	4.1400	12	1.5100	0.3175	2.5000	1	1	3.4930
13	2.1810	0.1524	2.5000	1	0	10.800	4.1400	13	1.4430	0.1524	2.4900	1	1	3.8000
14	7.7400	0.0170	2.2200	1	0	0.8500	1.2900	14	1.0300	0.2350	4.5500	1	1	3.9750
15	8.4500	0.0170	2.2200	1	0	0.7900	1.1850	15	1.0990	0.3180	2.5200	1	1	4.8500
16	3.9700	0.0790	2.2200	1	0	2.0000	2.5000	16	0.8250	0.2350	4.5500	1	1	4.9500
17	7.7300	0.0790	2.5500	1	0	1.0630	1.1830	17	1.1280	0.1590	2.3200	1	1	5.0000
18	4.6000	0.1270	10.200	1	0	0.9100	1.0000	18	0.8350	0.0800	2.3200	1	1	6.8000
19	5.0600	0.1570	2.3300	1	0	1.7200	1.8600	19	0.8290	0.1590	2.3200	1	1	6.8000
20	4.8050	0.1570	2.3300	1	0	1.8100	1.9600	20	0.8150	0.3180	2.3200	1	1	6.8000
21	6.5600	0.1630	2.5500	1	0	1.2700	1.3500	Synthesis of Triangular MSAs [13-14]						
22	5.6000	0.1630	2.5500	1	0	1.5000	1.6210	S. No.	5-Dimensional Input Parameters					S_t (cm)
23	6.2000	0.2000	2.5500	1	0	1.3370	1.4120		f_t (GHz)	h (cm)	ε_r	m	n	
24	7.0500	0.2420	2.5500	1	0	1.1200	1.2000	1	1.5190	0.0700	10.5000	1	0	4.1000
25	5.8000	0.2520	2.5500	1	0	1.4030	1.4850	2	2.6370	0.0700	10.5000	1	1	4.1000
26	5.2700	0.3000	2.5000	1	0	1.5300	1.6300	3	2.9950	0.0700	10.5000	2	0	4.1000
27	7.9900	0.3000	2.5000	1	0	0.9050	1.0180	4	3.9730	0.0700	10.5000	2	1	4.1000
28	6.5700	0.3000	2.5000	1	0	1.1700	1.2800	5	4.4390	0.0700	10.5000	3	0	4.1000
29	5.1000	0.4760	2.5500	1	0	1.3750	1.5800	6	1.4890	0.0780	2.3200	1	0	8.7000
30	8.0000	0.3300	2.5500	1	0	0.7760	1.0800	7	2.5960	0.0780	2.3200	1	1	8.7000
31	7.1340	0.4000	2.5500	1	0	0.7900	1.2550	8	2.9690	0.0780	2.3200	2	0	8.7000
32	6.0700	0.4500	2.5500	1	0	0.9870	1.4500	9	3.9680	0.0780	2.3200	2	1	8.7000
33	5.8200	0.4760	2.5500	1	0	1.0000	1.5200	10	4.4430	0.0780	2.3200	3	0	8.7000
34	6.3800	0.4760	2.5500	1	0	0.8140	1.4400	11	1.2800	0.1590	2.3200	1	0	10.0000
35	5.9900	0.5500	2.5500	1	0	0.7900	1.6200	12	2.2420	0.1590	2.3200	1	1	10.0000
36	4.6600	0.6260	2.5500	1	0	1.2000	1.9700	13	2.5500	0.1590	2.3200	2	0	10.0000
37	4.6000	0.8540	2.5500	1	0	0.7830	2.3000	14	3.4000	0.1590	2.3200	2	1	10.0000
38	3.5800	0.9520	2.5500	1	0	1.2560	2.7560	15	3.8240	0.1590	2.3200	3	0	10.0000
39	3.9800	0.9520	2.5500	1	0	0.9740	2.6200							
40	3.9000	0.9520	2.5500	1	0	1.0200	2.6400							
41	3.9800	1.0000	2.5500	1	0	0.8830	2.6760							
42	3.9000	1.1000	2.5500	1	0	0.7770	2.8350							
43	3.4700	1.2000	2.5500	1	0	0.9200	3.1300							
44	3.2000	1.2810	2.5500	1	0	1.0300	3.3800							
45	2.9800	1.2810	2.5500	1	0	1.2650	3.5000							
46	3.1500	1.2810	2.5500	1	0	1.0800	3.4000							

training samples. The detailed description of each step involved is being discussed here:

A. Patterns Generation and their Dimensionality

The theoretical/experimental patterns discussed in sections-2 and mentioned in Table 1 and Table 2 are used for training and testing of the proposed neural model. It is clear from these tables that the dimensionality of input pattern is symmetrical in six different cases except for the analyzing the rectangular MSAs. It means that the resonance frequency of the rectangular MSAs is the function of six dimensional input patterns i.e. [W_r L_r ε_r h m n] whereas the dimensionality of the input pattern is five each for synthesis of rectangular MSAs i.e. [f_r ε_r h m n], analysis of circular MSAs i.e. [R_c ε_r h m n], synthesis of circular MSAs i.e. [f_c ε_r h m n], analysis of triangular MSAs i.e. [S_t ε_r h m n] and the synthesis of triangular MSAs i.e. [f_t ε_r h m n]. Hence, if the dimensionality of input pattern for the analysis of rectangular MSAs reduces from six to five then, it becomes symmetrical with remaining six cases. Prior to applying the training on

neural model it has been decided to make the input patterns symmetrical in dimensionality for all seven cases.

For the fundamental mode (i.e. $m=1$ and $n=0$) of rectangular MSAs, the resonance frequency depends on the four parameters i.e. width and length of the patch, thickness and relative permittivity of the substrate. This four parameters dependency is represented here by variables 'x_1', 'x_2', 'x_3' and 'x_4', respectively. The fundamental mode used here is not varying, hence it can be represented by single integer 'x_5' instead of integers, 'm' and 'n' where $x_5=1$ means $m=1$and $n=0$. Thus this resonance frequency becomes the function of five variables; 'x_1', 'x_2', 'x_3', 'x_4' and 'x_5'. Now this is compatible with the remaining six cases. Similarly, the five-dimensional input pattern each for width and length calculation of the rectangular MSAs are taken as; the resonance frequency (x_1), dielectric thickness (x_2), relative permittivity (x_3), modes of propagation (x_4 and x_5). The five-dimensional input pattern each for circular MSAs and triangular MSAs analysis as well as synthesis is also created using the same approach and represented by the variables x_1, x_2, x_3, x_4 and x_5, respectively. To distinguish these seven different cases an additional variable, 'M' is also included in five dimensional input patterns which can be treated here as a mode-control. The mode-control, M, is selected as $M = 1$, $M = 2$ and $M = 3$ for computing the resonance frequency, width and length of rectangular MSAs, respectively, $M = 4$ and $M = 5$ for the resonance frequency and radius of circular MSAs and finally, $M = 6$ and $M = 7$ for calculating the resonance frequency and side-length of the triangular MSAs, respectively. This six-dimensional input pattern i.e.[x]→[x_1 x_2 x_3 x_4 x_5 M] is used as the training and testing pattern for computing seven different parameters of three different MSAs, simultaneously. Thus the input-output patterns with their original and modified dimensionalities for all seven different cases are also mentioned in Table 3.

Table 3: Dimensionality of Input Parameters for Training and Testing of ANN Model

Case-I (M=1); Resonance frequency of rectangular MSAs		**Case-II (M=2); Width of rectangular MSAs**	
Input parameters	**Output parameter (y) in MHz**	**Input parameters**	**Output parameter (y) in cm**
x_1→Width of the Patch (W_r)	Resonance Frequency of Rectangular MSAs (**Total 46 Patterns**)	x_1→Resonance Frequency (f_r)	Width of Rectangular MSAs (**Total 46 Patterns**)
x_2→Length of the Patch (L_r)		x_2→Dielectric Thickness (h)	
x_3→Dielectric Thickness (h)		x_3→Relative Permittivity (ε_r)	
x_4→Relative Permittivity (ε_r)		x_4→Mode of Propagation (m)	
x_5→Mode of Propagation (m & n)		x_5→Mode of Propagation (n)	
Case-III (M=3); Length of rectangular MSAs		**Case-IV (M=4); Resonance frequency of circular MSAs**	
Input Parameters	**Output Parameter (y) in cm**	**Input parameters**	**Output parameter (y) in MHz**
x_1→Resonance Frequency (f_r)	Length of Rectangular MSAs (**Total 46 Patterns**)	x_1→Radius (R_c)	Resonance Frequency of Circular MSAs (**Total 20 Patterns**)
x_2→Dielectric Thickness (h)		x_2→Dielectric Thickness (h)	
x_3→Relative Permittivity (ε_r)		x_3→ Relative Permittivity(ε_r)	
x_4→Mode of Propagation (m)		x_4→Mode of Propagation (m)	
x_5→Mode of Propagation (n)		x_5→Mode of Propagation (n)	
Case-V (M=5); Radius of circular MSAs		**Case-VI (M=6); Resonance frequency of triangular MSAs**	
Input parameters	**Output Parameter (y) in cm**	**Input parameters**	**Output parameter (y) in MHz**
x_1→Resonance Frequency (f_c)	Radius of Circular MSAs (**Total 20 Patterns**)	x_1→Side-Length of Patch (S_t)	Resonance Frequency of Triangular MSAs (**Total 20 Patterns**)
x_2→Dielectric Thickness (h)		x_2→Dielectric Thickness (h)	
x_3→Relative Permittivity (ε_r)		x_3→Relative Permittivity (ε_r)	
x_4→Mode of Propagation (m)		x_4→Mode of Propagation (m)	
x_5→Mode of Propagation(n)		x_5→Mode of Propagation (n)	
Case-VII (M=7); Side-length of triangular MSAs			
Input parameters	**Input parameters**	**Output parameter (y) in cm**	
x_1→Resonance Frequency (f_t)	x_4→Mode of Propagation (m)	Side-Length of Triangular MSAs (**Total 20 Patterns**)	
x_2→Dielectric Thickness (h)	x_5→Mode of Propagation (n)		
x_3→Relative Permittivity (ε_r)			

B. Structural Configuration and Training Strategy

To build a successful neural-networks application, training stage is one of the more critical phases. Training the neural networks basically consists of adjusting weights of the neural networks with the help of a training algorithm. Before doing training of the RBF model, all 208 patterns are normalized between +0.1 to +0.9 using MATLAB software [34].The training performance of the proposed neural networks is observed by varying the number of neurons in the hidden layer and after many trials it is optimized with forty five neurons for the best performance. Further, the training performance of the neural model is also observed with seven different training algorithms [35-37]; BFGS quasi-Newton(BFG), Bayesian regulation (BR), scaled conjugate-gradient (SCG), Powell-Beale conjugate gradient (CGP), conjugate gradient with Fletcher-Peeves (CGF), one step secant (OSS), and Levenberg-Marquardt (LM).

A RBF neural model proposed for computing seven different parameters is illustrated in Fig. 2 in which the

weight matrix is designated by *[w]* and the bias value by *b*, respectively. Initially some random values are assigned for the weights which are then optimized using LM training algorithm and coding for this implementation is created in MATLAB software [34]. In Fig. 2 the input matrix designated as [x]→[x_1 x_2 x_3 x_4 x_5 M] is of six dimensional. Here variable M is a mode control which is included to distinguish the seven different cases, respectively. Mode control, $M = 1$, $M = 2$ and $M = 3$ represents the output of the neural model as resonance frequency, width and length of the rectangular MSAs, respectively. Mode control, $M = 4$ and $M = 5$ indicates that the neural model's output is the resonance frequency and radius of the circular MSAs, respectively whereas for the resonance frequency and side-length of the triangular MSAs at the output of the neural model, the mode control, M is set as $M = 6$ and $M = 7$, respectively.

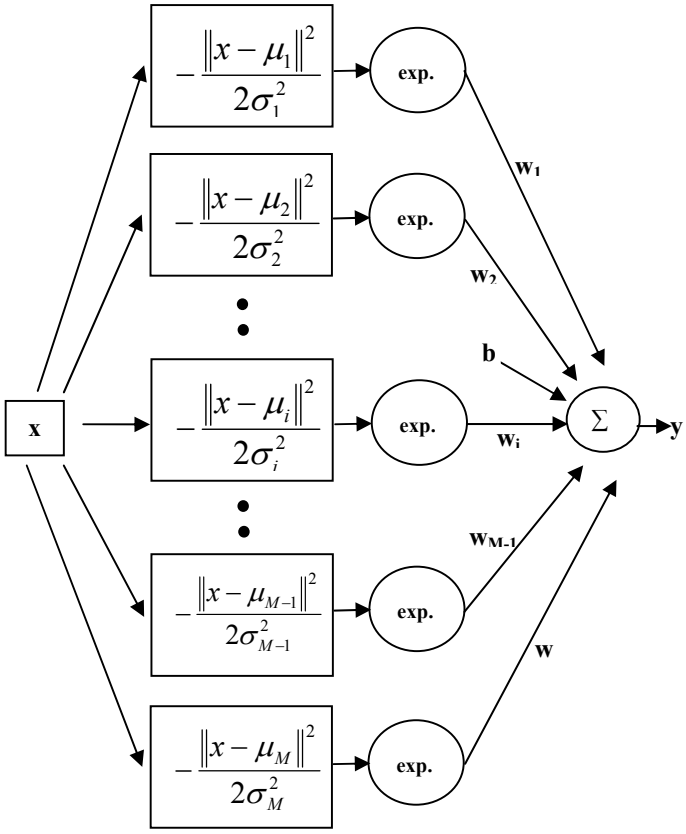

Fig.2: Proposed ANN Model

The basic approach for training the model can be understood by the flow-diagram shown in Fig. 3 in which the structural configuration of the model is optimized as [6-45-1]. It means that there are 6-neurons in the input layer, 45-neurons in the hidden layer and single neuron in the output layer. For the applied input pattern, some random numbers between *0* and *1* are assigned to the weights and the output of the model is computed corresponding to that input pattern. Some parameters like mean square error (MSE), learning rate, momentum coefficient and spread value required during training of the neural model are taken as: 5×10^{-7}, *0.1*, *0.5* and *0.5*, respectively. The MSE between the calculated and referenced results is then computed for 169 samples and according to this computed error all the weights are updated with the help of training algorithm. This updating process is carried out after presenting each set of input pattern until the calculated accuracy of the model is estimated satisfactory. Once it is achieved, the second phase i.e. testing algorithm is created with the help of these updated weights for remaining 39 samples in the MATLAB software [34]. The arbitrary set out of total 39 testing sets is now applied on the model and its corresponding result is obtained, respectively.

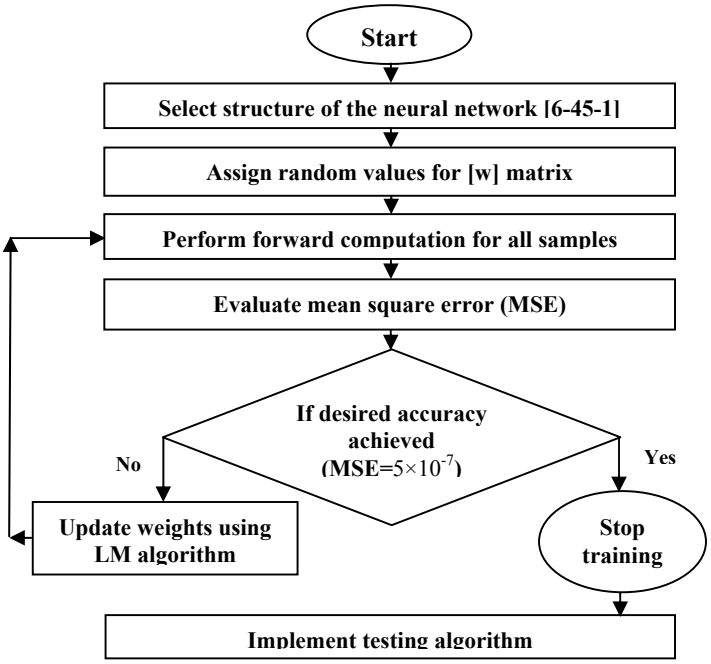

Fig. 3: Flow-Diagram for Training of ANN Model.

IV. CALCULATED RESULTS AND DISCUSSION

The training performance of the proposed ANN model is observed with seven different training algorithms; BFG, BR, SCG, CGP, CGF, OSS, and LM back propagation algorithms but only the Levenberg-Marquardt (LM) back propagation is proved to be the fastest converging training algorithm and produced the results with least mean-square-error (MSE) as mentioned in Table 4.

The results computed by present method each for analysis and synthesis of rectangular, circular and triangular microstrip antennas (MSAs) during training and testing of the generalized neural model are mentioned in Table 5. To determine the most suitable implication given in the literature [2-14], the computed results are compared with the theoretical/experimental results reported in the literature and this comparison is also mentioned in these tables. The computed results for analyzing and synthesizing the rectangular MSAs are compared to the theoretical/ experimental results of Chang et al. [2], Carver [3] and Kara [4 and 5], respectively, for circular MSAs these results are compared by the theoretical/experimental

results of Dahele and Lee [6 and7], Carver [8],Antoszkiewicz and Shafai [9], Howell [10], Itoh and Mittra [11] and Abboud et al. [12] whereas for equilateral triangular MSAs a comparison is made with the results of Chen et al. [13] and Dahele and Lee [14]. It is clear from Table 5 that most of the calculated points are very close to

Table 4: Comparison of Average Absolute Error vs. Training Algorithm

Training algorithm [34-36]	Average Absolute Error in Analysis and Synthesis						Number of Iteration Required
	Rectangular MSAs		Circular MSAs		Triangular MSAs		
	Analysis	Synthesis	Analysis	Synthesis	Analysis	Synthesis	
BFG	11.35MHz	1.1500cm	34.10MHz	1.8020cm	13.20MHz	1.4110cm	13049
BR	31.33MHz	2.1300cm	27.20MHz	1.0290cm	22.70MHz	1.1620cm	12046
SCG	25.53MHz	0.6800cm	25.80MHz	1.0310cm	24.50MHz	1.0110cm	19602
CGB	5.100MHz	1.0900cm	15.10MHz	1.2310cm	35.40MHz	0.0150cm	14021
CGF	14.50MHz	1.0300cm	14.30MHz	0.9160cm	18.50MHz	1.0130cm	11302
OSS	21.80MHz	1.7600cm	1.020 MHz	2.1060cm	23.70MHz	1.2040cm	14803
LM	**3.200MHz**	**0.0037cm**	**0.700MHz**	**0.0045cm**	**1.600MHz**	**0.0051cm**	**1476**

Table 5: Comparison of Reference Results [2-14] and ANN Computed Results

Comparison of Results for Rectangular MSAs						Comparison of Results for Circular MSAs			
Reference Results [2-5]			ANN Computed Results			Reference Results [6-12]		ANN Computed Results	
f_{rth} (GHz)	W_{rth} (cm)	L_{rth} (cm)	f_{rANN} (GHz)	W_{rANN} (cm)	L_{rANN} (cm)	f_{cth} (GHz)	R_{cth} (cm)	f_{cANN} (GHz)	R_{cANN} (cm)
2.3100	5.7000	3.8000	2.3047	5.6932	3.8080	6.6340	0.7400	6.6343	0.7409
2.8900	4.5500	3.0500	2.8846	4.5519	3.0445	4.9450	0.7700	4.9451	0.7708
4.2400	2.9500	1.9500	4.2348	2.9519	1.9453	6.0740	0.8200	6.0738	0.8208
5.8400	1.9500	1.3000	5.8415	1.9529	1.3041	5.2240	0.9600	5.2235▲	0.9608▲
6.8000	1.7000	1.1000	6.8024▲	1.7039▲	1.1049▲	3.7500	1.0400	3.7502	1.0329
7.7000	1.4000	0.9000	7.7029	1.4059	0.9052	4.7230	1.0700	4.7240	1.0711
8.2700	1.2000	0.8000	8.2659	1.2009	0.8041	4.4250	1.1500	4.4251	1.1508
9.1400	1.0500	0.7000	9.1354	1.0561	0.6939	4.0700	1.2700	4.0703	1.2708
4.7300	1.7000	1.1000	4.7309	1.6982	1.0490	2.0030	2.0000	2.0031	1.9909
7.8700	1.7000	1.1000	7.8700	1.7034	1.1039	1.3600	2.9900	1.3603▲	2.9502▲
2.2280	4.1000	4.1400	2.2281	4.1049	4.1421	1.5700	3.4930	1.5703	3.4782
2.2000	6.8580	4.1400	2.2009▲	6.8561	4.1409	1.5100	3.4930	1.5102	3.4852
2.1810	10.8000	4.1400	2.1809	10.8003	4.1449	1.4430	3.8000	1.4429	3.8004
7.7400	0.8500	1.2900	7.7389	0.8508	1.2912	1.0300	3.9750	1.0302	3.9761
8.4500	0.7900	1.1850	8.4486▲	0.7845▲	1.1835▲	1.0990	4.8500	1.0987	4.8504
3.9700	2.0000	2.5000	3.9686	1.9979	2.5049	0.8250	4.9500	0.8247	4.9505
7.7300	1.0630	1.1830	7.7305	1.0645	1.1895	1.1280	5.0000	1.1281	5.0008
4.6000	0.9100	1.0000	4.6011	0.9045	0.9997	0.8350	6.8000	0.8347	6.8009
5.0600	1.7200	1.8600	5.0592	1.7144	1.8609	0.8290	6.8000	0.8289▲	6.8011▲
4.8050	1.8100	1.9600	4.8049▲	1.8113▲	1.9605▲	0.8150	6.8000	0.8151	6.8005
6.5600	1.2700	1.3500	6.5601	1.2709	1.3472	Comparison of Results for Triangular MSAs			
5.6000	1.5000	1.6210	5.6005	1.5009	1.6218	Reference Results [13-14]		ANN Computed Results	
6.2000	1.3370	1.4120	6.2029▲	1.3345▲	1.4171▲	f_{tth} (GHz)	S_{tth} (cm)	f_{tANN} (GHz)	S_{tANN} (cm)
7.0500	1.1200	1.2000	7.0489	1.1201	1.2031	1.5190	4.1000	1.5178▲	4.1019▲
5.8000	1.4030	1.4850	5.7921	1.4016	1.4849	2.6370	4.1000	2.6357	4.1007
5.2700	1.5300	1.6300	5.268	1.5314	1.6309	2.9950	4.1000	2.9927	4.1089
7.9900	0.9050	1.0180	7.9834	0.9047	1.0198	3.9730	4.1000	3.9713	4.1033
6.5700	1.1700	1.2800	6.5702	1.1769	1.2817	4.4390	4.1000	4.4379	4.0900
5.1000	1.3750	1.5800	5.1000▲	1.3745▲	1.5749▲	1.4890	8.7000	1.4883	8.7018
8.0000	0.7760	1.0800	7.9999	0.7705	1.0745	2.5960	8.7000	2.5947	8.7022
7.1340	0.7900	1.2550	7.1331	0.7879	1.2553	2.9690	8.7000	2.9677	8.7043
6.0700	0.9870	1.4500	6.0635	0.9845	1.4503	3.9680	8.7000	3.9671▲	8.7005▲
5.8200	1.0000	1.5200	5.8129▲	1.0019▲	1.5131▲	4.4430	8.7000	4.4414	8.6909
6.3800	0.8140	1.4400	6.3748	0.8119	1.4398	1.2800	10.0000	1.2781	9.9935
5.9900	0.7900	1.6200	5.9823	0.7929	1.6205	2.2420	10.0000	2.2402	10.0002
4.6600	1.2000	1.9700	4.6523	1.2019	1.9635	2.5500	10.0000	2.5519	9.9853
4.600	0.7830	2.3000	4.6016	0.7811	2.3032	3.4000	10.0000	3.4013	10.0026
3.5800	1.2560	2.7560	3.5832▲	1.2509▲	2.7525▲	3.8240	10.0000	3.8237▲	9.9899▲
3.9800	0.9740	2.6200	3.9752	0.9709	2.6188	▲→testing results.			
3.9000	1.0200	2.6400	3.9039	1.0207	2.6345				
3.9800	0.8830	2.6760	3.9745	0.8815	2.6724				
3.9000	0.7770	2.8350	3.9013	0.7745	2.8349				
3.4700	0.9200	3.1300	3.4739	0.9239	3.1245				
3.2000	1.0300	3.3800	3.2189▲	1.0319▲	3.3749▲				
2.9800	1.2650	3.5000	2.9749	1.2645	3.4999				
3.1500	1.0800	3.4000	3.1529	1.0743	3.4208				

their theoretical/experimental value whereas only few are far-off. Hence, a very good agreement between the referenced results and the computed results supports the validity of the proposed neural approach.

Table 6: Comparison of Present Method and Previous Neural Methods

Method→	**Present Method**	**Ref. [19]**	**Ref. [23]**	**Ref. [24]**	**Ref. [25]**	**Ref. [26]**
Analysis of RMSAs	**3.20 MHz**	16.33 MHz	71.88 MHz	6.17 MHz	16.88 MHz	50.0 MHz
Method→	**Present Method**	**Ref. [26]**	-	-	-	-
Synthesis of RMSAs	0.0037cm	0.0041cm	-	-	-	-
Method→	**Present Method**	**Ref. [20]**	**Ref. [23]**	**Ref. [24]**	**Ref. [25]**	-
Analysis of CMSAs	0.30MHz	0.55 MHz	23.1 MHz	4.55 MHz	0.35 MHz	-
Method→	**Present Method**	**Ref. [15, 16, 17, 18, 19, 20, 21, 22, 23, 24, 25 and 26]**				
Synthesis of CMSAs	**0.0045 cm**	**No neural model is available in the literature [15-26]**				
Method→	**Present Method**	**Ref. [21]**	**Ref. [23]**	**Ref. [24]**	**Ref. [25]**	-
Analysis of TMSAs	**1.3730 MHz**	1.53 MHz	18.33 MHz	1.80 MHz	1.87 MHz	-
Method→	**Present Method**	**Ref. [22]**	-	-	-	-
Synthesis of TMSAs	**0.0051cm**	0.0090 cm	-	-	-	-

A comparison between the present method results and the results computed in previous neural models [19-26] is also given in Table 6. This table shows that in the neural models [19], [23], [24], [25] and [26] the average absolute error for analyzing the rectangular MSAs has been calculated as 16.33 MHz, 71.88 MHz, 6.17 MHz, 16.88 MHz and 50.0 MHz whereas in present model it is only 3.2 MHz. In case of synthesizing the rectangular MSAs, the model [26] is having the average absolute error of 0.0041cm whereas in present model it is calculated as 0.037cm. In case of analyzing the circular MSAs, the proposed method is having the average absolute error of only 0.30 MHz whereas in the methods [20], [23], [24] and [25] it has been calculated as 0.55 MHz, 23.1 MHz, 4.55 MHz and 0.35 MHz respectively. For synthesizing the circular MSAs, the present model is having the average absolute error of 0.0045cm whereas there is no neural model proposed for synthesizing the circular MSAs in the open literature [19-26]. For analyzing the equilateral triangular MSAs, the models [21], [23], [24] and [25] are having average absolute error as: 1.53 MHz, 18.33 MHz, 1.80 MHz and 1.87 MHz, respectively whereas in the present model, it is calculated as 1.373 MHz and in case of synthesizing triangular MSAs, the average absolute error in testing patterns of the present method is only 0.0051cm whereas in the model [22] it has been mentioned as 0.0090cm. It is clear from the comparison given in Table 5 that the computed results by the proposed neural model are more accurate than the neural results of other scientists [19-26].

V. CONCLUSION

In this paper, authors have proposed a simple and accurate generalized neural approach for computing seven different parameters of three different microstrip antennas as there is no such neural approach suggested in the referenced literature even for computing more than three parameters, simultaneously. The approach is capable for synthesizing the rectangular, circular and triangular MSAs, simultaneously as there is no neural model available in the literature for synthesizing the circular MSAs using neural networks and/or synthesizing the rectangular, circular and triangular MSAs simultaneously. As the proposed neural model has produced more encouraging results for all seven different cases simultaneously without having any complicated structure of the hidden nodes, hence it can be recommended to include in antenna CAD (computer aided design) algorithms. The concept of the proposed approach is so simple and accurate that it can be generalized for any number of parameters depending upon the number of hidden nodes and the distribution of the input-output patterns. The approach can be very useful to antenna designers to accurately predict any desired parameter (i.e. resonance frequency of rectangular MSAs, width of rectangular MSAs, length of rectangular MSAs, resonance frequency of circular MSAs, radius of circular MSAs, resonance frequency of triangular MSAs or side-length of equilateral triangular MSAs) of the microstrip antennas by inputting its corresponding parameters within a friction of a second after doing training of proposed generalized neural method successfully.

In general, computing 7-different performance parameters may require 7-different neural networks modules, whereas in the present work, only one module is fulfilling the requirement of 7-independent modules. Hence, the present approach has been considered more generalized in this sense.

REFERENCES

[1] I. J. Bahl and P. Bhartia, *Microstrip Antennas*. Dedham, MA: Artech House, 1980.

[2] E. Chang, S.A. Long and W.F. Richards, "An experimental investigation of electrically thick rectangular microstrip antennas," *IEEE Trans on Antennas and Propagat,* Vol. 34, pp.767-72, 1986.

[3] K. R. Carver, "Practical analytical techniques for the microstrip antennas," Proceedings of workshop on printed circuit antenna technology", New Mexico State University, Las Cruces, pp. 7.1-7.20, 1979.

[4] M. Kara, "The resonant frequency of rectangular microstrip antenna elements with various substrate thicknesses," *Microw Opt Technol Lett*, Vol. 11, pp. 55-59, 1996.

[5] M. Kara, "Closed-form expressions for the resonant frequency of rectangular microstrip antenna elements with thick substrates," *Microw Opt Technol Lett*, Vol. 12, pp. 131-136, 1996.

[6] J. S. Dahele and K.F. Lee, "Effect of substrate thickness on the performance of a circular-disk microstrip antennas," *IEEE Trans Antenna and Propagat*, Vol. 31, pp. 358-364, 1983.
[7] J. S. Dahele and K.F. Lee, "Theory and experiment on microstrip antennas with air-gaps," *Proceedings of IEE conference*, Vol. 132, pp. 455-460, 1985.
[8] K. R. Carver, "Practical analytical techniques for the microstrip antennas," *Proceedings of workshop on printed circuit antennas,* New Mexico State University, 1979.
[9] K. Antoszkiewicz and L. Shafai, "Impedance characteristics of circular microstrip patches," *IEEE Trans Antenna and Propag*, Vol. 38, pp. 942-946,1990.
[10] J. Q. Howell, "Microstrip antennas", *IEEE Trans Antenna and Propagat*, Vol. 23, 90-93, 1975.
[11] T. Itoh and R. Mittra, "Analysis of a microstrip disk resonator," *Arch Electron Ubertrugungs*, Vol. 27, pp. 456-458, 1973.
[12] F. Abboud, J.P. Damiano and A. Papiernik, "New determination of resonant frequency of circular disc microstrip antennas: application to thick substrate," *Electron Lett*, Vol. 24, pp. 1104-1106, 1988.
[13] W. Chen, K. F. Lee and J. S. Dahele, "Theoretical and experimental studies of the resonant frequencies of the equilateral triangular microstrip antennas," *IEEE Trans on Antennas and Propag*, Vol. 40, pp. 1253-1256, 1992.
[14] J. S. Dahele and K. F. Lee, "On the resonant frequencies of the triangular patch antennas," *IEEE Trans on Antenna and Propag,* Vol. 35, pp. 100-101, 1987.
[15] Q. J. Zhang and K.C. Gupta, *Neural Networks for RF and Microwave Design*, Artech House Publishers, 2000.
[16] P. M. Watson and K.C. Gupta, "EM-ANN models for microstrip vias and interconnects in multilayer circuits," *IEEE Trans Microw Theory Tech* Vol. 44, pp. 2495-503, 1996.
[17] P. M. Watson and K.C. Gupta, "Design and optimization of CPW circuits using EM-ANN models for CPW components", *IEEE Trans on Microw Theory and Tech*, Vol. 45, pp. 2515-2523,1997.
[18] P. M. Watson, K. C. Gupta and R. L Mahajan, "Development of knowledge based artificial neural network models for microwave components," *IEEE Int Microwave Dig*, Vol. 1, pp. 9-12, 1998.
[19] D. Karaboga, K. Guney, S. Sagiroglu and M. Erler, "Neural computation of resonance frequency of electrically thin and thick rectangular microstrip antennas," *IEEE Proc-Microwave Antenna Propag*, Vol. 146, pp. 155-159, 1999.
[20] Seref Sagiroglu, Karim Guney and Mehmet Erler, "Resonant frequency calculation for circular microstrip antennas using artificial neural networks," *International Journal of RF, Microw and CAE*, Vol. 8, pp. 270-277, 1998.
[21] S. Sagiroglu and K. Guney, "Calculation of resonant frequency for an equilateral triangular microstrip antenna with the use of artificial neural networks," *Microw and Opt Technol Lett*, Vol. 14, pp. 89-93, 1997.
[22] R. Gopalakrishnan and N. Gunasekaran, Design of equilateral triangular microstrip antennas using artificial neural networks," *Proceedings of IEEE International Workshop on Antenna Technology: Small Antennas and Novel Metamaterials,* 2005.
[23] Karim Guney, Seref Sagiroglu and Mehmet Erler, "Generalized neural method to determine resonant frequencies of various microstrip antennas," *International Journal of RF and Microw CAE*, Vol. 12, pp. 131-139, 2002.
[24] K. Guney and N. Sarikaya, "A hybrid method based on combining artificial neural network and fuzzy interference system for simultaneous computation of resonance frequencies of rectangular, circular, and triangular microstrip antennas," *IEEE Trans on Antenna and Propag*, Vol. 55, pp. 659-668, 2007.
[25] K. Guney and N. Sarikaya, "Concurrent neuro-fuzzy systems for resonant frequency computation of rectangular, circular, and triangular microstrip antennas," *Progress in Electromagnetics Research*, Vol. 84, pp. 253-277, 2008.
[26] Nurhan Turker, Filiz Gunes, and Tulay Yildirim, "Artificial neural design of microstrip antennas," *Turk J Elec. Engin*, Vol. 14, 2006.
[27] Taimoor Khan and Asok De, "Computation of different parameters of triangular patch microstrip antennas using a common neural model," *International Journal of Microwave and Optical Technology*, Vol. 5, pp. 219-224, 2010.
[28] Taimoor Khan and Asok De, "A common neural approach for computing different parameters of circular patch microstrip antennas," *International Journal of Microwave and Optical Technology*, Vol. 6, pp. 259-262, 2011.
[29] M. V. Schneider, "Microstrip lines for microwave integrated circuits," *Bell. Syst. Tech. J.,* Vol. 48, pp. 1421-1444, 1969.
[30] E. O. Hammerstad, "Equations for microstrip circuits design," *Proceedings of fifth European Microwave conference*, Hamburg, pp. 268-272, Sept. 1975.
[31] L. C. Shen, S. A. Long, M. R. Allerding, and M. D. Walton, "Resonant frequency of a circular disc, printed-circuit antenna," *IEEE Trans. Antennas Propagat*, Vol. 25, pp. 595-596, 1977.
[32] J. Helszajn, and D. S. James, "Planer triangular resonators with magnetic walls", *IEEE Trans. on Microwave Theory and Tech*, Vol. 26, pp. 95-100, 1978.
[33] S. Chen, C.F.N. Cowan and P.M. Grant, "Orthogonal least squares learning algorithm for radial basis function networks," *IEEE Trans on Neural Networks*, Vol. 2, pp. 302-309, 1991.
[34] Demuth, and M. Beale, "Neural network tool box for use with MATLAB", User's Guide (Fifth Edition), The Math works, Inc., 1998.
[35] P. E. Gill, W. Murray, and M. H. Wright, *Practical Optimization*, Academic Press, New York, 1981.
[36] L. E. Scales, *Introduction to Non-Linear Optimization*, Springer-Verlag New York, 1985.
[37] M. T. Hagan and M. Menhaj, "Training feed forward networks with the Marquardt algorithms," *IEEE Trans. on Neural Networks*," Vol. 5, pp. 989-993, 1994.
[38] S. Haykin, "Neural Networks: A Comprehensive Foundation". Prentice-Hall, 1999.
[39] J. W. Bandler, and M. H. Bakr, "A hybrid aggressive space mapping algorithm for EM optimization," *IEEE Trans. Microwave Theory Tech.*, Vol. MTT-47, pp. 2440-2440, 1999.

ESTIMATING PROJECT DEVELOPMENT EFFORT USING CLUSTERED REGRESSION APPROACH

Geeta Nagpal[1], Moin Uddin[2] and Arvinder Kaur[3]

[1]Dept. of Computer Science and Engg,
National Institute of Technology, Jalandhar
sikkag@gmail.com
[2]Pro Vice Chancellor, Delhi Technological University, Delhi
prof_moin@yahoo.com
[3]University School of Information Technology, GGSIPU, Delhi
arvinderkaurtakkar@yahoo.com

ABSTRACT

Due to the intangible nature of "software", accurate and reliable software effort estimation is a challenge in the software Industry. It is unlikely to expect very accurate estimates of software development effort because of the inherent uncertainty in software development projects and the complex and dynamic interaction of factors that impact software development. Heterogeneity exists in the software engineering datasets because data is made available from diverse sources. This can be reduced by defining certain relationship between the data values by classifying them into different clusters. This study focuses on how the combination of clustering and regression techniques can reduce the potential problems in effectiveness of predictive efficiency due to heterogeneity of the data. Using a clustered approach creates the subsets of data having a degree of homogeneity that enhances prediction accuracy. It was also observed in this study that ridge regression performs better than other regression techniques used in the analysis.

KEYWORDS

Software estimation, Clustering, Grey relational analysis, Feature weighted Grey relational based clustering

1. INTRODUCTION

Development of software is a creative process where each person's efficiency is different. It is initially difficult to plan and estimate as most software projects have deficient information and vague associations amongst effort drivers and the required effort. Software developers and researchers are using different techniques and are more concerned about accurately predicting the effort of the software product being developed.

Most commonly used algorithmic models for software cost estimation include Boehm's COCOMO [1], Albrecht's Function Point Analysis [2], and Putnam's SLIM [3]. These models require some cost drivers to estimate the effort of the project. In recent years, a number of soft computing and computationally intelligent techniques have been proposed in order to handle the unpredictability and inherent uncertainty contributed by cost drivers' judgment and environment

Jan Zizka (Eds) : CCSIT, SIPP, AISC, PDCTA - 2013
pp. 493–507, 2013. © CS & IT-CSCP 2013 DOI : 10.5121/csit.2013.3654

complexity of the projects. These techniques include artificial neural network, genetic algorithm, support vector regression, genetic programming, neuro-fuzzy inference system and case base reasoning. They use the historical datasets of completed projects as training data and predict the values for new project's effort based on previous training. Though, a significant improvement has been achieved using soft computing techniques in software cost estimation, yet there exist some limitations due to the heterogeneity in the datasets.

Soft computing techniques estimate accurately if there is some relationship between the tuples of the dataset. Due to this heterogeneity that exists amongst software projects, these techniques are not able to estimate optimally. This heterogeneity of data can be reduced by clustering the data into some similar groups. The goal of clustering is to create the groups of data that have similar characteristics. The clustering divides the data set X into *k* disjoint subsets that have some dissimilarity between them.

A clustered regression approach has been proposed in this study in order to generate more efficient estimation sub models. A feature weighted grey relational based clustering method has been integrated with regression techniques. The feature weighted grey relational clustering algorithm uses grey relational analysis for weighting features and also for clustering. The results obtained showed that clustering could decrease the effect of irrelevant projects on accuracy of estimations. Cluster specific regression models for the four publicly available data sets are generated. Empirical results have shown that regression when applied on clustered data provides some outstanding results, thus indicating that the methodology has great potential and can be used for software effort estimation. The results are subjected to statistical testing using Wilcoxon signed rank test and Mann_Whitney U Test.

The rest of the paper is organized as follows. Section 2 reviews some related works on clustering algorithm and GRG as a similarity measure for feature weighting. Section 3, introduces the modeling techniques. Further, in Section 4 we present the proposed methodology. Section 5, gives description of the data sets used in the study and the experimental results that demonstrate the use of proposed clustered regression approach in software effort estimation. In the end the conclusion is made in Section 6.

2. REVIEW OF LITERATURE

A number of data clustering techniques have been developed to find the optimal subsets of data from the existing datasets [4],[5],[6]. The main aim of clustering is to partition an unlabeled data set into subsets according to some similarity measure, called unsupervised classification. Clustering algorithms can be categorized into two main families: input clustering and input-output clustering [7]. In input clustering algorithms all the attributes are considered as independent. Hard *c*-means [8] and fuzzy *c*-means [9] algorithms fall into this category. In the case of input-output clustering each multi-attribute data point is considered as a vector of independent attribute with some corresponding dependent value. Let $S = \{(x_1,y_1), (x_2,y_2) ,\ldots (x_n, y_n)\}$ be a set of unlabelled input-output data pairs. Each independent input vector $x_i = [x_{1i}, x_{2i},\ldots x_{ki}]$ has a corresponding dependent value y_i. Research work has been done to motivate this category of classification [10],[11].

Kung and Su [12] developed an effective approach to establish affine Takagi-Sugeno (T-S) fuzzy model for a nonlinear system from its input – output data. Chunheng, Cui and Wang [13] proposed FCM-SLNMM clustering algorithm, consisting of two stages. The FCM algorithm was applied in the first stage and supervised learning normal mixture model was applied in the second stage. The clustering results of the first stage were used as training data. The experiments on the real world data from the UCI repository showed that the supervised learning normal mixture

model can improve the performance of the FCM algorithm sharply. Lin and Tsai [14] proposed a hierarchical grey clustering approach in which the similarity measure was a globalized modified grey relational grade instead of traditional distances. Chang and Yeh [15] generalized the concept of grey relational analysis in order to develop a technique for analyzing the similarity between given patterns. They also proposed a clustering algorithm to find cluster centers of a given dataset.

In this study, GRA a technique of GST which utilizes the concept of absolute point-to-point distance between features [16],[29] has been applied. GST a recently developed system engineering theory, was first established by Deng [18],[19],[20]. It draws out valuable information by generating and developing the partially known information. So far, GST has been applied in different areas of image processing [23], mobile communication [24], machine vision inspection [25], decision making [26], stock price prediction [27] and system control [28]. The success of GST motivated us to investigate its application in software effort estimation.

3. MODELING TECHNIQUES

The data available for software cost estimation is inherently non linear and hence accurate estimation of effort is difficult. Efficient estimation can be achieved if this non linearity that exists can be treated by tracing relationships among data values. In this study, we try to reduce the heterogeneity by applying feature weighted grey relational clustering methodology.

3.1 Regression

As discussed, a large number of techniques have been applied to the field of software effort estimation. The aim of this study is to assess which regression techniques perform best to estimate software effort. The following techniques are considered.

3.1.1 Ordinary Least Square Regression

It is the most popular and widely applied technique to build software cost estimation models. According to principle of least squares the `best fitting' line is the line which minimizes the deviations of the observed data away from the line. The regression parameters for the least square line, are estimates of the unknown regression parameters in the model. This is referred to as multiple linear regression and is given by:

$$y_i = \beta_0 + \beta_1 x_{i,1} + ...\beta_k x_{i,k} + \varepsilon_i \quad (1)$$

where, y_i is a dependent variable where as $x_1, x_2, \ldots\ldots x_k$ are k independent variables. β_o is the y intercept, β_1, β_2 are the slope of y, ε_i is the error term.

3.1.2 Ridge Regression (RR)

RR is an alternative regression technique that tries to address the potential problems with OLS that arise due to highly correlated attributes. In regression, the objective is to “explain” the variation in one or more “response variables”, by associating this variation with proportional variation in one or more “explanatory variables”, but the problem arises when the explanatory variables vary in similar ways reducing , their collective power of explanation. The phenomenon is known as *near collinearity*. As the different variables are correlated the covariance matrix XX will be nearly singular and as a result the estimates will be unstable. A small variation in error will have large impact on $\hat{\beta}$. Ridge regression reduces the sensitivity by adding a number δ to

the elements on the diagonal of the matrix to be inverted. δ is called the ridge parameter and it yields the following estimator of β.

$$\hat{\beta}_{\delta} = (X'X + \delta I_n)^{-1}(X'e) \tag{2}$$

where, I_n represents the identity matrix of rank n.

3.1.3 Forward Stepwise Regression

The purpose of stepwise regression is to generate regression model in which the detection of most predictive variables is carried out. It is carried out by a series of F tests. The method evaluates the independent variables at each step, adding or deleting them from the model based on user-specified criteria. In the first step, each of the independent variables are evaluated individually and the variable that has the largest F value greater than or equal to the F to enter value, is entered into the regression equation. In the subsequent steps, when a variable is added to the model based on their F value, the method also examines variables included in the model based on F to remove criteria, and if any variables are found they are removed.

3.1.4 Backward Stepwise Regression

The backward stepwise elimination procedure is basically a series of tests for significance of independent variables. The process starts with the maximum model, it eliminates the variable with the highest p -value for the test of significance of the variable, conditioned on the p -value being bigger than some pre-determined level (say, 0.05). In the next step, it fits the reduced model after having removed the variable from the maximum model, and also removes from the reduced model the variable with the highest p-value for the test of significance of that variable (if p>=0.05) and so on. The process ends when no more variables can be removed from the model at significance level 5%.

3.1.5 Multiple Adaptive Regression Splines(MARS)

MAR splines focuses on the development and deployment of accurate and easy-to-understand regression models. The MAR splines model is designed to predict continuous numeric and high quality probability models. MAR spline model is a regression model which automatically generates non-linearities and interactions between variables and is thus a promising technique to be used for software effort estimation[21]. MAR splines fits the data to the following equation.

$$e_i = b_0 + \sum_{k=1}^{K} b_k \Pi_{i=1}^{L} h_i(x_i(j)) \tag{3}$$

In this b_o and b_k are the intercept and slope. Parameters $h_i(x_i(j))$ are the hinge functions. They take the form *max (0, x_i (j)-b)* where, b is the knot. MAR splines is a multiple piece wise linear regression by adding multiple hinge functions.

3.2 Grey Relational Analysis

GRA is comparatively a novel technique in software estimations. It is used for analyzing the relationships that exists between two series. The magnetism of GRA to software effort estimation shoots from its flexibility to model complex nonlinear relationship between effort and cost drivers [16].

Grey Relational Grade by Deng's Method [18],[19],[20]

GRA is used to quantify all the influences of various factors and the relationship among data series that is a collection of measurements [16].The three main steps involved in the process are:

Data Processing: The first step is the standardization of the various attributes. Every attribute has the same amount of influence as the data is made dimensionless by using various techniques like upper bound effectiveness, lower bound effectiveness or moderate effectiveness.

Upper-bound effectiveness (i.e., larger-the-better) is given by:

$$x_i^*(k) = \frac{x_i(k) - \min_i x_i(k)}{\max_i x_i(k) - \min_i x_i(k)} \tag{4}$$

where i=1,2,…,m and k=1,2,…,n.

Difference Series: GRA uses the grey relational coefficient to describe the trend relationship between an objective series and a reference series at a given point in a system.

$$\gamma(x_0(k), x_i(k)) = \frac{\Delta_{\min} + \zeta\Delta_{\max}}{\Delta_{o,i}(k) + \zeta\Delta_{\max}} \tag{5}$$

where;

$\Delta_{0,i}(k) = |x_0(k) - x_i(k)|$ is the difference of the absolute value between $x_0(k)$ and $x_i(k)$;

$\Delta_{min} = min_j min_k |x_0(k) - x_j(k)|$ is the smallest value of $\Delta_{0,j}$ $\forall j \in \{1, 2, \ldots, n\}$;

$\Delta_{max} = max_j max_k |x_0(k) - x_j(k)|$ is the largest value of $\Delta_{0,j}$ $\forall j \in \{1, 2, \ldots, n\}$; and

ζ is the distinguishing coefficient, $\zeta \in (0, 1]$.

The ζ value will change the magnitude of $\gamma(x_0(k), x_i(k))$. In this study the value of ζ has been taken as 0.5 [17].

Grey Relational Grade: GRG is used to find overall similarity degree between reference tuple x_o and comparative tuple x_i. When the value of GRG approaches 1, the two tuples are "more closely similar". When GRG approaches a value 0, the two tuples are "more dissimilar". The GRG $\Gamma(x_0, x_i)$ between an objective series x_i and the reference series x_0 was defined by Deng as follows:

$$\Gamma(x_0, x_i) = \frac{1}{n}\sum_{k=1}^{n} \gamma(x_0(k), x_i(k)) \tag{6}$$

4. PROPOSED METHODOLOGIES

4.1 Clustered regression using grey relational analysis

In this methodology, in order to reduce the heterogeneity that exists in the datasets, the initial focus is to partition datasets into subsets according to some similarity measure, called unsupervised classification. The proposed clustering algorithm uses grey relational analysis for feature selection as well as for clustering. In this the maximum mean grey relational grade

between data points acts as an objective function instead of the minimum distance used by *k*-means. The structural flow chart is shown in figure 1.

The three main steps involved in the algorithm are:
Step 1: Using Grey relational analysis for finding feature weights.
Step 2: Using Grey relational analysis for clustering the datasets based on these feature-weights.
Step 3: Applying regression techniques on the clustered datasets.
Step 4: Effort Prediction by Regression Techniques

The detailed algorithm is described as follows:

Using Grey Relational Analysis for finding feature weights.

Feature Selection by GRA [16]

a. *Construction of data:* The columns in each cluster dataset are treated as series . The effort series $x_e = \{e_1, e_2, e_3 ..... e_n\}$ is taken as the reference series and the attribute columns are regarded as objective series.
b. *Normalization:* Each data series is normalized according to equation 4, so that they have same degree of influence on the dependent variable "effort".
c. *Generation of Grey Relational Grade:* Grey relational grade(GRG) is calculated for each series wrt reference series according to equation 6.

The GRG's are generated, normalized and used as the corresponding features weight w_k.

Using Grey Relational Analysis for clustering the datasets based on these feature-weights.

After finding the weights of the features from the first step it applies the clustered approach based on grey relational analysis. The detailed algorithm is described as follows:

a. Weight of each feature is generated as described earlier.
b. Normalize the data with larger the better as per equation 4,
c. Calculate distance between data points based on weighted GRG
   - Consider the i^{th} data point as reference series x_o
   - All the other data points as the objective series, $\{ x_1, x_2, x_3, \ldots\ldots x_{n-1} \}$
   - Calculate the grey relational coefficient with ζ=0.5 [17].Calculate weighted GRG of the reference series and feature weight calculated as in step 1 for all objective series.
d. Randomly select the number of desired of clusters center c_k.
e. GRG distance from data points to cluster centers is used as a basis to select cluster members, for which it has maximum GRG value.
f. Update the cluster centers by selecting centers based on the maximum mean GRG, then repeat step *e*.
g. Repeat steps *e* and *f*, until there is no change in the cluster head updating or the difference between the mean is less than some predefined threshold value.

5. EXPERIMENTAL RESULTS

5.1 Dataset

In order to evaluate the models based upon the proposed methodology, four well established datasets from the Promise repository [22] have been used for validating our model. These datasets are Desharnais, Finnish, Albrecht and Maxwell. The descriptive statistics of the datasets are shown in Table 1 given below. All the datasets have a varied range of effort values. These

datasets have been treated individually as they have distinct features. Also the clusters from each dataset have been treated separately. The prediction accuracy for all the models with and without clustering are then compared. In order to measure the accuracy of the software estimation, we have used three most popularly used evaluation criteria in software engineering *i.e MMRE*, *MdMRE* and *Pred(n).*

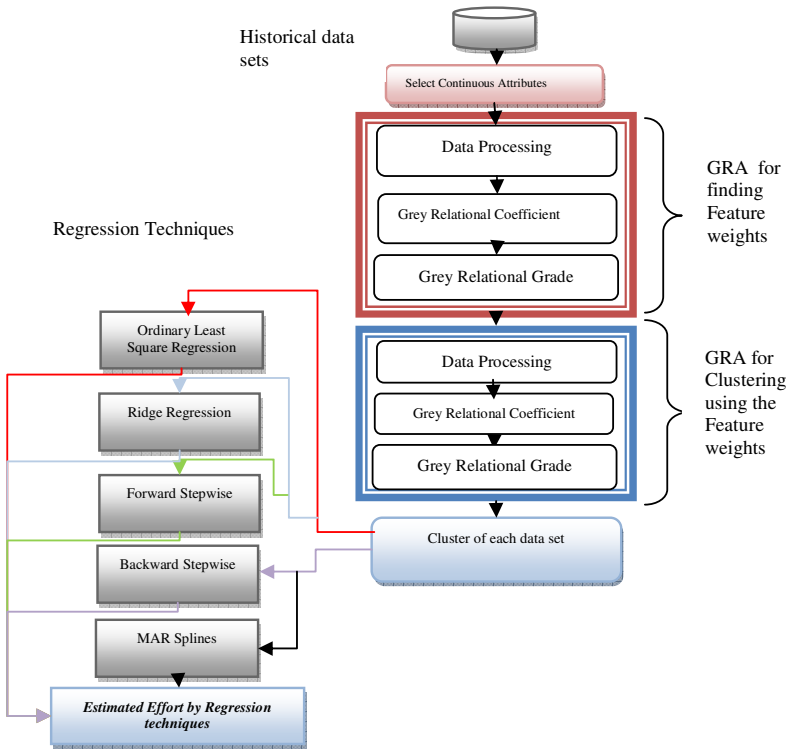

Figure1. Structural flowchart for feature weighted Grey Relational Clustering

Table1. Descriptive Statistics of the data sets

	Cases	Features	Effort Mean	Minimum (effort value)	Maximum (effort value)	Effort Std. Dev.
Albrecht	24	8	21.875000	0.50	105.20	28.417895
Desharnais	77	11	4833.9090	546	23940	4188.1851
Finnish	38	8	7678.2894	460	26670	7135.2799
Maxwell	62	23	8223	583	63694	10499.903

5.1.1 Comparison over Desharnais data set

The results obtained suggest that applying regression technique on clustered data produces more accurate estimation models than applying regression on the entire datasets. This is evident from the results obtained shown in Table 2. The *Pred(25)* accuracy has improved from 35.06 % to 50 % using OLS regression whereas, the *MMRE* and *MdMRE* has fallen from 0.5 to 0.32 and from 0.31 to 0.25 respectively. Similar observations can be notified from the table below for all other regression models also. Best results have been obtained on using the proposed feature weighted grey relational clustering.

Table 2. Prediction accuracy results (Desharnais data set)

	OLS	Ridge Regression	Forward Stepwise	Backward Stepwise	MAR Splines
			Desharnais		
MMRE	0.5	0.47	0.5	0.5	0.51
MdMRE	0.31	0.3	0.31	0.31	0.32
Pred(25)	35.06	41.56	37.66	37.66	35.06
			Desharnais(Cluster_1) using Grey Relational Clustering		
MMRE	0.32	0.35	0.33	0.39	0.39
MdMRE	0.25	0.23	0.24	0.21	0.20
Pred(25)	50	55.56	50	52.78	58.33

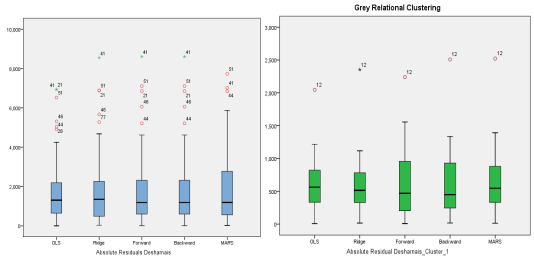

Figure 2. Boxplot of Absolute Residuals for Desharnais

The Boxplot of absolute residuals provide good indication of the distribution of residuals and can help better understand the mean magnitude of relative error and *Pred (25).*The results obtained were subjected to statistical tests using Wilcoxon Signed rank test and Mann Whitney U test.
The box plots of absolute residuals shown in figure 2 suggest that:

The medians for all regression techniques applied on Desharnais _Cluster are more close to zero, as it is clear from the values on the Y-axis, indicating that the residuals were closer to the minimum value. The Outliers are few and less extreme in cases of Desharnais_Clusters as compared to Desharnais data set. As the *p*-value in all the cases shown in Table 3 is greater 0.05 where in we conclude that the residuals obtained in all approaches are not significantly different from the test value zero. As a result, the proposed methods can be used for software effort estimation. The statistical tests were performed using SPSS 19 for windows.

Table 3. Wilcoxon signed rank test Test

	Desharnais		**Desharnais_Cluster_1 using Grey Relational**	
	Z	Asymp. Sig. (2-tailed)	Z	Asymp. Sig. (2-tailed)
OLS-Actual	-.419a	.675	-.236a	.814
Ridge – Actual	-.551a	.582	-.299a	.765
Forward - Actual	-.449a	.653	-.189a	.850
Backward- Actual	-.449a	.653	-.314a	.753
MARS– Actual	-.566a	.571	-.236a	.814

The results of Mann_Whitney U Test are provided in Table 4. Predictions obtained using the clustered approach presented statistically significant estimations.

Table 4. Results Mann-Whitney U Test

	Desharnais vs. Desharnais_Cluster_1 using Grey Relational Z
OLS Regression	-4.018
Ridge Regression	-4.079
Forward Stepwise	-4.252
Backward Stepwise	-4.227
MAR Splines	-4.240

5.1.2 Comparison over Finnish data set:

For the Finnish dataset, some significant results (as shown in Table 5.) were obtained on the clustered data. The *Pred(25)*accuracy improved from 36.84 % to 100 % using OLS regression whereas, the *MMRE* and *MdMRE* has fallen from 0.75 to 0.02 and from 0.36 to 0.02 respectively. Similar observations can be notified from the table below for all other regression models also.
The boxplot of absolute residuals for Finnish dataset and Finnish_cluster is shown in Figure 3. They suggest that:

The medians for all regression techniques applied on Finnish _Cluster are very close to zero, as it is clear from the values on the Y-axis, indicating that the estimates were closer to the minimum value. Outliers are less extreme in case of Finnish_Cluster. One sample Wilcoxon signed rank test has been applied in order to investigate the significance of the results by setting level of confidence to 0.05. From the results obtained as shown in Table 6, we can conclude that no significant difference exists between the residual median and hypothetical median.

Table 5. Prediction accuracy results (Finnish data set)

	OLS	**Ridge Regression**	**Forward Stepwise**	**Backward Stepwise**	**MAR Splines**
			Finnish		
MMRE	0.75	0.71	1.01	0.76	0.08
MdMRE	0.36	0.32	0.43	0.42	0.07
Pred(25)	36.84	36.84	36.84	36.84	97.37
			Finnish(Cluster_1) using Grey Relational Clustering		
MMRE	0.02	0.025	0.23	0.022	0.022
MdMRE	0.02	0.024	0.022	0.023	0.023
Pred(25)	100	100	100	100	100

Unsurprisingly, predictions based on clustered regression model presented statistically significant accurate estimations, measured using absolute residuals, confirmed by the results of boxplot of absolute residuals and also verified using Mann-Whitney U test (Table 7.)

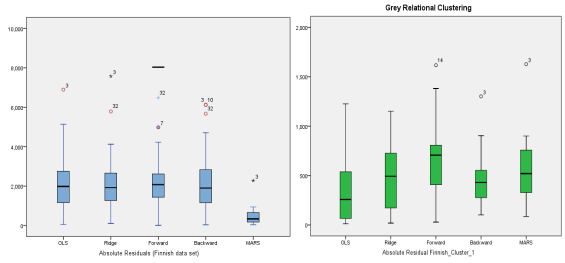

Figure 3. Boxplot of Absolute Residuals for Finnish

Table 6. Wilcoxon signed rank test

	Finnish		Finnish_Cluster_1 using Grey Relational	
	Z	AsympSig (2-tailed)	Z	Asymp.Sig. (2tailed)
OLS- Actual	-.268a	.788	-.408a	.683
Ridge – Actual	-.355a	.722	-.220b	.826
Forward- Actual	-.268a	.788	-.157b	.875
Backward- Actual	-.152a	.879	-.345a	.730
MARS– Actual	-.558a	.577	-.282a	.778

Table 7. Results Mann-Whitney U Test

	Finnish vs. Finnish_Cluster_1 using Grey Relational Z
OLS Regression	-2.022
Ridge Regression	-2.104
Forward Stepwise	-2.228
Backward Stepwise	-2.022
MAR Splines	-1.939

5.1.3 Comparison over Albrecht data set:

The results obtained using the proposed clustered regression approach produced more accurate models. This is evident from the *Pred(25)* accuracy that improved from 37.5 % to 85.71 % using OLS whereas, the *MMRE* and *MdMRE* has fallen from 0.9 to 0.09 and from 0.43 to 0.05 respectively. Similar observations can be notified for all other regression models also (Table 8).

Table 8. Prediction accuracy results (Albrecht data set)

	OLS	Ridge Regression	Forward Stepwise	Backward Stepwise	MAR Splines
			Albrecht		
MMRE	0.9	0.91	0.86	1	1.23
MdMRE	0.43	0.52	0.5	0.49	0.6
Pred(25)	37.5	37.5	41.67	37.5	29.17
	Albrecht(Cluster_1) using Grey Relational clustering				
MMRE	0.092	0.21	0.19	0.08	0.225
MdMRE	0.05	0.24	0.22	0.025	0.175
Pred(25)	85.71	50	57.14	85.71	57.14

The box plots of absolute residuals suggest that:

The medians for all regression techniques applied on Albrecht_Clusters are very close to zero, as it is clear from the values on the Y-axis, indicating that the residuals were closer to the minimum value. Outliers are less extreme in case of Finnish_Cluster.

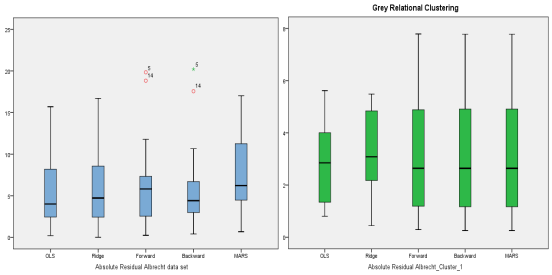

Figure 4. Boxplot of Absolute Residuals for Albrecht

The results of Wilcoxon signed rank conclude that no significant difference exists between the residual median and hypothetical median, thus indicating good predictions (Table 9.)

Table 9. Wilcoxon signed rank test

	Albrecht		**Albrecht_Cluster_1 using Grey Relational**	
	Z	Asymp.Sig. (2-tailed)	Z	Asymp.Sig (2-tailed)
OLS- Actual	-.029a	.977	-.031a	.975
Ridge – Actual	-.057a	.954	-.031a	.975
Forward - Actual	-.057a	.954	-.031a	.975
Backward Actual	-.086b	.932	-.031a	.975
MARS– Actual	-.029b	.977	-.031a	.975

Table 10. Results Mann-Whitney U Test

	Albrecht vs. Albrecht_Cluster_1 using Grey Relational Z
OLS Regression	-1.014
Ridge Regression	-1.014
Forward Stepwise	-.943
Backward Stepwise	-1.155
MAR Splines	-1.108

The results obtained using Mann-Whitney U test shown in Table 10, however didn't prove significant difference between the proposed approaches. This is because of the small size of the dataset. The data set comprises of 24 projects. It was divided into two clusters one with 20 projects and other with 4 projects. Clustered regression approach was applied on 20 projects.

5.1.4 Comparison over Maxwell Dataset

The results obtained in Table 11 using the proposed clustered regression approach produced more accurate models for Maxwell dataset also. This is evident from the Pred(25) accuracy that improved from 38.71 % to 51.51 % using OLS regression whereas, the *MMRE* and *MdMRE* has fallen from 0.59 to 0. 51 and from 0.38 to 0.24 respectively. For Ridge regression also, the *Pred(25)* accuracy has increased from 43.55% to 60.60% which is significant improvement, the *MMRE* and *MdMRE* has gone low from 0.54 to 0.33 and 0.3 to 0.18 respectively.

Table 11. Prediction accuracy results(Maxwell data set)

	OLS	Ridge Regression	Forward Stepwise	Backward Stepwise	MAR Splines
			Maxwell		
MMRE	0.59	0.54	0.53	0.59	0.7
MdMRE	0.38	0.3	0.32	0.33	0.46
Pred(25)	38.71	43.55	38.71	37.1	32.26
			Maxwell(Cluster_1) using Grey Relational Clustering		
MMRE	0.51	0.33	0.46	0.60	0.75
MdMRE	0.24	0.18	0.25	0.25	0.52
Pred(25)	51.51	60.60	48.48	48.48	24.24

The box plots of absolute residuals suggest that:

The medians for all regression techniques applied on Maxwell _Cluster are more close to zero, as it is clear from the values on the Y-axis, indicating that the estimates were closer to the minimum value. The medians are more skewed to the minimum value indicating that the predictions are good. Outliers are few and less extreme in case of Maxwell_Cluster as compared to entire dataset.

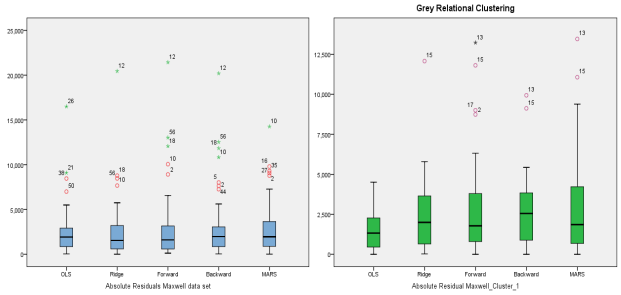

Figure 5. Boxplot of Absolute Residuals for Maxwell

Table 12. Wilcoxon signed rank test

	Maxwell		Maxwell_Cluster_1 using Grey Relational	
	Z	Asymp. Sig (2-tailed)	Z	Asymp. Sig (2-tailed)
OLS-Actual	-249a	.803	-.068a	.946
Ridge – Actual	-.508a	.611	-.616b	.538
Forward – Actual	-.691a	.490	-.068b	.946
Backward-Actual	-.831a	.406	-.023b	.982
MARS – Actual	-.109a	.913	-.205a	.838

Results of Wilcoxon signed rank test suggest that no significant difference exists between the residual median and hypothetical median. The results of Wilcoxon signed rank test are given in Table 12.

Concerning the statistical test based on Mann-Whitney U(Table 13), we found no significant difference between clustered regression approach and regression approach.

Table 13. Results Mann-Whitney U Test

	Maxwell vs. Maxwell_Cluster_1 using Grey Relational Z
OLS Regression	-1.431
Ridge Regression	-1.448
Forward Stepwise	-1.482
Backward Stepwise	-1.312
MAR Splines	-1.806

6. CONCLUSION

This work resolves the heterogeneity problems that exist in the datasets. In order to confirm the effectiveness of proposed work, four different data sets have been used for software estimation. Simulation results obtained provide a comparison of clustered regression approach over only regression. The results confirm that the proposed feature weighted grey relational clustering algorithm performed appreciably for software effort estimation. The statistical test based on Mann-Whitney U, further confirmed that statistical significant difference exists between the proposed clustered-regression models and regression models.

Further, this work can be extended by using clustered approach with different soft computing techniques with different similarity measures for feature selection. GRA can also be analyzed for feature subset selection Also, for enhanced efficiency in software estimation the techniques should be applied on large data sets with different clustering algorithms.

REFERENCES

[1] Boehm, B (1981) Software Engineering Economics Englewood Cliffs, NJ, Prentice Hall.
[2] Albrecht, A.J. & Gaffney, J.R. (1983) “Software measurement, source lines of code, and development effort prediction: a software science validation”, IEEE Transactions on Software Engineering, Vol. 9, No. 6, pp 639-648.
[3] Putnam, Lawrence H. (1978) "A General Empirical Solution to the Macro Software Sizing and Estimating Problem", IEEE Transactions on Software Engineering, Vol. SE-4, No. 4, pp 345-361.
[4] El-Zaghmouri, B. M. & Abu-Zanona, M. A. (2012) “Fuzzy C-Mean Clustering Algorithm Modification and Adaption for Application”, World of Computer Science and Information Technology Journal, ISSN: 2221-0741, Vol.2, No.1, pp 42-45.
[5] Lin, C. T. & Tsai, H. Y. (2005) “Hierarchical Clustering Analysis Based on Grey Relation grade”, Information and Management Sciences, Vol. 16, No. 1, pp 95-105.
[6] Wong, C.C. & Chen, C.C. (1998) “Data clustering by grey relational analysis”, J. Grey Syst, Vol. 10, No. 3, pp 281-288.
[7] Hu, Y.C., Chen, R. S., Hsu, Y. T., & Tzebg, G. H. (2002) “Grey self-organizing feature maps”, Neuro computing, Vol. 48, No.1–4, pp 863-877.
[8] Duda, R.O., & Hart, P.E. (1973) Pattern classification and scene analysis, John Wiley &Sons, Inc., New York.
[9] Bezdek, J. C., Ehrlich, R. & Full, W. (1984) “FCM: The Fuzzy c- Means Clustering Algorithm”, Computers & Geoscience, Vol. 10, No. 2-3, pp 191-203.
[10] Runkler, T.A. & Bezdek, J.C. (1999) “Alternating cluster estimation: a new tool for clustering and function approximation”, IEEE Trans. Fuzzy Syst., Vol. 7, No. 4, pp 377-393.
[11] Pedrycz, W.(1996) “Conditional fuzzy c-means”, Pattern Recogn. Lett.,Vol. 17, No. 6, pp 625-632.
[12] Kung C. C & Su J. Y. (2007) “Affine Takagi-Sugeno fuzzy modeling algorithm by Fuzzy c-regression models clustering with a novel cluster validity criterion”, IET Control Theory Appl., pp. 1255 – 1265.

[13] Wang, W., Wang, C., Cui, X. & Wang, A. (2008) "A clustering algorithm combine the FCM algorithm with supervised learning normal mixture model", ICPR 2008, pp 1-4.
[14] Lin, C. T. & Tsai, H. Y. (2005) "Hierarchical Clustering Analysis Based on Grey Relation grade", Information and Management Sciences, Vol. 16, No. 1, pp 95-105.
[15] Chang, K. C. & Yeh, M. F. (2005) "Grey Relational Based Analysis approach for data clustering", IEEE Proc.-Vis. Image Signal Process, Vol.152, No.2.
[16] Song, Q., Shepperd M., Mair C. (2005) "Using Grey Relational Analysis to Predict Software Effort with Small Data Sets". Proceedings of the 11th International Symposium on Software Metrics (METRICS'05), pp 35-45.
[17] Azzeh, M., Neagu, D. & Cowling, P. I., (2010) "Fuzzy grey relational analysis for software effort estimation", Journal of Empirical software Engineering, Vol.15, No.1, **[doi:**10.1007/s10664-009-9113-0]
[18] Deng, J. L. (1982) "Control problems of grey system", System and Control Letters, Vol. 1, pp 288-94.
[19] Deng, J. (1989) "Introduction to Grey System theory", The Journal of Grey System, Vol.1, No.1, pp 1-24.
[20] Deng, J. (1989) "Grey information space", The Journal of Grey System, Vol.1, No.1, pp 103-117.
[21] MATLAB® Documentation, http://www.mathworks.com/help/techdoc/
[22] PROMISE Repository of empirical software engineering data http://promisedata.org/ repository.
[23] Jou, J. M , Chen, P. Y & Sun, J. M. (1999) "The gray prediction search algorithm for block motion estimation", IEEE Transactions on Circuits and Systems for Video Technology, Vol.9, No.6, pp 843-848.
[24] Su, S. L., Su, Y. C. & Huang, J. F. (2000) "Grey-based power control for DS-CDMA cellular mobile systems", IEEE Transactions on Vehicular Technology, Vol.49, No.6, pp 2081-2088.
[25] Jiang, B.C, Tasi, S. L & Wang, C. C. (2002) "Machine vision-based gray relational theory applied to IC marking inspection", IEEE Transactions on Semiconductor Manufacturing, Vol.15, No.4, pp 531-539.
[26] Luo, R. C, Chen, T. M & Su, K. L. (2001) "Target tracking using a hierarchical grey-fuzzy motion decision making method", IEEE Transactions on Systems, Man and Cybernetics, Part A, Vol.31, No.3, pp 179-186.
[27] Wang, Y. F. (2003) "On-demand forecasting of stock prices using a real-time predictor", IEEE Transactions on Knowledge and Data Engineering, Vol.15, No.4, pp 1033-1037.
[28] Huang, S. J, Huang, C. L. (2000) "Control of an inverted pendulum using grey prediction model", IEEE Transactions on Industry Applications, Vol.36, No.2, pp 452-458.
[29] Li, G, Ruhe, J, Emran, A. Al & Richter, M.M. (2007) "A flexible method for software effort estimation by analogy", Empirical Software Engineering, Vol.12, pp 65-106. [doi:10.1007/s10664-006-7552-4]

Authors

Geeta Nagpal

Geeta Nagpal, Ph D in Computer Science & Engineering from National Institute of Technology, Jalandhar, INDIA. She completed her Master's degree in Computer Science from Punjab Agricultural University, Ludhiana. She is presently working as Associate Professor in the Department of Computer Science and Engineering at National Institute of Technology, Jalandhar. Her research interests are Software Engineering, Databases and Data mining.

Prof. Moin Uddin

Prof. Moin Uddin, Pro Vice Chancellor, Delhi Technological University, Delhi ,INDIA. He obtained his B.Sc. Engineering and M.Sc. Engineering (Electrical) from AMU, Aligarh in 1972 and 1978 respectively. He obtained hid Ph. D degree from University of Roorkee, Roorkee in 1994. Before Joining as the Pro Vice Chancellor of Delhi Technological University, he was the Director of NIT, Jalandhar for five years. He has worked as Head Electrical Engineering Department and Dean Faculty of Engineering and Technology at Jamia Millia Islamia (Central University) New Delhi. He supervised 25 Ph. D thesis and more than 30 M.Tech dissertations. He has published more than 40 research papers in reputed journals and conferences. Prof. Moin Uddin holds membership of many professional bodies. He is a Senior Member of IEEE.

Dr. Arvinder Kaur

Dr. Arvinder Kaur, Professor, University School of IT, Guru Gobind Singh Indraprastha University, Delhi, India. She completed her masters degree in Computer Science from Thapar Institute of Engineering and Technology and Ph D from Guru Gobind Singh Indraprastha University, Delhi. Prior to joining the school, she worked with Dr. B. R. Ambedkar Regional Engineering College, Jalandhar and Thapar Institute of Engineering and Technology. Her research interests include Software Engineering, Object-Oriented Software Engineering, Software Metrics, Microprocessors, Operating Systems, Artificial Intelligence, and Computer networks. She is a lifetime member of ISTE and CSI. She is also a member of ACM. She has published 45 research papers in national and international journals and conferences. Her paper titled, "Analysis of object oriented Metrics"was published as a chapter in the book Innovations in Software Measurement (Shaker-Verlag, Aachen 2005).

SCIENTIFIC REPORTS

OPEN

SUBJECT AREAS:
ELECTROCATALYSIS
BIOSENSORS
NANOSENSORS
MICROFLUIDICS

Received
22 May 2013

Accepted
27 August 2013

Published
27 September 2013

Correspondence and requests for materials should be addressed to V.V.A. (ved.varun@gmail.com; agrawalvv@nplindia.org); C.K. (cgkim@cnu.ac.kr); R.J. (renujohn@iith.ac.in) or B.D.M. (bansi.malhotra@gmail.com)

Highly Efficient Bienzyme Functionalized Nanocomposite-Based Microfluidics Biosensor Platform for Biomedical Application

Md. Azahar Ali[1,2], Saurabh Srivastava[1], Pratima R. Solanki[1,5], Venu Reddy[3], Ved V. Agrawal[1], CheolGi Kim[3], Renu John[2] & Bansi D. Malhotra[1,3,4]

[1]Department of Science and Technology Centre on Biomolecular Electronics, Biomedical Instrumentation Section, CSIR-National Physical Laboratory, Dr. K. S. Krishnan Marg, New Delhi-110012, India, [2]Indian Institute of Technology Hyderabad, Ordnance Factory Estate, Yeddumailaram, Hyderabad, Andhra Pradesh 502205, India, [3]Center for NanoBioengineering and SpinTronics, Department of Materials Science and Engineering, Chungnam National University, Daejeon 305-764, South Korea, [4]Department of Biotechnology, Delhi Technological University, Shahbad Daulatpur, Main Bawana Road, Delhi1 110042, India, [5]Special Centre for Nanosciences, Jawaharlal Nehru University, New Delhi-110067, India.

This report describes the fabrication of a novel microfluidics nanobiochip based on a composite comprising of nickel oxide nanoparticles (nNiO) and multiwalled carbon nanotubes (MWCNTs), as well as the chip's use in a biomedical application. This nanocomposite was integrated with polydimethylsiloxane (PDMS) microchannels, which were constructed using the photolithographic technique. A structural and morphological characterization of the fabricated microfluidics chip, which was functionalized with a bienzyme containing cholesterol oxidase (ChOx) and cholesterol esterase (ChEt), was accomplished using X-ray photoelectron spectroscopy (XPS) and scanning electron microscopy. The XPS studies revealed that 9.3% of the carboxyl (COOH) groups present in the nNiO-MWCNT composite are used to form amide bonds with the NH_2 groups of the bienzyme. The response studies on this nanobiochip reveal good reproducibility and selectivity, and a high sensitivity of 2.2 mA/mM/cm^2. This integrated microfluidics biochip provides a promising low-cost platform for the rapid detection of biomolecules using minute samples.

The ability to monitor desired biomolecules in real time via a microfluidics biochip or a micro-total analytical system (μ-TAS) has aroused considerable interest from the point-of-care (POC) diagnostics community[1,2]. The small geometry of a microfluidics biochip offers many advantages over macroelectrode-based biomedical devices due to its improved mass transport and diffusion, high signal-to-noise ratio, and low detection limit[3,4]. The characteristics of nanocomposites and the intrinsic benefits of microfluidics, including their laminar flow, low consumption of costly reagents and power, portability, minimal need for handling biohazardous materials, fast response time, multiplexing, and parallelization, are advantageous for the fabrication of a biochip[5,6]. The precise liquid control that occurs in a microfluidic platform is essential for the fabrication of microchannels. Polydimethylsiloxane (PDMS) is an attractive polymeric material for the fabrication of microchannels, which can be temporarily sealed with a glass substrate via conformal contact mediated by *Van der Waals* force. Additionally, the hydrophobic properties of PDMS provide good chemical compatibility with organic solvents and cause negligible swelling[5,6].

The microfluidics biochip is known to have many applications, such as enzymatic kinetics and immunoassay analyses; DNA amplification; and cell sorting, culturing, and counting[7]. However, the integration of the microfluidics biochip with a nanostructured material continues to be a challenge. In this context, 1D structures, such as nanotubes, nanowires, and nanocomposites, composed of carbon materials can play an important role in medicinal chemistry and diagnostics, including the creation of biochips for *in vitro* and *in vivo* investigations[3,8–13]. Multiwalled carbon nanotubes (MWCNTs), allotrope of carbon play an important role towards the development of biochips because of their high carrier mobility and tensile strength, as well as their high aspect ratio, which leads to quantum electron transport[12]. In addition, MWCNTs are non-reactive (like graphite) except at the nanotube caps (the tips when they are not cut), where the dangling bonds and edge-plane-like sites located at both ends are

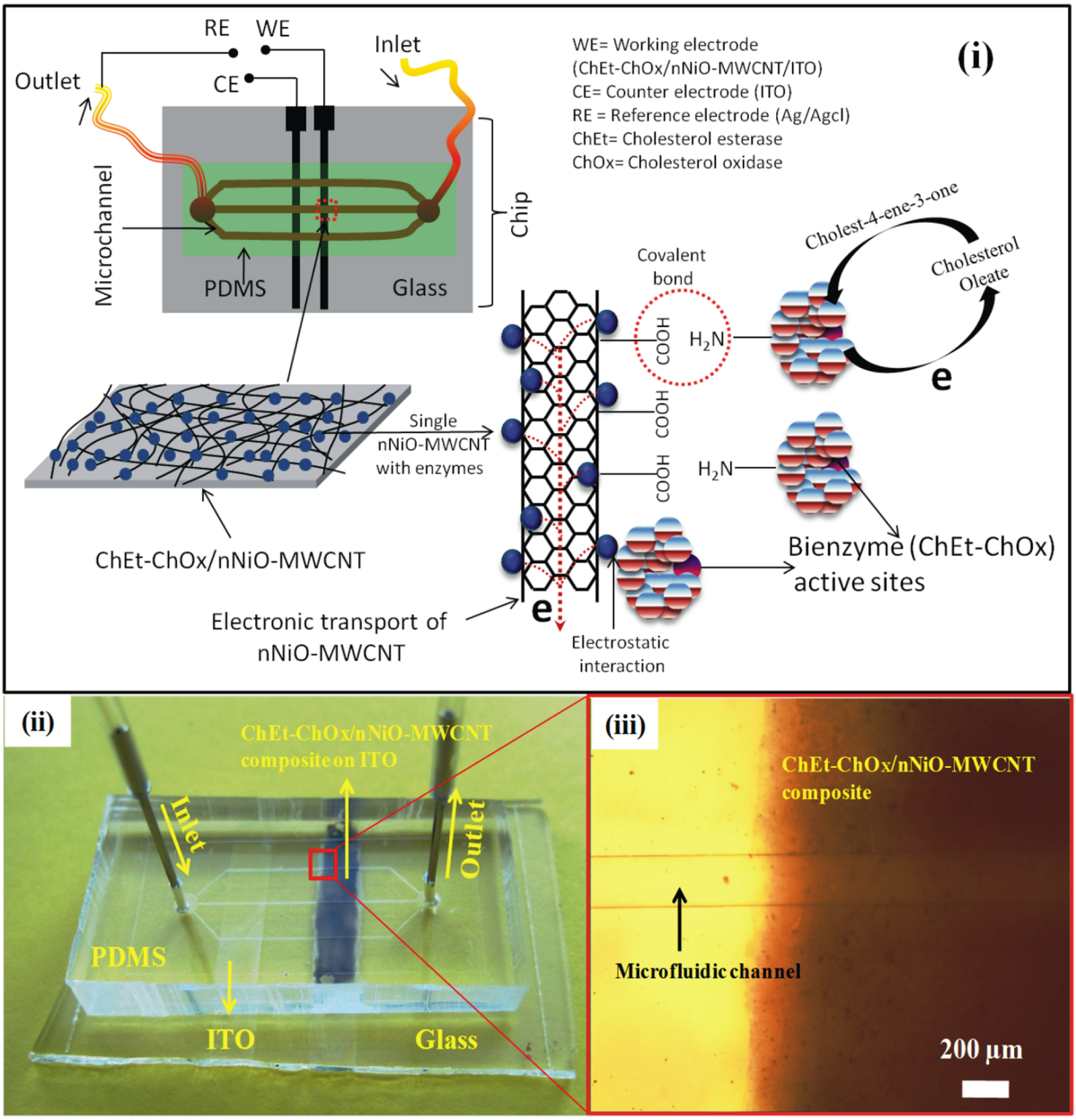

Figure 1 | (i) The schematic of the microfluidic biochip used for total cholesterol detection (the ordered arrangement of this microsystem is assumed). (ii) The photograph of real microfluidic biochip for cholesterol detection and (iii) the enlarged view of optical microscopic image of the microfluidic biochip.

open to reactions[14]. The MWCNTs are known to produce changes in energy bands close to the Fermi level[15,16]. The exciting electronic properties and high electrochemical reactivity of MWCNTs suggest that fast electron transfer reaction occurs when they are used as the electrode in an electrochemical biochip[15,16]. Lin et al. have developed a microfluidics electrochemical sensor for on-site, non-invasive monitoring of lead and chlorophenols[17]. Wisitsoraat et al. have developed an electrochemical biochip for cholesterol detection that has a sensitivity of 0.0512 nA/mg/dl, which is attributed to the direct growth of CNT on glass[18]. However, MWCNTs are known to agglomerate via *Van der Waals* interactions, resulting in poor film-forming ability. To overcome this problem, nanostructured metal oxides (NMOx) may be used to control the agglomeration of MWCNTs[19]. The covalent binding (or sidewall functionalization) of biomolecules (e.g., proteins, enzymes, and nucleic acids) to carboxyl-functionalized MWCNTs via diimide-activated amidation may provide improved stability and reproducibility[20–24]. In such a case, the large surface area of the MWCNTs and the presence of abundant functional groups may offer a suitable platform for biofunctionalization[20–25]. Additionally, MWCNTs may facilitate continuous conducting pathways to transport the charge carriers, allowing for a higher sensitivity[25]. Shim et al. have used functionalized CNT for biomolecular recognition in a streptavidin/biotin approach to investigate the adsorption of proteins on the sidewalls of carbon nanotubes[20].

A biosensor based on nanostructured nickel oxide (nNiO) has recently been explored to detect biomolecules such as DNA, antibody-antigen interactions, glucose, and cholesterol[26,27]. However, nNiO-based biosensors have limited applications due to the inherently poor electrical conductivity of nNiO[26]. The non-covalent immobilization of enzymes onto nNiO-based biochip has recently been found to result in poor stability of the desired biomolecules[26–28]. To improve the characteristics of a biosensing device, nNiO can be integrated with MWCNTs[29,30]. Zhang et al. have used CNT-NMOx to develop solar cells and gas sensors[21]. The sp^2 hybridization and

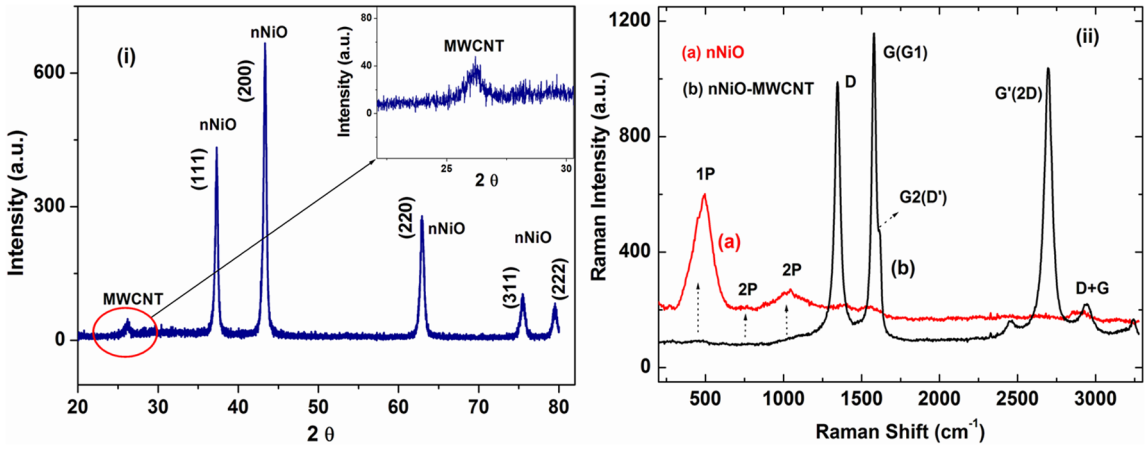

Figure 2 | (i) The X-ray diffraction pattern of nNiO-MWCNTs and (ii) the Raman spectroscopy spectra of the NiO nanoparticles (a) and nNiO-MWCNTs (b).

electronic properties of nNiO coupled with the specific recognition properties of immobilized MWCNTs could lead to a miniaturized biochip[29,30]. Chen et al. have reported the creation of a non-enzymatic electrochemical glucose sensor based on a MnO_2/MWCNT matrix[29]. Zhu et al. have utilized MWCNTs with ZnO nanoparticles for ultrafast, nonlinear optical switching[19].

In this study, we discuss the fabrication of a novel nNiO-MWCNT nanocomposite-based biochip for total cholesterol estimation. The biochip is immobilized with a bienzyme, composed of cholesterol esterase (ChEt) and cholesterol oxidase (ChOx), and integrated with PDMS microchannels. Unlike conventional methods, our procedure creates bienzyme functionalization through the carboxylation and amidation of the nNiO-MWCNT nanocomposite that serves as the sensing interface.

Results

To confirm the formation of the nanocomposite (nNiO-MWCNT) on the microfluidic electrode, we performed X-ray diffraction (XRD), Raman spectroscopy, X-ray photoelectron spectroscopy (XPS), zeta potential and electrochemical studies. The XRD studies of the nNiO-modified MWCNTs (Fig. 2(i)) revealed the purity and crystallinity of the synthesized NiO nanoparticles with the face-centered cubic configuration (*a*) (4.1 Å) and space group *Fm3m* (225) (JCPDS Card No. 78-0423). Figure 2(i) reveals a peak at 26° (2θ value) due to the (002) plane (JCPDS Card No. 75-1261) of the MWCNTs. However, the peak intensity of the MWCNTs is lower compared to other peaks due to the presence of defects. The other peaks observed in the diffraction pattern are attributed to the (111), (200), (220), (311), and (222) planes of the cubic NiO[26]. The peak intensity observed for the (200) plane at 2θ (43.3°) is higher than that of the (111) plane, indicating that the growth is mainly dominated by the (200) facet. The d_{200} value of 0.20 nm corresponds to the (200) plane.

The Raman studies (Fig. 2(ii)) show several bands at 532 nm (the excitation wavelength). The vibrational band of NiO (spectra (a)), arising due to one phonon (1P) sampling at 494 cm^{-1}, corresponds to transverse optical (TO) mode. The two-phonon (2P) peak observed at approximately 746 cm^{-1} is assigned to the 2TO and 2LO (longitudinal optical) modes (at approximately 1027 cm^{-1}). The band observed at approximately 713 cm^{-1} exhibits a low intensity at room temperature (298 K), indicating the presence of NiO. In spectra (b), two sharp intense peaks attributed to G (graphite) and D (disorder) bands at 1342 cm^{-1} and 1580 cm^{-1}, respectively, can be observed. The 2D band is found at 2695 cm^{-1} (the second order of the D band). A small feature near 1617 cm^{-1} can be assigned to the G2 or D band, and the peaks pertaining to the G + D band (approximately 2942 cm^{-1}), as well as a small peak at approximately 2450 cm^{-1}, can also be observed. The tangential G band (approximately 1580 cm^{-1}), derived from the graphite-like in-plane mode, splits into two distinct bands attributed to G1 (1577 cm^{-1}). The G2 (1610 cm^{-1}) peak arises due to changes in the curvature of the inner and outer cylinders.

Figure 3(i) shows an XPS wide-scan spectrum obtained for the nNiO-MWCNT/ITO (subfigure a) and ChEt-ChOx/nNiO-MWCNT/ITO (sub-figure b) electrodes. The peaks found at 284.6 and 530.6 eV are attributed to the C1s and O1s of the COOH-functionalized MWCNTs. In spectrum (b), the characteristic peak observed at 399 eV is attributed to the presence of N1s in the bienzyme (ChEt-ChOx). The additional peaks found at 66.0, 112.6, 777.6, 870.6, and 1009.0 eV are assigned to Ni $3p^3$, Ni 3S, Ni-Auger, Ni $2p^3$, and Ni $2P^1$, respectively. The Ni 2S peak is due to the incorporation of NiO onto the MWCNTs. The relative atomic concentrations (%) of carbon, nitrogen, oxygen, and nickel are summarized in Table I. The atomic concentration of nitrogen in the ChEt-ChOx/nNiO-MWCNT/ITO bioelectrode was found to be 9.93%. This result indicates that the nNiO-MWCNT/ITO surface facilitates the covalent functionalization of ChEt-ChOx via EDC-NHS chemistry. The XPS spectra of the carbon 1 s region of the deposited nNiO-MWCNT electrode (Fig. 3(ii)) was deconvoluted into characteristic peaks using the Shirley-type baseline and Lorentzian-Doniac-Sunsic curves, with a Gaussian profile. The peak found at 284.1 eV is graphitic (sp^2), the peak at 285.2 eV is due to a defect (sp^3), the peak at 286.3 eV is attributed to a hydroxyl group, the peak at 287.3 eV is assigned to a carbonyl group and the peak found at 288.2 eV is attributed to the carboxyl group (-O-C=O). In the ChEt-ChOx/nNiO-MWCNT/ITO electrode (Fig. 3(iii)), the binding energy peaks corresponding to functional groups are the same as those clearly visible in the spectra of the nNiO-MWCNT/ITO electrode. The observed lower intensities of the ChEt-ChOx electrode, as well as the slight shift in its binding energy positions (Fig. 3(iii)) compared with those of the nNiO-MWCNT/ITO electrode (Fig. 3(ii)), may perhaps be attributed to the covalent attachment of the bienzyme molecules to the film surface. In particular, the COOH group percentage decreased to 2.7% from the nNiO-MWCNT/ITO film's value of 13%, indicating that most of the COOH functional groups are used in bienzyme attachment (ChEt-ChOx). The deconvoluted peak observed at approximately 282 eV in both of the spectra may be due to the adsorption of nNiO to the MWCNTs in the sample. In Figure 3(iv), the typical binding energy peak observed at 398.2 eV is due to the core-level electron of N1s. The peak found at 400.3 eV for the ChEt-ChOx/nNiO-MWCNT bioelectrode corresponds to the amide nitrogen (CO-NH) present in the bienzyme molecules, whereas the peak

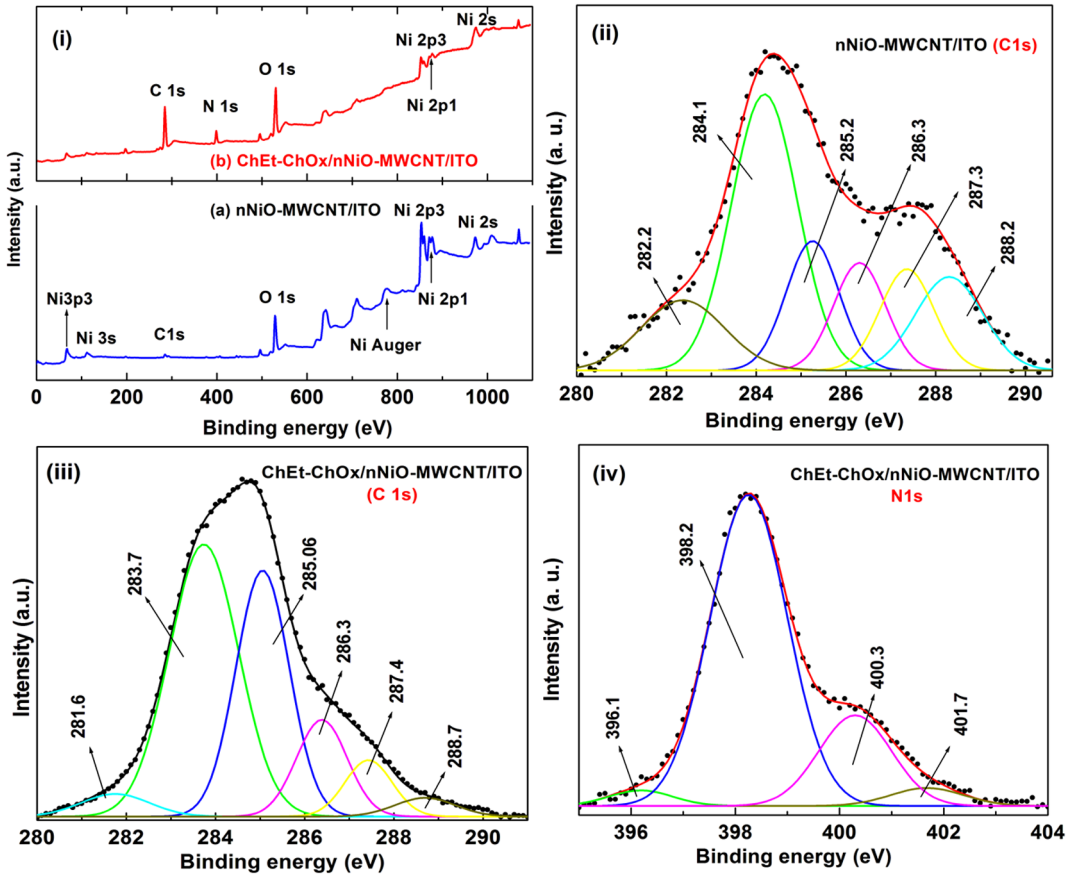

Figure 3 | (i) The wide-scan X-ray photoelectron spectra (XPS) of various films. (ii) The XPS spectra of the C1s region of the nNiO-MWCNT film after deconvolution; (iii) the C1s region of the ChEt-ChOx/nNiO-MWCNT/ITO film; and (iv) the N1s core-level spectra of the ChEt-ChOx/nNiO-MWCNT/ITO film.

observed at 401.7 eV, attributed to the ≡N species, confirms covalent functionalization. The value of the average surface potential of colloidal NiO nanoparticles was estimated to be +22.7 mV using zeta potential measurements. This value reveals that the NiO nanoparticles are positively charged (Supporting Information, Fig. S1(a)). The average surface potential of the MWCNTs was measured to be −6.7 mV, indicating the presence of negatively charged groups on the sidewalls of the carbon nanotubes (Supporting Information, Fig. S1(b)). The positively charged nNiO provides strong electrostatic interactions that link it to the negatively charged MWCNTs.

The scanning electron micrograph (SEM) studies (Fig. S2) were carried out as a morphological observation study at an accelerating voltage of 20 kV. The SEM image (Supporting Information, Fig. S2(i)) shows COOH-functionalized MWCNTs that are likely to be randomly oriented on the ITO substrate. The *in situ* incorporated MWCNTs, with deposited nNiO, are shown in Figure S2(ii). The NiO nanoparticles appear to be attached to the MWCNTs, which are not agglomerated, indicating that the presence of NiO nanoparticles prevented their agglomeration. The transmission electron microscopy (TEM) image shows spherical NiO nanoparticles with an average size of <70 nm (Fig. 4(i)). The high-resolution image of the individual MWCNTs shows outer and inner diameters of 34 and 12 nm, respectively. The selected area electron diffraction (SAED) pattern shows that graphitic (002) and (004) reflections are present in the MWCNTs (the inset in Figure 4(ii)). Figure 4(iii) shows that the well-dispersed COOH-functionalized tubular-shaped MWCNTs are entangled with NiO nanoparticles and randomly oriented. It appears that some of the NiO nanoparticles are aggregated on the MWCNT surfaces. A few NiO nanoparticles can be observed inside the carbon nanotubes (Fig. 4(iii), marked with dotted lines). The length range of the MWCNTs is several tens of micrometers, and they have an external diameter of approximately 20–80 nm. From the atomic-scale image of the nNiO-MWCNTs (Fig. 4(iv)), it can be concluded that this nanocomposite is crystalline in nature, with an interlayer spacing of 3.41 Å (d_{002} for MWCNT, shown in the subfigure inset). The lattice fringe spacing of the NiO nanocrystal is estimated to be 2.0 Å, which agrees with the results of the XRD studies. These results clearly reveal a successful formation of the nNiO-MWCNT composite, which can be used to fabricate the desired biochip.

The electrochemical behavior of the biochip, both before and after undergoing surface modification by the bienzyme (ChEt-ChOx), was investigated using cyclic voltammetry (CV) in phosphate buffer saline (PBS, pH 7.0) containing ferro/ferri cyanide (as a mediator) at a scan rate of 30 mV/s (Fig. 5(A)). The CV of the nNiO/ITO electrode

Table I | The atomic concentration (%) of the elements C, Ni, O, and N present in the nNiO-MWCNT/ITO and ChEt-ChOx/nNiO-MWCNT/ITO films obtained from XPS analysis

Elements/atomic concentration (%)	C	Ni	O	N
nNiO-MWCNT/ITO	12.52	33.72	53.76	
ChEt-ChOx/nNiO-MWCNT/ITO	59.11	3.88	27.08	9.93

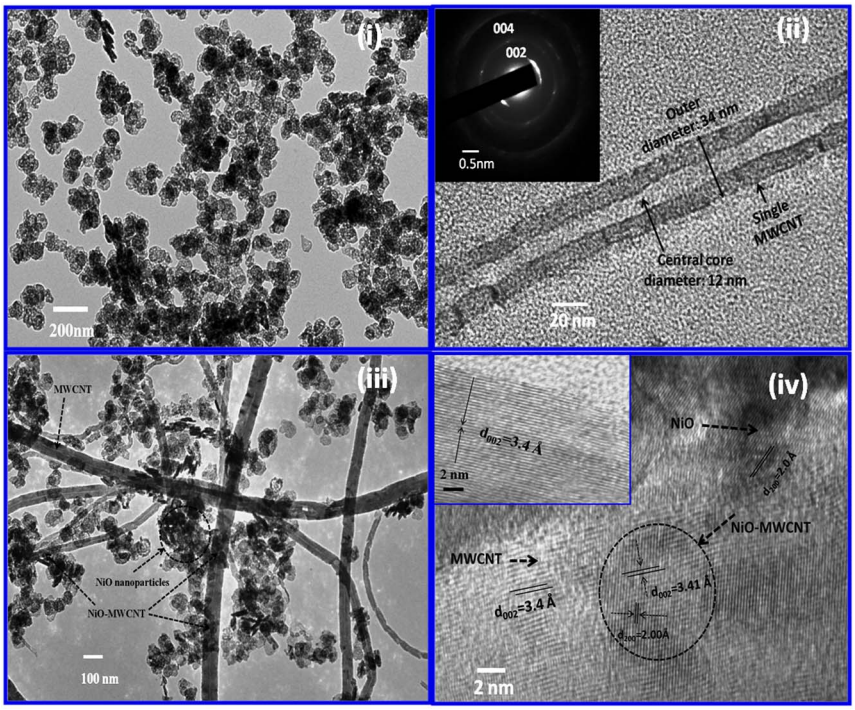

Figure 4 | The HR-TEM analysis of (i) the NiO nanoparticles, (ii) an individual MWCNT (inset: the SAED pattern of the MWCNT), (iii) the MWCNTs modified with NiO nanoparticles, and (iv) an atomic-scale image of a nNiO-MWCNT (inset: lattice fringes of the MWCNT).

exhibited well-defined oxidation/reduction peaks in the −0.8 V to +0.9 V potential range, with a peak-to-peak separation (ΔE) of 0.115 V (a). After the nNiO was incorporated into the MWCNTs (1.0%) (b), the electrochemical current increased to 28.0 μA because MWCNTs are more conductive than the nNiO/ITO electrode alone (23.0 μA). The large number of edge plane sites along the surface of the tubes, as well as the presence of defects in the MWCNTs, enhanced the electrochemical behavior. In addition, the outer and inner surfaces of the carbon nanotubes were accessible to the electrolyte solution containing Fe^{3+}/Fe^{2+} ions and became pathways for the transport of electrons toward the electrode, resulting in an enhanced faradic current. In the case of the nNiO-MWCNT(2.0%) /ITO electrode (c), the peak current increased to 31.2 μA. This increase is due to the presence of a large number of defect sites in the MWCNTs, leading to enhanced heterogeneous electron transfer. The resulting current can be controlled by varying the MWCNT concentration in the nNiO matrix. Furthermore, a redox current of 14.0 μA was obtained for the nNiO-MWCNT(2.0%)/ITO electrode after bienzyme functionalization (d), which is lower than that of the nNiO-MWCNT/ITO electrode; the bienzyme has insulating properties that block the transport of electrons toward the electrode. The magnitudes of the cathodic and anodic peaks increased linearly with the square root of the scan rate (30 to 100 mV s^{-1}), indicating a diffusion-controlled or quasi-reversible process and favourable electron transfer kinetics (Supporting Information, Fig. S3). The values of the slope, intercept, and correlation coefficient of the ChEt-ChOx/nNiO-MWCNT/ITO bioelectrode can be estimated using Eq. (1)–(4).

$$I_{pa} = 6.71\ \mu A + 3.55\left(\mu A m V^{-1} s\right)^{1/2} [\text{scan rate (mV/s)}]^{1/2};\ R^2 = 0.999 \quad (1)$$

$$I_{pc} = -0.137\ \mu A - 2.56\left(\mu A m V^{-1} s\right)^{1/2} [\text{scan rate (mV/s)}]^{1/2};\ R^2 = 0.997 \quad (2)$$

$$E_{pa} = 0.368\ V + 1.95\ s^{1/2}\ [\text{scan rate (mV/s)}]^{1/2};\ R^2 = 0.998 \quad (3)$$

$$E_{pc} = -0.235\ V - 1.54\ s^{1/2}\ [\text{scan rate (mV/s)}]^{1/2};\ R^2 = 0.993 \quad (4)$$

The anodic peak potential (E_{pa}) varied linearly with the natural logarithm of the scan rate (ln ν) and followed Eq. (5).

$$E_{pa} = 0.232 \ln \nu + 1.509 \quad (5)$$

The surface concentration of the ChEt-ChOx/nNiO-MWCNT/ITO bioelectrode was estimated using Laviron's theory (Eq. 6), and the slope is given by Eq. (7):

$$RT/\alpha nF = 0.232 \quad (6)$$

$$I_p = n^2 F^2 I^* / 4RT \quad (7)$$

where α is the transfer coefficient, *n* is the number of electrons transferred (1 in this case), F is the Faraday constant (96485.34 C/mol), I* is the surface concentration of the ChEt-ChOx/nNiO-MWCNT/ITO bioelectrode, ν is the scan rate (mV s^{-1}), R is the gas constant (8.314 J mol^{-1} K^{-1}), and T is the absolute temperature (298 K). The i_p/ν value can be calculated from the slope of the i_p versus ν plot. The total surface concentration of the ChEt-ChOx/nNiO-MWCNT/ITO bioelectrode was found to be 11.07 × 10^{-6} mol/cm^2, indicating a high coverage of ChEt-ChOx on the nNiO-MWCNT/ITO surface.

The flow rate was optimized for the ChEt-ChOx/nNiO-MWCNT microfluidics biochip using the chronoamperometric technique (inset of Fig. 5(A)). The chronoamperometric current response of the nNiO-MWCNT/ITO (i) and ChEt-ChOx/nNiO-MWCNT/ITO (ii) electrodes was obtained as a function of the flow rate (0.01–10 μL/min) and the corresponding current versus time, and the plots are shown in Figures S4 and S5 (Supporting Information), respectively. The chronoamperometric current increases for the nNiO-MWCNT/ITO electrode with an increasing buffer solution flow rate. The maximum current is 0.1 μL/min, after which point it reaches

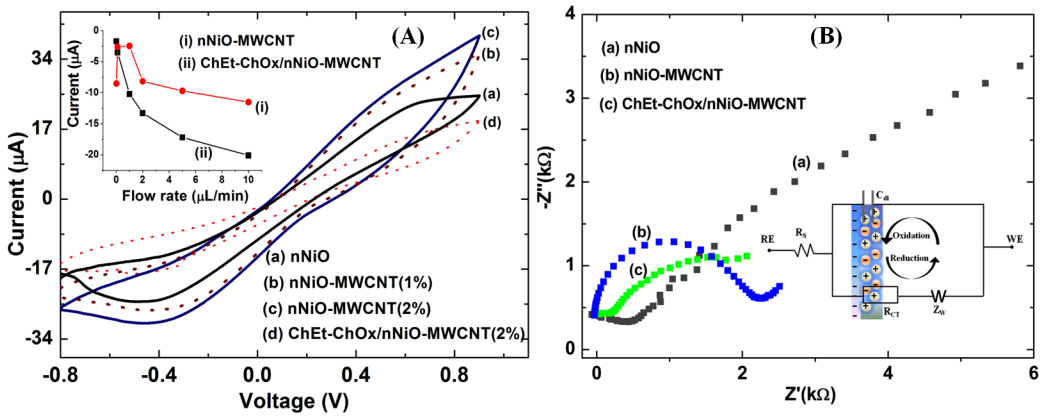

Figure 5 | (A) A cyclic voltammogram (CV) of the different electrodes in a PBS solution (50 mM, pH 7.0, 0.9% NaCl) containing 5 mM of $[Fe(CN)_6]^{3-/4-}$ (inset: current versus flow rate plot of the chronoamperometric response). (B) The electrochemical impedance spectroscopy (EIS) spectra of the electrodes (inset: a schematic representation of the Randles equivalent circuit model for impedance measurement).

saturation (i). This pattern is perhaps due to the diffusivity of the redox species, which increases with a higher buffer flow rate because of the improved mass transport. At a flow rate of 0.1 μL/min, the response time of the microfluidics electrode is 2 s, after which point the amperometric current becomes saturated (Supporting Information, Fig. S4). After its ChEt-ChOx functionalization, the nNiO-MWCNT/ITO electrode (inset of Fig. 5A(ii)) showed a high initial current that decreased as the flow rate increased (Supporting Information, Fig. S5). This response may be attributed to the retention time of the biocatalytic reaction. As the flow rate increases, the retention time becomes shorter, resulting in a decreased response current. It appears that the cholesterol molecules move away from the biochip-sensing surface prior to the completion of the biochemical reaction. The diffusion time was maximized (approximately 3 s) at a flow rate of 1.0 μL/min, so the chronoamperometric measurements were carried out at this optimum flow rate. These results indicate that the fluid flow through the rectangular microchannel is laminar due to the low Reynolds number (0.082).

Electrochemical impedance spectroscopy (EIS) studies were carried out by applying a small-amplitude sinusoidal AC signal (with a bias voltage of 0.35 V) as a function of the frequency (0.01 to 10^5 Hz) (Fig. 5(B)) using a frequency response analyzer (FRA). The electrical impedance (Z) is the ratio of the incremental change in voltage, V(t), to the resulting change in current, I(t), and Z is given by Eq. (8).

$$Z = \frac{V(t)}{I(t)} = \frac{1}{Y} = \frac{V_0 \sin(2\pi ft)}{I_0 \sin(2\pi ft + \varphi)} \quad (8)$$

where V_0 and I_0 are the maximum voltage and current signals, respectively, f is the frequency, t is the time, φ is the phase shift between the voltage-time and current-time function, and Y is the complex admittance. The impedance is described either by the modulus $|Z|$ and the phase shift φ or by its real (Z′) and imaginary (Z″). The most frequently used equivalent circuit for modeling the EIS experimental data is the Randles circuit (inset of Fig. 5(B)), which contains the electrolyte resistance (R_S) in series with a double-layer capacitance (C_{dl}), charge-transfer resistance (R_{CT}), and Warburg impedance (Z_w). The Nyquist plot includes a semicircle region lying on the real axis, which is followed by a straight line. The linear portion ($\varphi = \pi/4$), observed in the low-frequency range, implies a mass-transfer limited process; the semicircle portion, observed in the high-frequency range, implies a charge-transfer-limited process. The imaginary component decreases to zero at a high frequency because it offers no impedance. As the frequency drops, the capacitance (C_{dl}) offers higher impedance and the current flows primarily through the R_{CT} and R_S segments. The R_{CT} value of the nNiO-MWCNT/ITO electrode is 1.9 kΩ (shown in curve b), which is lower than the value of the nNiO/ITO electrode (19 kΩ; curve b). This result is due to the presence of the MWCNTs, which cause enhanced catalytic activity

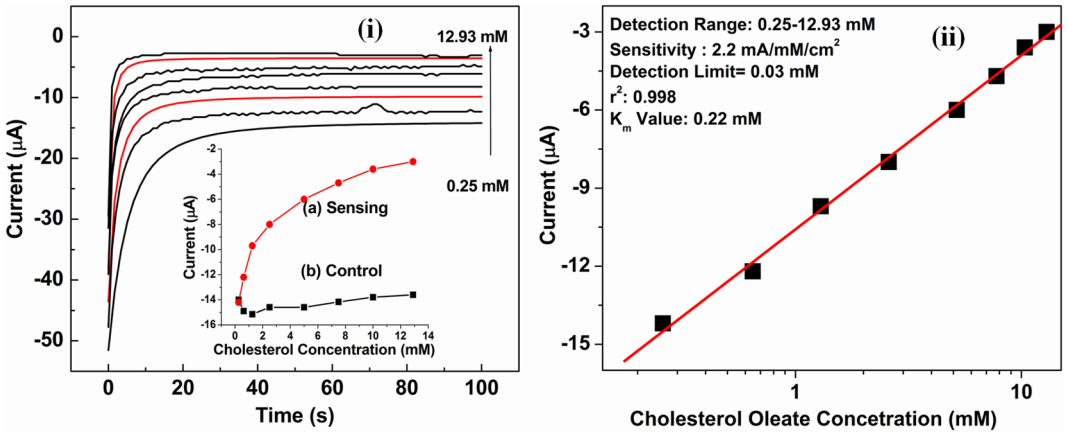

Figure 6 | (i) The chronoamperometric response of the ChEt-ChOx/nNiO-MWCNT/ITO-based biochip as a function of the cholesterol oleate concentration (0.25–12.93 mM) in a PBS solution containing 5 mM of $[Fe(CN)_6]^{3-/4-}$. The experiment was controlled using a syringe pump attached to the inlet of the microsystem (inset: the response current as a function of the cholesterol concentration obtained for both (a) ChEt-ChOx/nNiO-MWCNT/ITO and (b) nNiO-MWCNT/ITO electrodes). (ii) A calibration plot showing the logarithm of the cholesterol concentration (mM) and the amperometric current of the biochip during sensing.

Table II | The sensing characteristics of the nanomaterial-based biochip designed for total cholesterol estimation

Electrode materials	Microfluidic used	Detection limit (M)	Sensitivity (/mM/cm²)	Detection range	K_m Value (mM)	Stability (days)	Ref.
CNT	Yes	0.25×10^{-3}	0.0512 nA	1.25–10.0 mM	.....	.....	18
Anatase-TiO_2	Yes	1.2×10^{-3}	0.094 mA	0.64–10.3 mM	0.14 mM	35	34
nNiO	Yes	0.65×10^{-3}	0.12 mA	0.64–10.3 mM	0.16 mM	60	26
ZnO	No	37×10^{-9}	23.7 μA	1.0 to 500.0 nM	4.7 mM	50	35
Pt nanoparticles	No	0.2×10^{-6}	2.07 μA	Upto 4.0 μM	5 mM	3	36
Polyelectrolyte-MWCNT	No	0.2×10^{-3}	0.559 μA	Upto 6.0 mM	7.17 mM	.....	37
Chitosan/silica-MWCNT	No	1×10^{-6}	1.55 μA	4.0 μM–0.7 mM	0.24 mM	50	33
nNiO-MWCNT	Yes	0.03×10^{-3}	2.2 mA	0.25–12.93 mM	0.22 mM	40	Present Work

and favorable electron-transfer kinetics; improved kinetics leads to a greater diffusion of the $Fe^{2+/3+}$ ions from the bulk solution to the electrode surface. The R_{CT} value of the ChEt-ChOx/nNiO-MWCNT/ITO bioelectrode increases to 3.9 kΩ (curve c), a value greater than that of the nNiO-MWCNT/ITO (curve b) electrode, implying that the bienzyme absorbed onto the nNiO-MWCNT surface provides steric hindrance to the diffusion of electrons through the electrode-electrolyte interface.

Discussion

The successful formation of the nNiO-MWCNT composite and its bienzyme functionalization were confirmed via XRD, Raman, XPS, SEM, and TEM studies. The chronoamperometric response of the biochip (ChEt-ChOx/nNiO-MWCNT/ITO) was measured (Fig. 6(i)) as a function of the cholesterol oleate concentration (0.25–12.93 mM). During this chronoamperometric measurement, the solutions containing various concentrations of cholesterol oleate in PBS were injected through an inlet of the microchannel at regular intervals. The sensing potential was maintained at −0.4 V during the measurements, when the specific oxidative reaction of the bienzyme ChEt-ChOx was dominant. The chronoamperometric current of the microfluidics biochip increased linearly in the range of 0.25–12.93 mM, after which point it was saturated (inset, Fig. 6(i)a). First, esterified cholesterol was converted into fatty acids and cholesterol in the presence of ChEt. ChOx molecules containing flavin-adenine-dinucleotide (FAD) sites reacted with the cholesterol to produce cholesterol-4-ene-3-one and H_2O_2 via catalytic conversion. The produced H_2O_2 further oxidized to H_2O and oxygen by losing two electrons. These generated electrons (not mediated electrons) are responsible for the enhanced chronoamperometric current that was observed, and the current is directly proportional to the concentration of the injected esterified cholesterol. The enzymatic reactions used for total cholesterol detection are given by Eq. (9–10).

$$\text{Cholesterol Oleate} + \text{Choleaterol Esterase} \rightarrow \text{Fatty Acid} + \text{Cholesterol} \quad (9)$$

$$\text{Cholesterol} + \text{Choleserol Oxidase} \rightarrow \text{Cholest}-4-\text{ene}-3-\text{one} + 2e^- \quad (10)$$

A control experiment was conducted using the nNiO-MWCNT/ITO electrode without bienzyme functionalization under similar conditions (inset, Fig. 6(i)b). The current versus time response plot of this control experiment is shown in Figure S5 (Supporting Information). We did not observe any significant change in the current response of the nNiO-MWCNT/ITO electrode with increasing concentrations of esterified cholesterol. These results reveal that the nNiO-MWCNT/ITO electrode surface did not react with the esterified cholesterol molecules, and therefore, the electrochemical current remained unchanged.

Table II shows the characteristics of the fabricated microfluidics biosensor along with those reported in the literature for other devices. It can be observed that the nNiO-MWCNT composite-based microfluidics biodevice exhibits a much higher sensitivity (2.2×10^3 μA/mM/cm²), lower response time (2 s), lower K_m^{app} (0.22 mM), and more extended linearity (0.25–12.93 mM) than other total cholesterol sensor reported in the literature[33,35–37]. The observed low K_m^{app} value, obtained using the Lineweaver-Burk plot (1/concentration vs. 1/current) and the best linear fit (Table II) indicates that ChEt-ChOx has a high affinity for cholesterol oleate and was properly functionalized onto the nNiO-MWCNT surface. The 20-fold higher sensitivity, 2.2×10^3 μA/mM/cm², may be due to the integration of the high-aspect-ratio microfluidics device with the nNiO-MWCNT matrix, as well as an improved biofunctionalization of the bienzyme. The composite material (nNiO-MWCNT) has enhanced electrochemical properties, and the micro-dimensions of the fabricated electrode can cause improved electron diffusion. Additionally, the MWCNTs provide a channel for electron conduction with long electron mean free paths toward the electrode and thus have the capability to support very large current densities. The detection limit of this nanobiochip was found to be a cholesterol concentration of 0.03×10^{-3} M, which corresponds to a physiological range of 2.07–6.2 mM in human blood. The comparatively higher detection limit

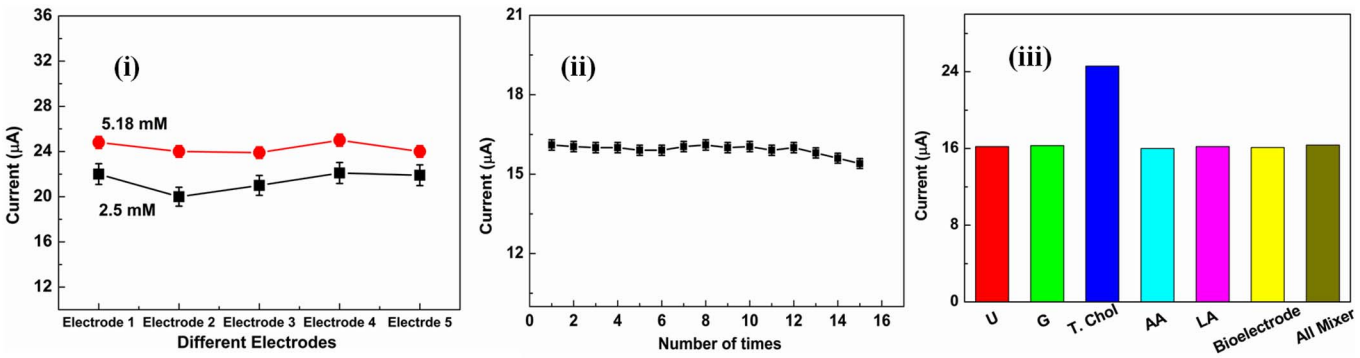

Figure 7 | (i) Reproducibility studies of the ChEt-ChOx/nNiO-MWCNT/ITO microfluidics bioelectrodes under similar conditions. (ii) Stability studies of the ChOx-ChEt/nNiO-MWCNT/ITO bioelectrode and (iii) selectivity studies of the ChOx-ChEt/nNiO-MWCNT/ITO-based biochip.

of the ChEt-ChOx/nNiO-MWCNT/ITO microfluidics total cholesterol sensor may be caused by either insufficient electrical conductivity of the nNiO or the morphological changes arising as a result of interactions between the bienzyme (ChEt-ChOx) and the nNiO-MWCNT nanocomposite surface[18,26,34,37].

Our biochip shows good reproducibility for cholesterol concentrations of 2.59 and 5.18 mM (Fig. 7(i)) as is evidenced by the low standard deviations (RSD) found (4.19% and 2.13%, n = 5), indicating good precision. The ChEt-ChOx/nNiO-MWCNT/ITO bioelectrode also shows good repeatability, as evidenced by its low RSD of 1.12% (n = 15) for a cholesterol concentration of 2.50 mM. No significant decrease in the current was observed after 12 uses; in further procedures, the bioelectrode showed slight decreases in its current response due to the denaturation of the biomolecules (Fig. 7 (ii)).

The selectivity of the ChEt-ChOx/nNiO-MWCNT/ITO bioelectrode was demonstrated using lactic acid (LA), glucose (G), ascorbic acid (AA), uric acid (UA), and other interferents in a buffer solution. We found that the present bioelectrode is highly specific to total cholesterol (5.18 mM) and shows a negligible change in its response current in the presence of other analytes (interferents) (Fig. 7(iii)). The shelf life of this biochip was determined by measuring the change in the current response at regular 5-day intervals for approximately 3 months; the chip exhibited a 93.7% response after approximately 40 days (data not shown). The ChEt-ChOx/nNiO-MWCNT/ITO bioelectrode was stored at 4°C when not in use. This integrated microfluidics nanobiochip reached 92% of its steady-state current in less than 2 s, indicating that a fast electron exchange was occurring between the active sites of the bienzyme and the nNiO-MWCNT/ITO electrode.

In summary, our miniaturized microfluidics-integrated biochip based on a nNiO-MWCNT composite allows for the rapid detection of biomolecules at a low cost. The nNiO serves as a support for the dispersion of MWCNTs and helps exfoliate smaller bundles or individual nanotubes. The covalent functionalization through reactions of desired chemical groups onto the π-conjugated skeleton of this nNiO-MWCNT composite matrix offers considerable advantages for the development of a nanobiochip to detect molecules such as cholesterol. In particular, the COOH groups on the MWCNTs provide simple biofunctionalization and a higher loading capacity of biomolecules on the microfluidic transducer surface. The 9.3% of the carboxyl groups that were present on the nNiO-MWCNT surface were used to covalently bind with the bienzyme. The synergistic electrocatalytic activity of the MWCNTs provides straight conducting pathways for carriers such as electrons and ions, resulting in a higher sensitivity than nNiO-based biochips. This bienzyme functionalized and integrated microfluidics biochip was highly sensitive to cholesterol oxidation and was both highly reproducible and stable, allowing it to be utilized for total cholesterol monitoring. Our platform exhibits improved detection limits and a faster response time. This highly efficient composite microfluidics biochip could be used to create an array-based biochip that simultaneously monitors multi-analytes, including low-density lipoproteins and triglycerides, making it a promising platform for biomedical applications.

Methods

Nickel nitrate $[Ni(NO_3)_2]\cdot H_2O$ and potassium hydroxide (KOH) were procured from Sigma-Aldrich, USA. N-hydroxisuccimide (NHS), N-ethyl-N′-(3-dymethylaminopropyl carbodiimide) (EDC), cholesterol oxidase (ChOx), cholesterol esterase (ChEt), and cholesterol oleate were purchased from Sigma-Aldrich, USA. Different concentrations of cholesterol oleate, from 0.25 to 12.93 mM, were prepared in 0.9% NaCl solution. SU8-100 negative photoresist and SU-8 developer were purchased from Microchem (Newton, MA, USA).

Instrumentation. The nanostructured nickel oxide (nNiO) and the nNiO-MWCNT matrices were characterized using X-ray diffraction (XRD, Cu Kα radiation, Rigaku), Raman spectroscopy, and transmission electron microscopy (TEM; JEOL JEM-2000 EX). The XPS measurements were performed using an X-ray photoelectron spectrometer (XPS, Multilab 2000, Thermo Scientific) equipped with an alpha 110 hemispherical electron energy analyzer and an X-ray source. The XPS measurements were made in the binding energy range of 0–1100 eV to confirm the ChEt-ChOx functionalization of the nNiO-MWCNT matrix. The electrochemical studies were performed using an electrochemical analyzer (AUT-84275) in PBS at pH 7.0 containing 5 mM of $[Fe(CN)_6]^{3-/4-}$ as a redox species.

PDMS microchannel fabrication. The three rectangular PDMS microchannels were fabricated using the soft lithography technique[26]. The channel height and width were each 200 μm, and the length was 2.0 cm. The microchannels had reservoirs at the end, which were fabricated by punching holes in the PDMS slab at the desired position. The three fabricated channels were connected to reservoirs via a single inlet and outlet (Fig. 1(i)). The principal reason to use three channels is to increase the sensor surface area of the biochip.

Microelectrode fabrication. The indium tin oxide (ITO)-coated glass substrate (with a thickness of approximately 150–300 Å) had a sheet resistance of 70–100 Ω and was used to fabricate the microelectrode (0.6×0.26 cm^2) via wet chemical etching. The masked ITO was dipped in ITO etchant solution (HNO_3:HCl:H_2O in a 1 : 10 : 10 ratio) for 15 min, and ITO was selectively etched from the glass substrate. The ITO electrode was cleaned with acetone and then sonicated with acetone (10 min) and water (2 min) several times. The glass substrate containing the electrodes was hydrolyzed using a mixture of $H_2O : H_2O_2 : NH_3$ (5 : 1 : 1) and washed with deionized water. It was then dried in an oven at 100°C for approximately 4 h.

Synthesis of the nNiO-MWCNT composite. The MWCNTs (90%) were synthesized by catalytic chemical vapor deposition using a mixture of ferrocene as the catalyst and toluene as the hydrocarbon source[31]. These MWCNTs were purified and functionalized by refluxing in a concentrated solution of nitric acid and sulfuric acid, which generated a large number of COOH groups on the nanotube surfaces[32]. The drop-wise addition of 0.2 M KOH solution and COOH-terminated MWCNTs to a solution of 0.5 M $Ni(NO_3)_2\cdot 6H_2O$ (nickel nitrate) in de-ionized water with constant stirring results in a blackish-green precipitate of nickel hydroxide, $Ni(OH)_2$, at a pH of approximately 11.8. Excess solvents were evaporated to obtain the precipitate, which was dried at 80°C for 24 h to create a transparent viscous solution of nickel hydroxide-modified MWCNTs. This precipitate was maintained at a pH of 10.0. The thick gel-like $Ni(OH)_2$-modified MWCNT solution was deposited onto patterned ITO electrodes on the glass substrate via dip coating. The electrodes were initially dried at approximately 110°C for 1 h, and they were then annealed at 400°C under ambient conditions for approximately 2 h to remove any solvent, causing the nNiO-MWCNTs (weight 1.0%) and nNiO-MWCNTs (weight 2.0%) to adhere to the ITO surface.

Functionalization of the bienzyme (ChEt-ChOx). A mixture of ChEt (1 mg/ml) and ChOx (1 mg/ml) in a 1 : 1 ratio was spread onto the nNiO-MWCNT/ITO microelectrode through physical absorption (Fig. 1(i)); the electrode was then kept in a humid chamber for 4 h at room temperature (298 K). The carboxyl-terminated MWCNTs and the NiO nanoparticles are negatively and positively charged, respectively, resulting in increased electrostatic interactions. However, the carboxylic groups can undergo an amidation reaction with the amino acids of proteins. One approach to covalently bind proteins or enzymes utilizes the diimide-activated amidation of carboxylic acid functionalized carbon nanotubes. The COOH terminal group was activated using EDC (0.4 M) as the coupling agent and NHS (0.1 M) as the activator. The formation of strong covalent (C-N) amide bonds between the COOH groups of the MWCNTs and the NH_2 groups of the bienzyme (Fig. 1(i)) was confirmed via XPS studies. It is possible that the nNiO molecules with a high isoelectric point (an IEP of 10.0) interact with the bienzyme directly through electrostatic interactions due to their low IEP (5.5).

Microfluidics biochip integration. A lithographically fabricated rectangular PDMS microchannel slab was sealed temporarily (irreversible) with the ITO glass substrate using a conformal contact[38] that contained the modified nNiO-MWCNT and ChEt-ChOx electrodes (Fig. 1(i). The photograph of real microfluidic nanobiochip for cholesterol detection is shown in Fig. 1(ii). Fig. 1(iii) shows the enlarged view of optical microscopic image of this microfluidic nanobiochip. The PDMS surface provides an adhesive layer that plays an important role, making the bonding with the glass substrate irreversible through weak *Van der Waals* forces[38]. Again, the inlet reservoir of the PDMS microchannel was used to introduce the syringe pump, which was based on a stepped motor, to control the fluid flow in the microfluidics biochip. The outlet reservoir was used to accommodate an Ag/AgCl wire that served as the reference electrode (RE). The bare ITO acted as the counter electrode (CE), and the ChEt-ChOx/nNiO-MWCNT/ITO bioelectrode was used as a sensor for total cholesterol detection. All of these three electrodes contained a glass substrate and PDMS microchannels and were embedded on the same biochip.

1. Chován, T. & Guttman, A. Microfabricated devices in biotechnology and biochemical processing. *Trends Biotechnol.* **20**, 116–122 (2002).
2. Hansen, C. & Quake, S. R. Microfluidics in structural biology: smaller, faster. better. *Curr. Opin. Struct. Biol.* **13**, 538–544 (2003).
3. Crevillen, A. G., Avilla, M., Pumera, M., Gonzalez, M. C. & Escarpa, A. Food analysis on microfluidic devices using ultrasensitive carbon nanotubes detectors. *Anal. Chem.* **79**, 7408–7415 (2007).

4. Kim, J., Li, Z. & Park, I. Direct synthesis and integration of functional nanostructures in microfluidic devices. *Lab Chip* **11**, 1946–1951 (2011).
5. Choi, S., Goryll, M., Sin, L. Y. M., Wong, P. K. & Chae, J. Microfluidic-based biosensors toward point-of-care detection of nucleic acids and proteins. *Microfluid. Nanofluid.* **10**, 231–247 (2011).
6. Gervais, L., Rooij, N. & Delamarche, E. Microfluidic chips for point-of-Care immunodiagnostics. *Adv. Mater.* **23**, H151–H176 (2011).
7. Bashir, R. BioMEMS: state-of-the-art in detection, opportunities and prospects. *Adv. Drug. Deliv. Rev.* **56**, 1565–1586 (2004).
8. Wang, J., Chen, G., Wang, M. & Chatrathi, M. P. Carbon-nanotube/copper composite electrodes for capillary electrophoresis microchip detection of carbohydrates. *Analyst* **129**, 512–515 (2004).
9. Fu, Q. & Liu, J. Integrated single-walled carbon nanotube/microfluidic devices for the study of the sensing mechanism of nanotube sensors. *J. Phys. Chem. B* **109**, 13406–13408 (2005).
10. Bange, A., Halsall, H. B. & Heineman, W. R. Microfluidic immunosensor systems. *Biosens. Bioelectron.* **20**, 2488–2503 (2005).
11. Erickson, D. & Li, D. Integrated microfluidic devices. *Anal. Chim. Acta* **507**, 11–26 (2004).
12. Wei, W., Sethuraman, A., Jin, C., Monteiro-Riviere, N. A. & Narayan, R. J. Biological properties of carbon nanotubes. *J. Nanosci. Nanotechnol.* **7**, 1284–97 (2007).
13. Chen, X., Lee, G. S., Zettl, A. & Bertozzi, C. R. Biomimetic engineering of carbon nanotubes by using cell surface mucin mimics. *Angew. Chem. Int. Edn.* **43**, 6111–6 (2004).
14. Balasubramanian, K. & Burghard, M. Chemically functionalized carbon nanotubes. *Small* **1**, 180–192 (2005).
15. Balasubramanian, K. & Burghard, M. Biosensors based on carbon nanotubes. *Anal. Bioanal. Chem.* **385**, 452–468 (2006).
16. Yang, W., Thordarson, P., Gooding, J. J., Ringer, S. P. & Braet, F. Carbon nanotubes for biological and biomedical applications. *Nanotechnology* **18**, 412001 (2007).
17. Lin, Y., Timchalk, C. A., Matson, D. W., Wu, H. & Thrall, K. D. Integrated microfluidics/electrochemical sensor system for monitoring of environmental exposures to lead and chlorophenols. *Biomed. Microdevices* **3**, 331–338 (2001).
18. Wisitsoraat, A. *et al.* Fast cholesterol detection using flow injection microfluidic device with functionalized carbon nanotubes based electrochemical sensor. *Biosens. Bioelectron.* **26**, 1514–1520 (2010).
19. Zhu, Y. *et al.* Multiwalled carbon nanotubes beaded with ZnO nanoparticles for ultrafast nonlinear optical switching. *Adv. Mater.* **18**, 587–592 (2006).
20. Shim, M. *et al.* Functionalization of carbon nanotubes for biocompatibility and biomolecular recognition. *Nano Lett.* **2**, 285–288 (2002).
21. Zhang, W.-D., Xu, B. & Jiang, L.-C. Functional hybrid materials based on carbon nanotubes and metal oxides. *J. Mater. Chem.* **20**, 6383–6391 (2010).
22. Balasubramanian, K. & Burghard, M. Electrochemically functionalized carbon nanotubes for device applications. *J. Mater. Chem.* **18**, 3071–3083 (2008).
23. Tasis, D., Tagmatarchis, N., Bianco, A. & Prato, M. Chemistry of carbon nanotubes. *Chem. Rev.* **106**, 1105–1136 (2006).
24. Katz, E. & Willner, I. Biomolecule-functionalized carbon nanotubes: applications in nanobioelectronics. *ChemPhysChem* **5**, 1085–104 (2004).
25. Vashist, S. K., Zheng, D., Al-Rubeaan, K., Luong, J. H. T. & Sheu, F.-S. Advances in carbon nanotube based electrochemical sensors for bioanalytical applications. *Biotech. Adv.* **29**, 169–188 (2011).
26. Ali, Md. A. *et al.* A highly efficient microfluidic nano biochip based on nanostructured nickel oxide. *Nanoscale* **5**, 2883–2891 (2013).
27. Mohan, S., Srivastava, P., Maheshwari, S. N., Sundar, S. & Prakash, R. Nanostructured nickel oxide based DNA biosensor for detection of visceral leishmaniasis (Kala-azar). *Analyst* **136**, 2845–51 (2011).
28. Solanki, P. R., Kaushik, A., Agrawal, V. V. & Malhotra, B. D. Nanostructured metal oxide-based biosensors. *NPG Asia Materials* **3**, 17–24 (2011).
29. Chen, J., Zhang, W.-D. & Ye, J.-S. Nonenzymatic electrochemical glucose sensor based on MnO_2/MWNTs nanocomposite. *Electrochem. Commun.* **10**, 1268–1271 (2008).
30. Zhang, W.-D., Chen, J., Jiang, L.-C., Yu, Y.-X. & Zhang, J.-Q. A highly sensitive nonenzymatic glucose sensor based on NiO-modified multi-walled carbon nanotubes. *Microchim. Acta* **168**, 259–265 (2010).
31. Mathur, R. B., Chaterjee, S. & Singh, B. P. Growth of carbon nanotubes on carbon fibre substrates to produce hybrid/phenolic composites with improved mechanical properties. *Compos. Sci. Technol.* **68**, 1608–1615 (2008).
32. Datsyuk, V. *et al.* Chemical oxidation of multiwalled carbon nanotubes. *Carbon* **46**, 833–840 (2008).
33. Tan, X., Li, M., Cai, P., Luo, L. & Zoua, X. An amperometric cholesterol biosensor based on multiwalled carbon nanotubes and organically modified sol-gel/chitosan hybrid composite film. *Anal. Biochem.* **337**, 111–120 (2005).
34. Ali, Md. A. *et al.* Nanostructured anatase-titanium dioxide based platform for application to microfluidics cholesterol biosensor. *Appl. Phys. Lett.* **101**, 084105 (2012).
35. Umar, A., Rahman, M. M., Vaseem, M. & Hahn, Y.-B. Ultra-sensitive cholesterol biosensor based on low-temperature grown ZnO nanoparticles. *Electrochem. Commun.* **11**, 118–121 (2008).
36. Dey, R. S. & Raj, C. R. Development of an amperometric cholesterol biosensor based on graphene-Pt nanoparticle hybrid material. *J. Phys. Chem. C* **114**, 21427–21433 (2010).
37. Guo, M., Chen, J., Li, J., Nie, L. & Yao, S. Carbon nanotubes-based amperometric cholesterol biosensor fabricated through layer-by-layer technique. *Electroanalysis* **16**, 23 (2004).
38. Kumar, S. *et al.* Microfluidic-integrated biosensors: Prospects for point-of-care diagnostics. *Biotechnol. J.* **8**, DOI 10.1002/biot.201200386 (2013).

Acknowledgements

The authors would like to thank the Director of the NPL, New Delhi, India, for the use of their facilities. Md. Azahar Ali and Saurabh Srivastava are thankful to CSIR, India, for the award of Senior Research Fellowships. Financial support was received from the Department of Science and Technology from the government of India (DST/TSG/ME/2008/18), the Indian Council of Medical Research (ICMR/RHN/ADHOC/5/2012-2013), and the Ministry of Education, Science and Technology (WCP program, R32-20026) of Korea. V. V. Agrawal would like to thank the CSIR Empower project for providing funding. The authors also thank Shiju Abraham, of BHU, UP, for the Raman studies.

Author contributions

Md. A.A., R.J. and B.D.M. wrote the manuscript. Md. A.A., S.S. and B.D.M. participated in the experiment design and performance and analyzed the data. S.S. and P.R.S. performed the Raman and HRTEM studies, respectively. V.R. and C.K. carried out the XPS studies. V.V.A., R.J. and B.D.M. supervised the studies and discussed the results. All of the authors reviewed the manuscript and participated in discussions on the results of this research.

Additional information

Supplementary information accompanies this paper at http://www.nature.com/scientificreports

Competing financial interests: The authors declare no competing financial interests.

How to cite this article: Ali, M.A. *et al.* Highly Efficient Bienzyme Functionalized Nanocomposite-Based Microfluidics Biosensor Platform for Biomedical Application. *Sci. Rep.* **3**, 2661; DOI:10.1038/srep02661 (2013).

This work is licensed under a Creative Commons Attribution-NonCommercial-ShareAlike 3.0 Unported license. To view a copy of this license, visit http://creativecommons.org/licenses/by-nc-sa/3.0

Int. J. Emerg. Sci., 3(3), 279-288, September 2013
ISSN: 2222-4254
© IJES

Identification and Integration of QoS parameters in Cognitive Radio Networks using Fuzzy Logic

Nisar A. Lala[1], Moin Uddin[2], N.A. Sheikh[3]

[1]Division of Agricultural Engineering,SKUAST(K), Presently persuing Ph.D at NIT Srinagar, J & K, India ,
[2]Delhi Technological University, Delhi, India,
[3]Department of Mathematics,National Institute of Technology,Srinagar J & K, India,

lalanisar_ae@rediffmail.com, prof_moin@yahoo.com, neyaznit@yahoo.co.in

Abstract. Cognitive radio is a technology initiated by many research organizations and academic institutions to raise the spectrum utilization of underutilized spectrum bands through dynamic spectrum access. Quality of service (QoS) provisioning in cognitive radio network is a challenging task due to limited and intermittent availability of the spectrum. In this paper, we have identified eighteen parameters which affect the QoS in cognitive radio network. Further, we have selected three critical parameters; throughput, delay and mobility to analyze their impact on QoS using fuzzy logic based approach. The simulated results provide the impact analysis of these selected parameters on perceived QoS and open new issues in designing protocol structure for spectrum sensing and management for cognitive radio.

Keywords: Cognitive radio, QoS, fuzzy logic, spectrum sensing, spectrum management.

1 INTRODUCTION

As per the survey of Federal Communications Commission (FCC), the spectrum remains underutilized most of the time at a specific location and time [1]. The concept of cognitive radio was introduced by Mitola. J [2][3]. According to well known definition [4], the cognitive radio is an intelligent wireless communication system that is aware of its environment and uses the methodology of understanding-by-building to learn from the environment and adapt to statistical variations in the incoming radio frequency stimuli in real time with two primary objectives: 1) highly reliable communication whenever and wherever needed and 2) efficient utilization of radio spectrum.

Provisioning QoS in cognitive radio is a challenging and highly difficult task. It is the capability of various components, devices and service providers to ensure to satisfy minimum service requirements of an application. The QoS is a mechanism for controlling the performance, reliability and usability of a network [5]. QoS is a

complex, nonlinear, multifunctional and difficult to model mathematically. QoS is defined as the collective effect of service performance, which determines the degree of satisfaction of a user of the service and ability to segment traffic or differentiate between traffic flows differently from others [6][7]. The requirement of QoS depends upon the nature of flows (voice, data or multimedia) and the type of the networks (like mobile, adhoc, sensor and TV as well as cognitive radio). The QoS depends on multiple parameters and these parameters are imprecise and uncertain by nature. Fuzzy logic provides a better solution suitable to handle vague, imprecise and noisy information. In this paper, we have proposed fuzzy logic technique to analyze the impact of multiple parameters on the QoS of a communication channel in a cognitive radio network. Initially, fuzzy logic was applied to many control system applications [8][9] and later on, its applications have been extended to telecommunication networks[10][11][12]. Fuzzy logic was applied to cellular networks for admission control in order to satisfy its QoS requirements [13] and for routing in next generation networks [14]. Fuzzy logic was applied to cognitive radio network for controlling the transmission power in order to reduce harmful interference to licensed user [15] and for cross layer optimization between medium access control layer and transport layer [16]. It was proposed for controlling the spectrum access [17][18] and also for spectrum handoff in cognitive radio network [19][20][21].

The paper is organized as follows. Section 2 provides the brief introduction to cognitive radio and identification of QoS parameters. Section 3 proposes the fuzzy logic based framework. Section 4 presents the simulated results and the conclusion is incorporated in section 5.

2 PRELIMINARIES

2.1 Cognitive Radio

Cognitive radio possesses the ability to sense its environment in order to find out spectrum holes or opportunity at any time and location. These spectrum holes are used by the cognitive radio opportunistically for their transmission to increase the utilization of the underutilized spectrum bands. The spectrum can be accessed with the constraint of noninterference to the licensed user [22].

The main functions of the cognitive radio are:

1) Spectrum sensing: A cognitive user continuously monitors the wideband spectrum in order to find spectrum holes and arrival of licensed user with the help of different spectrum sensing techniques such as transmitter detection, interference based detection and cooperative detection. Each technique has its merits and demerits.

2) Spectrum management: Out of large number of idle bands, the CR has to select the best band that will satisfy its QoS requirements. The spectrum management functions can be classified as spectrum analysis and spectrum decision.
3) Spectrum mobility: Due to appearance of the licensed user on the band occupied by the CR at that time, the CR has to change instantly its operating frequency band to other idle band. The switching to other idle band should be seamless so that there is minimum QoS degradation of the application running on the CR.
4) Spectrum sharing: After deciding the transmitting frequency, the CR handshakes with its receiver and starts transmitting. A fair spectrum scheduling mechanism is to be devised for sharing of the spectrum with other users.

2.2 Identification of QoS Parameters

QoS consists of several parameters depending upon nature of traffic (voice, data, and multimedia) and type of networks. Eighteen parameters have been identified which have critical influence on the QoS of a cognitive radio network. The parameters are 1) Transmission Power 2) Bandwidth 3) Delay 4) Delay jitter 5) Throughput 6) Mobility 7) Handoff 8) Bit error rate (BER) 9) Signal strength 10) Signal to interference and noise ratio (SINR) 11) Dynamic availability of idle channels 12) Expected Holding time of idle channel 13) Spectrum efficiency (bit/s/Hz) 14) Interference mitigation 15) Degree of complexity 16) Amount of overhead (cost) 17) Reliability 18) Low power capabilities of mobile devices.

3 PROPOSED FUZZY LOGIC BASED ALGORITHM

The designed fuzzy logic based algorithm is used to analyze the effect of multiple parameters, such as throughput, delay and moblity, on the QoS perceived by the secondary user in a cognitive radio network. The three antecedents used for the system are:

1) Antecedent 1: Throughput (bps)
2) Antecedent 2: Delay
3) Antecedent 3: Mobility

and the consequence is the perceived QoS of cognitive radio as shown in Figure 1.
The three antecedents are characterized by the term set of three fuzzy sets, such as low, medium and high, as shown in (1) defined over a specific universe of discourse

T(throughput) = T(delay) = T(mobility) = { low, medium, high} (1)

and the consequence by term set of five fuzzy sets, such as poor, average, good,

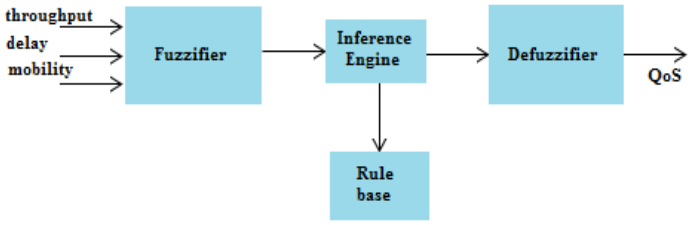

Figure. 1. Fuzzy inference system with three antecedents and a consequent.

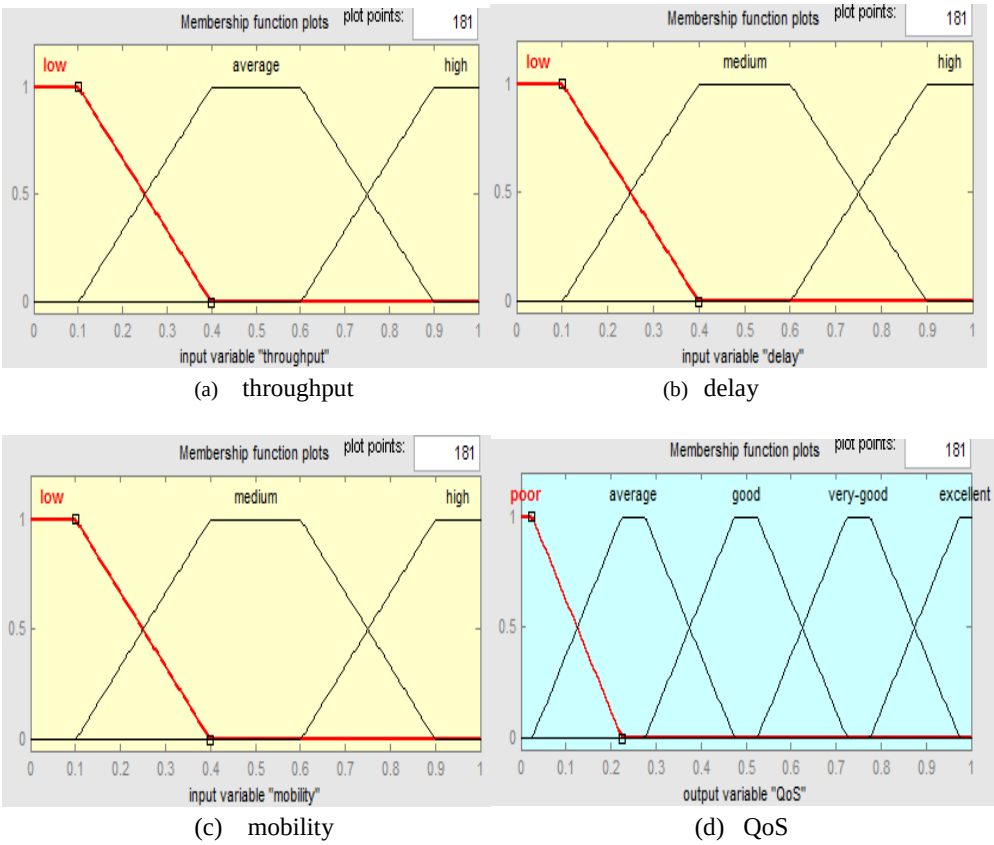

(a) throughput (b) delay

(c) mobility (d) QoS

Figure. 2. The membership functions used to represent the linguistic variables: (a) Antecent 1 (throughput), (b) Antecent 2 (delay), (c) Antecent 3 (mobility), and (d) Consequent (QoS)

very good and excellent, as shown in (2) defined over a specific universe of discourse

T(QoS) = { poor, average, good, very good, excellent} (2)

We have used trapezoidal membership functions (MFs) for three antecedents and the consequence as shown in Figure 2(a), 2(b), 2(c) and 2(d). The analysis of the algorithm has been performed over the normalized values of the antecedents and the

consequence between [0, 1]. Table 1 demonstrates the fuzzy inference rules contained in the rule base. The logic behind their definition is to realize the values

Table 1. Rule base of fuzzy inference system

Rule #	Antecedent 1 throughput	Antecedent 2 delay	Antecedent 3 mobility	Consequent QoS
1	high	low	low	excellent
2	high	low	medium	very good
3	high	low	high	good
4	high	medium	low	very good
5	high	medium	medium	good
6	high	medium	high	average
7	high	high	low	good
8	high	high	medium	average
9	high	high	high	poor
10	medium	low	low	very good
11	medium	low	medium	good
12	medium	low	high	average
13	medium	medium	low	good
14	medium	medium	medium	average
15	medium	medium	high	poor
16	medium	high	low	average
17	medium	high	medium	poor
18	medium	high	high	poor
19	low	low	low	average
20	low	low	medium	poor
21	low	low	high	poor
22	low	medium	low	average
23	low	medium	medium	poor
24	low	medium	high	poor
25	low	high	low	poor
26	low	high	medium	poor
27	low	high	high	poor

of the three conflicting antecedents so as to satisfy the QoS requirements of an application. For example, as per rule 1, if the throughput is high and delay is low and mobility is low, then QoS will be excellent, this corresponds to the situation of ideal channel conditions, where throughput of the communicating channel is very good, delay is negligible and mobility is very low, therefore, perceived quality of transmission will be very good. Also as per rule 27, if the throughput is low and

delay is high and mobility is high then QoS will be poor, this corresponds to the situation of very small data carrying capability of the communication channel, high delay and high mobility, therefore, the QoS requirement of the application cannot be satisfied.

4 SIMULATION RESULTS

The simulation of the algorithm was done in Fuzzy logic toolbox of Matlab 7.6. Two types of simulations were performed. In the first simulation setup, QoS is analyzed as a function of one parameter while keeping other two parameters constant. Figures 3(a), 3(b) and 3(c) show how the throughput, delay and mobility influence the QoS. It can be seen from Figure 3(a), that with the increase in

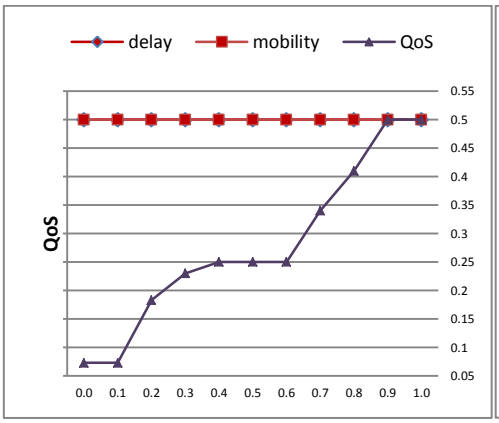

(a) throughput

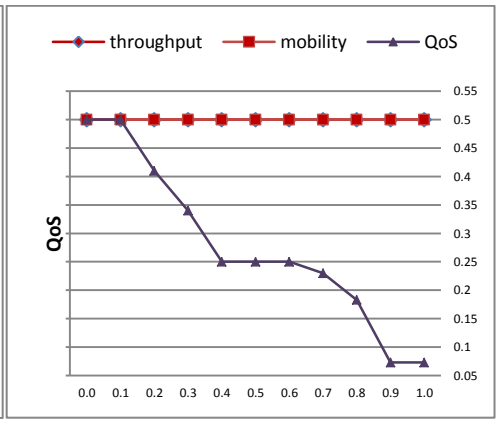

(b) delay

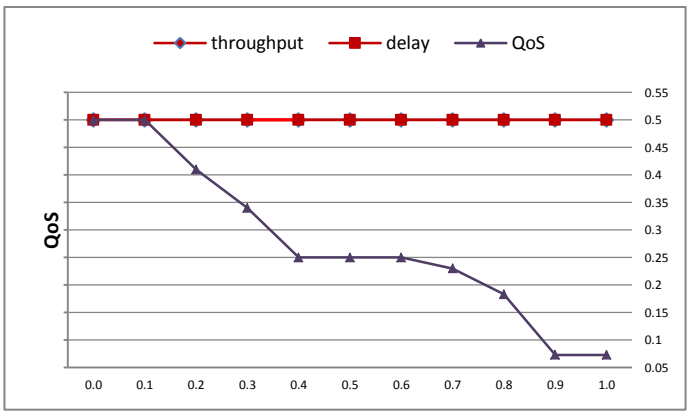

(c) mobility

Figure. 3. Simulation results: (a) Effect of throughput on QoS at constant delay, mobility = 0.5 (medium) (b) Effect of delay on QoS at constant throughput, mobility=0.5 (medium) (c) Effect of mobility on QoS at constant throughput, delay=0.5 (medium).

throughput of a communication channel there is a corresponding increase in the perceived QoS of an application. It can be seen from Figure 3(b), that with the

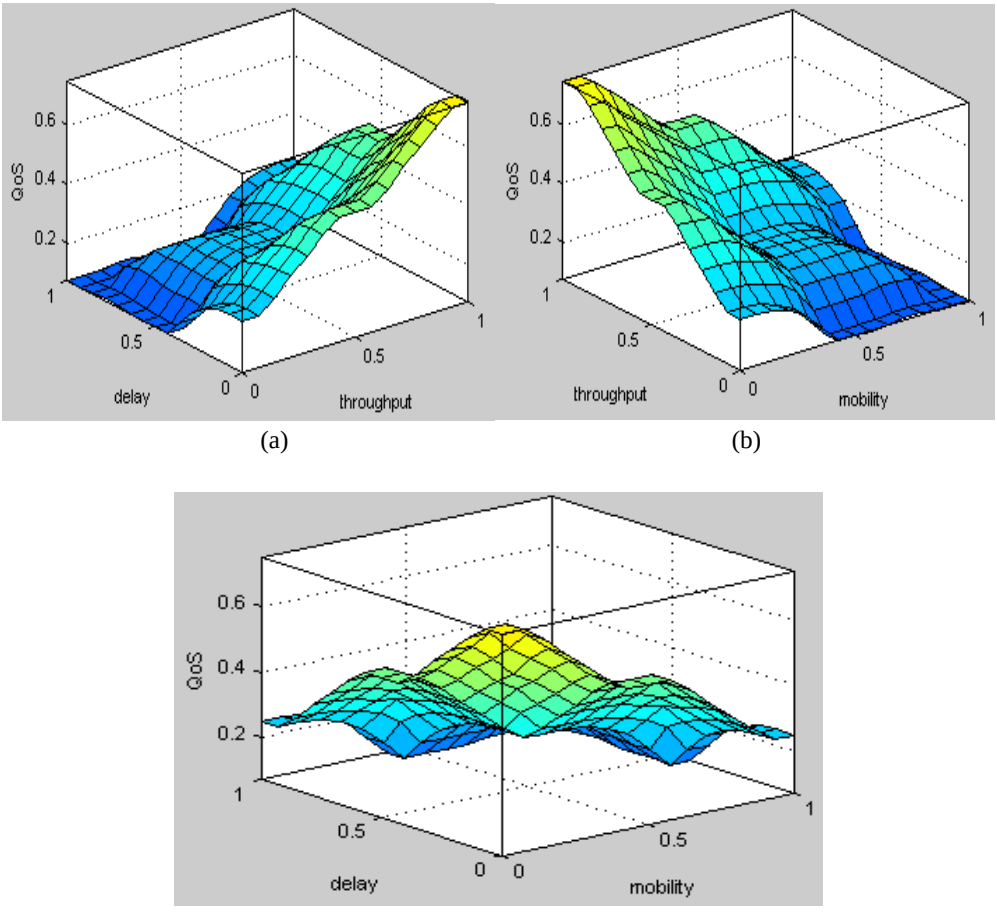

Figure. 4. Simulation results: Surface diagrams show (a) Effect of throughput and delay on QoS at constant mobility=0.5 (medium) (b) Effect of throughput and mobility on QoS at constant delay =0.5 (medium) (c) Effect of delay and mobility on QoS at constant throughput=0.5 (medium).

increase in delay of a communication channel there is decrease in the perceived QoS of an application. It can be seen from Figure 3(c), that with the increase in mobility of a user there is decrease in the perceived QoS of an application.

In the second simulation setup, QoS is analyzed as a function of two parameters while keeping third parameter constant. Figure 4(a) shows simultaneous influence of delay and throughput on QoS at constant mobility= 0.5 (medium). The results show that perceived QoS of an application increases with decrease in delay and increase in throughput of an application and the maximum value of QoS is attained when delay is at minimum value and throughput is at maximum value. Figure 4(b) shows simultaneous influence of mobility and throughput on QoS at constant delay=0.5 (medium). The results show that perceived QoS increases with increase in throughput and decrease in mobility of a user and QoS attains the maximum value when throughput reaches the maximum value and mobility is at minimum. Figure 4(c) shows simultaneous influence of delay and mobility on QoS at constant throughput=0.5 (medium). The results show that perceived QoS increases with simultaneous decrease in delay and mobility of a user and maximum value of QoS is attained when both delay and mobility are at minimum values.

5 CONCLUSION

In this paper, we have presented important characteristics of cognitive radio network and definitions of QoS in the literature. We have identified eighteen parameters influencing the QoS in cognitive radio network. The parameters selected for analysis are heterogeneous and decisions are to be taken based on imprecise, uncertain and ill-defined information. Fuzzy logic is known to be used to deal with such situations. Fuzzy 27 IF-THEN rules were designed to help the fuzzy inference engine to take decisions. The work presented in this paper, provides the impact analysis of three parameters, namely throughput, delay and mobility. The algorithm using fuzzy logic has been used to estimate the QoS of a communication channel. This work will be extended by developing QoS enabled algorithm for spectrum management in cognitive radio network.

FEFERENCES

1. FCC, Notice of Proposed Rulemaking and Order, No. 03- 222, Dec. 2003.
2. Mitola. J, "Cognitive Radio: An Integrated Agent Architecture for Software Defined Radio", Ph.D. Dissertation: KTH Royal Institute of Technology 2000.
3. Mitola. J and Maguire. GQ, "Cognitive Radio: Making Software Radios More Personal", IEEE Personal Communications 1999; 6(4):13-18.
4. Haykin. S, "Cognitive Radio: Brain Empowered Wireless Communications", IEEE Journal on Selected Areas in Communications 2005; 23(2).

5. ITU-T Recommendation, "Terms and Definitions Related to Quality of Service and Network Performance Including Dependability", E. 800 1994.
6. ETSI Network Aspects (NA), "General Aspects of Quality of Service (QoS) and Network Performance (NP)", ETSI Technical Report ETR 003, 2nd edition, 1994.
7. Chen. S, "Routing Support for Providing Guaranteed End to End Quality of Service", University of Illinois at Urbana-Champaign.
8. Kickert. WJM and Lemke. HR, "Applications of a Fuzzy Controller in a Warm Water Plant", Automatica 1976; 12(4): 301-308.
9. King. PJ and Mamdani. EH, "The Application of Fuzzy Control Systems to Industrial Processes", Automatica 1977; 13(3): 235-242.
10. Ghosh. G, Razouqi. Q, Schumacher. HJ and Celmins. A, "A Survey of Recent Advances in Fuzzy Logic in Telecommunication Networks and New Challenges", IEEE Trans. on Fuzzy Systems 1998; 6(3).
11. Chemovil. P, Khalfet. J and Lebourges. M, "A Fuzzy Control Approach for Adaptive Traffic Routing" , IEEE Communications Magazine 1995: 70-76.
12. Mendel. JM, "Fuzzy Logic Systems for Engineers: A tutorial", in Proc. of IEEE 1995; 83(3): 345-377.
13. Ma. Y, Hu. X, Zhang. Y and Zhao. E, "A Fuzzy Call Admission Control Scheme in Cellular Multimedia Networks", IEEE 2005, 844-847.
14. Zhang. R and Long. K, "A Fuzzy Routing Mechanism in Next Generation Networks", in Proc. IASTED Int. Conf. on Intelligent Systems and Control (ISC) 2002: 86-91.
15. Le. H-ST and Liang. Q, "An Efficient Power Control Scheme for Cognitive Radios", in Proc. of WCNC 2007: 2561-2565.
16. Baldo. N and Zorzi. M, "Fuzzy Logic for Cross Layer Optimization in Cognitive Radio Networks", IEEE Communication Magazine 2008: 64-72.
17. Le. H-ST and Ly. HD, "Opportunistic Spectrum Access using Fuzzy Logic for Cognitive Radio Networks", in 2nd Int. Conf. on Communications and Electronics (ICCE) 2008: 240-245.
18. Kaur. P, Moin Uddin and Khosla. A, "Fuzzy Based Adaptive Bandwidth Allocation Scheme in Cognitive Radio Networks", in Int. Conf. on ICT and knowledge Engineering 2010: 41-45.
19. Giupponi. L and Perez-Neira. AI, "Fuzzy Based Spectrum Handoff in Cognitive Radio Networks", in 3rd Int. Conf. on Cognitive Radio Oriented Wireless Networks and Communications CrownCom 2008: 1-6.
20. Kaur. P, Moin Uddin and Khosla. A, "An Efficient Spectrum Mobility Management Strategy in Cognitive Radio Networks", in 1st UK-India Int. Workshop on Cognitive

Wireless Systems UKIWCWS 2009.

21. Wanbin. T and Dong. P, "Spectrum Handoff in Cognitive Radio with Fuzzy Logic Control", Journal of Electronics (China) 2010: 708-714.
22. Akyildiz. IF, Lee. W-Y, Vuran. MC and Mohanty. S, "Next Generation/dynamic Spectrum Access/Cognitive Radio Wireless Networks: A survey", Computer Networks 2006: 2127-2159.

Accepted Manuscript

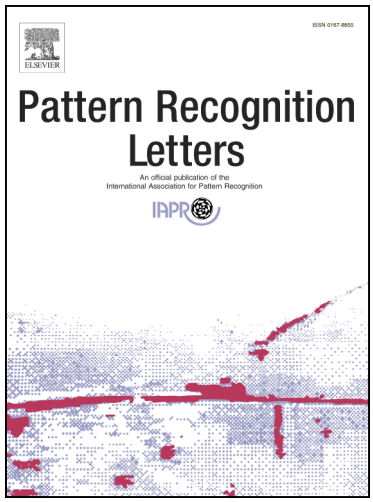

Image Enhancement Using Exposure Based Sub Image Histogram Equalization

Kuldeep Singh, Rajiv Kapoor

PII: S0167-8655(13)00328-0
DOI: http://dx.doi.org/10.1016/j.patrec.2013.08.024
Reference: PATREC 5808

To appear in: *Pattern Recognition Letters*

Received Date: 14 February 2013

Please cite this article as: Singh, K., Kapoor, R., Image Enhancement Using Exposure Based Sub Image Histogram Equalization, *Pattern Recognition Letters* (2013), doi: http://dx.doi.org/10.1016/j.patrec.2013.08.024

This is a PDF file of an unedited manuscript that has been accepted for publication. As a service to our customers we are providing this early version of the manuscript. The manuscript will undergo copyediting, typesetting, and review of the resulting proof before it is published in its final form. Please note that during the production process errors may be discovered which could affect the content, and all legal disclaimers that apply to the journal pertain.

ACCEPTED MANUSCRIPT

Image Enhancement Using Exposure Based Sub Image Histogram Equalization

Kuldeep Singh [a,*], *Rajiv Kapoor* [b]

[a] *Central Research Lab, Bharat Electronics Ltd, Ghaziabad, India, 201010, Phone No: +91-9910101592, email: kuldeep.er@gmail.com*

[b] *Department of Electronics & Communication, Delhi Technological University, Delhi, India, 110042, email: rajivkapoor@dce.ac.in*

Abstract:

This paper presents a novel Exposure based Sub-Image Histogram Equalization (ESIHE) method for contrast enhancement for low exposure gray scale image. Exposure thresholds are computed to divide the original image into sub-images of different intensity levels. The histogram is also clipped using a threshold value as an average number of grey level occurrences to control enhancement rate. The individual histogram of sub images is equalized independently and finally all sub images are integrated into one complete image for analysis. The simulation results show that ESIHE outperforms other conventional Histogram Equalization (HE) methods in terms of image visual quality, entropy preservation and better contrast enhancement.

Key Words: Histogram equalization, Image Information content, Image Exposure

1. Introduction:

Image enhancement techniques have gained attention of researchers from early years. Image enhancement improves the appearance of image and enhances the finer details of image having low luminance. These enhancement techniques can be broadly divided into two categories-

ACCEPTED MANUSCRIPT

Transform domain and spatial domain (Gonzalez and Woods, 1992). The first category involves techniques operating on frequency transform of an image. Spatial domain techniques such as contrast enhancement operate directly on the pixel level of the image. Histogram equalization (HE) is most extensively utilized contrast enhancement technique due to its simplicity and ease of implementation. Histogram Equalization (Gonzalez and Woods, 1992) flattens the density distribution and stretches the dynamic range of gray levels to improve the overall contrast of the image. HE utilizes the cumulative density function (CDF) of image for transformation of the gray levels of original image to the levels of enhanced image. The main drawback of HE is that it tends to change the mean brightness of the image to the middle level of the dynamic range and results in annoying artifacts and intensity saturation effects. This drawback makes HE technique unsuitable for most of consumer electronics applications such as TV, Cameras etc.

Various methods have been suggested in literature to overcome the above-mentioned shortcomings. Kim (1997) was the first one to propose Brightness preserving bi histogram equalization (BBHE) for preserving the mean brightness of image while improving the contrast. BBHE divides the histogram in two parts based on the input mean brightness and equalizes the two sub histograms independently. Dualistic sub image histogram equalization (DSIHE) (Wang et al., 1999) method claimed that it is better than BBHE in terms of preservation of brightness and average information content (entropy) of an image. DSIHE divides the histogram in two sub histograms containing equal number of bins and the division is based on median value instead of mean brightness.

Chen and Ramli (2003) introduced minimum mean brightness error bi-histogram equalization (MMBEBHE) for preserving the mean brightness “optimally”. This method is an improvement

ACCEPTED MANUSCRIPT

on BBHE, which calculates the absolute mean brightness error (AMBE) for gray levels 0 to L-1 and bisects the histogram based on the intensity value X_T, which yields minimum AMBE.

Chen and Ramli (2003) proposed another approach named recursive mean-separate histogram equalization (RMSHE). This method recursively performs the BBHE in which the histogram is divided into two parts on the basis of average input brightness and BBHE is performed to each sub histogram independently. Sim et al (2007) introduced a similar technique to RMSHE known as recursive sub-image histogram equalization (RSIHE).This algorithm performs the division of histogram based on median value of brightness instead of mean brightness. Finding the optimal value of iteration factor is a big challenge for producing significant enhancement results in RMSHE and RSIHE method.

These above discussed techniques do not provide mechanism for adjusting the level of enhancement. New class of techniques based on clipping of histogram (Wang and Ward, 2007, Kim and Paik, 2008 and Ooi et.al, 2009) was proposed as a solution for controlling enhancement rate as well as preserving the original brightness. These methods controls maximum value of histogram by clipping histograms higher than the pre specified threshold. These methods provide different approach for determination of clipping threshold.

Although various techniques are available to cater specific problem of contrast enhancement, but enhancement for low exposure images is still less explored area. We propose an algorithm named Exposure based Sub-Image Histogram Equalization (ESIHE), which is very effective for low exposure gray scale images and preserves entropy along with control on enhancement rate. The authors believe that the ESIHE technique that achieves the multiple objectives of entropy

ACCEPTED MANUSCRIPT

maximization and control on over enhancement is a better approach to image enhancement specifically for under exposed images.

This paper is organized as follows: Section 2 describes the proposed ESIHE method. Section 3 gives experimental results, and section 4 concludes the paper.

2. Exposure based Sub Image Histogram Equalization

Poor contrast images do not occupy complete dynamic range. Images having histogram bins concentrated towards lower part or the darker gray levels possess low intensity exposure whereas images having histogram bins concentrated towards higher part or the brighter part possess high intensity exposure. Images can be broadly classified as under exposed and over exposed based on the intensity exposure.

In this section, the algorithm of ESIHE is presented. The algorithm consists of three steps, namely Exposure thresholds calculation, Histogram Clipping and Histogram Sub division & Equalization. The description of each step is presented in the following subsections.

2.1. Exposure Threshold calculation

A parameter named exposure threshold (Hanmandlu et al, 2009) is defined which denotes the measure of intensity exposure of the image. This parameter is being used to divide the image in under exposed and over exposed sub images .The normalized range of exposure value is [0-1]. If the value of exposure for a particular image is more than 0.5 and tends towards 1, it means that the image has majority of overexposed region and if this value is less than 0.5 and tending towards 0 then image is containing majority of under exposed regions. In both cases image

ACCEPTED MANUSCRIPT

contains poor contrast and need contrast enhancement. Image intensity exposure value can be calculated as eq. (1).

$$exposure = \frac{1}{L} \frac{\sum_{k=1}^{L} h(k)k}{\sum_{k=1}^{L} h(k)} \quad (1)$$

Where h(k) is histogram of image and L is total number of gray levels.

Another parameter X_a (as calculated in eq. 2) related to exposure is defined, which provides the value of gray level boundary that divides the image into under exposed and over exposed sub images.

$$X_a = L(1 - exposure) \quad (2)$$

This parameter attains a value of greater or lesser than L/2 (gray level) for exposure value lesser or greater than 0.5 respectively for an image having dynamic range 0 to L.

2.2. *Histogram Clipping*

The idea behind histogram clipping is to prevent over enhancement leading to natural appearance of image. For limiting the enhancement rate, we need to limit the first derivative of histogram or the histogram itself (Ooi et. al., 2009).The histogram bins having the value greater than the clipping threshold are limited to the threshold (Fig.1). The clipping threshold is calculated as an average number of grey level occurrences.

The formula for clipping threshold T_c is presented in (3) and (4) calculates the clipped histogram

$$T_c = \frac{1}{L} \sum_{k=1}^{L} h(k) \quad (3)$$

$$h_c(k) = T_c \qquad for\ h(k) \geq T_c \quad (4)$$

Where $h(k)$ and $h_c(k)$ are the original and clipped histogram respectively. This method of

ACCEPTED MANUSCRIPT

histogram clipping is computationally efficient and consumes lesser time.

2.3. Histogram Sub Division and Equalization

The original histogram is first bisected based on exposure threshold value X_a as calculated in (2). The Histogram Sub Division process results in two sub images I_L and I_U ranging from gray level 0 to X_a and $X_a + 1$ to $L-1$ and can be termed as under exposed and over exposed sub images (Fig. 1). $P_L(k)$ and $P_U(k)$ are corresponding PDF of these sub images as defined in eq. (5-6)

$$P_L(k) = h_c(k) / N_L \qquad for\ 0 \le k \le X_a \tag{5}$$

$$P_U(k) = h_c(k) / N_U \qquad for\ X_a + 1 \le k \le L - 1 \tag{6}$$

Where N_L and N_U are total number of pixels in sub images I_L and I_U respectively. $C_L(k)$ and $C_U(k)$ are corresponding CDF of individual sub images and CDFs can be defined as eq. (7-8)

$$C_L(k) = \sum_{k=0}^{Xa} P_L(k) \tag{7}$$

$$C_U(k) = \sum_{k=Xa+1}^{L-1} P_U(k) \tag{8}$$

The next step of ESIHE is to equalize all the four sub histograms individually. The transfer functions for Histogram Equalization based on eq. (7-8) can be defined as eq. (9-10)

$$F_L = X_a \times C_L \tag{9}$$

$$F_U = (X_a + 1) + (L - X_a + 1) C_U \tag{10}$$

F_L and F_U are the transfer functions used for equalizing the sub histograms individually. The final step involves the integration of both sub images into one complete image. The ESIHE-ed output image is produced by combination of both transfer functions for further visual quality inspection and performance evaluation.

ACCEPTED MANUSCRIPT

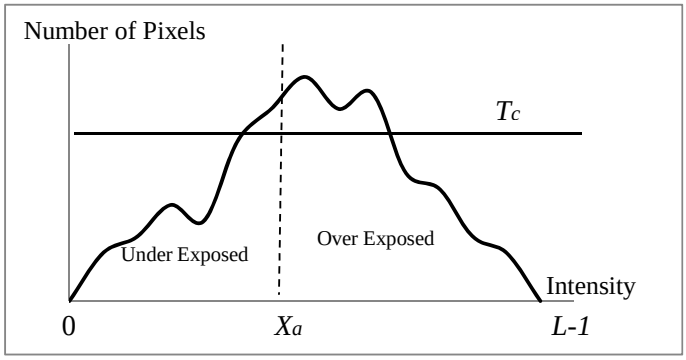

Fig.1. Process of Histogram Sub Division and Clipping

2.4 Algorithm of ESIHE

Step 1: Compute the histogram *h(k)* of image.

Step 2: Compute the value of exposure and threshold parameter X_a.

Step 3: Compute the clipping threshold T_c and clip the histogram $h_c(k)$.

Step 4: Divide the clipped histogram into two sub histograms using the threshold parameter X_a.

Step 5: Apply the histogram equalization on individual sub histograms.

Step 6: Combine the sub images into one image for analysis.

3. Results and discussion

In this section, the simulation results of proposed method ESIHE are compared with existing histogram equalization based methods i.e. BBHE, MMBEBHE, DSIHE, RMSHE and RSIHE. In order to analyze and compare the existing methods we use nine test images: Hands, Fish, Mosque, Tank, Cat, Butterfly, Aircraft, Couple and Field. Visual quality comparison of four images i.e. Hands, Fish, Tank and Cat is shown in figure 2-5.

ACCEPTED MANUSCRIPT

To evaluate the performance of ESIHE, Average Information content is being used as image quality measure (Chen, 2012). Average information content (entropy) is a measure of richness of details of the image and usually measured in units as bits. The entropy here refered is the Shannon Entropy and it measures of the uncertainty associated with gray levels in the image. Larger value of the entropy indicates that more information content is available in the image. Eq. (11) defines Entropy

$$ENT(p) = -\sum_{l=0}^{L-1} P(l)\log P(l) \tag{11}$$

Where *P(l)* is probabily density function of a given image at intensity level *l* and *L* is total number of gray levels in the image. An image with higher entropy value have richness in details and perceived to have better quality.

3.1. Performance Assessment based on Average Information Content

The discrete entropy computed for the methods used in this work for all 9 images are tabulated in Table 1.ESIHE produces highest entropy for all the images thus becomes best suitable approach for bringing out information contents of the image.Specifically for Butterfly,aircraft, Mosque and fish image the entropy values are almost equal to original image. However for HE and MMBEBHE the entropy value for all the images is very less then the corresponding original image. DSIHE method which claimed that it is better in terms of average information content of image is having entropy values lesser than the proposed method. The average of entropy produced by ESIHE method for all images is 5.39 that is very close to average entropy (5.43) for original images, however average entropy of other methods is much smaller in comparison with original image. The entropy closer to original image guarantees bringing out maximum information content of the image.

ACCEPTED MANUSCRIPT

3.2. *Assessment of Visual Quality*

Qualitative assessment of contrast enhancement is necessary along with quantitative assessment. The enhancement results can only be appreciated if the resultant image gives pleasing effect in appearance. By Visual Quality inspection the judgment of annoying artifacts, over enhancement and unnatural enhancement can be done.The visual assesment results are effective quality measures to judge the performance of contrast enhancement algorithm.

Table 1

Entropy Results of different methods

Images	Original	HE	BBHE	MMBEBHE	DSIHE	RSIHE(r=2)	RMSHE(r=2)	ESIHE
Butterfly	4.89	4.70	4.83	4.78	4.83	4.81	4.86	4.89
Aircraft	4.00	3.75	3.90	3.86	3.87	3.95	3.94	3.99
Tank	5.49	4.97	5.42	5.31	5.38	5.45	5.46	5.47
Field	6.56	5.96	6.46	6.41	6.46	6.52	6.49	6.52
Fish	4.49	4.43	4.38	4.22	4.48	4.43	4.48	4.49
Cat	6.01	4.85	5.62	5.64	5.69	5.85	5.68	5.88
Hands	3.99	2.89	3.73	3.79	3.86	3.55	3.80	3.92
Mosque	6.26	5.83	6.11	6.06	6.09	6.08	6.10	6.26
Couple	7.20	5.96	7.01	7.01	7.01	7.06	7.04	7.12
Average	5.43	4.82	5.27	5.23	5.30	5.30	5.32	5.39

ACCEPTED MANUSCRIPT

Wide varieties of standard images ranging from under exposed to over exposed low contrast to high contrast, dark back ground to bright background , are chosen to test the robustness and versatility of ESIHE method. The analysis of visual results from Figure 2-5 shows the supremacy of ESIHE in all the images in terms of contrast enahancement and control on over enhancement. The concrete results in terms of contrast enhancement can be clearly observed in Fig. 2 of *Hands* image.HE,DSIHE and RSIHE results of *Hands* image are over enhanced, however ESIHE image provides control on over enhancement leading to good contrast enhancement results.The original *Fish* image in Fig. 3. is low exposed image even though ESIHE has emproved the quality of image in a big way.The objects in ESIHE-ed *Fish* image are clearly visible however except HE, other methods are not able to enhance the image and object as well as background is not clearly visible in enhanced images.

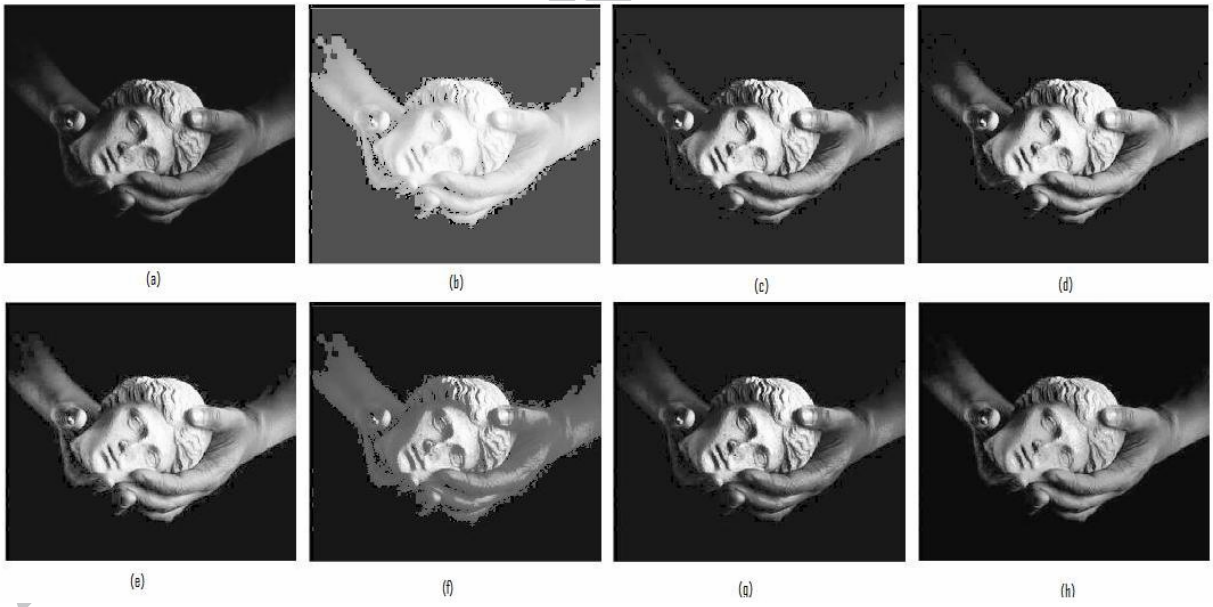

Fig.2. Enhancement results of *Hands* image (a) Original, (b) HE, (c) BBHE, (d) MMBEBHE, (e) DSIHE, (f) RSIHE, (g) RMSHE and (h) ESIHE

ACCEPTED MANUSCRIPT

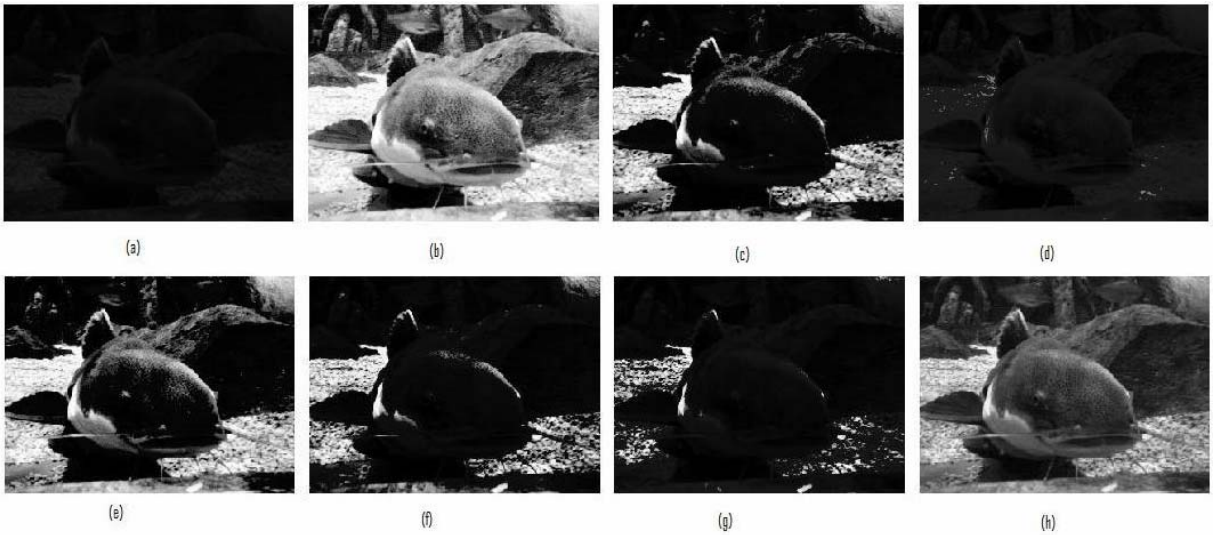

Fig. 3. Enhancement results of Fish image: (a) Original, (b) HE, (c) BBHE, (d) MMBEBHE, (e) DSIHE, (f) RSIHE, (g) RMSHE and (h)ESIHE

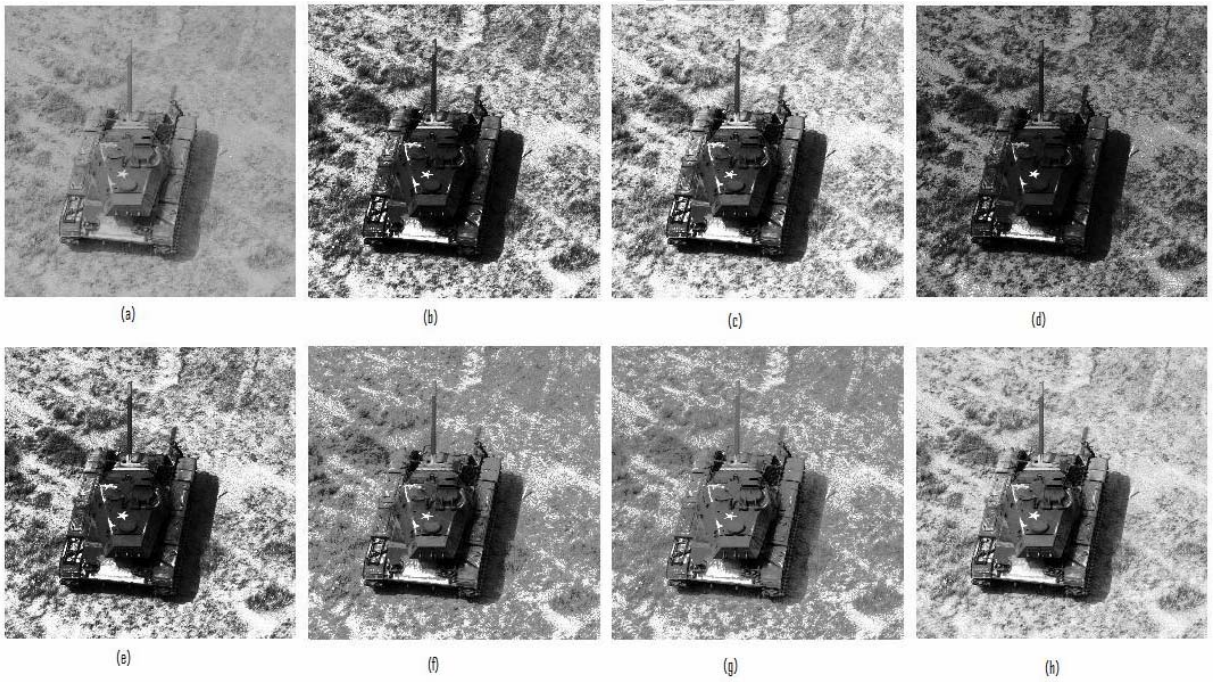

Fig. 4. Enhancement results of Tank image: (a) Original, (b) HE, (c) BBHE, (d) MMBEBHE, (e) DSIHE, (f) RSIHE, (g) RMSHE and (h)ESIHE

ACCEPTED MANUSCRIPT

The *Tank* image in Fig. 4. is a low contrast image and ESIHE yields contrast enhanced image along with natural appearance. The HE, BBHE, DSIHE and MMBEBHE outputs don't provide clear vision of object in case of *Tank* image. From Fig. 5. of *Cat* image it is clearly noticeable that the ESIHE-ed image enhances the low exposed part of image i.e. the left ear of the cat effectively. Although the ESIHE results in Fig. 5 for *Cat* image and Fig. 4 for *Tank* image are visually comparable to other methods but proposed method yields highest entropy value for these images. This shows that ESIHE method produces images with richness of details.

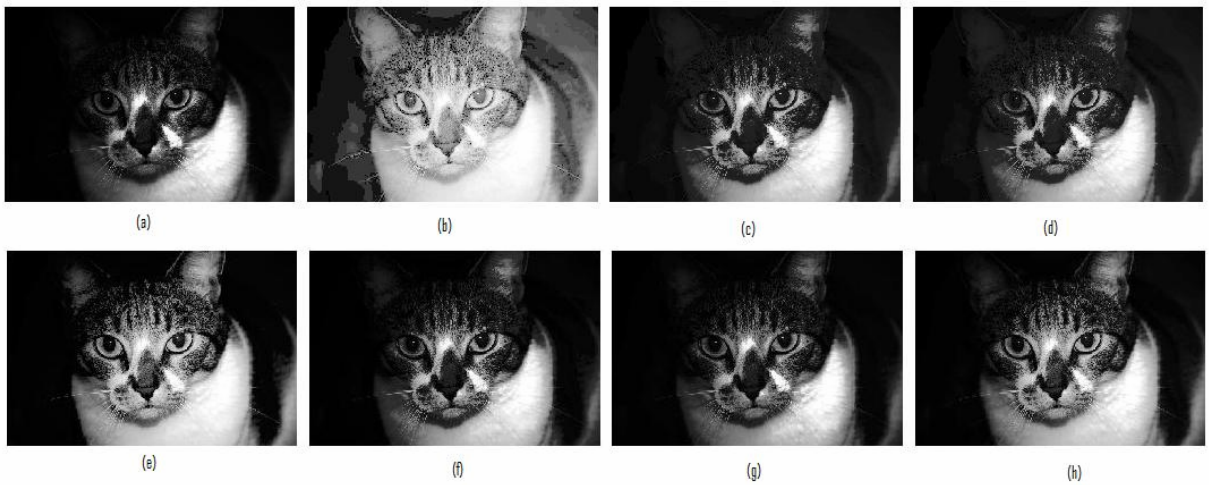

Fig. 5. Enhancement results of Cat image: (a) Original, (b) HE, (c) BBHE, (d) MMBEBHE, (e) DSIHE, (f) RSIHE, (g) RMSHE and (h)ESIHE

3.3. Summary of Assessment and Discussion

After visual inspection and assessment of entropy measures it can be concluded that:

i) ESIHE method is well suited for under exposed images in comparison to other methods.

ii) ESIHE technique is best among other methods in terms of richness in details i.e. provides highest entropy.

iii) ESIHE produces images with good contrast enhancement and control on over enhancement .

ACCEPTED MANUSCRIPT

The objective of this paper is to maximize entropy, enhance under exposed images and control the over enhancement. Bisecting the image on the basis of a parameter related to exposure value plays the role for enhancement of low exposure part and maximizing entropy.

The deciding factor for division of image depends on exposure value and it possess values greater then L/2 gray level for under exposed images (exposure value less than 0.5) and compensates for low exposure by introducing higher gray levels in sub image so that after individual histogram equalisation process the over all exposure value increases. The inverse is true for the over exposed images where the sub division of images is done on the gray level lesser than L/2 gray level.Over enhancement can be controlled by histogram clipping approach by restricting the enhancement rate. The combination of all above mentioned process termed as ESIHE meets the objective of the paper and produces images which are not only quantitatively better but also better in terms of quality in comparison to other conventional HE methods.

4. Conclusion

This paper presents new method for sub division of image based on exposure related parameter. Exposure based division of image and histogram equalization of sub images proved very effective technique for enhancing under exposed images. The histogram clipping technique is also combined with histogram equalization to provide control on over enhancement that leads to natural enhancement. The entropy measures of ESIHE method clearly shows that it outperforms other HE based methods. The Visual quality of ESIHE-ed images shows the robustness of the method and supremacy on other methods for wide variety of images.

5. References

ACCEPTED MANUSCRIPT

C.H. Ooi, N.S.P. Kong and H. Ibrahim," Bi-Histogram Equalization with a Plateau Limit for Digital Image Enhancement", IEEE Trans., Consumer Electronics, vol. 55, no. 4, pp. 2072–2080, Nov. 2009.

K. S. Sim, C. P. Tso and Y. Y. Tan, "Recursive Sub-Image Histogram Equalization Applied to Gray Scale Images", Pattern Recognition Letters, vol. 28, no. 10, pp. 1209-1221, 2007.

M. Hanmandlu, O.P. Verma, N.K. Kumar and M. Kulkarni, A novel optimal fuzzy system for color image enhancement using bacterial foraging, IEEE Trans. Inst. Meas. 58 (8) (2009) 2867–2879.

Q. Wang, and R. K. Ward, "Fast Image/Video Contrast Enhancement Based on Weighted Thresholded Histogram Equalization", IEEE Trans. Consumer Electronics, vol. 53, no. 2, pp. 757-764, May 2007.

R. C. Gonzalez and R. E. Woods, Digital Image Processing, 2nd ed., Prentice Hall, 2002.

Y.T. Kim, "Contrast Enhancement Using Brightness Preserving Bi-Histogram Equalization", IEEE Trans., Consumer Electronics, vol. 43, no. 1, pp. 1-8, Feb. 1997.

S. D. Chen and A. R. Ramli, "Contrast Enhancement Using Recursive Mean-Separate Histogram Equalization for Scalable Brightness Preservation", IEEE Trans., Consumer Electronics, vol. 49, no.4, pp. 1301-1309, Nov. 2003.

S. D. Chen and A. R Ramli, "Minimum Mean Brightness Error Bi-Histogram Equalization in Contrast Enhancement", IEEE Trans., Consumer Electronics, vol. 49, no. 4, pp. 1310-1319, Nov. 2003.

S. D. Chen, "A new image quality measure for assessment of histogram equalization-based contrast enhancement" Digital Signal Processing vol. 22, pp. 640–647, Apr. 2012.

ACCEPTED MANUSCRIPT

248 T. Kim and J. Paik, “Adaptive Contrast Enhancement Using Gain-Controllable Clipped
249 Histogram Equalization”, IEEE Trans. on Consumer Electronics, vol. 54, no. 4, pp. 1803-
250 1810, Nov. 2008.
251 Y. Wan, Q. Chen and B. M. Zhang, “Image Enhancement Based on Equal Area Dualistic Sub-
252 Image Histogram Equalization Method”, IEEE Trans., Consumer Electronics, vol. 45, no. 1,
253 pp. 68-75, Feb. 1999.

ACCEPTED MANUSCRIPT

ACCEPTED MANUSCRIPT

Highlights of Image enhancement Using Exposure Based Sub Image Histogram Equalization

- Exposure based sub image HE proved to be very effective for contrast enhancement.
- The histogram clipping is combined with HE to provide control on over enhancement.
- This method proved to be very effective for enhancing under exposed images.
- The entropy measures of ESIHE method outperform other HE based methods.

ACCEPTED MANUSCRIPT

Magnetotransport behaviour of nanocrystalline $Pr_{1-x}Sr_xMnO_3$ ($0.40 \leq x \leq 0.60$)

Neelam Maikhuri[1,3], Anurag Gaur[1,*], Vasudha Aggarwal[2], Umesh Gaur[4] and H.K. Singh[2]

[1]Department of Physics, National Institute of Technology, Kurukshetra-136119, India

[2]National Physical Laboratory, Dr. K.S. Krishnan Marg, New Delhi-110012, India

[3]Department of Applied Physics, Delhi Technological University, Delhi-110042, India

[4]Centre of Nanotechnology, Indian Institute of Technology, Roorkee -247667, India

Abstract

The nanocrystalline samples of $Pr_{1-x}Sr_xMnO_3$ (PSMO) (x=0.40, 0.50, 0.55, 0.60) were synthesized by wet-chemical sol-gel route. Structural, magnetic and magnetotransport properties have been studied systematically. It is found that $Pr_{1-x}Sr_xMnO_3$ samples with Sr content x=0.40 & 0.50 show paramagnetic to ferromagnetic (PM-FM) transition at T_C~308 K with no trace of FM-AFM transition within the temperature range 77-350 K. However, interestingly a second transition is observed at T~273 and 255 K respectively for sample x=0.55 and 0.60 corresponds to an A-AFM magnetic structure. This indicates that sample x=0.40 and 0.50 are ferromagnetic below T_C, while other samples (x=0.55 & 0.60) have a mixed phase consisting of FM and A-type AFM phases. Resistivity vs temperature (ρ–T) curve shows that the resistivity of all the samples is much larger than the single crystals of corresponding compositions due to large contribution of grain boundaries in the present nanocrystalline samples. Moreover, the decrease in metallic component at higher Sr concentration is also evidenced by the successive reduction in magnetoresistance (MR) with increasing Sr content from x=0.40 to 0.60.

Keywords: Manganites; Magnetic properties; Magnetoresistence

* Corresponding author Email: anuragdph@gmail.com

Tel.: +91-01744-233549; Fax: +91-01744-238050

1. Introduction

Several experimental and theoretical studies have focused on the exploration of grain size effect on the structural, magnetic and electrical transport properties of alkaline earth doped rare earth perovskite manganites chemically represented by $RE_{1-x}AE_xMnO_3$ (RE=rare earth cation and AE=alkaline earth cation) because of their unusual magnetic and electronic properties like colossal magnetoresistance (CMR), charge ordering, orbital ordering and phase separation [1-10]. These studies focus on and clearly highlight the significance of broken Mn-O-Mn exchange bonds at the grain surface and their likely impact on the magnetic and electrical transport properties. Since size reduction leads to increased contribution from the surface regions, the broken Mn-O-Mn bonds are indeed expected to have a definite impact of magneto-electrical properties in manganites. However, in view of the fact that manganites exhibit a strong competition and correlation between various structural and electronic degrees of freedom even more intriguing and complex phenomena are expected. It has been shown that in nano-manganites, size reduction below ~ 100 nm renders the charge and orbitally ordered (CO-OO) ground state with unstable antiferromagnetic (AFM) spin order, giving rise to a ferromagnetic (FM) ground state [3, 11]. Size induced transition from the AFM/CO to the weak ferromagnetic (WFM) state was observed in both nanowires [3] and nanoparticles [4]. It has been shown by Lu et al. [11] that destabilization of the AFM-CO state and formation of a FM order can result in an enhancement of magnetization by two orders of magnitude. The WFM ground state in nanomanganites resulting from the destabilization of AFM ground state has been regarded as a direct consequence of size reduction because when the size is small enough (e.g., 20 nm), the effect of surface spin disordering would become more evident. However, WFM induced by the destabilization of the AFM order has been also reported in single crystals [12, 13] as well as epitaxial thin films [14]. This suggests that evolution of WFM out of the AFM-CO state cannot

be a consequence of material downsizing to nanometric scale alone and that some additional effects such as orbital disordering may also be equally important [13-17].

The effect of material downsizing can have more dramatic effect in the vicinity of compositions that possess strong magnetic phase coexistence and hence show bicritical/multi-critical points. Among the manganites, $Pr_{1-x}Sr_xMnO_3$ (PSMO) has larger band width than $Nd_{1-x}Sr_xMnO_3$ (NSMO) and exhibits PM-FM at T_C~320 K for x~0.30-0.40 [15,17,18]. In single crystals, epitaxial thin films and large grain polycrystalline bulk, insulator to metal (I-M) transition is also observed simultaneous to the PM-FM transition. At higher Sr concentrations (x>0.50), it transforms into an A-type AFM metal and when x exceeds 0.75 the magnetic structure becomes C-type AFM insulator. Therefore, it is interesting to study the behavior of this compound in this critical range, x=0.40 to 0.60 for its nanocystalline particles.

In view of above, we have tried to understand the magnetic and magnetotransport behaviour of nanocrystalline $Pr_{1-x}Sr_xMnO_3$ in this critical range, x=0.40 to 0.60. The $Pr_{1-x}Sr_xMnO_3$ (x=0.40, 0.50, 0.55, 0.60) nanoparticles are prepared by wet-chemical sol-gel route and studied their magnetic and magnetotransport properties for their nanometric size (~40 nm) grains.

2. Experimental procedure

The wet-chemical sol-gel route has been adopted to synthesize $Pr_{1-x}Sr_xMnO_3$ (with x=0.40, 0.50, 0.55, 0.60) nanosized particles at a significantly lower sintering temperature as compared to conventional solid-state reaction method. In this technique, the aqueous solution of high purity $Pr(NO_3)_3 \cdot 6H_2O$, $Sr(NO_3)_2 \cdot 4H_2O$ and $Mn(NO_3)_2 \cdot 4H_2O$ have been taken in the desired stoichiometric proportions. An equal amount of ethylene glycol has been added to this solution with continuous stirring. This solution is then heated on a hot plate at a temperature of ~100–140 °C till a dry thick brown colour sol is formed. At this temperature ethylene glycol polymerizes

into polyethylene glycol, which disperses the cations homogeneously forming a cation polymer network. The polymerized ethylene glycol assists in forming a close network of cations from the precursor solution and helps the reaction enabling the phase formation at low temperatures as compared to that in bulk synthesis via solid state route. The gel forms a resin and the high viscosity of the resin prevents different cations from segregating and ensures a high level of homogeneity. This has been further decomposed in an oven at a temperature of ~250 °C to get a polymeric precursor in the form of a black resin-like material. This material was then finely grounded into powder. Same procedure was used to synthesize all the samples and then pellets were made for each sample. A pellet from each sample was finally sintered at ~ 900 °C for about 12 hrs. All the synthesized samples have been subjected to phase identification and structural characterizations using a powder X-ray diffractometer [XRD, PhilipsPW1710] using CuKα radiation at room temperature and microstructural characterization by the scanning electron microscopic technique [SEM, Philips XL20]. The magnetotransport measurements have been performed by standard dc four-probe technique in the temperature range of 300–77 K at an applied magnetic field of 3 kG. The magnetic characterizations have been carried out by temperature dependent ac susceptibility measurements in the temperature range 77 – 350 K.

3. Results and Discussion

3.1 Structural and Microstructural Characterization

The powder X-ray diffraction (XRD) patterns of $Pr_{1-x}Sr_xMnO_3$ (PSMO) (x=0.40, 0.50, 0.55 and 0.60) samples are shown in Fig. 1. All the samples are single phase, polycrystalline and possess orthorhombic structure (space group Pbnm). The degree of crystallinity remains almost unaffected by the value of x (Sr content). In all the samples, the most intense diffraction maxima is corresponds to the (112) plane followed by (312)/(132) and (220) etc. The lattice parameters of all the PSMO samples were evaluated from the XRD data and are listed in Table 1. For clarity,

the variation of the lattice parameters and unit cell volume with Sr content (x) are plotted in Fig. 2 and 3 respectively. From the XRD data of table 1 and Fig. 2, it is clear that as the Sr content increases, the in plane lattice parameters, viz., *a* and *b* come closer, and the structure becomes nearly tetragonal. The out of plane lattice parameter c first decreases and then again increases slightly. This variation in the lattice parameters is in agreement with the previously reported results [15, 17]. However, in the present case, the in plane lattice parameters are slightly larger than the previously reported values. This could be due to the nanocrystalline nature of the present samples where strain is expected to be more dominant than in microcrystalline samples.

The average crystallite size (CS) of the samples are obtained by the x-ray line width using Scherer formula, $CS = k\lambda/\beta Cos\theta$, where $k = 0.89$ is the shape factor, λ is the wavelength of X-rays, β is the actual FWHM due to CS only and θ is the angle of diffraction. The average CS of a samples having Sr content x=0.40, 0.50, 0.55 and 0.60 are found to be approximately equal to ~ 19 nm, 18 nm, 17 nm and 15 nm respectively. This suggests that Sr concentration (x) also affects the crystallite size. The variation of CS is plotted in Fig. 4. The CSs, lattice parameters and unit cell volumes obtained for the different samples are listed in table 1.

The surface microstructure of the samples, as revealed by scanning electron microscopy (SEM), was found to consist of nanometric grains. The average grain size is found to be ~40 nm in all the samples. This grain size is larger than the crystallite size calculated from the XRD data. This difference is due to the fact that grains are composed of several crystallites, probably due to the internal stress or defects in the structure. A representative typical micrograph showing the surface morphology of the fractured portion of x=0.40 sample is shown in Fig. 5. The crystallite size was also determined by TEM. All the samples were observed to consist of nanocrystalline crystallites of average size ~40 nm and in majority of cases these nano-crystals were found to be present in form of clusters. The TEM investigations also revealed that the crystallite size was not

uniform and in some areas crystals as large as 60-70 nm were also observed. However, the density of such crystals was relatively small. A representative TEM micrograph unraveling local area microstructure and the corresponding selected area electron diffraction pattern showing the presence of nano-crystals and nanocrystalline cluster is shown in figure 6.

3.2 Magnetic Characterization

The magnetic phase characterization was carried out by the temperature dependent AC susceptibility (χ-T) which was measured using the lock-in technique. The variation of AC susceptibility with temperature is shown in Fig. 7 (Left panels). The paramagnetic to ferromagnetic (PM-FM) phase transition temperature (T_C) was determined from the first order temperature derivative ($d\chi/dT$) of the χ-T data, which is plotted in the right panel of Fig. 7. The T_C has been defined as the temperature corresponding to the peak in the $d\chi/dT$ curve. The sample with Sr content x=0.40 shows onset of transition around 315 K and a sharp PM-FM transition at T_C=308 K (value corresponding to the peak in the first order derivative ofχ). This value is nearly equal to the values reported for single crystals of similar composition [15] and similar to the bulk samples. There is no trace of FM –AFM transition within the temperature range 77-350 K. The half doped sample with Sr content x=0.50 also shows transition from PM-FM state at around 308 K but in this case, the transition width has slightly larger value, as shown by relatively broader peak in the $d\chi/dT$. On the lower temperature side, the susceptibility decreases around T~225 K. This could be due to appearance of A-type AFM ordering. In samples with Sr content x=0.55 and 0.60, the FM transition temperature is found to decrease slightly to T_C~300 K and the transition width also increases. But the most interesting observation is the occurrence of a second transition for the samples with Sr content x=0.55 and 0.60 that generally corresponds to an A-AFM magnetic structure. The PM-FM transition is followed by a

kink and change in the slope of the χ - T curve (marked by double arrow in Fig. 7). The smaller peak, which occurs at T~273 and 255 K respectively for sample x=0.55 and 0.60, in the $d\chi/dT$ curve corresponds to this transition. This is due to the presence of a second magnetic phase that has a lower magnetic moment, such as the A-AFM phase that consists of two dimensional ferromagnetic sheets coupled in an antiferromagnetic manner. In samples having Sr concentration x=0.55 and 0.60, the presence of the AFM phase is also evidenced by sharp decrease in the susceptibility in the lower temperature regime. Thus the present results show that at x=0.40 and 0.50 samples are ferromagnetic below T_C, while other samples (x=0.55 & 0.60) have a mixed phase consisting of FM and A-type AFM phases. In nano-manganites with an AFM ground state, the superexchange interaction drives AFM, which is diluted by the surface disorder [6,16,19,20]. This induces a reorganization of the disordered surface spins and has been explained in terms of the core-shell model [19,20].

3.3 Electrical Transport Characterization

Electrical transport characterization of all samples was performed by resistance measurements in zero magnetic field as well as a DC magnetic field H=3 kOe by four probe technique. The resistivity was calculated from the formula $R=\rho L/A$, where R is the resistance, ρ is the resistivity, L is the distance between the voltage probes and A is the cross sectional area of the sample. Percentage magnetoresistance /magnetoressitivity (MR) was calculated by $MR = (\rho_0 - \rho_H)\times 100/\rho_0$, where ρ_0 is the resistivity at zero magnetic field and ρ_H is the resistivity at H=3 kOe. The temperature dependence of resistivity (in the temperature range 4.2-350 K) and MR (in temperature range 77-300 K) is plotted in Fig. 8. The resistivity of all the samples is much larger (~few Ω-cm) than the single crystals of corresponding composition [15,18] which is of the order mΩ-cm or even smaller. This is due to large contribution of the grain boundaries in the

present nanocrystalline samples. Because of the increased surface area which leads to increased grain boundary disorder as discussed in a previous section, the carrier scattering is strongly enhanced in the GB region. As seen in the ρ - T curves plotted in Fig. 8, for the sample x=0.40 the resistivity first increases on lowering the temperature up to 165 K and then shows an insulator to metal (I-M) transition, which is much lower than the PM-FM transition temperature T_C. In case of x=0.50 sample, the resistivity first increases on lowering the temperature and then show a hump or plateau like region. However, no I-M transition is seen in this case and in fact below the humped region, the resistivity shows a very strong enhancement. Nearly similar trend is shown samples having higher Sr concentration (x=0.55 and 0.60). Disappearance of the I-M transition at x=0.50 or higher, is indicative of the fact that in these samples metallic component is reduced. In the composition range x=0.50 – 0.60, the electrical characteristic is determined by competing metallic and insulating phases. The metallic phases are generally contributed by FM and A-AFM phases, while the insulating characteristics are mainly due to the presence of grain boundaries. The absence of I-M transition shows that the contribution of grain boundaries is rather dominant in these samples (x=0.50-0.60) and one possible scenario is that the induced FM phase is not metallic but insulating or has relatively lower conductivity. This can attributed to the nanocrystalline nature of the sample. Because of the small grain/crystallite size the electrical transport is dominated by the contribution from the grain boundaries. The grain boundary contribution envelopes the I-M transition, which occurs in the vicinity of T_C in single crystalline materials.

The decrease in the metallic component at higher Sr concentration is also evidenced by the successive reduction in the magnetoresistance (MR) as Sr content increases from x=0.40 – 0.60. As seen in the right panel of Fig. 8, sample x=0.40 shows the highest MR ~12 % at 77 K and H=3 kOe. The MR values are measured to be ~ 8, 4.5 and 3.5 % for x=0.50, 0.55 and 0.60

respectively. This gradual and systematic decrease in MR magnitude confirms the conjecture that induced FM phase in the present nanocrystalline samples may not be metallic.

4. Conclusions

We have synthesized $Pr_{1-x}Sr_xMnO_3$ (x=0.40, 0.50, 0.55 and 0.60) nanocrystalline samples by wet-chemical sol-gel route and studied their structural, magnetic and electrical transport properties. All the samples are single phase and possess orthorhombic structure with space group Pbnm. The samples with x=0.40 and 0.50 show a paramagnetic to ferromagnetic (PM-FM) transition at T_C~308 K. However, interestingly a second transition is observed at T~273 and 255 K respectively for sample x=0.55 and 0.60 corresponds to an A-AFM phase which indicates that below T_C, samples with x=0.55-0.60 have a mixed phase consisting of FM and A-type AFM phases. In these nanocrystalline samples, the resistivity is much larger than the single crystals of corresponding compositions due to large contribution of grain boundaries. Moreover, the gradual decrease in the MR from ~12 to 3.5 % is observed with increasing the Sr content from x=0.40 to 0.60 which also indicate the decrease in the metallic component at higher Sr concentration.

References

1. Y. Tokura and Y. Tomioka, J. Magn. Magn. Mater. **200**, 1 (1999).
2. F. Chen, H. W. Liu, K. F. Wang, H. Yu, S. Dong, X. Y. Chen, X. P. Jiang, Z. F. Ren, and J.-M. Liu, J. Phys.: Condens. Matter **17**, L467 (2005).
3. S. S. Rao, K. N. Anuradha, S. Sarangi, and S. V. Bhat, Appl. Phys. Lett. **87**, 182503 (2005).
4. S. S. Rao, S. Tripathi, D. Pandey, and S. V. Bhat, Phys. Rev. B **74**, 144416 (2006).
5. Z. Q. Wang, F. Gao, K. F. Wang, H. Yu, Z. F. Ren, and J.-M. Liu, Mater. Sci. Eng., B **136**, 96 (2007).
6. A. Biswas and I. Das, Phys. Rev. B **74**, 172405 (2006).
7. A. Biswas, I. Das, and C. Majumdar, J. Appl. Phys. **98**, 124310 (2005).

8. K. S. Shankar, Sohini Kar, G. N. Subbanna, and A. K. Raychaudhuri, Solid State Commun. **129**, 479 (2004).
9. T. Zhang, C. G. Jin, T. Qian, X. L. Lu, J. M. Bai, and X. G. Li, J. Mater. Chem. **14**, 2787 (2004).
10. S. Dong, F. Gao, Z. Q. Wang, J.-M. Liu, and Z. F. Ren, Appl. Phys. Lett. **90**, 082508 (2007).
11. C. L. Lu, S. Dong, K. F. Wang, F. Gao, P. L. Li, L. Y. Lv, and J.-M. Liu, Appl. Phys. Lett. **91**, 032502 (2007).
12. M. Nagao, T. Asaka, D. Akahoshi, R. Hatakeyama, T. Nagait, M. Saito, K. Watanabe,M. Tanaka, A. Yamazakia, T. Hara, K. Kimoto, H. Kuwahara, and Y. Matsui, *J. Phys.: Condensed Matter*, **19** 492201 (2007).
13. D. Akahoshi, R. Hatakeyama, M. Nagao, T. Asaka, Y. Matsui, and H. Kuwahara, *Phys. Rev. B*, **77** 054404 (2008).
14. R. Prasad, M. M. Singh, P. K. Siwach, P. Fournier and H. K. Singh *Europhys. Lett*. 84 27003 (2008)
15. Y. Tokura *Rep. Prog. Phys.* **69** 797 (2006)
16. Y. Moritomo, T. Akimoto, A. Nakamura, K. Ohoyama and M. Ohashi, *Phys. Rev*. **B58** 5544 (1998).
17. H. Kawano, R. Kajimoto, H. Yoshizawa, Y. Tomioka, H. Kuwahara and Y. Tokura, *Phys. Rev. Lett*. **78** 4253 (1997).
18. J. A. Fernandez-Baca, P. Dai, H. Y. Hwang, C. Kloc, and S.-W.Cheong, Phys. Rev. Lett. **80**, 4012 (1998)
19. R. N. Bhowmik, R. Nagarajan, and R. Ranganathan, *Phys. Rev*. B**69**, 054430 (2004)
20. T. Zhang, T. F. Zhou, T. Qian, and X. G. Li, *Phys. Rev. B* **76** 174415 (2007)

Table and Figure captions:

Table 1: Variation of CSs, lattice parameters and unit cell volumes of $Pr_{1-x}Sr_xMnO_3$ samples with different Sr concentrations.

Fig. 1: XRD patterns of $Pr_{1-x}Sr_xMnO_3$ samples with x= 0.40, 0.50, 0.55 and 0.60.

Fig. 2: Variation of lattice parameters of $Pr_{1-x}Sr_xMnO_3$ with different Sr concentration (x)

Fig. 3: Variation of Unit cell volume of PSMO samples with different Sr concentration (x)

Fig. 4: Variation of crystallite size of PSMO samples with different Sr concentration (x)

Fig. 5: SEM picture showing the morphology of a fractured portion of $Pr_{1-x}Sr_xMnO_3$ (x=0.40).

Fig. 6: Representative TEM picture showing the crystallite size of $Pr_{1-x}Sr_xMnO_3$ (x=0.40). The inset shows the corresponding selected area diffraction pattern.

Fig. 7: Temperature dependent AC susceptibility (left panel) and corresponding temperature derivatives (right panel) of $Pr_{1-x}Sr_xMnO_3$ samples with x= 0.40, 0.50, 0.55 and 0.60.

Fig. 8: The temperature dependent resistivity (left) and MR (right) plots of $Pr_{1-x}Sr_xMnO_3$ samples with x= 0.40, 0.50, 0.55 and 0.60.

Table 1

Sr Concentration (x)	**a (Å)**	**b (Å)**	**c (Å)**	**Volume of unit cell (Å)^3**	**Crystalline size (CS) (nm)**
0.40	5.489	5.467	7.703	229.293	19
0.50	5.494	5.452	7.662	229.502	18
0.55	5.494	5.467	7.667	230.283	17
0.60	5.487	5.485	7.672	230.898	15

Fig. 1

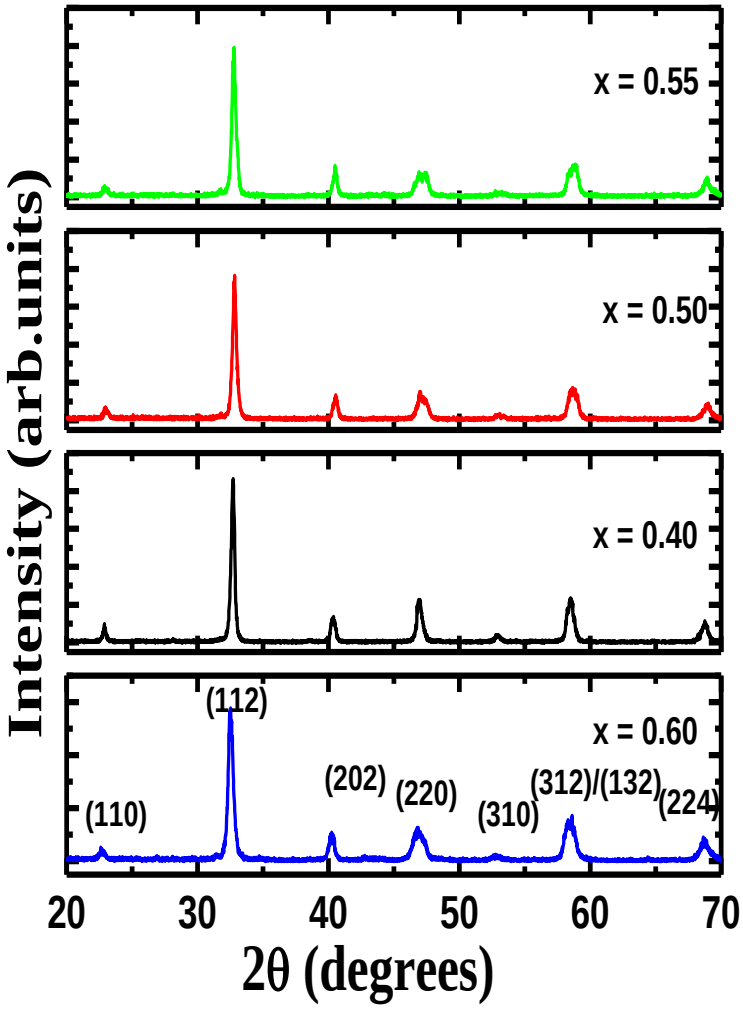
x = 0.55
x = 0.50
x = 0.40
x = 0.60
(112)
(110)
(202)
(220)
(310)
(312)/(132)
(224)
Intensity (arb.units)
20
30
40
50
60
70
2θ (degrees)

/

Fig. 2

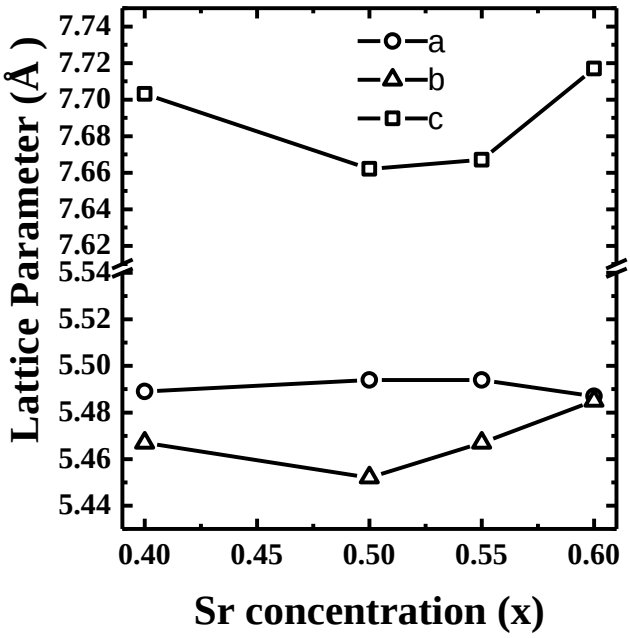
Lattice Parameter (Å)
7.74
7.72
7.70
7.68
7.66
7.64
7.62
5.54
5.52
5.50
5.48
5.46
5.44
a
b
c
0.40
0.45
0.50
0.55
0.60
Sr concentration (x)

Fig. 3

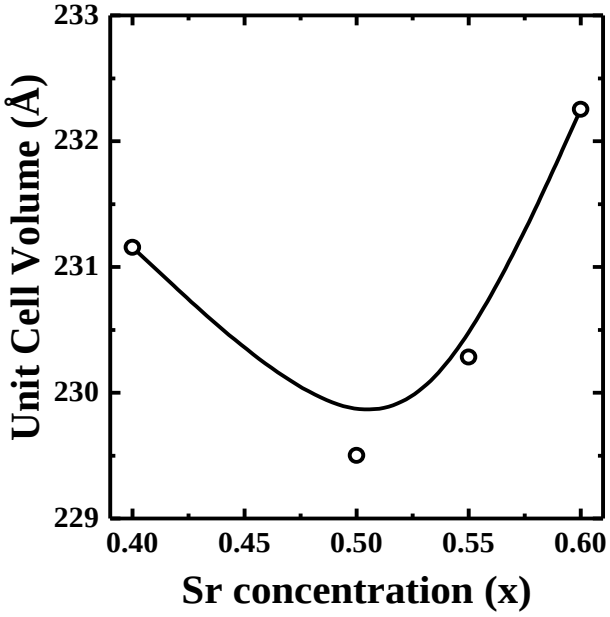
Unit Cell Volume (Å)
233
232
231
230
229
0.40
0.45
0.50
0.55
0.60
Sr concentration (x)

Fig. 4

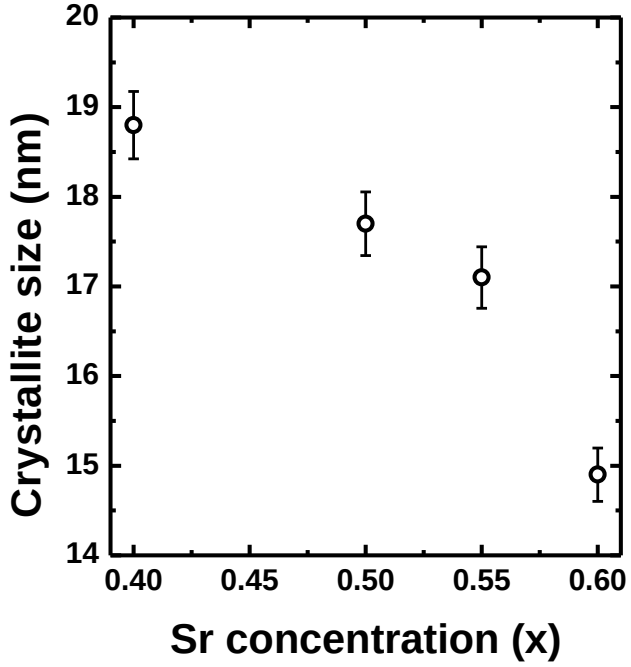
Crystallite size (nm)
20
19
18
17
16
15
14
0.40
0.45
0.50
0.55
0.60
Sr concentration (x)

Fig. 5

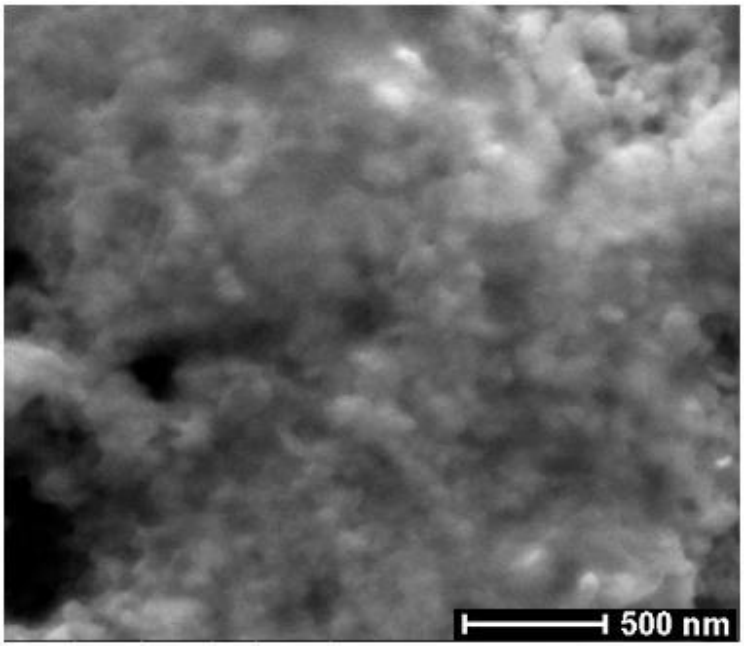

Fig. 6

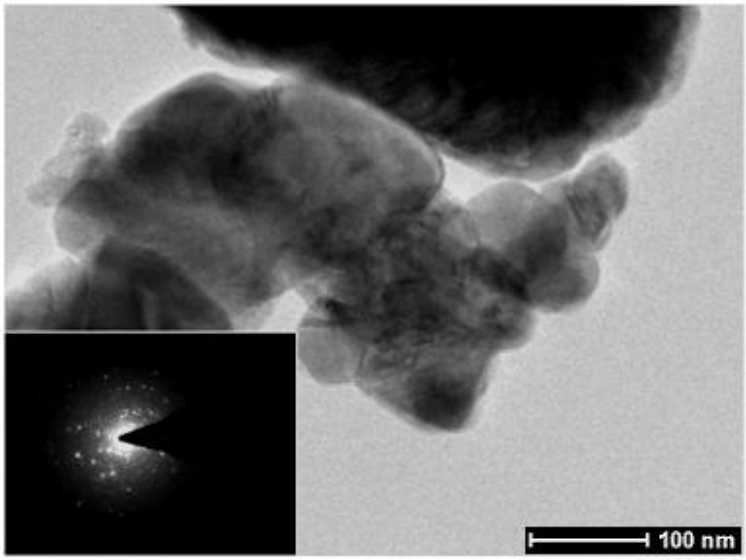

Fig. 7

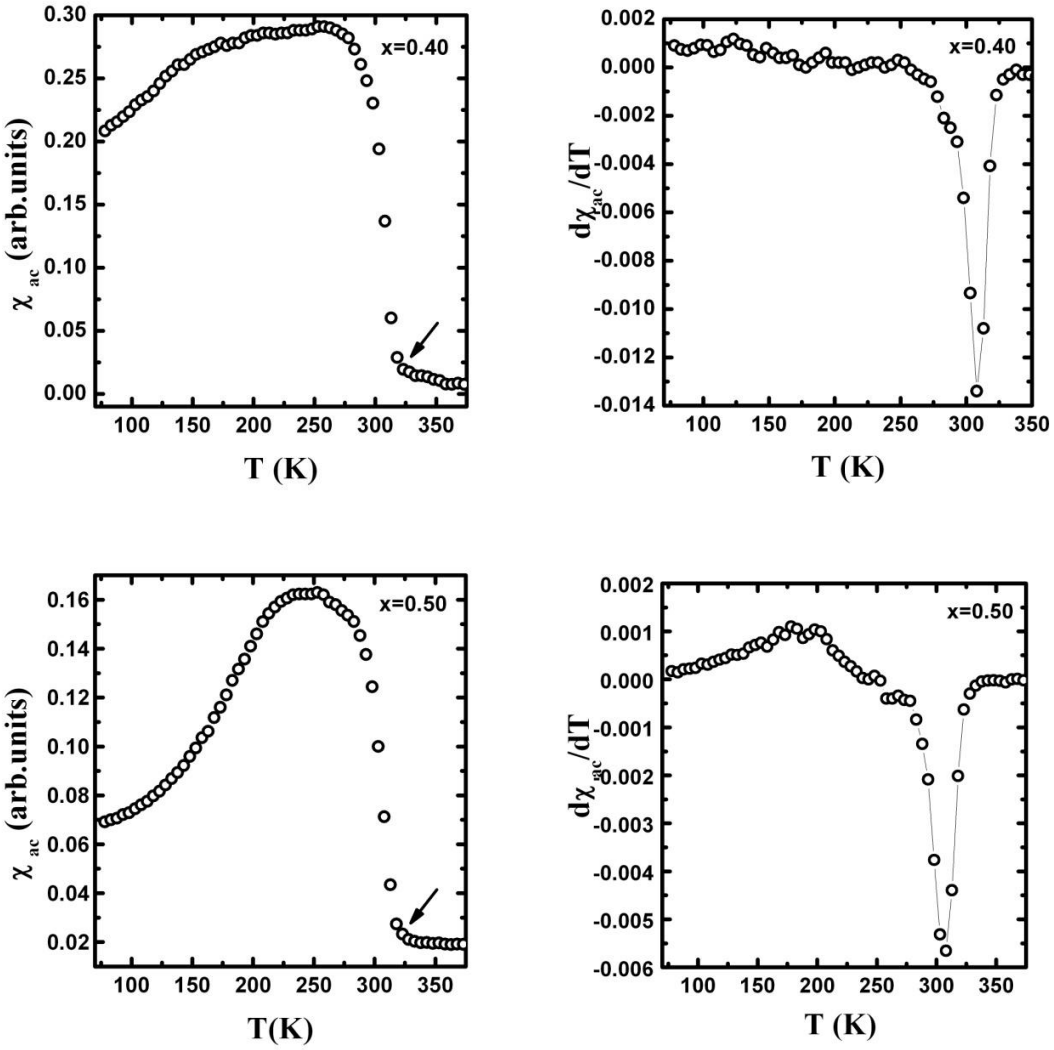
x=0.40
χ_{ac} (arb.units)
T (K)
x=0.40
$d\chi_{ac}/dT$
T (K)
x=0.50
χ_{ac} (arb.units)
T(K)
x=0.50
$d\chi_{ac}/dT$
T (K)

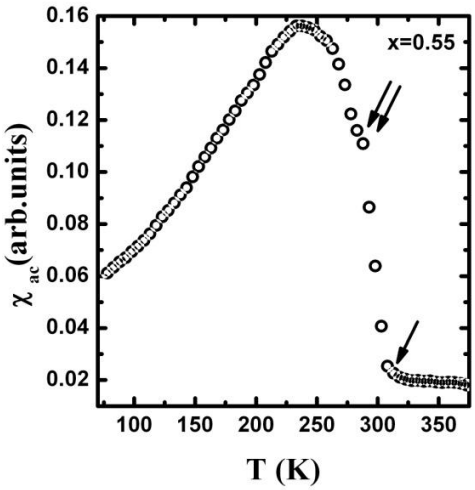
x=0.55
χ ac (arb.units)
T (K)

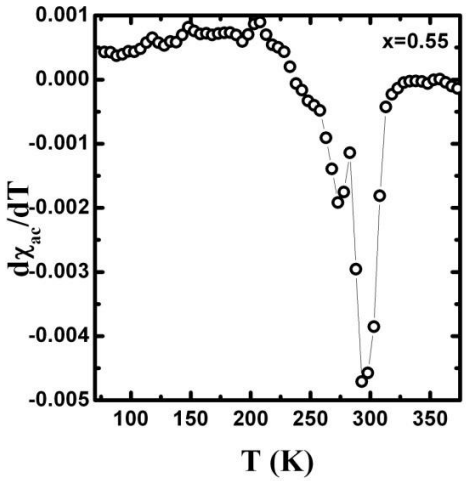
x=0.55
dχac /dT
T (K)

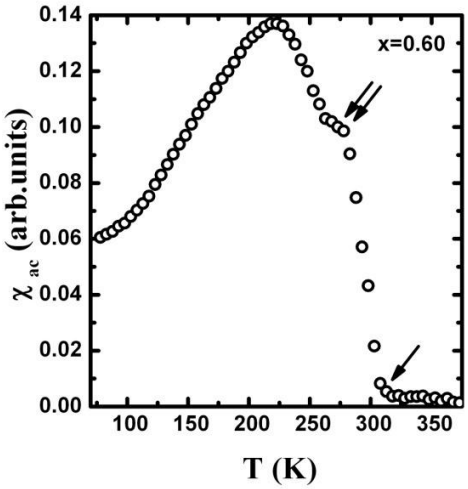
x=0.60
χ ac (arb.units)
T (K)

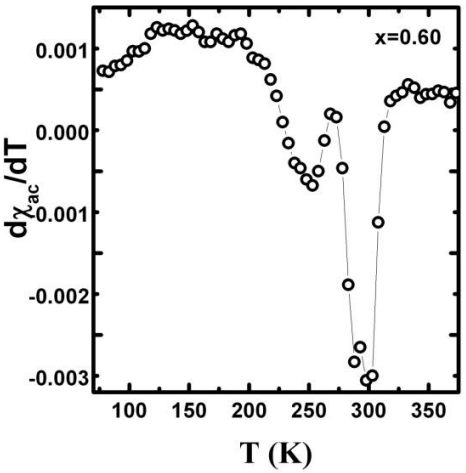
x=0.60
dχac /dT
T (K)

Fig. 8

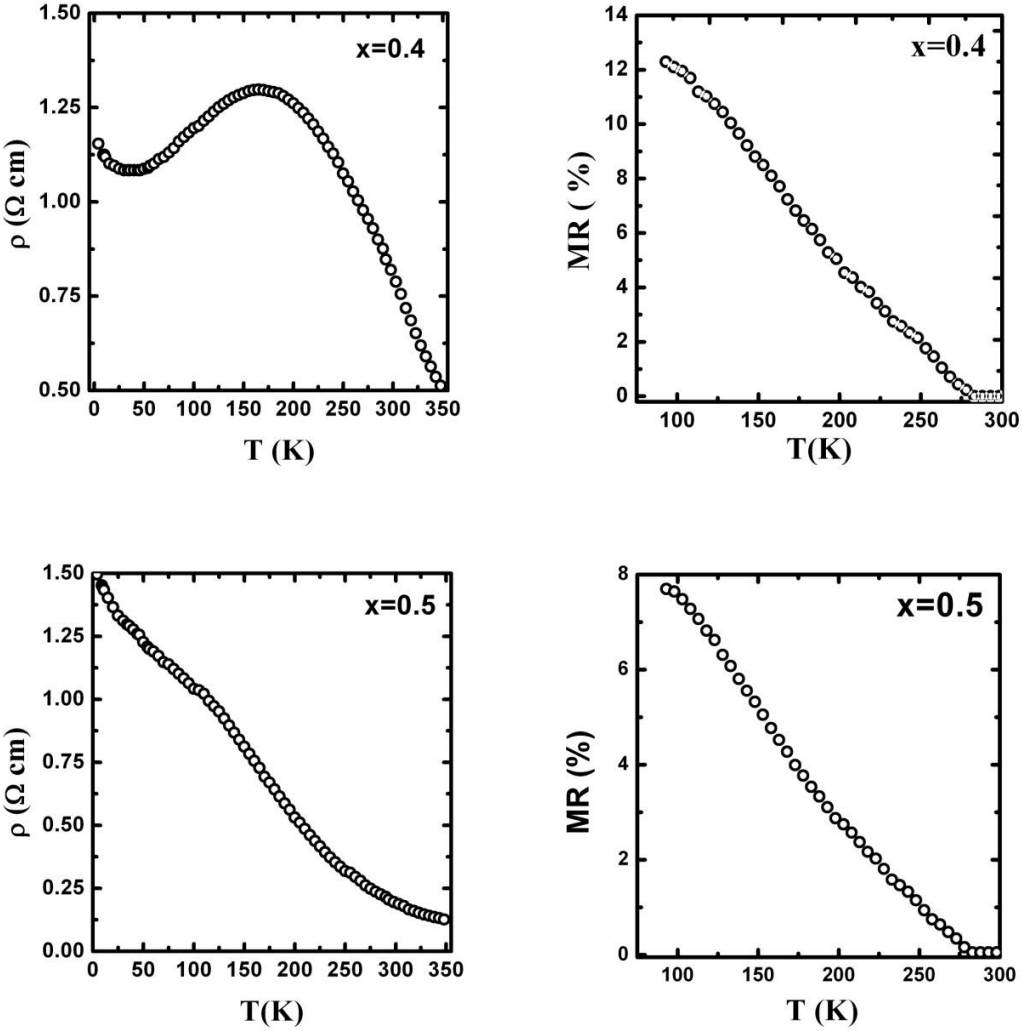

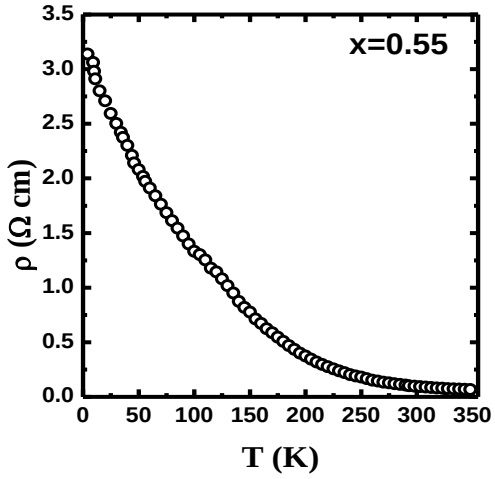
x=0.55
ρ (Ω cm)
T (K)

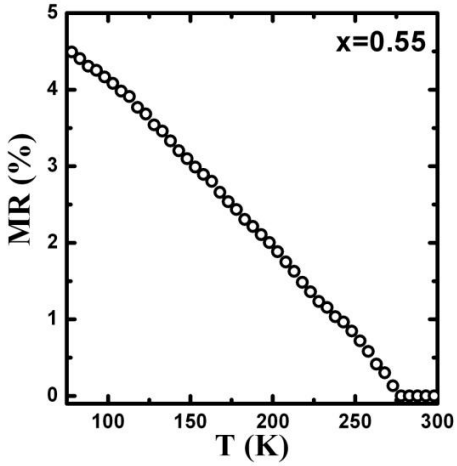
x=0.55
MR (%)
T (K)

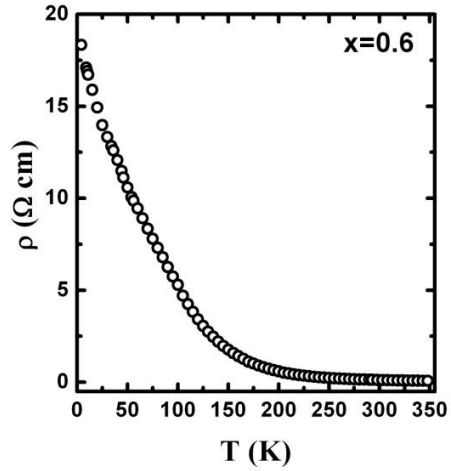
x=0.6
ρ (Ω cm)
T (K)

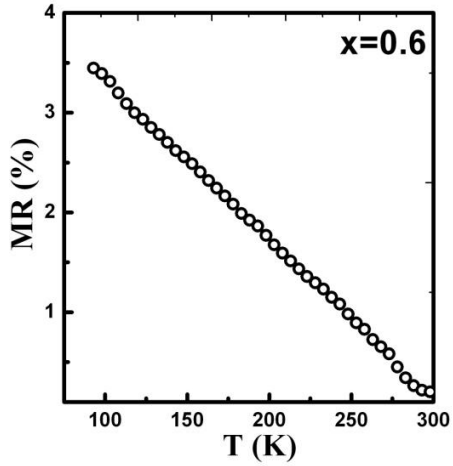
x=0.6
MR (%)
T (K)

I.J. Information Technology and Computer Science, **2013, 11, 103-110**
Published Online October 2013 in MECS (http://www.mecs-press.org/)
DOI: 10.5815/ijitcs.2013.11.11

Novel Spectrum Handoff in Cognitive Radio Networks Using Fuzzy Logic

Nisar A. Lala
Division of Agricultural Engineering SKUAST-(K) Srinagar, J & K, India
E-mail: lalanisar_ae@rediffmail.com

Moin Uddin
Delhi Technological University, Delhi, India
E-mail: prof_moin@yahoo.com

N.A. Sheikh
Department of Mathematics, National Institute of Technology Srinagar, J & K, India
E-mail: neyaznit@yahoo.co.in

***Abstract*—** Cognitive radio is a technology initiated by many research organizations and academic institutions to raise the spectrum utilization of underutilized channels in order to alleviate spectrum scarcity problem to a larger extent. Spectrum handoff is initiated due to appearance of primary user (PU) on the channels occupied by the secondary user (SU) at that time and location or interference to the PU exceeds the certain threshold. In this paper, we propose a novel spectrum handoff algorithm using fuzzy logic based approach that does two important functions: 1) adjusts transmission power of SU intelligently in order to avoid handoff by reducing harmful interference to PUs and 2) takes handoff decisions intelligently in the light of new parameter such as expected holding time (HT) of the channel as one of its antecedent. Simulated results show impact analysis of selection of the channel in the light of HT information and the comparison with random selection algorithm demonstrates that there is considerable reduction in handoff rate of SU.

***Index Terms*—** Spectrum Handoff, Cognitive Radio, Fuzzy Logic, Holding Time, Transmission Power

I. Introduction

The spectrum is a precious natural resource and is presently regulated by governmental agencies to avoid interference among users. The spectrum is allocated by fixed spectrum allocation policy. The fast growth of new wireless applications and services has resulted in increased demand of radio spectrum access. But most of the radio spectrum stands already allocated by fixed allocation policy and it becomes difficult to find unallocated spectrum for these upcoming new applications and services. As per the survey of Federal Communications Commission (FCC) [1], up to 85% of the assigned spectrum is underutilized. This allocation policy has created a situation where there appears an artificial scarcity of the spectrum. This ever increasing demand for spectrum for these new applications cannot be fulfilled unless an alternate scheme to regulate the scarce spectrum is not found. Therefore, FCC has suggested a new communication paradigm for accessing the assigned spectrum dynamically [2] known as cognitive radio (CR). CR is a key technology that will make the dynamic spectrum access (DSA) a reality. DSA allows the SU to dynamically adjust its certain operating parameters in order to adapt to the varying radio environment and utilize the idle spectrum opportunistically [3][4][5] , which is not used by the primary user at that time and location. In addition to spectrum sensing and management, another important function a CR should perform is spectrum mobility and gives rise to a different type of handoff in cognitive radio network known as spectrum handoff. The aim of spectrum handoff is to help the SU to release the occupied channels quickly to avoid interference to the primary user and find suitable idle channels to restart the interrupted transmission. The handoff to new channels should be seamless so that an application running on the SU perceives minimum quality of service (QoS) degradation [6] . The selection procedure of the idle channel for future handoffs can be classified as proactive and reactive methods. In case of proactive method, the decision of channel selection is taken before actual handoff [7][8][9][10] and after handoff decision, in case of reactive decision handoff [11][12][13][14].

There has been little work in literature applying fuzzy logic to cognitive radio networks. The authors of [15], proposed fuzzy logic for controlling the transmission power of SU and [16] applied for cross layer optimization between medium access control layer (MAC) and transport layer. Fuzzy logic has been

Copyright © 2013 MECS

proposed for controlling the spectrum access [17][18] and for spectrum handoff [19][20]. In this paper, we propose a novel spectrum handoff algorithm based on fuzzy logic. The works in [19][20] are most related to our work. Our work differs from previous works, that we propose to introduce expected holding time (HT) of the channel as one of the antecedent to fuzzy logic controller (FLC) in order to take handoff decision and we have used trapezoidal membership functions in place of triangular membership functions for the antecedents and the consequent. Our algorithm will take intelligent handoff decisions in the light of HT information (i.e. PU activity) of the channel and will select those channels for transmission of SU having largest HT parameter (or lowest PU activity).

The remainder of this paper is organized as follows: Section 2 provides the brief introduction to cognitive radio and expected holding time (HT) of the channel. Section 3 proposes the fuzzy logic based handoff algorithm. Section 4 presents the simulated results. Conclusion is provided in section 5.

II. Preliminaries

2.1 Cognitive Radio

The main functions of the cognitive radio are [21]: Spectrum sensing: A cognitive user continuously monitors the wideband spectrum in order to find spectrum holes (or white spaces) and arrival of PU with the help of spectrum sensing techniques such as transmitter detection, interference based detection and cooperative detection. Each technique has its merits and demerits.

Spectrum management: Out of large number of idle channels, the SU has to select the best channels that will satisfy its QoS requirements. The spectrum management functions can be classified as spectrum analysis and spectrum decision.

Spectrum mobility: Due to appearance of the primary user on the channels occupied by the SU at that time, the SU has to change instantly its operating channels to other idle channels. The switching to these idle channels should be seamless so that there is minimum QoS degradation of the application running on the SU.

Spectrum sharing: After deciding the transmitting channel, the SU handshakes with its receiver and starts transmitting. A fair spectrum scheduling mechanism is to be devised for sharing of the spectrum with other SUs.

2.2 Expected Holding Time (HT) of the Channel

The licensed channels to be used opportunistically by the SUs depend on the activities of the PUs at a particular location and time in cognitive radio networks. In literature, licensed channel occupancy is modeled as ON-OFF process. The ON represents the channel is used by PU at that time and OFF represents the channel is idle at that time. The wideband spectrum is sensed continuously to generate usage pattern statistics of all channels. Then average idle period known as expected holding time (HT) of every channel is calculated. HT is defined as the average time duration that the SU can utilize for its data transmission before PU reclaims the channel back. If HT is high, more time is available to the SU for its data transmission. To acquire knowledge about HT parameter, SU has to continuously sense the wideband spectrum which will put more computational burden on SU and also increases its power consumption. We assume in this paper, that HT data is available either provided by spectrum server [22] or SU has the capability to compute HT parameter. By incorporating the HT information (i.e., PU activity) into the decision making, its impact on handoff probability is analyzed using fuzzy logic based approach.

III. Proposed Fuzzy Logic based Handoff Algorithm

The proposed scheme is implemented by means of hierarchical fuzzy logic controller (FLC) as shown in Fig. 1. The 1st FLC estimates the optimal transmission power of SU in order to control harmful interference to PUs and hence, avoids unnecessary handoff. The 2nd FLC takes intelligent handoff decision based on information of transmit power of SU (SUpower), required data rate (SUdatarate) and expected holding time (HT) information based on PU activity of the channel. In this case, handoff is initiated if the selected power of SU is not enough to sustain the QoS (i.e. data rate) of the SU and interference to PU is high. Our algorithm can operate both in overlay and underlay mode by intelligently controlling the transmission power of SU. The undesired spectrum handoff can be avoided by controlling the transmission power and by selecting the channels having largest holding time (i.e. lowest PU activity) among the available idle channels to achieve a considerable reduction in handoff rate.

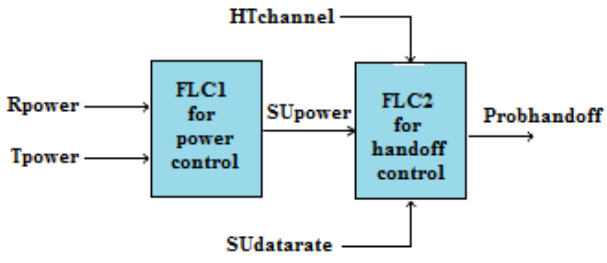

Fig. 1: Hierarchical fuzzy logic system

3.1 Fuzzy Logic Controller (FLC1) for Power Control

After a specific time interval, the SU measures the power of the PU at SU (Rpower) and estimates the

actual transmission power of the PU (Tpower). It is assumed that SU has the capability to estimate the Tpower. Then comparison is made between Rpower and Tpower in order to take a decision on the optimal transmission power of SU (SUpower). The two antecedents (or inputs) used for FLC1 to determine the SUpower are:

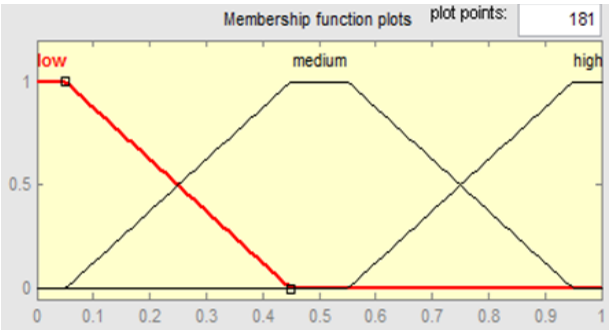

Rpower and Tpower

Fig. 2: Membership functions used for Antecedent 1 (Rpower) and Antecedent 2 (Tpower)

Antecedent 1: Rpower i.e. power received by SU from PU (dBm).

Antecedent 2: Tpower i.e. actual transmission power of PU (dBm). and the consequent is optimal transmission power of SU (SUpower) (dBm).

The two antecedents and the consequent are characterized by a term set 'T(x)' of three fuzzy sets each such as low, medium and high, as shown in (1), defined over a specific universe of discourse

$$T(\text{Rpower}) = T(\text{Tpower}) = T(\text{SUpower}) = \{\text{low, medium, high}\} \quad (1)$$

We have used trapezoidal membership functions for two antecedents (Rpower, Tpower) and the consequent (SUpower) as shown in Fig. 2 and Fig. 3.

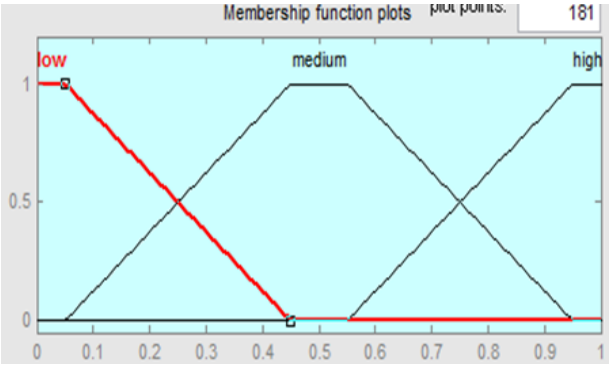

SUpower

Fig. 3: Membership function used for the consequent (SUpower)

The analysis of the algorithm has been performed over normalized values of the antecedents and the consequent between [0, 1]. Table 1 show the rules contained in the rule base of FLC1. Fuzzy nine IF-THEN rules were designed to help the fuzzy inference engine to take decisions. The logic behind their definition is to realize optimal transmission power of the SU. For example, as per rule 3, if the Rpower is low and Tpower is high then the SUpower is high, this corresponds to the situation of very low interference in the communication channel and therefore, allocates the maximum admissible transmission power to the SU. Also as per rule 9, when the Rpower and Tpower is high then SUpower $_{is}$ low, this corresponds to the situation of high interference in the communication channel. Therefore, the transmitted power is reduced and allocation of power is minimum in order to avoid harmful interference to PU.

Table 1: Rule base of FLC1 for transmission power control

Rule #	Rpower	Tpower	SUpower
1	Low	Low	Low
2	Low	Medium	Medium
3	Low	High	High
4	Medium	Low	Low
5	Medium	Medium	Low
6	Medium	High	Medium
7	High	Low	Low
8	High	Medium	Low
9	High	High	Low

3.2 Fuzzy Logic Controller (FLC2) for Handoff Decision

This FLC is in charge of taking the handoff decisions based on three descriptors (antecedents) such as transmit power (SUpower), required data rate i.e. QoS (SUdatarate) and HT information (HTchannel) of the channel. The three antecedents and one consequent are:

Antecedent 1: HT information of the channel (HTchannel) (seconds).

Antecedent 2: required data rate (SUdatarate) (bps).

Antecedent 3: transmission power of SU (SUpower) (dBm). and the consequent is handoff probability (probhandoff).

The three antecedents are characterized by a term set 'T(x)' of three fuzzy sets each such as low, medium and high, as shown in (2), defined over a specific universe of discourse

$$T(\text{HTchannel}) = T(\text{SUdatarate}) = T(\text{SUpower}) = \{\text{low, medium, high}\} \quad (2)$$

And the consequent is characterized by a term set 'T(x)' of four fuzzy sets such as No, Probably No, Probably Yes and Yes, as shown in (3), defined over a specific universe of discourse

Copyright © 2013 MECS

T(Probhandoff) = {No, PNo, PYes, Yes} (3)

We have used trapezoidal membership functions for three antecedents and the consequent are shown in Fig. 4 and Fig. 5. The analysis of the algorithm has been performed over normalized values of the antecedents and the consequent between [0, 1]. Table 2 show the rules contained in the rule base of FLC2. Fuzzy 27 IF-THEN rules were designed to help the fuzzy inference engine to take handoff decisions. The logic behind their definition is to take the ideal handoff decision. For example, as per rules 7, 8 and 9, the algorithm take the decision of not to handoff and as per rules 22, 23 and 24, the algorithm take the decision of handoff to other idle channels.

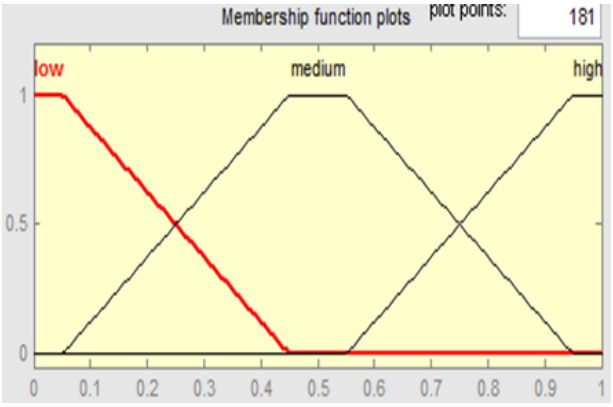

HTchannel, SUpower and SUdatarate

Fig. 4: Membership functions used for three inputs of FLC2 i.e. Antecedent 1 (HTchannel), Antecedent 2 (Supower) and Antecedent 3 (SUdatarate)

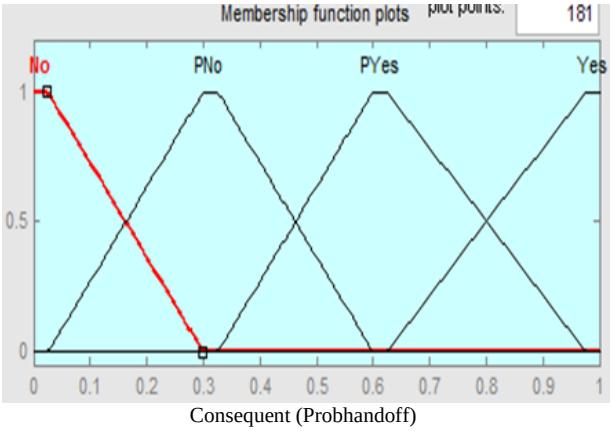

Consequent (Probhandoff)

Fig. 5: Membership function used for consequent of FLC2 i.e. Probhandoff

Table 2: Rule base of FLC2 for spectrum handoff decision

Rule #	HTchannel	SUpower	SUdatarate	Probhandoff
1	high	low	low	PYes
2	high	low	medium	Yes
3	high	low	high	Yes
4	high	medium	low	No
5	high	medium	medium	No
6	high	medium	high	PNo
7	high	high	low	No
8	high	high	medium	No
9	high	high	high	No
10	medium	low	low	Yes
11	medium	low	medium	Yes
12	medium	low	high	Yes
13	medium	medium	low	No
14	medium	medium	medium	PNo
15	medium	medium	high	PYes
16	medium	high	low	No
17	medium	high	medium	No
18	medium	high	high	PNo
19	low	low	low	Yes
20	low	low	medium	Yes
21	low	low	high	Yes
22	low	medium	low	Yes
23	low	medium	medium	Yes
24	low	medium	high	Yes
25	low	high	low	PYes
26	low	high	medium	PYes
27	low	high	high	PYes

IV. Simulated Results

The proposed algorithm has been simulated in fuzzy logic toolbox of Matlab 7.6.

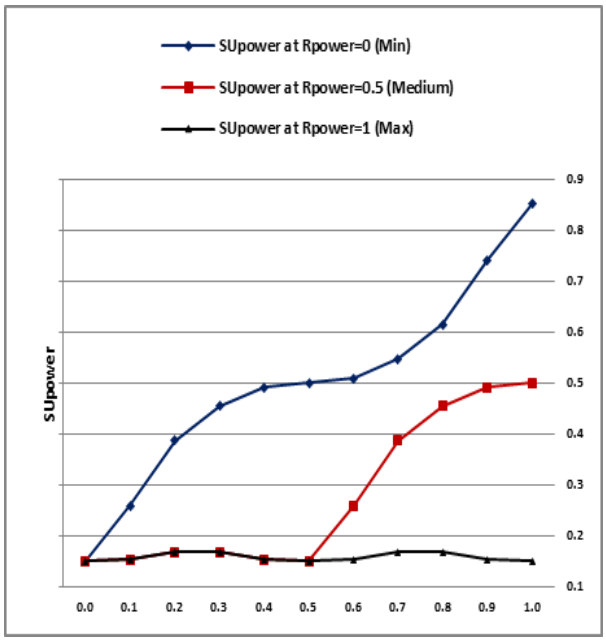

Tpower

Fig. 6: Simulation results show impact of Tpower on SUpower at constant three values (i.e. min., medium and max.) values of Rpower

4.1 Simulation Results For FLC1

Here, we simulate the SUpower as a function of Rpower and Tpower. Fig. 6 shows the impact of Tpower, at three different constant values of Rpower, on SUpower while Fig. 7 shows impact of Rpower, at three different constant values of Tpower, on SUpower.

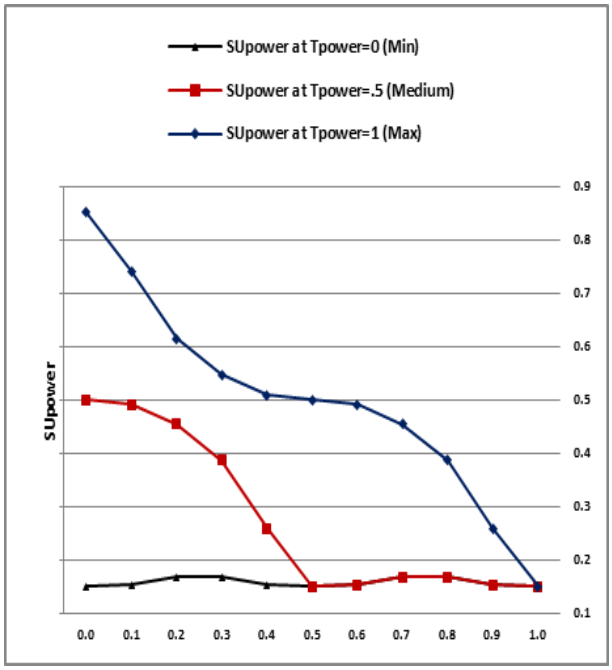

Fig. 7: Simulation results show impact of Rpower on SUpower at three constant (i.e. min., medium and max.) values of Tpower

The results show that SUpower remains at minimum value when Rpower ≥ Tpower and there has been linear increase in SUpower when Tpower > Rpower. As can be seen from Fig. 8, the maximum value of SUpower is attained when Rpower is at minimum value and Tpower is at maximum value. Our algorithm helps SU to change the transmission power gradually in order to adapt to the dynamic channel condition.

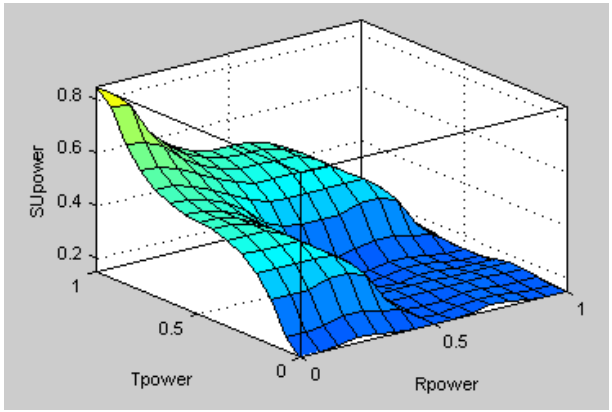

Fig. 8: Simulation results show simutaneous impact of Rpower and Tpower on SUpower

4.2 Simulation Results for FLC2

This fuzzy logic system is in charge of taking handoff decision. When Probhandoff ≥ 0.5, the algorithm takes the decision of spectrum handoff, therefore, switches to other idle channels. Fig. 9, Fig. 10 and Fig. 11 show the impact of HTchannel, SUdatarate and SUpower on the handoff probability.

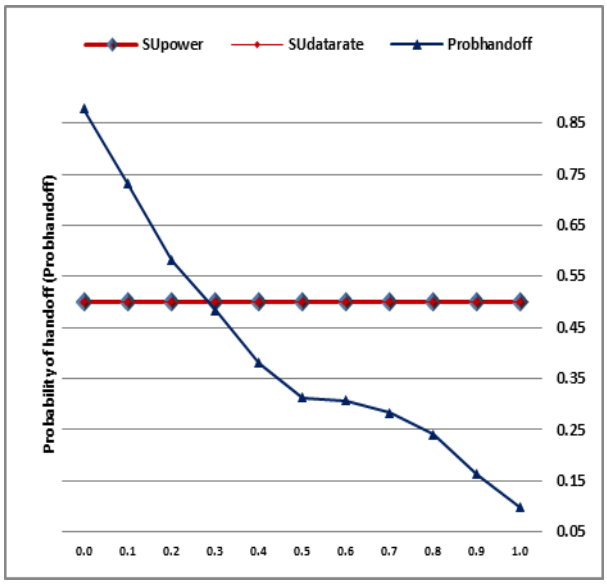

Fig. 9: Simulation results show impact of HTchannel on Probhandoff at constant values of SUpower, SUdatarate=0.5 (medium)

As can be seen from Fig. 9 that with increase in HTchannel, at constant values of SUpower and SUdatarate, the probability of handoff decreases. The proposed algorithm helps in selection of channel having largest HT value (i.e. idle period), which results in higher throughput and lesser number of handoff.

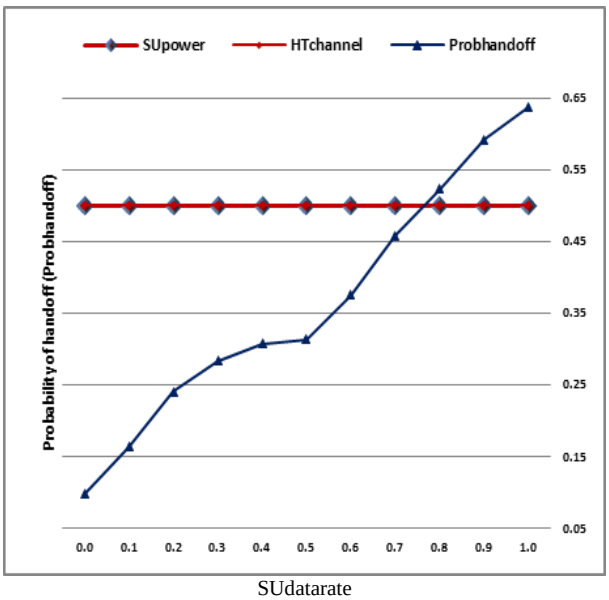

Fig. 10: Simulation results show impact of SUdatarate on Probhandoff at constant values of SUpower, HTchannel=0.5 (medium)

As can be seen from Fig. 10 that with increase in SUdatarate, at constant values of SUpower and HTchannel, the probability of handoff increases.

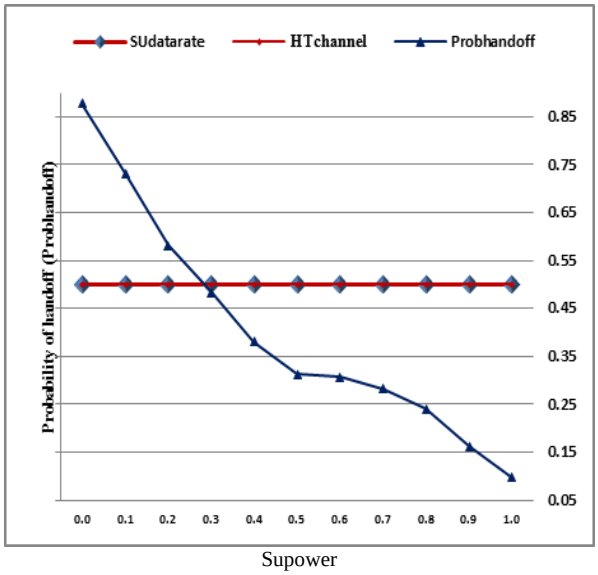

Fig. 11: Simulation results show impact of SUpower on Probhandoff at constant values of SUdatarate, HTchannel=0.5 (medium)

As can be seen from Fig. 11 that with increase in SUpower, at constant values of SUdatarate and HTchannel, the probability of handoff decreases. By adjusting the SUpower, the harmful interference to PU can be mitigated that reduces the necessity of handoff and hence results in reduction of number of handoffs.

Fig. 12 shows simultaneous impact of SUpower and HTchannel, at constant value of SUdatarate, on the probability of handoff. It can be seen that probability of handoff decreases with increase in HTchannel and SUpower and obtains a minimum value when HTchannel and SUpower are both at maximum values.

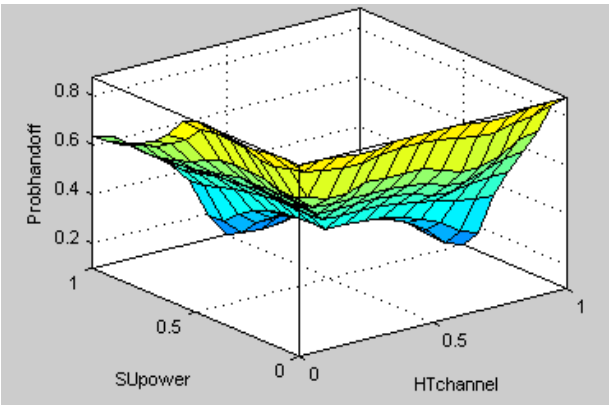

Fig. 12: Simulation results show impact of SUpower and HTchannel on Probhandoff at constant value of SUdatarate=0.5 (medium)

Fig. 13 shows simultaneous impact of SUdatarate and HTchannel, at constant value of SUpower, on the probability of handoff. It can be seen that handoff probability decreases with increase in HTchannel and decrease in SUdatarate and obtains a minimum value when HTchannel is at maximum value and SUdatarate is at minimum value.

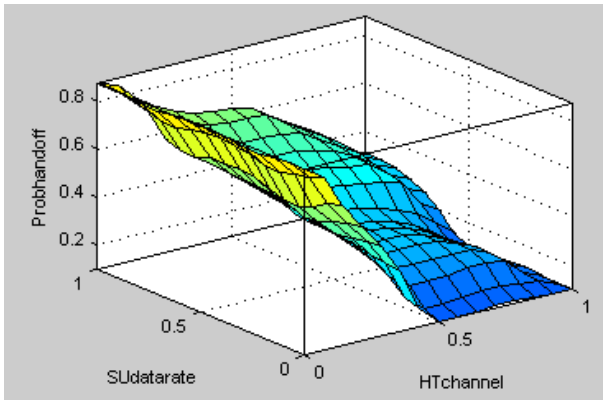

Fig. 13: Simulation results show impact of SUdatarate and HTchannel on Probhandoff at constant value of SUpower=0.5 (medium)

Fig. 14 shows the impact of SUpower and SUdatarate, at constant value of HTchannel, on the probability of handoff. It can be seen that handoff probability decreases with increase in SUpower and decrease in SUdatarate and obtains a minimum value when SUpower is at maximum value and SUdatarate is at minimum value.

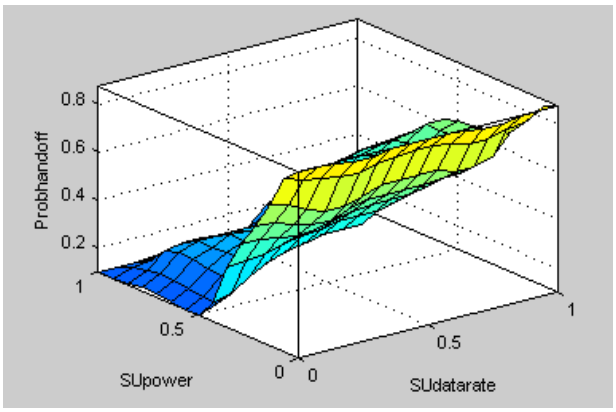

Fig. 14: Simulation results show impact of SUpower and SUdatarate on Probhandoff at constant value of HTchannel=0.5 (medium)

4.3 Comparison of Proposed Algorithm with Random Selection Algorithm (i.e. Without HT Information)

In this simulation, we have compared two algorithms as a function of deviation from largest HT value. As can be seen from Fig. 15, the handoff probability of the proposed algorithm remains constant and always selects the channel having largest HT value. In case of random selection, the handoff probability increases with increase in deviation from largest HT value as the average idle period of channel decrease with increase in deviation from largest HT value. Therefore, for same service time requirement of SUs, the random selection algorithm experiences necessity of earlier handoff due

Copyright © 2013 MECS

to shorter idle period of the selected channels which result in higher number of handoffs. Therefore, the proposed algorithm experiences lesser number of handoffs due to selection of channels having largest HT value (i.e. average idle period). As a result, there is considerable reduction in handoff rate of the proposed algorithm.

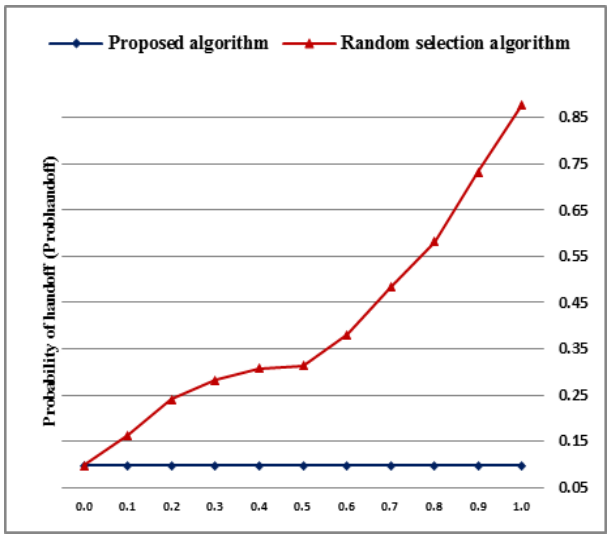

Fig. 15: Comparison of proposed algorithm and random selection algorithm

V. Conclusion

In this paper, we have proposed a novel spectrum handoff algorithm using fuzzy logic approach for cognitive radio networks. The algorithm selects the optimal transmission power for SU in order to avoid interference to PU and takes handoff decision based on knowledge of transmission power, data rate and HT (i.e. average idle period) of a channel. The proposed algorithm helps in selection of the channel having largest HT value, which results in achieving higher quality of service (QoS) for the application running on the SU. Hence, the proposed algorithm reduces the number of required handoffs. The simulated results validate the findings.

References

[1] FCC. Notice of proposed rulemaking and order No. 03-222. Dec. 2003.

[2] Et docket No.03-237, Nov. 2003. [Online] Available: http://hraunfoss.fcc.gov/edocs_public/attachmatch/FCC-03-289A1.pdf.

[3] Mitola J. Cognitive radio: an integrated agent architecture for software defined radio. Ph. D. Dissertation: KTH Royal Institute of Technology, 2000.

[4] Mitola J, Maguire GQ. Cognitive radio: making software radios more personal [J]. IEEE Personal Communications, 1999, 6(4):13-18.

[5] Haykin S. Cognitive radio: Brain empowered wireless communications [J]. IEEE Journal on Selected Areas in Communications, 2005, 23(2): 201-220.

[6] Liu HJ, Wang ZX, Ll SF, Yl M. Study on the performance of spectrum mobility in cognitive wireless network [C]. In: Proceedings of (IEEE) International Conference on Communication Systems (ICCS), 2008.

[7] Song Y, Xie J. Proactive spectrum handoff in cognitive radio adhoc networks based on common hopping coordination [C]. In: Proceedings of (IEEE) INFOCOM, 2010.

[8] Zheng S, Yang X, Chen S, Lou C. Target channel sequence selection scheme for proactive- decision spectrum handoff [J]. IEEE Communication Letters, 2011, 15(12):1332-1334.

[9] Song Y, Xie J. ProSpect: A proactive spectrum handoff framework for cognitive radio adhoc networks without common control channel [J]. IEEE Transactions on Mobile Computing, 2012, 11(7):1127-1139.

[10] Wang C-W, Wang L-C. Modeling and analysis for proactive decision spectrum handoff in cognitive radio networks [C]. In: Proceedings of (IEEE) International Conference on Communications (ICC), 2009.

[11] Willkomm D, Gross J, Wolisz A. Reliable link maintenance in cognitive radio systems [C]. In: Proceedings of (IEEE) International Symposium on Dynamic Spectrum Access Networks (DySPAN), 2005.

[12] Tian J, Bi G. A new link maintenance and compensation model for cognitive UWB radio systems [C]. In: Proceedings of International Conference on ITS Telecommunications, 2006.

[13] Wang L-C, Wang C-W. Spectrum handoff for cognitive radio networks: reactive sensing or proactive sensing [C]. In: Proceedings of (IEEE) International Performance Computing and Communications Conference (IPCCC), 2008.

[14] Wang C-W, Wang L-C, Adachi F. Modeling and analysis for reactive decision spectrum handoff in cognitive radio networks[C]. In: Proceedings of (IEEE) GLOBECOM, 2010.

[15] Le H-S T, Liang Q. An efficient power control scheme for cognitive radios [C]. In: Proceedings of Wireless Communications and Networks Conference, 2007:2559-2563.

Copyright © 2013 MECS

[16] Baldo N, Zorzi M. Fuzzy logic for cross layer optimization in cognitive radio networks [J]. IEEE Communication Magazine, 2008:64-72.

[17] Le H-S T, Ly HD. Opportunistic spectrum access using fuzzy logic for cognitive radio networks [C]. In: Proceedings of 2nd International Conference on Communications and Electronics (ICCE), 2008: 240- 245.

[18] Kaur P, Moin Uddin, Khosla A. Fuzzy based adaptive bandwidth allocation scheme in cognitive radio networks [C]. In: Proceedings of International Conference on ICT and knowledge Engineering, 2010: 41-45.

[19] Giupponi L, Perez-Neira AI. Fuzzy based spectrum handoff in cognitive radio networks [C]. In: Proceedings of 3rd International Conference on Cognitive Radio Oriented Wireless Networks and and Communications CrownCom 2008: 1-6.

[20] Kaur P, Moin Uddin, Khosla A. An efficient spectrum mobility management strategy in cognitive radio networks. 1st UK-India International Workshop on Cognitive Wireless Systems UKIWCWS, 2009.

[21] Akyildiz IF, Lee WY, Vuran MC, Mohanty S. Next generation/dynamic spectrum access/cognitive radio wireless networks: A survey [J]. Computer Networks (Elsevier), 2006, 50: 2127–2159.

[22] Dahi S, Tabbane S. Radio resource management on the basis of temporal characterization of spectrum holes in cognitive radio networks [C]. In: Proceedings of 14th International Symposium on Wireless Personal Multimedia Communication (WPMC), 2011.

Authors' Profiles

Mr. Nisar Ahmad Lala received his B. Sc. and M.Sc. in Electronics in 1990 and 1994 respectively from University of Kashmir, J & K, India. He is working as Assistant Professor in the division of Agricultural Engineering, S. K. University of Agricultural Sciences and Technology (Kashmir) Srinagar, J & K, India. He is currently pursuing Ph.D. at National Institute of Technology Srinagar, J&K, India. His research interests include cognitive radio networks and fuzzy modeling.

Prof. Moin Uddin is a senior member, IEEE. Moin Uddin did his B.Sc. and M.Sc. Engineering in 1972 and 1978 from Aligarh Muslim University, Uttar Pradesh, India. He completed his Ph.D. in 1993 from Roorkee University, India. He has more than 30 years of experience in academics and research and is currently serving as Pro-ViceChancellor, Delhi Technological University, Delhi. Prior to this, he was Director of Dr. B R Ambedkar National Institute of Technology, Jalandhar, India. He has large number of publications in international and national Journals and fourteen research scholars have completed their Ph.D. under his guidance and five more are pursuing the same. He has designed the computer engineering curriculums of many international and national universities and institutions and is among the expert panel of these universities. Prof. Moin Uddin is a life member ISTE national society and member, board of studies, of many institutions.

Dr. N. A. Sheikh received his M.Sc., M.phil and Ph.D. (Applied Mathematics) in 1991, 1993 and 1996 from Aligarh Muslim University, Uttar Pradesh, India. He is working as Assistant Professor in the department of Mathematics, National Institute of Technology Srinagar, J & K, India. He has fourteen publications in international and national Journals. His research interests include walsh functions and its applications, functional analysis and some results on wavelets.

ISSN: 2249-7137 Vol. 3, Issue. 8, August 2013

Published by: South Asian Academic Research Journals

ACADEMICIA:

An International Multidisciplinary Research Journal

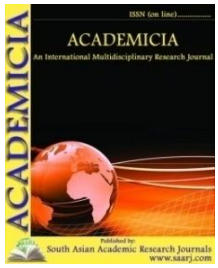

OCCUPATIONAL SAFETY AND HEALTH IN MANUFACTURING SECTOR: COMPARATIVE STUDY OF INDIA AND CHINA

Meha Joshi*; Dr. Ritu Bajaj**

*Assistant Professor,
Delhi School of Management,
Delhi Technological University,
India.
**Professor,
JIMS,
Delhi, India.

www.IndianJournals.com
Members Copy, Not for Commercial Sale
Downloaded From IP - 180.149.53.83 on dated 18-Sep-2013

ABSTRACT

Occupational Health and safety have not been ambit of focus for once. But today the realisation is such, that occupational health and safety is true indicator of country's success. If they are well taken care of, the productive results may be achieved.

The paper gives an overview of the issues of India and China relating to the occupational health and safety, the occupational injuries and fatalities sustained by them, the initiatives taken by them to foster safety culture and above all the recommended health and safety plans which need to be enforced. The paper further tries to demonstrate the difference between practices followed by India and China and by means of it illustrates the points which can help India strengthen in form of capacity building of the units. It also aims at providing an answer as to how the accidents can be prevented and thus a better safety culture can be implemented in the organisations.

INTRODUCTION

Occupational Health and safety have not been ambit of focus for once. But today the realisation is such, that occupational health and safety is true indicator of country's success. If they are well taken care of, the productive results may be achieved.

Logically, manufacturing industry is one of the riskiest industries when it comes to health and safety of employees. Interruptions in production caused by fires and accidents easily lead to significant economic losses, and potential hazards to humans and the environment(1)

Health and safety are important responsibilities that every industry must consider. Health and safety are serious risks that companies face. These risks directly and indirectly affect business operations. Consequently, for a company to grow and prosper, it is pertinent that risks are effectively managed, because by managing business risks, an organization's health, assets and opportunities will be secured and taken full advantage of (2)

Most organizations operate in an environment of risk and the key to business success is to reduce this risk to an acceptable or tolerable level. Health and safety represents one of the many risks to which organizations are exposed and therefore managing health and safety effectively should be as important as managing any other business risk. Health and safety should be a strategic issue for senior management, as good performance brings rewards beyond merely a reduction in the levels of accidents and ill-health. Although accident and ill-health statistics may provide a useful guide for indicating those areas where an organization's main risks exist, it should always be remembered that the absence of accidents and ill-health in operational areas, especially those involving low probability and high consequence events, does not necessarily indicate that these areas are managed effectively. While health and safety management systems provide the foundations for developing an acceptable safety performance (1), a move towards excellence is accelerated by the adoption of a continuous improvement philosophy (2) that is supported by the process of benchmarking (3).

The paper gives a complete overview of the concerns of India and China on the issues relating to the occupational health and safety, the occupational injuries and fatalities sustained by them, the initiatives taken by them to foster safety culture and above all the recommended health and safety plans which are yet to be enforced.

Both India and China are the members of International Labour Organisation (ILO) and have been working on the ratifications of the conventions laid by the ILO from time to time. The paper tries to address issues related to health and safety of employees in factories. Although China and India have been trying to put these issues in focus and have formulated several guidelines in their respective National Policies, yet discrepancy areas are still a question of concern.

RESEARCH METHODOLOGY

The conceptual framework within which the research is carried out is primarily descriptive in nature and the source of data collection is secondary. The mode of data collection is various authentic reports , research articles in journals of repute and internet.

The objectives of this paper are:

- To gain an insight into the occupational safety and Health Profile of India and China.
- To determine the present status of Training on OSH and to highlight the training needs of India and China.

www.IndianJournals.com
Members Copy, Not for Commercial Sale
Downloaded From IP - 180.149.53.83 on dated 18-Sep-2013

- To suggest action plans in terms of Capacity Building , motivation enhancement and collaborative linkages with institutions in order to improve the Occupational Health and Safety Aspects at work.

AN OVERVIEW OF OCCUPATIONAL SAFETY AND HEALTH PROFILE OF INDIA

ROLE OF GOVERNMENT AND POLICIES ON OSH

India with 270294 working factories employs 13100129 people in factories has numerous laws concerning the safety and health of the workers. The Factories Act, 1948 deals with it and has numerous provisions stating the well being of employees. There are in all 16 laws in India dealing with hours of work, employment, conditions of service, welfare and safety and so on.(4)

In fact in February 2009, The Government of India has declared National Policy on Safety, Health and Environment at Work place in February 2009 and has set to build and maintain national preventive and safety & health culture, as a goal. In order to achieve the aforesaid goal in the national agenda, government has stressed to promote inclusion of safety, health and environment improvement at the workplace as an important component for quality of working life. (5)

The scenario at present is such that there is no agency or department of Government of India which is dealing with matters of OSH exclusively and moreover the OSH skills OF key workers are required to be enhanced. It even calls for capacity building of the employees. Moreover the report presented by Planning commission also stated that there is a need to strengthen the employees and also there is a need to amend Factories Act, 1948.DGFASLI report for 2009 indicates that 6,809 factory medical officers, 2,642 safety officers and 55 certifying surgeons for 13.1 million workers are employed in registered factories(6)

But the condition of OSH implementation is not like everywhere. There are many industries which are progressive ones and they opt of certifications like OHSAS 18001: 2007also. (7)

ROLE OF DGFASLI

In India, Directorate General, Factory Advice Service and Labour Institute DGFASLI is the technical organisation of the ministry of labour which takes care of Occupational Safety and Health and other issues of Factory workers. It provides training for Factory Inspectors and coordinates. It has 5 regional Labour Institutes. Besides this, the autonomous organisation of national repute is National Safety Council, Central Board of worker's education and National Institute of Occupational health. It also assists the Ministry of Labour and employment in Operation of National Safety Awards, Vishwakarma Rashtriya Puraskar and prime Minister's Shram Award(8).

ILO CONVENTIONS ON OSH AND RATIFICATIONS MADE BY INDIA

ILO has passed 58 conventions on OSH out of which till now only 3 have been ratified. In past 10 years, it has ratified only 1 .There is an important convention 155 which if ratified would

www.IndianJournals.com
Members Copy, Not for Commercial Sale
Downloaded From IP - 180.149.53.83 on dated 18-Sep-2013

bring workers in most economic sectors under the law , offering them health and safety at workplace. Except India, all other BRIC countries have ratified it.(4)

ROLE OF NON GOVERNMENTAL ORGANISATIONS

Besides this, there are some nongovernmental organisations like IAOH(Indian Association of Occupational Health)are working for the cause and has the membership of moe than 3000 OSH Professionals .It has been regularly conducting conferences for creating awareness, proactively influencing national policy through appropriate linkages since past 64 years.(7)

ACCIDENTS REPORTED BY INDIA TO ILO AND THE ACTUAL NUMBER OF CASES

As per Safety Science 44(2006), In India, yearly over 48000 workers die of occupational accidents and about 37 million occupational accidents cause at least 3 days' absence from work. Fatality rate is 11.4 per 1 lakh workers and accident rate is 8700 per 1 lakh workers and moreover India did not actually report any occupational accident to ILO.

OCCUPATIONAL HEALTH AND SAFETY PROFILE OF CHINA

LAWS APPLICABLE

China, which is a primarily manufacturing driven economy with 46.8% of contribution of secondary sector towards GDP and employing 34919000 people in the factories. Law of Work safety and Labor Laws of People's republic of China is applicable.

NON GOVERNMENT ORGANISATION

Besides this there's an intervention of non government bodies in ensuring health and employees which applies to India also. There are a few non governmental

bodies like China Association of Work safety which is into the play with the major tasks of organising research relating to work safety and make the suggestions and recommendations for formulating national laws and regulations on work safety, to collect, analyse and exchange work safety information and China occupational safety and Health Association which is established on voluntary basis by OSH Practitioners and also China Chemical Safety association.(9)

ACCIDENTS REPORTED BY CHINA TO ILO AND THE ACTUAL NUMBER OF CASES

As per Safety Science 44(2006), China stands closer to India with the estimated fatality rate of 10.5 per 1 lakh workers and accident rate of 8038 per 1 lakh workers.

www.IndianJournals.com
Members Copy, Not for Commercial Sale
Downloaded From IP - 180.149.53.83 on dated 18-Sep-2013

TABLE 1 THE TABLE 1 ABOVE SHOWS THE COMPARISON BETWEEN INDIA AND CHINA AS PER SAFETY SCIENCE (2006) IN TERMS OF ECONOMICALLY ACTIVE POPULATION , TOTAL EMPLOYMENT, ESTIMATED NUMBER OF FATAL ACCIDENTS, FATALITY RATE ,NON FATAL ACCIDENTS WITH ABSENCE LESS THAN 3 DAYS AND ACCIDENT RATE

	Economically active population	Total Employment	Estimated number of fatal accidents	Fatality rate	Non fatal accidents with absence less than 3 days(LOWER LIMIT)	Non fatal accidents with absence less than 3 days(UPPER LIMIT)	Accident rate
India	458720000	419560000	48176	11.5	.19%	.10%	8763
China	708218102	699771000	73615	10.5			8028

Annually over 73000 fatal accidents happen and number of occupational accidents with at least days'absence from work is 56 million and no. of accidents reported toILO was just 1 % of the actual number.

TABLE2 SHOWS FATAL ACCIDENTS REPORTED BY FACTORIES TO DGFASLI BY INDIA AND TO ILO BY CHINA FROM 2006 TO 2010

Year wise data	No. Of Fatal Accidents reported by Manufacturing units in India from 2006 to 2010 as per DGFASLI	No. Of Fatal Accidents reported by Manufacturing units in China from 2006 to 2010 as reported to ILO
2006	1349	4,290
2007	1453	4,787
2008	1369	4,531
2009	1509	4,268
2010	1454	3,796

www.IndianJournals.com
Members Copy, Not for Commercial Sale
Downloaded From IP - 180.149.53.83 on dated 18-Sep-2013

From the statistics stated in Table 2, it can be made out that no. of fatal accidents and injuries reported in India is showing that despite, the efforts put in on Safety issues are not showing much of the improvements. With a total of 13100129 people employed in 270294 working factories , the fatal accidents are increasing and showed a slight downturn as against the figures in 2009.It is quite clear from the data that the condition of occupational accidents has actually been showing an increase.Whereas it could be seen that though the numbers are quite high in a primarily manufacturing driven economy of China, with a total of 34919000 workforce employed in factories , yet from 2007, the figures are declining , thereby showing an improvement in the scenario.

UNDERSTANDING THE TRAINING NEEDS OF OCCUPATIONAL SAFETY AND HEALTH IN INDIA

Occupational health in India has to compete with primary & curative health for its budget. While 4% of the gross domestic product (GDP) is spent on health care, almost 75% of this is spent on curative health. (7)

In India, occupational health is not integrated with primary health care. Occupational Safety and Health till date remains under the mandate of the Ministry of Labour and not the Ministry of Health. Enforcement is carried out through the Directorate of Industrial Safety and Health at state levels that operate through factory inspecting engineers and medical inspectors of factories.

The occupational health training is carried out in a few medical colleges for graduate and postgraduate diplomas and degrees. The Central Labour Institute under DGFASLI offers a 3-month certificate course in Industrial Health, which is statutorily approved.(7)

Ministry of Labour has five regional labour institutes. These Institutes carry out training and research related to industrial safety and health. Until recently, CLI was the only institute conducting statutory training / certification course. The certification is mandatory for all industrial medical officers employed in hazardous industries. National Institute of Occupational Health [NIOH] is one of the prime institutes of the Indian Council of Medical Research [ICMR] and has two Regional Occupational Health Centers (ROHC) at Bangalore (1977) and Calcutta (1980) for catering to regional needs. Established in 1966 and originally designated as the Occupational Health Research Institute and it was re-designated as the National Institute of Occupational Health (NIOH), in 1970. Its major activity is research in occupational health. The Institute has published over 500 research papers in national and international journals. The other activities of the Institute include short-term training programmes for industrial medical officers, industrial hygienists, factory inspectors, workers and trade unions, etc. The Institute advises the Ministry of Health, Ministry of Labour, Ministry of Environment and Ministry of Commerce on issues related to occupational health, safety and environment.(6)

STATUS OF TRAINING AND NEED FOR TRAINING

1. The numbers of trained professional are grossly inadequate for a country with bludgeoning workers population. A lot of demand for safety officers is there but training on OSH is still in infancy .There are around 1125 qualified occupational health

www.IndianJournals.com
Members Copy, Not for Commercial Sale
Downloaded From IP - 180.149.53.83 on dated 18-Sep-2013

professionals in India and only around 100 qualified hygienists as against a requirement of over 8000 qualified occupational health doctors. (6)

2. Only the organized sector is monitored by various enforcement agencies and consequently the unorganized sector is neglected .

3. WHO in its sixtieth World Health Assembly has also expressed concerns over major gaps between and within countries in the exposure of workers and local communities to occupational hazards and in their access to occupational health services. (6)

There is a need for capacity building of employees as there is wide gap between the number of OSH professionals needed and the available ones.

India has a comparatively high need for training as only a few health and safety professional could not make the scenario better. Government has been working on framing policies for developing appropriate training mechanism. DGFASLI takes the certification courses on training safety inspectorates and others and some NGO'S on regular basis organise conferences and influence the national policies on Safety and Health

www.IndianJournals.com
Members Copy, Not for Commercial Sale
Downloaded From IP - 180.149.53.83 on dated 18-Sep-2013

STATUS OF TRAINING IN CHINA

China has pioneered by means of establishing 127 universities and colleges which have established work on Safety Engineering. Besides this, they have a very sound mechanism of training , the result of which is the 3661 training units with qualifications on training for OSH, by the end of the year 2010. Between 2006 and 2010, 83177 million people belonging to factories, mines, commercial and trade businesses were trained on OSH , with a training rate of about 88% . As compared to China, India's training rate of OSH is very low. (9)

Besides this there are a lot of awareness programmes which are taken up by China for long and several such activities can be enumerated as

NATIONAL LEVEL ACTIVITIES CONDUCTED BY CHINA FOR OSH

1. As a part of the regular activities taken up for OSH, National Safety Month is observed every year in the month of June.

2. 5000 Kilometre Work safety tour is organised every year for the past 10 years and it has really been positively conceived by people for creating a safety culture, promoting laws related to safety promoting stability and improving the work all throughout China

3. National Safety and Health cup Contest is organised under the joint auspices of SAWS and ACFTU for acknowledging the companies implementing best safety and health practices , enhancing the awareness of safety and health and further lowering the rate of accidents .

4. The activities of Youth Work Safety demonstration have been organised by CCYL and SAWS for improving young workers skills in work safety and participation in management.(9)

CHINA'S INTERNATIONAL TECHNICAL COOPERATION ON OSH

There have been numerous International Technical Cooperation on OSH in China like

1. COOPERATION BETWEEN SAWS AND ILO

a. SAWS(State Administration at work safety) has sent several officials to attend both regional and International Labour Conference meetings in the last few years. They actively participated in the development of ILO standards on occupational safety and health.

b. In terms of safety culture and safety knowledge popularization, SAWS and ILO have jointly organized a series of activities, such as the celebration of the World Day for Safety and Health at Work on April 28; the China International Forum on Work Safety, and also other

c. In March 2006, the SAWS cooperated with the ILO and WHO to organize a National OSH Planning Workshop to help China improve the national OSH plan.

(4) besides this SAWS has bilateral collaborative asscociations with OSH supervision of various departments and institutions of various countries like the United States, Australia, Japan, Russia, Germany, the United Kingdom, France, Denmark, Finland, Spain, Poland, Czech, Canada, New Zealand, Brazil, South Africa, the Republic of Korea, India, Singapore, Malaysia, Indonesia, and Vietnam. China has also established governmental cooperation mechanisms with USA, Australia, Germany, Japan, Poland and India in

www.IndianJournals.com
Members Copy, Not for Commercial Sale
Downloaded From IP - 180.149.53.83 on dated 18-Sep-2013

2. COOPERATION WITH INTERNATIONAL ORGANIZATIONS

The SAWS has established a cooperative relationship with the World Health Organization (WHO), International Social Security Association (ISSA) and the International Association of Labour Inspection (IALI). In 2003 and 2004, SAWS joined the ISSA and IALI as both a contact member and formal member respectively and carried out cooperative and communication activities with the UNDP, UNIDO, OECD, World Bank (WBG), Asian Development Bank (ADB), EU, ASEAN, etc.

3. It has Cooperation with non-governmental organizations and enterprises of other countries as well like China-Japan Cooperation Project on Work Safety with emphasis on laying standards for work safety. A series of activities were organized, such as training on Zero Accident, training courses in Japan, accident cases analysis, joint inspection on work safety, and cooperation between companies.

AN OVERVIEW OF NATIONAL PLANS ON SAFETY AND HEALTH FOR 5 YEARS, AS PROPOSED BY INDIA AND CHINA

China is planning in terms of bringing in economic reforms. In accordance with the National Plan laid for the 5 years, the fatality rate per 100 million Yuan GDP wil drop by 36%and fatality rate together in factories, mines and other commercial trades will drop by 26%.It si predicted that no. of major accidents will decrease by 50% or more and by 2020, work safety would improve considerably.(9)

India has been planning hard on developing on the below mentioned issues

During the 12th Five Year Plan Period (2012 – 2017), DGFASLI proposes to operate the following seven Plan Schemes.

1. Strengthening of DGFASLI Organisation and OSH in Factories

2. Development of Regional Labour Institute, Faridabad as Centre of Excellence inSafety Systems in MSME & Chemical Process Units

3. Effective Implementation of Occupational Safety, Health and Environment Systems at Work place in Manufacturing and Port Sector

4. Identification, Elimination and Control of Silicosis in India

5. Strengthening of Enforcement Systems in Factories

6. Safety, Occupational Health and Work Environment Centre in the State Factory

7. Directorate - Centrally Sponsored Scheme (5)

www.IndianJournals.com
Members Copy, Not for Commercial Sale
Downloaded From IP - 180.149.53.83 on dated 18-Sep-2013

SUGGESTED FRAMEWORK FOR ENHANCING THE STATUS OF OSH:

1. NEED FOR AN APEX BODY

The Apex government body taking care of OSH needs to be created which works exclusively for Occupational Health and Safety issues.

2. NEED OF CREDIBLE UNIVERSITIES AND INSTITUTIONS

There is a need to have credible Universities and Institutions offering specialised courses to the students to learn OSH which could help improve the Occupational Safety and Health situation as there is a wide gap between required professionals for improving the Occupational Safety and Health of Employees and the available ones and it would also increase the level of employment,. For this matter , the action plan could be offering OSH as specialisation in M.B.A and disciplines of Engineering with the expert training to the students opting for it and at the end of the training, the OSH trainees could be given employment. In the similar fashion, live projects to the interns in terms of surprise audits can be conducted

3. LINKING SAFETY WITH REWARDS FOR THE EMPLOYERS

The motivation level of employers to have adequate Safety and Health systems can be reinforced by linking the credits (to the practitioners of Occupational Health and Safety in conjunction with the laws) and then those credits may be linked to some considerable tax relief

4. NEED OF SPECIFICITY OF OBJECTIVES AND COORDINATION WITH INTERNATIONAL BODIES FOR SHAPING THE NATIONAL POLICIES

The objectives of the policies framed are required to be more specific rather than broad statements and integration with the international bodies for reshaping with required changes in the National Policies and implementation of safety and health policies is needed.

5. INTEGRATION OF OCCUPATIONAL HEALTH WITH PRIMARY HEALTH CARE

There is a need to integrate Occupational Health with primary health care.

6. NEED FOR AMENDMENT IN THE FACTORIES ACT

There is a need to make amendments in the Factories Act with more provision and separate chapters on Occupational Health and Safety. In 1987 after Bhopal gas Tragedy, some chapters on Occupational Safety and Health were added but there is a need to revise Factories Act 1948, keeping in view the present day scenario.

7. INTERNATIONAL COLLABORATIONS

More number of International Collaborations are a must to stay abreast with the standards set and implemented in other parts of the globe. Some lessons are worth learning from China and other countries which are holding joint and collaborative projects with the other parts of the globe on Work Safety and Health of Employees.

8. ADDRESSING THE PROBLEM OF NON REPORTING OF ACCIDENTS

To curtail the problem of non reporting of accidents, integration of Information Technology can work. In order to strengthen the system of OSH, a web portal may be created (wherein the accidents and unsafe practices can be reported) to keep employers on alert in maintaining a safe and healthy work environment.

9. EXTENDING THE OUTREACH OF BASIC EDUCATION TO THE WORKERS

- The motivation level of employees needs to be boosted, so as to enforce safety culture in the organisations. This has to be taken up jointly by the employers and the government. In this regards, behavioural training can make a lot of difference.

- Web portal can also be used for imparting basic education on safety to the workers. Course credits can be made mandatory at joining/ regular intervals and promotions.

- Video films for impeccable effects on the minds of the workers can be created by projecting the “heroes” from the similar establishments so that other employees are able to relate to it and retain the learning for long.

- Emphasis needs to be put on Activity based learning of the employees and for the feedback, suggestion boxes may be put.

www.IndianJournals.com
Members Copy, Not for Commercial Sale
Downloaded From IP - 180.149.53.83 on dated 18-Sep-2013

- After the training on safety and health safety issues and practices (to be applied) has been imparted, there is a need to keep a check on whether those safety measures are being made a part of their regular working style or not.

- Accident case analysis can be used as a technique to improve safety culture and education to the employees.

10. FOLLOWING AN INTELLIGENCE LED AND TARGETED APPROACH

A good safety culture can be created by creating an intelligence led and targeted approach towards resolving safety related issues like highly prone industries can be identified and can be kept under close surveillance by the government.

11. ADEQUATE COMMUNICATION OF SAFETY POLICIES BY THE TOP MANAGEMENT

The policies framed by the professional at the top level of management related to OSH needs to be disseminated properly so as to bridge the gap between documented and actual practices.

www.IndianJournals.com
Members Copy, Not for Commercial Sale
Downloaded From IP - 180.149.53.83 on dated 18-Sep-2013

REFERENCES

1. Health and Safety Executive (2000), Successful Health and Safety Management, HSG65, HSE Books, Sudbury.

2. Fuller (1997), "Key performance indicators for benchmarking health and safety management in intra- and inter-company comparisons", Benchmarking for Quality Management & Technology, Vol. 4 No.3, pp.165-74.

3. Vassie, L.H. (1998), "A proactive team-based approach to continuous improvement in health and safety management", Employee Relations, Vol. 20 No.6, pp.577-93

4. www.ilo.org/ilolex/english/subjectE.htm

5. Ministry of Labour and employment. (2012). Report on working group on Occupational Health and Safety for 2012-17. Delhi: Minisrty of Labor and Employment.

6.Saiyed H.N./TiwariRR(2004), Occupational Health Research in India :Industrial Health, 2012, 50, 161-171

7. Pingle, Shyam. (2012). Occupational Health and Safety in India: Now and Future. Delhi: Industrial Health, 2012,50,161-171.

8.Safety Statistics-http://www.dgfasli.nic.in/info1.htm. Accessed January, 2013.

9. ILO.org/safework/countries/asia/china/wcms_186991/index.htm. (2012, March 1). Retrieved february 13, 2013, from ilo.org: http://www.ilo.org/wcmsp5/groups/public/---ed_protect/---protrav/---safework/documents/policy/wcms_186991.pdf

10. National Policy on Safety Health and Environment at workplace. http://www.dgfasli.nic.in/info 1 .htm. Accessed January, 2013.

SpringerPlus

SpringerOpen

This Provisional PDF corresponds to the article as it appeared upon acceptance. Fully formatted PDF and full text (HTML) versions will be made available soon.

Quantifying uncertainty in measurement of mercury in suspended particulate matter by cold vapor technique using atomic absorption spectrometry with hydride generator

SpringerPlus 2013, **2**:453 doi:10.1186/2193-1801-2-453

Nahar Singh (naharsingh@mail.nplindia.org)
Tarushee Ahuja (tarushi_sai@yahoo.co.in)
Vijay Narain Ojha (vnojha@mail.nplindia.org)
Daya Soni (dsoni@mail.nplindia.org)
S Swarupa Tripathy (tripathyss@mail.nplindia.org)
Ivo Leito (ivo.leito@ut.ee)

ISSN 2193-1801

Article type Case study

Submission date 17 June 2013

Acceptance date 3 September 2013

Publication date 11 September 2013

Article URL http://www.springerplus.com/content/2/1/453

This peer-reviewed article can be downloaded, printed and distributed freely for any purposes (see copyright notice below).

For information about publishing your research in *SpringerPlus* go to

http://www.springerplus.com/authors/instructions/

For information about other SpringerOpen publications go to

http://www.springeropen.com

© 2013 Singh *et al.*
This is an open access article distributed under the terms of the Creative Commons Attribution License (http://creativecommons.org/licenses/by/2.0), which permits unrestricted use, distribution, and reproduction in any medium, provided the original work is properly cited.

Quantifying uncertainty in measurement of mercury in suspended particulate matter by cold vapor technique using atomic absorption spectrometry with hydride generator

Nahar Singh[1*]
[*] Corresponding author
Email: naharsingh@mail.nplindia.org

Tarushee Ahuja[2]
Email: tarushi_sai@yahoo.co.in

Vijay Narain Ojha[1]
Email: vnojha@mail.nplindia.org

Daya Soni[1]
Email: dsoni@mail.nplindia.org

S Swarupa Tripathy[1]
Email: tripathyss@mail.nplindia.org

Ivo Leito[3]
Email: ivo.leito@ut.ee

[1] CSIR-National Physical Laboratory, Dr K.S. Krishnan Marg, New Delhi 110012, India

[2] Department of Applied Chemistry, Delhi College of Engineering, University of Delhi, Bawana Road, Delhi 110042, India

[3] Institute of Chemistry, University of Tartu, Ravila 14a, Tartu 50411, Estonia

Abstract

As a result of rapid industrialization several chemical forms of organic and inorganic mercury are constantly introduced to the environment and affect humans and animals directly. All forms of mercury have toxic effects; therefore accurate measurement of mercury is of prime importance especially in suspended particulate matter (SPM) collected through high volume sampler (HVS). In the quantification of mercury in SPM samples several steps are involved from sampling to final result. The quality, reliability and confidence level of the analyzed data depends upon the measurement uncertainty of the whole process. Evaluation of measurement uncertainty of results is one of the requirements of the standard ISO/IEC 17025:2005(European Standard EN IS/ISO/IEC 17025:2005, issue1:1-28, 2006). In the presented study the uncertainty estimation in mercury determination in suspended particulate matter (SPM) has been carried out using cold vapor Atomic Absorption Spectrometer-Hydride Generator (AAS-HG) technique followed by wet chemical digestion process. For the calculation of uncertainty, we have considered many general potential sources of uncertainty.

After the analysis of data of seven diverse sites of Delhi, it has been concluded that the mercury concentration varies from 1.59 ± 0.37 to 14.5 ± 2.9 ng/m^3 with 95% confidence level (k = 2).

Keywords

Mercury, Atomic absorption spectrometer-hydride generator, Uncertainty evaluation, High volume sampler

Introduction

Mercury is a highly toxic element found as naturally and as a contaminant in the environment. Natural sources of atmospheric mercury include volcanoes, geologic deposits, and volatilization from the ocean, rocks, sediments, water, and soils. The toxic effects of mercury depend on its chemical form and the route of exposure. Methyl mercury [CH_3Hg^+] is the most toxic form, absorbed readily and excreted slower than other forms of mercury. It affects the immune system, damages the nervous system, alters genetic enzyme systems and also affects the senses of touch, taste, and sight.

There are several instrumental techniques like Atomic Fluorescence Spectrometry (AFS), inductively coupled plasma atomic emission spectroscopy (ICPAES), nevertheless, the cold vapor AAS is the best technique sensitivity wise and to take care of interference of the other species during measurements. Several researchers (Singh and Sarkar 2003; Walcerz et al. 1993; Erdem and Henden 2004 and Barth et al. 1992) have analyzed mercury by AAS–HG cold vapor techniques and have demonstrated interference from other hydride forming elements which affects the results. The toxic effects of mercury on plants, animals and human beings has been studied by Moore and Ramamoorthy 1984 and indicated the natural and anthropogenic sources through which it reaches in different medium. Laser ionization mass spectrometric investigations have shown that stratosphere contains 1–5 ng m^{-3} of mercury and out of which 90% mercury is present as gas-phase (Murphy et al. 1998; Schroeder and Munthe 1998) as elemental mercury. The concentrations of gaseous mercury and other trace metals in aerosols were measured at Hel site, Gulf of Gdansk (Bełdowska et al. 2006) during summer season. Elemental mercury vapor released from broken thermometers, causes tremors, gingivitis, and excitability when inhaled over a long period of time.

In chemical metrology most of the important decisions are based on the quality and the reliability of analytical results. This reliability, quality and confidence can be achieved by correct estimation of uncertainty of the measurements following the ISO/EURACHEM guidelines. In this regard ISO has published, “Guide to the expression of uncertainty in measurement (GUM)” in 1995 in collaboration with BIPM, IEC, IFCC, IUPAC, and OIML, which recently was revised as VIM: JCGM 200:2008, Evaluation of measurement data-Guide to the expression of uncertainty in measurement. In last several years the uncertainty estimations for Hg in different matrixes (Kayal et al. 2009 & Kayal and Singh 2010 Synek et al. 2000; Kumar and Riyazuddin, 2007) have been carried out by various authors. However, determination of mercury in suspended particulate matter (SPM) and evaluating the uncertainty value of the result is a difficult task as there are many parameters involved from sampling to final value, which influence the result. To the best of our knowledge there is no study published, which describes the determinations of mercury in SPM samples with the total uncertainty budget. So in this study, an attempt has been made for the evaluation and

expression of uncertainty in measurement for the determination of mercury in environmental samples collected through HVS by AAS-HG, following the ISO GUM guideline (JCGM 100:2008) as well as additional relevant guidance documents(ISO ISO/DTS 21748:2003 and European Standard EN ISO/IEC 17025:2005).

Experimental details

Instruments and apparatus

The suspended particulate matter (SPM) sampling was carried out using a High-Volume Sampler (HVS-410, Make: Envirotech). SPM was collected on pre-desiccated cellulose filter papers. Before sampling, the filter papers were dried for 3 hrs in an oven at 105°C to remove moisture, if any, and to get constant weight. After drying, the filter papers were kept in a desiccator at room temperature. For weighing of sample Mettler Toledo make balance model AX 204 capacity 220 g has been used. Atomic Absorption Spectrometer (AAS) of Analytik Jena make Vario-6 with a hydride generator accessory was used for the analysis of mercury. The mercury measurements were carried out at 253.7 nm wavelength at optimum conditions of acids and reducing agent. The pipette of 5 mL and volumetric flask of 50 mL capacity used were of Borosil glass works, India Limited. The pipettes and volumetric flasks were calibrated prior to analysis by the National Physical Laboratory (National Metrology Institute of India) following international standard procedure and protocol. The reference standards stock solution of 1.0 mg/litre (BND 601.02) of mercury was used (prepared by NPL-India) after diluting up to the working range for the calibration of AAS-HG instrument. A reagent blank was also prepared and the correction applied wherever required. Mean absorbance value of the three measurements of two replicates of each sample was taken into consideration for the calculation of the concentration of mercury. All the acid digestion and dilution work was carried out in a cleaned laminar flow bench equipped with the proper exhaustive system.

Reagents

Hydrochloric acid (35%) and Nitric acid (69%), of GR grade (Guaranteed Reagent), which were further purified by sub boiling point distillation in a quartz glass device. Hydrogen peroxide (50%) and Sulphuric acid (98%) all of E. Merck (India) make were used. De-ionized water (18.2 MΩ resistivity) prepared from Millipore milli-Q element water purification system, USA was used throughout the process.

Sampling sites and description

New Delhi is located 160 km south of the Himalayas at latitude $28^0$24’ to $28^0$53’N and longitude $76^0$20’E to $77^0$20’E with an altitude of about 216 meter above mean sea level. Delhi’s climate is mainly influenced by its inland position and the prevalence of continental air during major part of the year. Delhi has three distinct seasons: summer, monsoon and winter. In the proposed study seven sites were selected namely Ashram (S-1; Heavy traffic site), Azadpur (S-2; Industrial site), Loni Road (S-3; densely populated + traffic site), Pitampura (S-4; Ambient site), Highway no. 56 (S-5; Traffic site), Naraina (S-6; Industrial site) and NPL (S-7; Mixed site).

Sample preparation procedure

Two replicates of 18 × 11.5 cm^2 size (known weight at deposited area) of all the seven sites were taken for the determination of mercury into separately cleaned poly-tetrafluoroethylene (PTFE) vessels used in the microwave digestion system. To these vessels 15 mL of sub boiled nitric acid, 5mL of hydrogen peroxide and 5mL of DI water were added and closed tightly with PTFE vessel lid. The PTFE vessels containing the samples were kept for overnight at room temperature. After keeping the PTFE vessel overnight, 4 to 5 drops of sulphuric acid was added and the PTFE vessel was kept on hot plate by covering with Teflon lid at 100°C for 15–20 minutes and then heated again at 150°C. Then the lid of the PTFE vessel was opened and it was heated again after addition of 10 ml sub boiled concentrated hydrochloric acid. To ensure the complete removal of nitric acid the sample was heated once again with 5 mL hydrochloric acid. Finally the solutions were boiled with 15 ml 1:1 de-ionized water and sub boiled concentrated hydrochloric acid mixture. After digestion the whole content of the vessel was transferred into a 100 mL quartz centrifuge tube and it was centrifuged at 5000 rotations per minute for 2–3 minutes to separate solid particles from the solutions. The supernatant liquid was transferred into a glass beaker. The remaining residue in the vessel was washed several times with hot water to ensure complete transfer of digested sample from the vessel. The final solutions were made 50 mL by addition of de-ionized water. In this solution mercury was determined by AAS-HG using the respective standards and principal resonance line after reducing mercury in the presence of sodium borohydride (3%), sodium hydroxide (1%) and hydrochloric acid (1%) by cold vapor techniques (ambient room temperature). Mean absorbance values of six readings of two replicates (three each) were taken into the consideration for calculation of the concentration of mercury. Procedural blank for cellulose filter paper without sample was also done to check the blank levels for mercury and correction was applied wherever required.

Determination of recovery

For determining the recovery of the wet digestion procedure we have taken three separate SPM deposit filter papers of the same matrix assuming uniform deposition of mercury on the filter paper. The filter paper was divided in two parts (18 cm × 11.5 cm^2 each). One part was treated as such, while in the second part 10 ml of 1000 μg/L mercury solution was added in a PTFE vessel along with the filter paper and the remaining procedure was the same as in the case of test samples. The dilutions of the spiked samples were carried out in the calibration range of AAS-HG before analysis. When keeping samples for long time there is a danger of loss of mercury in the low concentration range. In the present study we analyzed all samples within one week after digestion. From our experience we know that when we analyze mercury by AAS-HG in the low concentration range, we have to prepare fresh standards every week (calibration range: 10 μg/L to 50 in μg/L). After one week, there is a loss of 5% to 7% in the predetermined value at 27 ± 3°C (ambient conditions of our lab). The concentration range of mercury in the samples was 15 μg/L to 30 μg/L. The concentration of hydrochloric acid in the final solution should be at least 4-5%. In 4% or higher concentration of hydrochloric acid there is no loss due to adsorption over glass substrate, however mercury may be lost due to evaporation and microbial growth within the solution.

Determination of concentration of mercury in SPM sample and its uncertainty

Measurement model

In the determination of mercury in SPM samples the major sources of the uncertainty have been included in the calculation of combined uncertainty according to the EURACHEM/GUM guidelines. Following EURACHEM/GUM guidelines concentration of mercury $C(M_{Hg})$ in the SPM samples has been evaluated using AAS-HG technique by following equation.

$$C\left(M_{Hg}\right)=\frac{C_{Hg}\times V_{TEST}\times W_{TSPM}}{V_{HVS}\times R_{HVS}\times W_{ANA}}=ng/m^3 \quad (1)$$

Where; $C(M_{Hg})$ = Concentration of mercury in ng/m^3; C_{Hg} = Concentration of mercury analyzed from AAS-HG in μg/litre; V_{TEST} = Volume made of the test sample after wet digestion process in mL; W_{TSPM} = Total weight of SPM deposit on 18cm × 23 cm area; V_{HVS} = volume of the air processed through high volume sampler (HVS); W_{ANA} = Weight of SPM deposit on 18 cm × 11.5 cm area taken for wet digestion process. R_{HVS} = Total recovery of the method containing the contribution of HVS in capturing mercury and possible losses of mercury during sample preparation.

The evaluated values for the above factors are given in Table 1. The important parameters that contribute towards the uncertainty are also shown in the Cause and effect diagram in Figure 1. In accordance with GUM, the combined uncertainty for the mathematical model, which is in a product or quotient form, is given by:

Table 1 Various evaluated components for the determination of mercury in SPM samples

Sample I.D.	SPM (µg/m^3)	Concentration of mercury obtained from AAS-HG after reducing blank (µg/litre) [C_{Hg}]	Volume made for test samples (mL) [V_{TEST}]	Total weight of SPM deposited on 18 cm × 23 cm filter paper (g) [W_{TSPM}]	Weight of SPM deposited on 18cm × 11.5 cm filter paper area taken for analysis (g) [W_{ANA}]	Volume of air processed through HVS at STP, (m^3) [V_{HVS}]	Recovery of the analytical procedure (%) [R_{HVS}]	**Concentration of mercury in ng/m^3 C(M_{Hg})
S-1	395	58.22 (2.82)*	50	0.17744	0.08872	493.52	94.39	12.55 ± 2.44
S-2	203	23.41 (2.13)*	50	0.09124	0.04562	414.97		6.00 ± 1.23
S-3	2337	62.32 (4.13)*	50	1.05086	0.52543	457.16		14.50 ± 2.87
S-4	251	6.83 (1.12)*	50	0.11279	0.05639	456.66		1.59 ± 0.37
S-5	338	14.04 (0.92)*	50	0.15214	0.07607	471.24		3.17 ± 0.63
S-6	429	23.11 (1.62)*	50	0.19300	0.09650	417.58		5.89 ± 1.17
S-7	347	16.6 (1.33)*	50	0.62306	0.31153	391.63		4.51 ± 0.91

* Value in parentheses is the standard deviation of six determinations of two replicates (three each).

** Concentration of metal mercury has been calculated by using eq.-1 and values reported with expanded uncertainty in ng/m^3.

Figure 1 Fish bone diagram for potential sources of uncertainty in mercury measurement by HG-AAS.

$$\left[u_c(y) / y \right]^2 = \sum_{i=1}^{N} \left[p_i u(x_i) / x_i \right]^2 \quad (2)$$

The combined uncertainty is given by:

$$\left[\frac{u_c\left(C(M_{Hg})\right)}{C(M_{Hg})} \right]^2 = \left[\frac{u(C_{Hg})}{C_{Hg}} \right]^2 + \left[\frac{u(V_{TEST})}{V_{TEST}} \right]^2 + \left[\frac{u(W_{TSPM})}{W_{TSPM}} \right]^2 + \left[\frac{u(W_{ANA})}{W_{ANA}} \right]^2 + \left[\frac{u(V_{HVS})}{V_{HVS}} \right]^2 + \left[\frac{u(R)}{R} \right]^2 \quad (3)$$

The uncertainty evaluation of all the input quantities is discussed in the following sub-sections.

Practicalities of uncertainty estimation

An uncertainty source may be 'Type A', which is evaluated by statistical analysis of a series of observations, or 'Type B', which is evaluated by using means other than the statistical analysis of a series of observations. To calculate standard uncertainty from the parameters of two most important distribution functions, if the limits x ± a are given without a confidence limit, it is appropriate to assume a rectangular distribution with a standard deviation of a/√3, but if values are given with confidence level, it is triangular distribution with a standard deviation of a/√6 (Ellison et al. 2000). Normal distribution is assumed when an estimate is made from repeated observation of a randomly varying process. In analytical chemistry, an expanded uncertainty (U) is used, which is obtained by multiplying the combined standard uncertainty, by a coverage factor k. The choice of coverage factor is based on the level of confidence. For an approximate level of confidence of 95%, the value of k is 2.

Uncertainty components in the measurement of concentration of mercury obtained from AAS-HG [C_{Hg}]

Referring to Figure 1, the major sources of the uncertainty for C_{Hg} are due to reference standard stock solution, repeatability, dilution in 50 mL volumetric flask from stock solution to working range and five mL capacity pipette used for dilution.

Reference standard stock solution

According to the certificate the concentration of the mercury standard stock solution is 1.00 ± 0.02 mg/L. Assuming normal distribution the standard uncertainty will be 0.01 mg/L. This stock solution was used for calibration of AAS-HG after proper dilution up to the working range.

Uncertainty evaluation due to repeatability

The repeatability in concentration of mercury was determined experimentally by analyzing six determinations of two independently digested replicates (three each). The standard deviation of six values (three each) has been used for calculation of standard uncertainty following EURACHEM guide.

Uncertainty in 50 ml volumetric flask used for dilution from 1000 ug/L to working range

The final volume of standard mercury solution made was 50 mL after several dilutions. The factors which include uncertainty in 50 ml volumetric flask are given in Figure 1. The major uncertainties were due to calibration and temperature. The uncertainty due to calibration and temperature has been calculated as below.

Uncertainty due to calibration

As per calibration certificate of supplier the expanded uncertainty for 50 mL flask is ± 0.02 mL at k = 2 assuming normal distribution, hence the standard uncertainty will be $u(V_{cal})$ = 0.01 mL.

Uncertainty due to temperature

According to calibration certificate the flask has been calibrated at 25°C and the laboratory temperature varies within the limits of ± 3°C. The volume expansion coefficient for water is 2.1×10^{-4}°C^{-1}, which leads to volume variation according to following equation.

$$\pm (V \times \Delta T \times 2.1 \times 10^{-4}) \qquad (4)$$

Where V is the volume of volumetric flask and ΔT is temperature variation in the laboratory. Volume variation for 50 mL flask = $\pm (50 \times 3 \times 2.1 \times 10^{-4}) = 0.0315 mL$

The standard uncertainty due to temperature effect, $u(V_T)$ is calculated using assumption of a rectangular distribution i.e. $u(V_T) = 0.0315/\sqrt{3} = 0.018$ mL.

The combined uncertainty for temperature and calibration in 50 mL volumetric flask has been calculated as; $u(VF) = \sqrt{[(0.01)^2 + (0.018)^2}} = 0.021\ mL$

Uncertainty due to five mL pipette used for dilution

5 mL aliquot was taken by 5 mL pipette for making dilution upto 50 mL. As per Figure 1 the main uncertainties were due to temperature variation and calibration accuracy (± 0.02 mL) assuming normal distribution as quoted by the manufacturer. The effect of temperature on 5 mL pipette has also been considered as per section 5.3. The uncertainty of every dilution is different but this difference is negligible. Therefore for simplicity we have considered the uncertainty of first dilution even after performing the dilution second times.

$$u(pipette) = \sqrt{[(0.01)^2 + (0.002)^2}} = 0.01\ mL$$

Combined uncertainty of section 5.0 has been calculated by using subsection 5.1, 5.2, 5.3, and 5.4 using following equation.

$$\left[\frac{u_c\left(C_{Hg}\right)}{C_{Hg}}\right]^2=\left[\frac{u(precision)}{X_{\Pr ecision}}\right]^2+\left[\frac{u(cal\ std)}{X_{cal}}\right]^2+\left[\frac{u(VF)}{V_{Flask}}\right]^2+\left[\frac{u(pipette)}{V_{pipette}}\right]^2 \quad (5)$$

Uncertainty due to recovery

The recovery of mercury from the SPM filter paper depends on the storage of the samples and the method adopted for digestion. The loss of mercury in a closed system is less problematic during digestion process in comparison to an open system. The loss of mercury while keeping at low temperature i.e. 10 ± 5°C has been found at our laboratory to be 15-20%, while at ambient temperature 30 ± 5°C the loss of mercury was around 45-50% (both during one year period). For determining recovery of the wet digestion procedure we have taken three separate SPM deposit filter papers with the same matrix assuming uniform deposition of mercury on the filter paper. The mercury deposited filter paper was divided in two parts (18 cm × 11.5 cm each). One part was treated as such, while in the second part (200µg/L) 10 ml of 1000 µg/L were added in the PTFE vessel along with filter paper and the remaining procedure was the same as in the case of test samples. The final solutions after digestion were made to 50 mL by de-ionized water. The dilutions of the spiked samples were carried out in the calibration range of AAS-HG before analysis. The recovery has been done as; Recovery % = Concentration of spiked sample/ (200 µg/L + concentration of non spiked sample). Following the same approach the average recovery of the spiked samples were found to be 94.39 ± 0.80%.

Uncertainty evaluation in 50 mL volumetric flask used in making volume after wet chemical digestion [V_{TEST}]

The known area having known weight of the sample was processed through wet chemical route and the final volume was made to 50 mL. Referring to Figure 1, the sources of uncertainty for V_{TEST} are due to calibration uncertainty and effect of temperature variation on 50 mL volumetric flask volume of aliquot taken. The uncertainty associated with temperature for 50 mL volumetric flask is carried out as per section 5.3. The combined uncertainty for V_{TEST} has been calculated on the basis of Figure 1 as follows;

$$u\left(V_{TEST}\right)\sqrt{(0.01)^2+(0.018)^2}=0.021\text{ml}$$

Uncertainty evaluation due to volume of air processed through high volume sampler [V_{HVS}]

The volume of air sampled through HVS has been calculated on the basis of equation-6 and the volume of air processed at standard temperature and pressure (STP) is calculated by using equation-7 given below.

$$\text{Volume of air sampled}=Time(\text{min})\times Flow\,rate\left(m^3/\text{min}\right)=500\times1.1=550m^3 \quad (6)$$

$$\text{Volume of air processed through HVS at STP}=\frac{V_1\times P_1\times T_1}{T_2\times P_2} \quad (7)$$

Where, V_1- Total volume of air processed through HVS, P_1- Atmospheric pressure on the date of measurement (mm of mercury); T_1- Standard temperature (273); T_2- working temperature [temperature of the sampling site °C + standard temperature] + standard temperature] and P_2- Standard pressure (760 mm of mercury).

Substituting value from Table 2 in eq.7

Table 2 Uncertainty due to high volume sampler (V_{HVS}) for measuring volume of air at STP

Name of the site	Date of sampling	Sampling starting time	Sampling end time	Flow rate of air sampled through HVS (m^3/min)	Time (in min.)	Volume of air processed through HVS (m^3) V_1	Atmospheric pressure measured on site (mbar)	Atmospheric pressure in mm of mercury (mbar × 0.75) P_1	Average temperature of the sampling site (°C)	Average temperature of the sampling site (K) T_1	Volume of air processed through HVS at STP (m^3) [V_{HVS}]*
Heavy traffic site; Ashram zone (S-1)	31-1-08	9.10 am	5.30pm	1.1	500	550	994.2	745.65	25.5	298.5	493.52
Industrial site; Azadpur zone (S-2);	1-2-08	10.0 am	5.00 pm	1.1	420	462	995.2	746.40	25.5	298.5	414.97
Densely populated + Traffic site Loni Road (S-3);	2-2-08	9.45 am	5.30 pm	1.1	465	511.5	993.6	745.20	26.5	299.5	457.16
Ambient site Pitampura zone (S-4);	3-2-08	9.45 am	5.30pm	1.1	465	511.5	992.5	744.37	26.5	299.5	456.66
Traffic zone; Highway No. 56 (S-5);	4-2-08	10.30 am	6.30 pm	1.1	480	528	995.5	746.63	27.5	300.5	471.24
Industrial site; Nariana zone (S-6)	5-2-08	9.15 am	6.00 pm	1.1	425	467.5	996.3	747.22	27.5	300.5	417.58
Mixed site; NPL zone (S-7)	6-2-08	10.0 am	4.40 pm	1.1	400	440	992.8	744.60	27.5	300.5	391.63

* [V_{HVS}] is calculated using equation-7 in section- 8.

$$\text{Volume of air processed through HVS for S-1 at STP} = \frac{550 \times 745.65 \times 273}{(25.5 + 273) \times 760} = 493.52\ (m^3)$$

Similarly V_{HVS} for sample S-2 to S-7 has been calculated. Referring to Figure 1 the sources of the uncertainty for V_{HVS} are flow rate of air through HVS, time recording by stop watch, ambient pressure measurement and measurement of temperature of the site. The uncertainty estimates of the parameters are taken from the calibration certificates. The sampling is carried out in open atmosphere so it is not possible to control the temperature of the atmosphere. So we have taken normal distribution for temperature variation, while the other analytical experiments were carried at controlled room temperature. The combined standard uncertainty for volume of HVS has been calculated using equation-8

$$\left[\frac{u_c(V_{HVS})}{V_{HVS}}\right]^2 = \left[\frac{u(Flow)}{X_{Flow}}\right]^2 + \left[\frac{u(Time)}{X_{Time}}\right]^2 + \left[\frac{u(\text{Pressure})}{X_{\text{Pressure}}}\right]^2 + \left[\frac{u(Temp)}{V_{Temp}}\right]^2 \qquad (8)$$

Uncertainty evaluation due to balance used for weighing the blank and SPM deposited filter paper [W_{TSPM}] and [W_{ANA}]

As per the certificate of balance the Linearity (mg) /readability (mg) / repeatability (mg); ± 0.2/0.01/0.07 has been used for calculation and the standard uncertainty has been calculated assuming rectangular distribution and dividing each by √3. The contribution needs to be counted twice, once for tare, and the other for gross weight. So the combined standard uncertainty due to balance is 0.00024g.

The total weight of the SPM deposited on filter paper and weight of the filter paper used for wet digestion process was calculated as follows;

(I) Total area of the cellulose filter paper for sampling =20.3cm × 25.4cm = 515.62 cm^2

(II) Total area of the filter paper used for deposition (18 cm × 23cm) = 414 cm^2

(III) Total weight of the cellulose filter paper used for sampling (515.6 cm^2) = 4.25504 g

(IV) Total weight of the cellulose filter paper after deposition (515.6 cm^2) = 4.47603g

(V) Total suspended particulate matter deposit on the filter paper (515.6 cm^2) = (IV-III) = 0.22099 g

(VI) Total suspended particulate matter deposit on the filter paper (*414 cm^2); $W_{TSPM} = \frac{0.22099 \times 414}{515.62} = 0.17744\,g$

* It has been considered that the thickness of the cellulose filter used is uniform throughout the area. On this basis we have calculated the weight of the deposit area, which is 414 cm^2. Weight of the SPM deposited area (18cm × 11.5cm) taken for analysis, W_{ANA} = 0.08872g.

(VII) The weight calculations for samples S-2 to S-7 were also done in same way as given above for sample-1.

Calculation of concentration and associated uncertainty of mercury for S-1; (ng/m^3)

The concentration of mercury in the seven SPM samples has been determined by AAS-HG using eq.1. Substituting the values from Table 1 into eq.1, the concentration of mercury (ng/m^3) in S-1 sample: $C\left(M_{Hg}\right)=\frac{58.22\times 50\times 0.17744\times 100}{0.08872\times 493.52\times 94.39}=12.55\,\mathrm{ng/m^3}$

The combined uncertainty in measurement of mercury have been calculated after putting values of various parameters from Table 3 (summary table) in eq.3

Table 3 Uncertainty components (Summary Table) for calculation of combined uncertainty

S.N.	$u(C_{Hg})/ C_{Hg}$	$u(V_{TEST})/ V_{TEST}$	$u(W_{TSPM})/ W_{TSPM}$	$u(W_{ANA})/ W_{ANA}$	$u(V_{HVS})/ V_{HVS}$	u(R)/R
S-1	1.30/ 58.22	0.021/50	0.00024/ 0.17744	0.00024/ 0.08872	46.54/ 493.52	0.80/ 94.39
S-2	0.90/ 23.41	0.021/50	0.00024/ 0.09124	0.00024/ 0.04562	39.13/ 414.97	0.80/ 94.39
S-3	1.80/ 62.32	0.021/50	0.00024/ 1.05086	0.00024/ 0.52543	43.11/ 457.16	0.80/ 94.39
S-4	0.46/ 6.83	0.021/50	0.00024/ 0.11279	0.00024/ 0.05639	43.06/ 456.66	0.80/ 94.39
S-5	0.40/ 14.04	0.021/50	0.00024/ 0.15214	0.00024/ 0.07607	44.44/ 471.24	0.80/ 94.39
S-6	0.70/ 23.11	0.021/50	0.00024/ 0.19300	0.00024/ 0.09650	39.38/ 417.58	0.80/ 94.39
S-7	0.57/ 16.6	0.021/50	0.00024/ 0.62306	0.00024/ 0.31153	36.93/ 391.63	0.80/ 94.39

$$\left[\frac{u_c\left(C\left(M_{Hg}\right)\right)}{12.55}\right]=\sqrt{\left[\frac{1.30}{58.22}\right]^2+\left[\frac{0.021}{50}\right]^2+\left[\frac{0.00024}{0.17744}\right]^2+\left[\frac{0.00024}{0.08872}\right]^2+\left[\frac{46.54}{493.52}\right]^2+\left[\frac{0.80}{94.39}\right]^2}$$

$$u_c\left[C\left(M_{Hg}\right)\right]=12.55\times\sqrt{(0.00947)};u_c\left(M_{Hg}\right)=12.55\times0.097=1.22;$$

$$U_{ex}=1.22\times2=2.44\,ng/m^3\,(at\,95\%\,confidence\,level;k=2)$$

Therefore, Concentration of mercury in sample S-1 is = 12.5 ± 2.4 ng/m^3. Similarly concentration of mercury and combined uncertainty for mercury measurements have been calculated for samples S-2 to S-7. Table 4 shows the analytical results of the seven sites and a graphical representation of mercury concentration along with associated uncertainty is given in Figure 2.

Table 4 Results of mercury with uncertainty in SPM analyzed by AAS-HG

Name of the site	SPM in µg/m^3	Concentration of mercury in ng/m^3 with expanded uncertainty at 95% confidence; k = 2
Heavy traffic site (S-1); Ashram zone	395	12.6 ± 2.4
Industrial site (S-2) ; Azadpur zone	203	6.0 ± 1.2
Densely populated + Traffic site (S-3); Loni Road	2,337	14.5 ± 2.9
Ambient site (S-4) ; Pitampura zone	251	1.59 ± 0.37
Traffic site (S-5); Highway No.56	338	3.17 ± 0.63
Industrial site (S-6) ; Nariana zone	429	5.9 ± 1.2
Mix Zone (S-7); NPL zone	347	4.51 ± 0.91

Figure 2 Concentration of each sample with associated uncertainty value.

Result and discussion

Accurate determination of mercury in air is not easy due to the difficulties in measuring the air volume, losses during sample digestion process due to its vaporizing nature. The evaluation of combined uncertainty in mercury concentration in SPM sample is very complicated as there are various parameters, which contribute uncertainty in the entire process. On determining the uncertainty for mercury content measurement we were redundantly meticulous in identifying all uncertainty sources. In a routine determination of uncertainty we recommended that it is possible to be much less pedantic, and only reveal and realistically quantify the most significant components. The uncertainty components, which contribute a negligible value, could be ignored from the calculation of combined uncertainty value. The uncertainty components, which are found to contribute significantly during the subsequent computations, can be quantified more precisely and the final combined uncertainty can be recalculated. Mae and Dan 2010 also suggested how uncertainty can be reduced in measurement of atmospheric mercury and also suggested mercury in the air is measured as three forms like gaseous elemental mercury, reactive gaseous or gaseous oxidized and particle-bound mercury.

The concentration of mercury on the S-4 site is 1.57 ± 0.37 ng/m^3, which is the lowest (ambient site), while on the S-4 site (traffic/densely populated) the gighest concentration 14.5 ± 2.9 ng/m^3 was observed. The relative uncertainty in the measurement of mercury by FAAS-

HG varies from 19 to 23%. Gajghate et al. 2011 have also estimated analytical uncertainty in quantification of mercury in different fractions of PM_{10} using microwave digestion and DMA-80 mercury analyzer. The mercury concentrations in ambient air in different various fractions of PM_{10} were found to be in the range of 3.13 ng m^{-3} (26%) – 22.96 ng m^{-3} (15%) with respective expanded relative uncertainty. Synek et al. 2000 estimated uncertainties in mercury determinations in biological materials by atomic absorption spectrometer – AMA 254 and suggested major uncertainty (52%) is due to sample absorbance measurement.

In the proposed determination of mercury concentration (S-1), there are five main uncertainty sources, which directly influence the final results those are C_{Hg}, V_{TEST}, W_{TSPM}, W_{ANA}, V_{HVS} and R_{HVS}, with relative contributions 4.2%, 0.001%, 0.02%, 0.06%, 95.1% and 0.6% respectively. It is clear from the Figure 3 that flow rate (V_{HVS}) is the crucial parameter, which contributes the highest uncertainty of the value. The flow rate can be changed by several factors such as oily nature of the sample, presence of photochemical smog; wood smoke. These factors may block the filter paper and cause a rapid drop in air flow. Besides these high humidity and dense fog can cause the filter to become wet and thus airflow reduces through the filter paper. So sampling through HVS is the additional source, which also contributes uncertainty in mercury determination. Traffic and industry are the major sources, which contribute major contamination of mercury in environment.

Figure 3 Contribution of each uncertainty source.

Competing interests

The authors declare that they have no competing interests.

Authors' contributions

NS participated in the design of the study, carried out sampling, wet digestion of the sample and written work. TA and DS have contributed in analysis of the mercury analysis by AAS-HG. VNO and SST have contributed in calculation of various uncertainties, which have been identified in the experiments. IL has given valuable suggestion during writing of manuscript and also helped how to incorporate recovery of the process in the final calculation. All the authors have read and approved the final manuscript.

Acknowledgement

The authors are grateful to Prof. R. C. Budhani; Director, National Physical Laboratory for encouragement and permission to publish this work. The authors are thankful to Sh Prabhat K. Gupta, Head Analytical Chemistry for his support. The authors also thank Dr. J. K. Bassin, Director, NEERI for providing their sites for sampling.

References

Barth P, Krivan V, Hausbeck R (1992) Cross-interferences of hydride-forming elements in hydride-generation atomic absorption spectrometry. Anal Chim Acta 263:111–118

Bełdowska M, Falkowska L, Lewandowska A (2006) Airborne trace metals (Hg, Cd, Pb, Zn) of the coastal region, Gulf of Gdansk Oceanological and Hydrobiological Studies. Int J Oceanological Hydrobiology 5(2):159–169

Ellison SLR, Rosslein M, Williams A (2000) Quantifying Uncertainty in Analytical Measurement. EURACHEM / CITAC 1:2000

Erdem N, Henden E (2004) Preconcentration and determination of inorganic arsenic using a multisyringe flow injection system and hydride generation-atomic fluorescence spectrometry. Anal Chim Acta 505:59–65

European Standard EN ISO/IEC 17025 (2005) General Requirements for the Competence of the Testing laboratories. European Committee for Standardization, Brussels, 14(2000) revised as *ISO/IEC* 17025

Gajghate DG, Pipalatkar PP, Khaparde VV, Rao CVC, Pustode TM (2011) Uncertainty estimation in analysis of particulate-bound mercury in different size fractions of PM10 in ambient air. Accred Qual Assur 16:459–465

ISO ISO/DTS 21748 (2003) Guide to the Use of Repeatability, Reproducibility and Trueness Estimate. In: Measurement Uncertainty Estimation. ISO, Geneva, Switzerland

JCGM 100 (2008) Evaluation of measurement data-Guide to the expression of uncertainty in measurement. JCGM guidance document is shared jointly by the JCGM member organizations (BIPM, IEC, IFCC, ILAC, ISO, IUPAC, IUPAP and OIML), Geneva, Switzerland

Kayal N, Singh N (2010) Uncertainty calculation in the quantitative estimation of silica in rice husk ash by titrimetric method. Journal of MAPAN-Journal of Metrology Society of India 25(2):115–123

Kayal N, Singh N, Ojha VN, Gupta PK (2009) Evaluation and expression of uncertainty in the determination of alumina in deodorants by complexometric method. Test And Eva (ASTM) 37(4):321–328

Kumar AR, Riyazuddin P (2007) Underestimation of total arsenic concentration in groundwater samples determined by hydride generation quartz furnace atomic absorption spectrometry due to sample characteristics. Accred Qual Assur 12:455–458

Mae G, Dan J (2010) Reducing the Uncertainty in Measurement and Understanding of Mercury in the Atmosphere. Environ Sci Technol 44:2222–2227

Moore W, Ramamoorthy S (1984) Heavy metals in natural waters; Applied Monitoring and Impact Assessment. Springer, New York

Murphy DM, Thomson DS, Mahoney MJ (1998) In situ measurements of organics, meteoritic material, mercury, and other elements in aerosols at 5 to 19 kilometers. Science 282:1664–1669

Schroeder WH, Munthe J (1998) Atmospheric Mercury, An overview. Atmos Environ 5:809–822

Singh N, Sarkar AK (2003) Determination of Mercury in Fly ash ore by flameless cold vapor Atomic Absorption spectrometry using Hydride generator. Asian J Chem 159(3):1327–1330

Synek V, Subrt P, Marecek J (2000) Uncertainties of mercury determinations in biological materials using an atomic absorption spectrometer. Accred Qual Assur 5:58–66

VIM: JCGM 200 (2008) International vocabulary of metrology-basic and general concepts and associated terms (VIM). JCGM guidance document is shared jointly by the JCGM member organizations (BIPM, IEC, IFCC, ILAC, ISO, IUPAC, IUPAP and OIML)

Walcerz M, Bulska E, Hulanicki A (1993) Study of some interfering processes in the arsenic, antimony and selenium determination by hydride generation atomic absorption spectrometry. Fresenius J Anal Chem 346:622–626

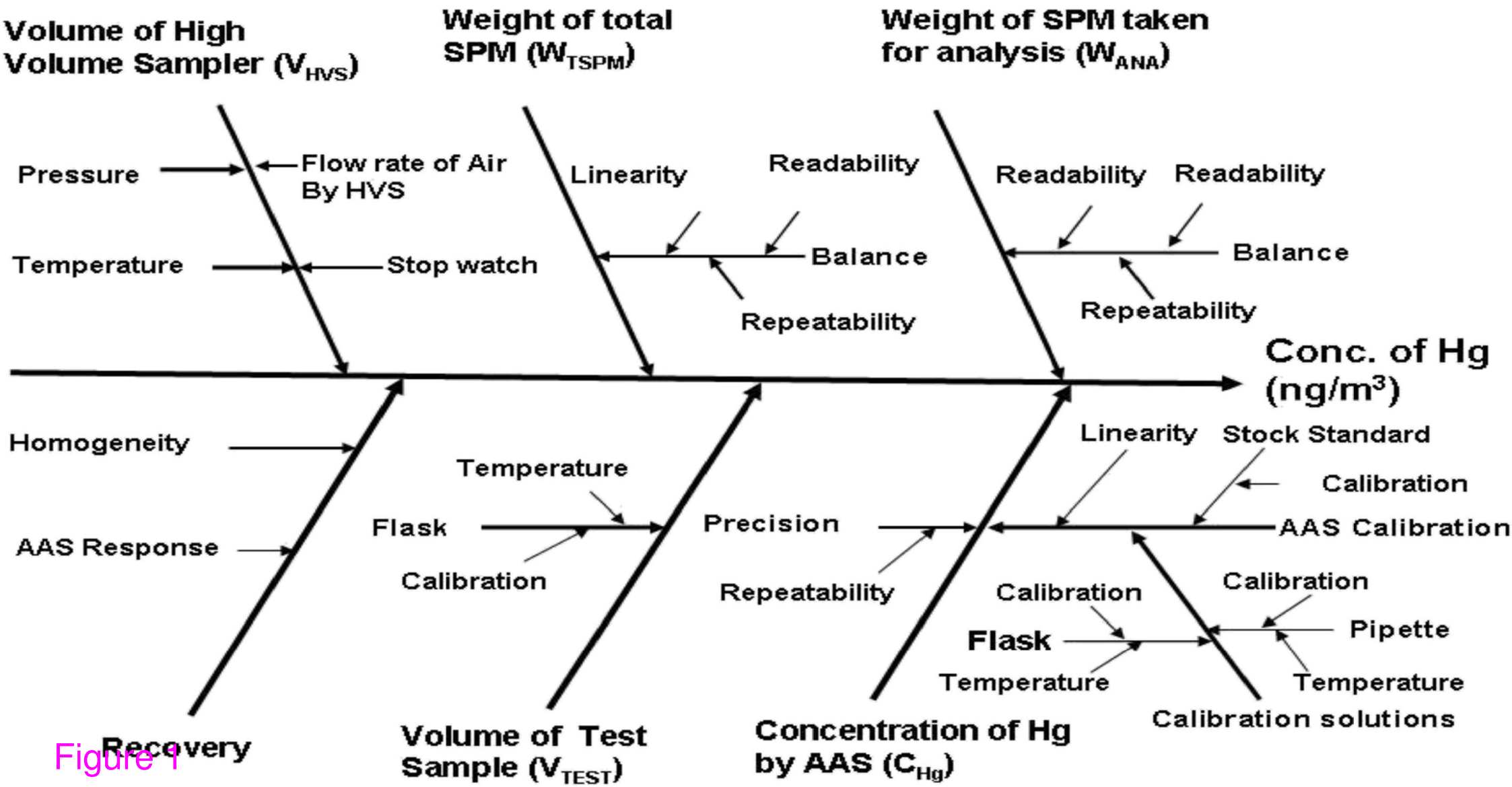
Volume of High Volume Sampler (V_{HVS})
Weight of total SPM (W_{TSPM})
Weight of SPM taken for analysis (W_{ANA})
Pressure
Flow rate of Air By HVS
Temperature
Stop watch
Linearity
Readability
Balance
Repeatability
Readability
Readability
Balance
Repeatability
Conc. of Hg (ng/m³)
Homogeneity
AAS Response
Recovery
Temperature
Flask
Calibration
Volume of Test Sample (V_{TEST})
Precision
Repeatability
Concentration of Hg by AAS (C_{Hg})
Linearity
Stock Standard
Calibration
AAS Calibration
Calibration
Flask
Temperature
Calibration
Pipette
Temperature
Calibration solutions

Figure 1

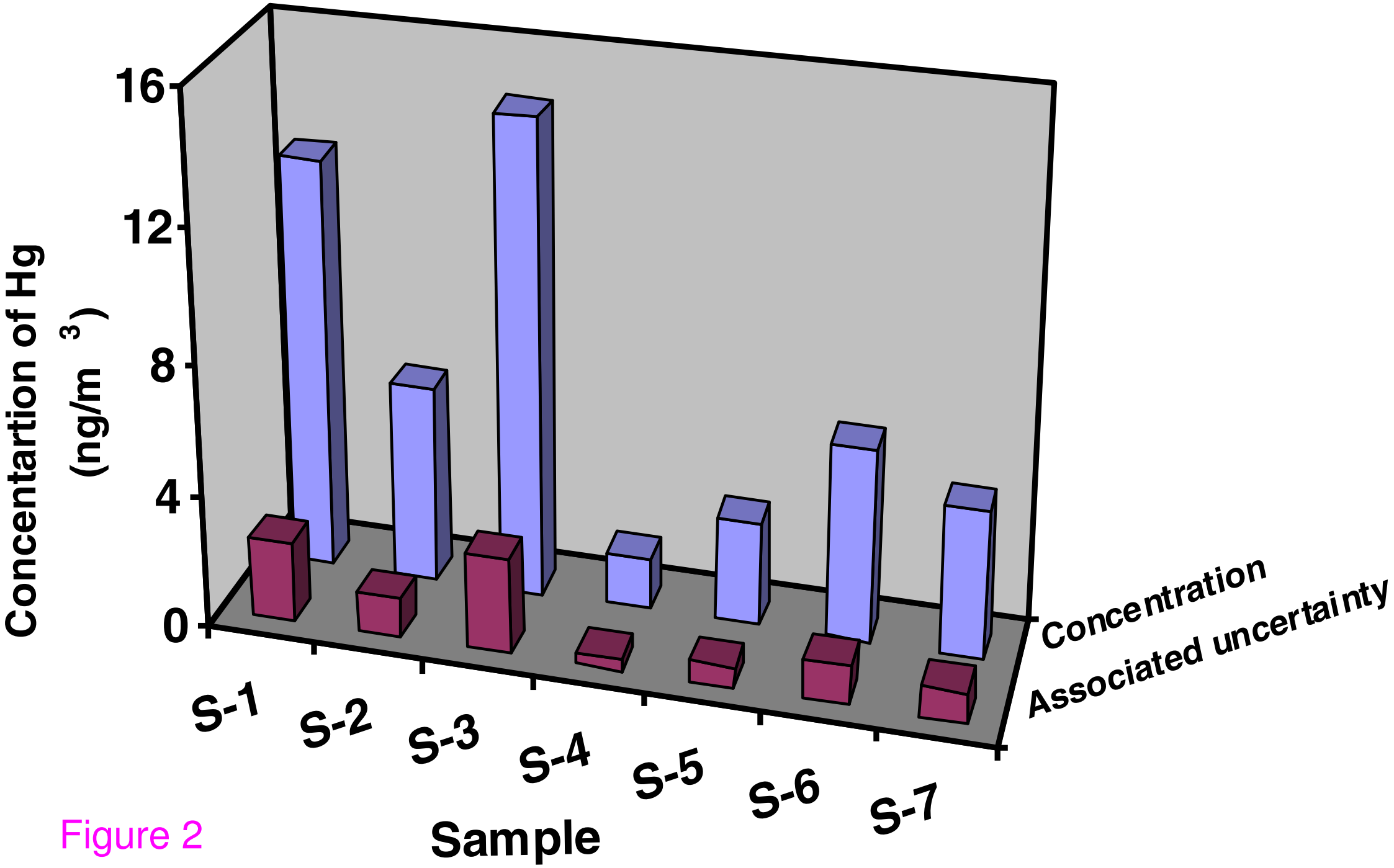
Concentartion of Hg
(ng/m 3)
16
12
8
4
0
S-1
S-2
S-3
S-4
S-5
S-6
S-7
Sample
Concentration
Associated uncertainty

Figure 2

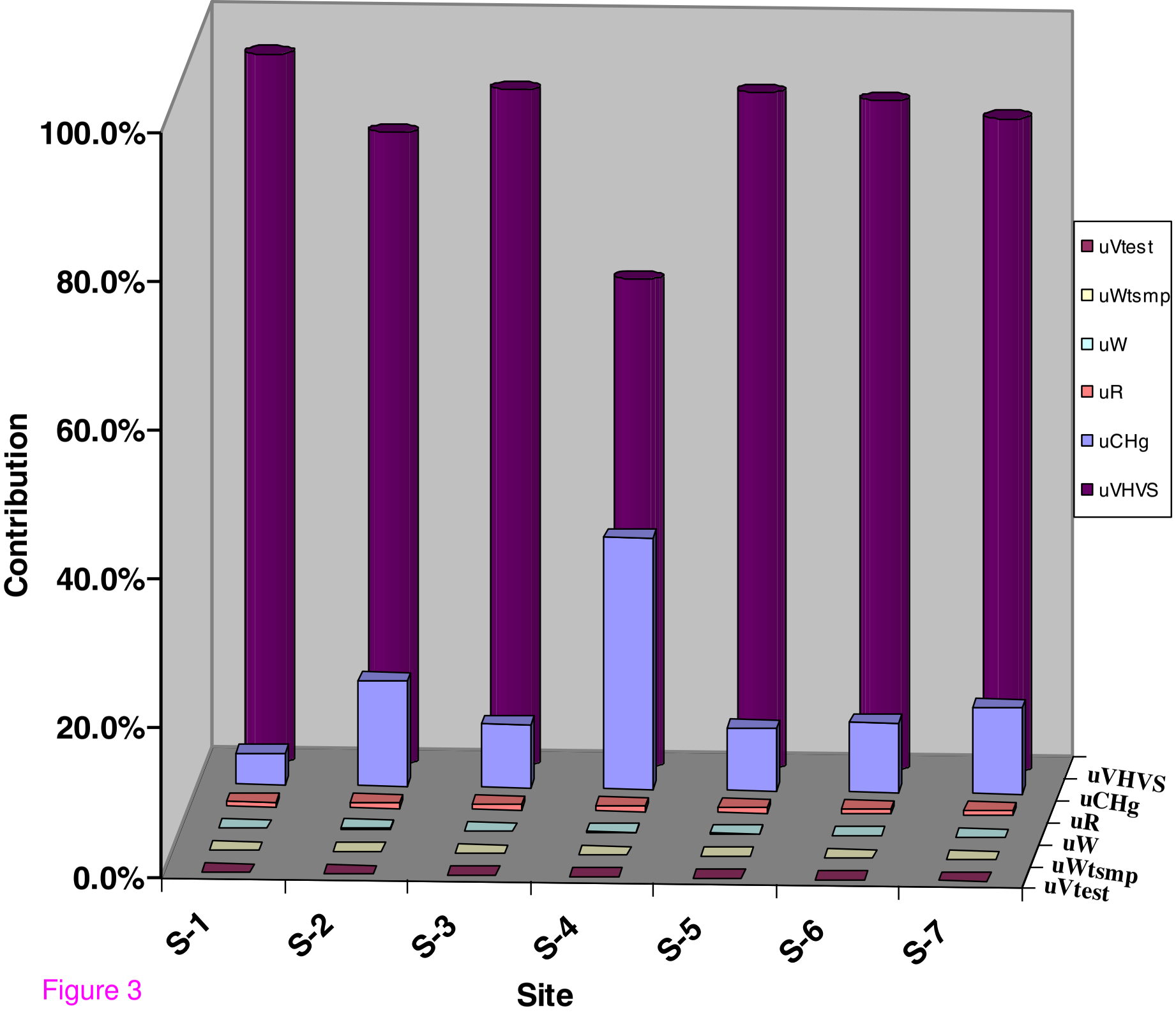
100.0%
80.0%
60.0%
40.0%
20.0%
0.0%
Contribution
S-1
S-2
S-3
S-4
S-5
S-6
S-7
Site
uVtest
uWtsmp
uW
uR
uCHg
uVHVS
uVHVS
uCHg
uR
uW
uWtsmp
uVtest

Figure 3

Additional files provided with this submission:

Additional file 1: 1766762699101189_add1.doc, 133K
http://www.springerplus.com/imedia/2083920286107954/supp1.doc
Additional file 2: 1766762699101189_add2.doc, 25K
http://www.springerplus.com/imedia/7452900341079545/supp2.doc

International Association of Scientific Innovation and Research (IASIR)
(An Association Unifying the Sciences, Engineering, and Applied Research)

ISSN (Print): 2279-0047
ISSN (Online): 2279-0055

International Journal of Emerging Technologies in Computational and Applied Sciences (IJETCAS)
www.iasir.net

Spectrophotometric Determination of Pt (II) and Pd (II) in Environmental Samples Collected from Highly Polluted Areas of Delhi Region of India

Pushpa Ratre[1], Devendra Kumar[2]
[1, 2] Department of Applied Chemistry and Polymer Technology
Delhi Technological University (Formerly Delhi College of Engineering)
Shahbad Daulatpur, Bawana Road, Delhi-10042, INDIA.

Abstract*: A simple and highly selective spectrophotometric method for the determination of platinum and palladium emitted by automobiles catalyzed with catalytic converters in highly polluted areas of Delhi region of India is proposed. The proposed method is based on the formation of mixed complexes of Pt (II)[pH 6.0] and Pd(II) [pH 4.5] with 2-(5-Bromo-2-pyridylazo)-5-diethylaminophenol (5-Br-PADAP) in the presence of dodecyl benzene sulphonic acid sodium salt. Both the complexes are extractable with dichloromethane. The Pt (II) and Pd (II) complexes have shown maximum absorbance at 570 nm and 550 nm, respectively. The optimum concentration ranges for the determination of Pt (II) and Pd (II) complexes are 1.0 -3.6 and 0.1- 2.0μg/ mL, respectively. The methods are free from the interference of the platinum group metals.*

Keywords*: Automobile exhaust, Extraction, Dodecyl benzene sulphonic acid sodium salt, Platinum (II), Palladium (II)*

I. Introduction

The automobile catalytic converter is a part of the automobile exhaust system. It converts harmful compounds like hydrocarbons of unburned gasoline, carbon monoxide and nitrogen oxide in exhaust into harmless compounds like carbon dioxide, water, nitrogen and oxygen. Automobile catalysts are mobile sources of platinum and palladium. The particulate of platinum and palladium released from an auto catalyst ranged from 4 to 108 ng/Km. The increasing use of platinum group metals (PGMs) in vehicle catalytic converters in addition to its use in chemical industry, jewelry making, pharmaceuticals etc. leads to the emission of PGMs into the environment. These metals are naturally found at very low concentration in the earth crust, but the increasing anthropogenic PGMs concentration poses a risk to living organisms and human beings [1].

Some rare metals belonging to PGMs are more environmentally mobile and thus bio-available to plants and trees. Under appropriate pH and redox potential conditions, PGMs can bind with peptides or humic or fulvic acids in the aquatic environment. Concentrations of PGMs in surface fresh water and surface salt water were found to be in the range of 0.4 to 22 ng/L and 19 to 70 pg/L, respectively whereas in the dense traffic road soil samples, concentration of PGMs were found to be in the range of less than 0.7 to 47 µg/Kg. Other PGMs concentrations in sewage sludge, sludge contaminated by discharges from the local jewelry industry and drinking-water samples were 18 to 260 µg/Kg, 4700 µg/Kg, less than 24 ng/L, respectively [2].

A lot of advanced techniques, namely graphite furnace atomic absorption spectrometry (GFAAS) [3,4] and inductively coupled plasma mass spectrometry (ICP-MS) [5-7], stopped-flow injection spectrophotometric determination [8], flow injection analysis (FIA) [9], flame atomic absorption spectrometry (FAAS) [10], electrothermal vaporization inductively coupled plasma mass spectrometry (EVICP-MS) [11], electrothermal atomization-laser induced fluorescence ion chromatography [12], polarography [13], have been developed for the determination of trace amount of platinum and palladium in various complex matrices such as ores, alloys, seawater, biological samples and autocatalytic exhaust samples.

Although, all the above techniques are good but spectrophotometric method is more popular due to being cheaper technique. Literature reveals that a small amount of work has been done for the analysis of platinum and palladium in catalytic converter based on spectophotometric method.

William et al. [14] developed a complicated extraction method for the determination of Pd (II) and Pt (II) complexes with dibenzyldithiooxamide in chloroform. Marczenko et al. [15, 16] developed a less sensitive separation method for palladium and platinum which was extracted with dithizone in carbon tetrachloride. Toral et al. [17] developed a method for the determination of Pd and Pt complexes with 3-(2-thiazolylazo)-2, 6-diaminopyridine (2, 6-TADAP) in the presence of 1.7 mol L^{-1} perchloric acid solution which had drawback of heating upto 90° C for 30 min. Mojski et al. [18] developed a less sensitive extractive separation of platinum from macroamounts of palladium using triphenylphosphine oxide. Kavlentis et al. [19, 20] a less sensitive

method using a reagent 2-allylthiourea and thiocyanate with isoamyl alcohol, benzyltriethylammonium ion and iodide in the presence of EDTA. Manku et al. [21] developed a less sensitive method of extraction with oximidobenzotetronic acid which suffered from matrix interferences of common metal ions.

In the proposed method, the reagent, namely 2-[(5-bromo-2-pyridylazo)]-5-diethylaminophenol (5-Br-PADAP), forms mixed-ligand colored stable complexes with Pt(II) and Pd(II) due to the presence of the –N-$(CH_3)_2$ and halogen group. Complexes made with Pt (II) and Pd (II) are extractable with dichloromethane in the pH range of 4.0-6.5. The proposed method is free from interference of most of platinum group elements, even with no interference from Cu (II) and Fe (III) ions.

II. Experimental

A. Reagents

All chemicals used were procured from Sigma Aldrich and E. Merck. Millipore double distilled water was used for the preparation of all solution. The standard solution of platinum was prepared by dissolving a 1 g-ampoule of $PtCl_4$ in 50 mL of 6 mol L^{-1} HCl and then diluting to 1 Liter in a volumetric flask with the double distilled water. The stock solution was standardized by the gravimetric method [22].

The standard solution of 1000μg mL^{-1} palladium was prepared by dissolving weighed amount of $PdCl_2$ (1.66g) in 3.3 mL of concentrated HCl and then diluted to 100 mL in a volumetric flask with water. After the standardization of stock solution by the dimethylglyoxime gravimetric method [23], the exact morality of stock solution was found to be 9.39×10^{-3} mol L^{-1}. A diluted solution of platinum (IV) and palladium (II) was prepared by diluting the stock solution as required. A (5%, w/v) solution of $SnCl_2$ was used in 10 mol L^{-1} HCl. A 8.60×10^{-4} mol L^{-1} or (0.03%, w/v) 2-[2-(5-bromopyridyl) azo]-5-dimethyl-aminophenol **(**5-Br-PADAP) (97.0% pure) solution in ethanol (95.0% pure) was employed for color development. An aqueous solution of 0.02869 mol L^{-1} or (1%, w/v) of dodecyl benzene sulphonic acid sodium salt (DBSA) was prepared. Acetate buffer was prepared by mixing 0.1 mol L^{-1} solution of sodium acetate with 0.1 mol L^{-1} solution of acetic acid used for pH adjustment [24]. The stock solution of desired diverse ions was prepared as described in the literature and its 1mg/mL solution was prepared by dilution [24].

B. Instrumentation

For the characterization of maximum absorbance at appropriate wavelength of the complexes of Pt (II) and Pd (II), double beam UV-Visible spectrophotometer 54440SS model equipped with 1cm quartz cell was used. A digital pH meter (DB-1011) was calibrated regularly with a standard buffer solution of acid and base before being utilized.

C. General Procedure

Take an aliquot of the standard solution containing up to 0.1-3.5μg of Pt(IV) in a 125mL separatory funnel. To the above solution, add 0.9 mL of 0.1 mol L^{-1} $SnCl_2$ in HCl for complete reduction of Pt (IV) to Pt (II), then add 0.9 mL of (1%, DBSA) and 1.0 mL of 5-Br-PADAP and then adjust the total volume of 10 mL with acetate buffer solution of pH 6.0±0.2 and shake the violet color aqueous complex vigorously for 2 min with 5 mL dichloromethane. After drying over anhydrous sodium sulfate (≈2 gm), all the extracts were transferred to a 10 mL volumetric flask and made up to 10 mL with dichloromethane. Further, absorbance of the complex against solvent at λ_{max} 570 nm was measured.

For the preparation of Pd(II) complex, take an aliquot of 0.5-20 μg of Pd (II) in a 125mL separatory funnel and mix it with 0.4 mL of 1% DBSA and 1.2 mL of 5-Br-PADAP and then adjust the total volume upto 10 mL with acetate buffer solution of pH 4.5±0.2. In the case of extraction of Pd (II), follow the same extraction procedure as done earlier for Pt (II). Further, absorbance of the Pd (II) complex against solvent at λ_{max} 550 nm was measured.

D. Sampling and Sample Preparation

a. Automobile Exhausts Fume (Sample "A")

With conical flask connected to catalytic converter maintaining temperature between 0-5ºC and stand-alone car maintaining speed at 20 Km L^{-1} for 2h, exhaust fume samples collected condense into liquid. The collected exhaust fume samples from 4 different types of four-wheelers, were diluted to 100 mL with distilled water in a volumetric flask, and with 1mL fume sample, the procedure given at para II(C) are to be followed.

b. Automobile Exhaust Scrape (Sample "B")

Automobile exhaust samples were collected from the exhaust scrape of Bharat II type cars equipped with catalytic converter (PGMs). About 1.0 g of usable catalyst obtained as scratches from exhausts pipe, was

weighed and treated with 15 mL of aqua regia on a hot plate for 30 min. After cooling, the solution was filtered and the filtrate was heated to dryness. Another 5 mL of aqua regia was added and then procedure was repeated. The residue was dissolved in 10 mL of 0.1 mol L^{-1} H_2SO_4 and then solution was filtered off and made up to 50 mL with distilled water.

c. Roadside Dusts (Sample "C")

The roadside dust was collected from heavy traffic road areas. The samples were crushed in an agate mortar and sieved through 200 meshes. These samples were separately treated with aqua regia (50 mL) with 4-5 mL of HF in a Teflon beaker to dissolve silica, if present. The solution is heated to dryness and treated with 10 mL of 0.1 mol L^{-1} H_2SO_4 and made up to 25 mL with distilled water in volumetric flask.

d. Vegetation (Sample "D")

Plant leaves were heated in an oven to dryness and crushed into fine particles in an agate mortar and then sieved through 200 meshes. Samples were treated in a same fashion as described above for the automobile catalyst samples and made up to 25 mL with distilled water in 25 mL volumetric flask. In all sample preparation, the solutions were filtered through Whatman Filter paper no. 42 after digestion.

III. Results and Discussion

A. Absorption Spectra

The choice of suitable solvent and use of appropriate amounts of buffer, surfactant and reagent significantly increase the sensitivity, selectivity and molar absorptivity of the system.

The complexes of Pt (II) and Pd (II) in dichloromethane exhibit a maximum absorbance at around 570 and 550 nm, respectively against the solvent in their respective pH ranges of 6.0±0.2 and 4.5±0.2, as shown in Fig. 1. The reagent blank and solvent show negligible absorbance (A=0.05) in this region, hence it was used for whole experimental work.

Figure 1 Absorption spectra of the complexes, Pt(II) at pH 6.0 and Pd(II) at pH 4.5: Pt(IV)=2.96×10^{-7} mol L^{-1}, $SnCl_2$=1.72×10^{-2} mol L^{-1}, DBSA=2.57×10^{-3} mol L^{-1}, 5-Br-PADAP=5.72×10^{-5} mol L^{-1}, Pd(II) = 3.38×10^{-6} mol L^{-1}, DBSA=1.43×10^{-3} mol L^{-1}, 5-Br-PADAP=1.03×10^{-4} mol L^{-1}

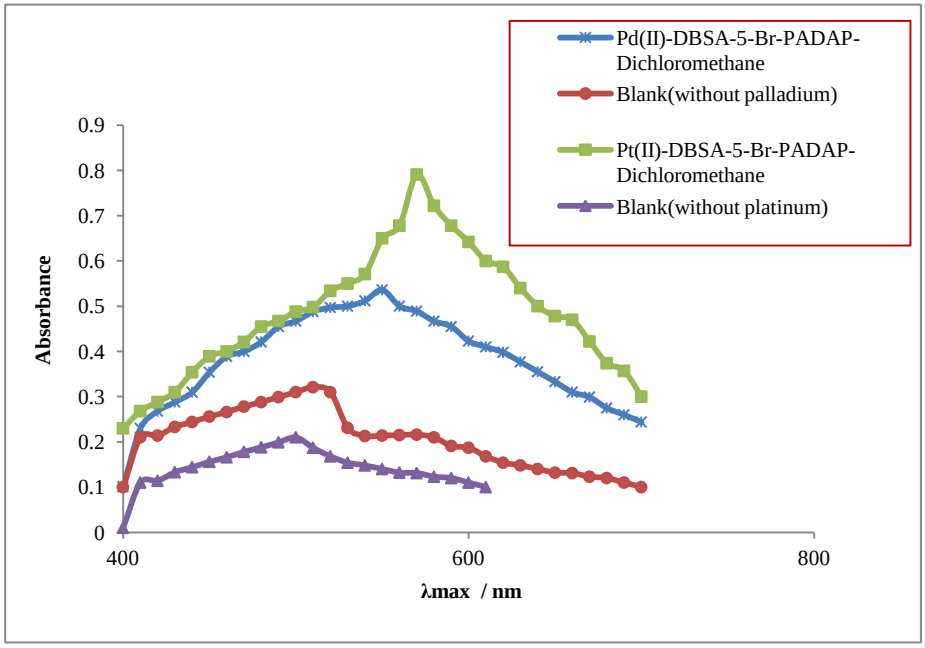

B. Choice of Solvent

Both Pt (II) and Pd (II) complexes are extractable with many organic polar and non-polar solvents, such as ethyl acetate, isobutyl methyl ketone, toluene, benzene, carbon tetrachloride, chloroform, dichloromethane as listed in Table 1. Maximum extraction (>99%) in terms of absorbance of the complexes were observed with dichloromethane as compared with the other solvents. Since dichloromethane is less toxic than the chloroform, therefore, it was chosen as solvent for present work.

Table 1 Effect of solvent on the extraction of Pt(II) and Pd(II) complexes.
Pt(IV)=2.96×10^{-7} mol L^{-1}, $SnCl_2$=1.72×10^{-2} mol L^{-1} DBSA=2.57×10^{-3} mol L^{-1}, 5-Br-PADAP=5.72×10^{-5} mol L^{-1}
Pd(II) = 3.38×10^{-6} mol L^{-1} DBSA=1.43×10^{-3} mol L^{-1}, 5-Br-PADAP=1.03×10^{-4} mol L^{-1}

Solvent	Pt(II), λ_{max}, nm	Molar absorptivity(ε) L mol^{-1} cm^{-1} ×10^5	Pd(II), λ_{max}, nm	Molar absorptivity(ε) L mol^{-1} cm^{-1} ×10^4
Ethyl acetate	400	0.113	500	3.40
Isobutyl methyl ketone	575	0.730	570	4.25
Xylene	560	0.235	550	2.35
Benzene	420	0.122	480	3.66
Toluene	440	0.410	440	3.19
Carbon tetrachloride	560	0.121	550	2.02
Chloroform	570	1.270	550	9.57
Dichloromethane	570	1.270	550	9.57

C. Effect of pH

The effect of pH on the extraction of Pt (II) and Pd (II) complex were studied with different buffer of pH ranges of 1.0-14.0. The Pt (II) complex show stable and maximum absorbance with acetate buffer in the pH range of 3.0-6.5, so pH 6.0±0.2, at 570 nm was kept constant throughout the experiment. The Pd (II) complex show constant absorbance at the pH range of 4.0-5.5, so pH 4.5±0.2 at 550 nm, using an acetate buffer solution.

D. Effect of Surfactants

Effect of nine surfactants, namely cetyltrimethylammonium bromide, cetylpyridinium bromide, benzyldimethyltetradecylammonium chloride (Zephiramine), sodium lauryl sulfate, sodium dodecyldimethylamino acetate, nonyl phenoxy polyethoxyethanol OP,Tween-60, Tween-80 and dodecyl benzene sulphonic acid sodium salt (DBSA) were tried. It was found that only dodecyl benzene sulphonic acid sodium salt (DBSA) was able to decrease the consuming time of color development increasing the sensitivity and molar absorptivity of both complexes.

E. Effect of Reagents

Pt (IV) reduces to Pt (II) in the presence of tin (II) chloride at room temperature (30±0.2°C). Tin (II) chloride developed a maximum color in the final aqueous solution with concentration varying between the range (0.95-1.90) ×10^{-2} mol L^{-1}. Hence, a 1.72×10^{-2} mol L^{-1} solution of tin (II) chloride was kept constant throughout the experiment.

The concentration of DBSA in the range of (1.14-2.29) ×10^{-3} mol L^{-1} was required for maximum color development and constant absorbance of Pt (II) complex. Hence, a 1.43×10^{-3} mol L^{-1} solution was kept constant throughout experiment. But for the formation of Pd (II) complex, the reagent range (2.0-2.86)×10^{-3} mol L^{-1} was required for maximum color development of Pd (II) complex. So, 2.57×10^{-3} mol L^{-1} solution was kept constant through experiment.

The reagent 5-Br-PADAP indicated that at least concentration range of (2.86-6.29)×10^{-5} mol L^{-1} in methanol was required for maximum color development of Pt (II) complex and therefore 5.72×10^{-5} mol L^{-1} of 5-Br-PADAP was kept constant throughout the experiment. But for the formation of Pd (II) complex, the reagent range (0.77-1.11)×10^{-4} mol L^{-1} solution in methanol was required for constant and maximum absorbance. A 1.03×10^{-4} mol L^{-1} of 5-Br-PADAP was kept constant throughout the experiment.

F. Effect of Temperature, Electrolyte and Dilution

The study of the variation of temperature on the extraction of the metal complex with dichloromethane showed no change in absorbance of the Pt (II) and Pd (II) complexes between the temperature 10-50ºC. Beyond this temperature, the absorbance of the complexes decreased. Hence, all the extraction works were carried out at a temperature of 30 ± 2ºC.

Addition of electrolytes such as potassium chloride or potassium sulfate or ammonium chloride upto 1.5 mol L^{-1} did not change the absorbance and λ_{max} of the complexes. The effect of variation in the volume of the aqueous phase, keeping the other variables constant, on the extraction of the metal complexes with dichloromethane was studied. No change in the absorbance of the complex and λ_{max} was observed while varying the volume ratio

of the organic to aqueous phase(1:4 to 1:1. Hence the 1:1 organic:aqueous phase was chosen for the entire experiment.

G. Composition of the Metal Complexes

The composition of the Pt(II) and Pd(II) complexes were determined by using the curve fitting method (Sillen)[25] and Job's continuous variation method [26]. A graph was plotted between log D (distribution ratio) of metal versus log M (concentrations of ligand). The corresponding mole ratio of the metal to ligand for Pt (II) complex and Pd(II) complex are 1:1:2 [M: DBSA: 5-Br-PADAP] and 1:1:3 [M:DBSA: 5-Br-PADAP]. The probable reaction mechanism is given as below:

$[PtCl_2(SnCl_3)_2]^{2-}$(Yellow color) +DBSA+ 2(5-Br-PADAP) $\Leftrightarrow$ $\{[(DBSA)PtCl_2(SnCl_3)_2(5\text{-Br-PADAP})_2]\}_o$ (Violet color) +3HCl

$[PdCl_2]$(Transparent color) + DBSA + 3(5-Br-PADAP) $\Leftrightarrow$ $\{[\{PdCl_2(5\text{-Br-PADAP})_3(DPBA)]\}_0$ (Blue color)+4HCl

Subscript "o" here describes the organic phase or dichloromethane.

H. Analytical Parameters

The system obeyed Beer's law upto 1.0-3.6µg Pt (II) mL^{-1} and 0.5-2.0 µg Pd (II) mL^{-1} in the organic phase as shown in Fig 2. All the parameter such as correlation coefficient, slope, intercept, molar absorptivity, Sandell's sensitivity, detection limit (2σ), standard deviation, relative standard deviation, percentage of error, etc. are listed in Table 2.

Figure 2 Plot of calibration curve for determination of Pt(II) and Pd(II) complexes in dichloromethane.

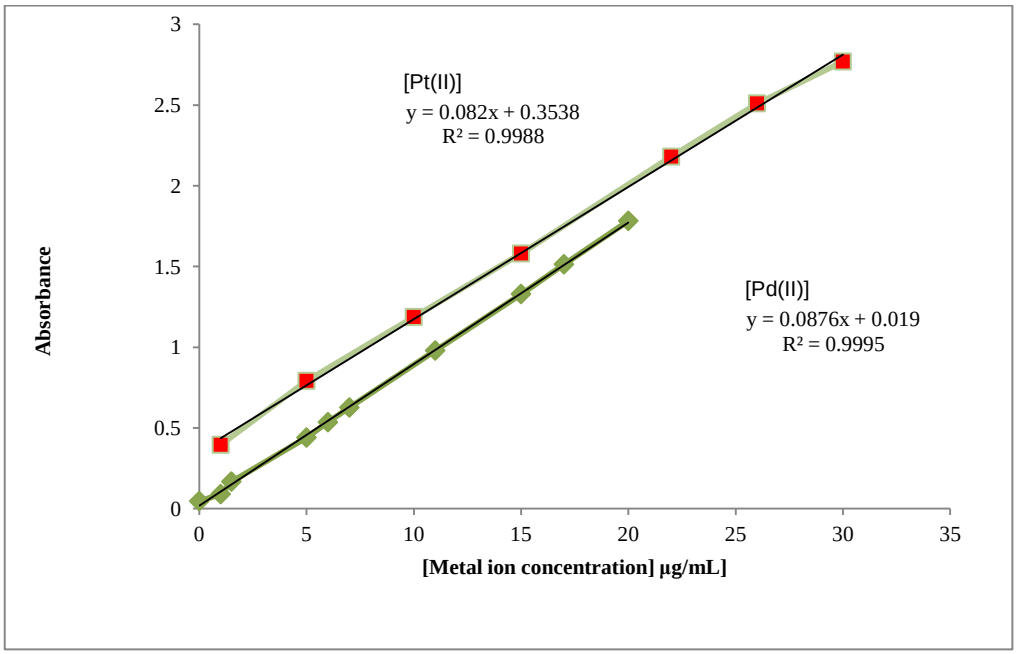

I. Effect of Diverse Ions

A 10µg Pt(II) mL^{-1} and a 6µg Pd(II) mL^{-1} in aqueous phase were used for the study of the effect of diverse ions [28]. Different amount of foreign ions were introduced into a fixed amount of Pt(II) and Pd(II) which changed the absorbance. Foreign ions interfered when there was a change in the absorbance of the Pt(II) and Pd(II) complexes (Absorbance) by $\geq \pm$ 2%. The important feature of the method is that PGEs, namely Ru(IV), Rh(III), Pt(IV), Ir(III) and Os(VIII) do not interfere with the proposed method. The tolerance limit of various diverse ions in the determination of metal complex is summarized in Table 3.

J. Analytical Applications

The samples like automobile engine exhaust scrape, roadside dust, vegetation samples etc were collected from the different polluted places of Delhi region, namely Chandani chowk area of South Delhi, Maduban Chowk area of North Delhi and Janakpuri and Vasantgunj of West Delhi and Dilshad Garden, Modi Nagar and Ghaziadad region of National Capital Territory of Delhi.

The proposed method required minimal volume of the final sample solution with several fold preconcentration of the analyte, deposited at the mouth of exhaust vehicle [29]. The actual concentration of Pt(II) and Pd(II) in samples were determined using the calibration curve. The average concentration of Pt(II) and Pd(II) in automobile exhaust fume, automobile exhaust scrape and in the environmental samples (plants and dust) were found to be in the range of 0.068-185 μg/mL and 0.020-0.81 μg/mL, respectively, as shown in Fig. 3 and Fig. 4. The average recovery of Pt (II) and Pd (II) is calculated to be 99.5 ± 0.1% with RSD value ranging between 0.1-4.6% and the same is listed in Table 4. So, the proposed method is suitable for the spectrophotometric determination of trace amount of Pt(II) and Pd(II) in the automobile exhaust fume and scrape, and environmental samples (plants and dust) in Delhi region of India. **,**

IV. Conclusion

A sensitive and selective spectrophotometric method for the determination of Pt (II) and Pd (II) at trace level in automobile exhaust fume and automobile exhaust scrape, and environmental samples (plants and dust) in highly polluted areas of Delhi region is described here. The high concentration of Pt (II) and Pd (II) were found in East and West Delhi region of India because of the densly established industry and also due to emission of toxic gases through unserviceable automobiles running on the road. Some results obtained were: (i) The average concentration of Pt (II) and Pd (II) ranged 0.030-0.085 μg/mL and 0.020-0.090 μg/mL, respectively. (ii) The average recovery of Pt (II) and Pd (II) calculated to be 99.5 ± 0.1% with RSD value ranging between 0.1-4.6%. The methods are very sensitive and selective as it is free from the interference of PGMs element i.e. Ru(IV), Rh(III), Pt(IV), Ir(III) and Os(VIII). The present work provides for a new method for quantitative analysis of Pt (II) and Pd (II) in automobile exhaust and environmental samples as very few literature is available for the determination of Pt (II) and Pd (II) using spectrophotometric method in such samples.

Table 2 Analytical characteristics of Platinum (II) and Palladium (II) complexes in dichloromethane.

Parameters	**Pt (IV) to Pt (II)**	**Pd (II)**
Color of the complexes	Violet	Blue
λ_{max}	570 nm	550nm
pH	6.0±0.2	4.5±0.2
Concentration of 5-Br-PADAP	5.72×10^{-5} mol L^{-1}	1.03×10^{-4} mol L^{-1}
Concentration of DBSA	2.57×10^{-3} mol L^{-1}	1.43×10^{-3} mol L^{-1}
Concentration of $SnCl_2$	1.72×10^{-2} mol L^{-1} at 30ºC	-------
Solvent	Dichloromethane	Dichloromethane
Composition of complex (M: L:L)	1:1:3	1:2:3
Stability up to,	12.0h	18.0h
Beer's law	1.0 to 3.6 μg/10 mL	0.1 to 2.0 μg/10 mL
Molar absorptivity	1.54×10^{5} L mol^{-1} cm^{-1}	9.57×10^{4} L mol^{-1} cm^{-1}
Detection limit (2σ)	22.4ng mL^{-1}	21.0ng mL^{-1}
Sandell's sensitivity	12.0 ng cm^{-2}	11.2 ng cm^{-2}
Standard deviation(S), N=10	0.31%	0.348%
Relative standard deviation(RSD)	1.5%	1.62%
Intercept, slope, correlation coefficient	0.82, 0.0050, ±0.995	-0.00070, 0.060, 1.0
Error	±1.2%	±0.52%

Table 3 Tolerance limit of diverse ion in the determination of Pt (II) and Pd (II) complexes.

Ions added	Tolerance limit* in mg 10 mL^{-1} aqueous phase	
	10µg Pt (II) /mL	6µg Pd(II) /mL
Cu(II)	0.20	0.20
Ir(III), Rh(III), Os(VIII)	0.05	2.0
Au(III), Zr(IV), Re(VII)	0.9	3.0
Pt(IV), Pt(II)	----	4.0
Pd(II)	1.5	------
Sb(III), Bi(III), U(VI), Ta(V), Mo(VI)	1.0	4.5
Ni(II),Ti(IV),V(V), Cr(VI), Mn(VII)	2.0	5.0
Al(III)	3.0	6.5
Zr(II)	6.0	7.1
Co(II), Fe(III)	10	7.5
Bromide	18	4.0
Oxalate	20	4.3
EDTA	50	5.5
Fluoride	80	10.0
Acetate	100	14.2
Citrate	20	15.0
Tartrate	80	25.0

*Foreign ions interfere when there is a change in the absorbance by $\geq \pm$ 2%of the Pt(II) and Pd(II) complexes

Figure 3 Concentration of Platinum (II) in Delhi Region of India

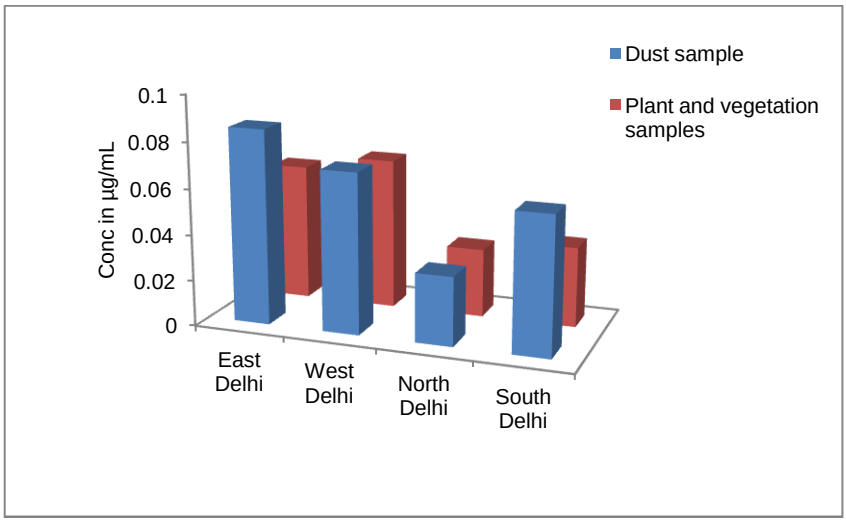

Figure 4 Concentration of Palladium (II) in Delhi Region of India

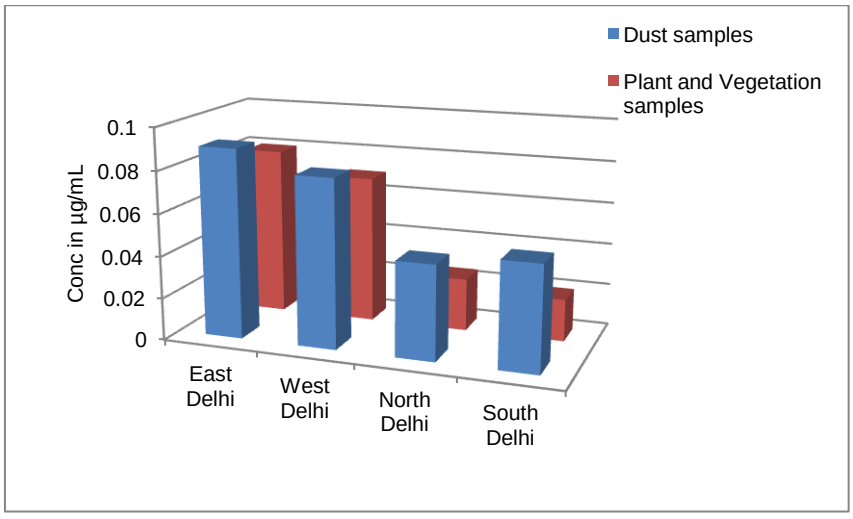

Table 4 Determination of Platinum (II) and Palladium (II) by using standard addition method

Samples	Amount of Pt(IV) & Pd(II) added to the sample (µg/mL)	Present method Concentration of Pt^{II} & Pd^{II} µg/mL, N=4		Reported method Bazel et al.[30] Karthikeyan et al.[31] Concentration of Pt^{II} & Pd^{II} in µg/mL, N=4	
		Pt^{II}, ±%, RSD	Pd^{II}, ±%, RSD	Pt^{II}, ±%, RSD	Pd^{II},±%, RSD
A_1	1.0	1.135 ± 1.9	1.850 ± 4.0	1.136 ± 1.6	1.851 ± 4.2
A_2	1.0	1.138 ± 2.9	1.550 ± 4.1	1.140 ± 2.8	1.458 ±4.0
A_3	1.0	1.068 ± 2.1	1.721 ± 4.3	1.065 ± 2.2	1.718 ± 4.6
A_4	1.0	1.095 ± 2.2	1.620 ± 4.1	1.092 ± 2.3	1.622 ± 4.2
B_1	1.0	1.100 ± 2.5	1.135 ± 0.1	1.098 ± 2.5	1.049 ± 1.1
B_2	1.0	1.152 ± 2.6	1.105 ± 0.2	1.151 ± 2.5	1.038 ± 1.2
B_3	1.0	1.160 ± 1.1	1.150 ± 0.1	1.161 ± 1.2	1.080 ± 1.1
B_4	1.0	1.185 ± 1.5	1.180 ± 0.1	1.183 ± 1.6	1.100 ± 1.1
(C1)East Delhi	2.0	2.085 ± 2.0	2.090 ± 1.1	2.082 ± 1.9	2.090 ± 2.2
(C2)West Delhi	2.0	2.070 ± 2.6	2.080 ± 1.1	2.068 ± 2.5	2.085 ± 2.0
(C3)North Delhi	2.0	2.030 ± 2.2	2.045 ± 1.5	2.031 ± 2.2	2.000 ± 2.5
(C4)South Delhi	2.0	2.060 ± 2.1	2.050 ± 1.8	2.033 ± 2.2	1.030 ± 2.6
(D1)East Delhi	2.0	2.060 ± 2.8	2.080 ± 2.1	2.058 ± 2.9	1.078 ± 2.1
(D2)West Delhi	2.0	2.066 ± 2.4	2.070 ± 2.0	2.045 ± 2.9	1.085 ± 2.0
(D3)North Delhi	2.0	2.030 ± 2.5	2.025 ± 2.5	2.032 ± 2.6	1.000 ± 2.2
(D4)South Delhi	2.0	2.035 ± 1.9	2.020 ± 2.8	2.034 ± 1.8	1.030 ± 2.6

LIGENDS:
N : Number of determinations, A_1, A_2, A_3, & A_4 : Automobile exhaust fume samples,
B_1, B_2, B_3, & B_4 : Automobile exhaust scrape samples, C_1, C_2, C_3, & C_4 : Roadside dust samples
D_1, D_2, D_3. D_4 : Vegetation samples collected from road side trees and plants present near highly polluted areas of Delhi region

V. References

[1] F. Alt and F. Zereini, Anthropogenic Platinum-Group-Element Emissions and their Impact on Man and Environment, Springer Verlag: Berlin, 1999.

[2] F. Alt, E. Helmers, H.Urban, F. Zereni and B. Skerstupp, "Geochemical behavior of platinum-group elements (PGE), in particulate emissions by autotomobile exhaut catalyst Experimental investigations", *Sci. Total Environ*, vol. 206, 1997, pp.137-146.

[3] B. Godlewska-Zylkiewicz, "Biosorption of platinum and palladium for their separation/preconcentration prior to graphite furnace atomic absorption spectrometric determination", *Spectrochim. Acta Part B: Atomic Spectro.*, vol. 58(8), Aug. 2003, pp. 1531-1540.

[4] P. S. Hooda, A. Miller and A.C. Edwards, "The distribution of automobile catalysts-cast platinum, palladium and rhodium in soils adjacent to roads and their uptake by grass", *Sci. Total Environ*, vol. 384(1-3), Oct. 2007, pp. 384-392.

[5] P. Petrova, S. Velichkov, N. Velitchkova, I. Havezov and N. Daskalova, "Problems, possibilities and limitations of inductively coupled plasma atomic emission spectrometry in the determination of platinum, palladium and rhodium in samples with different matrix composition", *Spectrochim. Acta Part B: Atomic Spectro*, vol. 65(2), Feb. 2010, pp. 130-136.

[6] C. Colombo and A. John monhemius, "Platinum, palladium and rhodium release from vehicle exhaust catalysts and road dust exposed to simulated lung fluids", *Ecotoxi. Environ. Safety*, vol. 71(3), Nov. 2008, pp. 722-730.

[7] C. Colombo, A. John monhemius and A. Plant Jane, "The estimation of the bioavailabilities of platinum, palladium and rhodium in vehicle exhaust catalysts and road dusts using a physiologically based extraction test", *Sci. Total Environ.*, vol. 389(1), Jan. 2008, pp.46-51.

[8] N. Anthemidis Aristidis, G. Themelis Demetrius and A. Stratis John, "Selective stopped-flow injection spectrophotometric determination of palladium(II) in hydrogenation and automobile exhaust gas converter catalysts", *Anal. Chim. Acta*, vol. 412(1-2), May 2000, pp. 161-167.

[9] R.K. Klaus and D. Auer, "Determination of platinum and palladium in strongly acid solution by means of flow injection analysis", *Talanta*, vol. 40(12), 1993, pp. 1975-1980.

[10] I.A. Kovalev, L.V. Bogacheva, G.I. Tsysin, A.A. Formanovsky and Yu.A. Zolotov, "FIA-FAAS system including on-line solid phase extraction for the determination of palladium, platinum and rhodium in alloys and ores", *Talanta*, vol. 52(1), May 2000, pp. 39-50.

[11] S. Woinska and B. Godlewska-Zylkiewicz, "Determination of platinum and palladium in road dust after their separation on immobilized fungus by electrothermal atomic absorption spectrometry", *Spectrochimi. Acta Part B: Atomic Spectro.*, vol. 66(7), July 2011, pp. 522-528.

[12] E. Masera, P. Mauchien and Y. Lera, "Electrothermal atomization-laser induced fluorescence determination of iridium, rhodium, palladium, platinum and gold at the ng/l level in pure water", *Spectrochim. Acta Part B: Atomic Spectro*., vol. 51(5), 1996, pp.543-548**.**

[13] J.G.M.Van Der Linden and A.H. Dix, "Electrochemical redox behaviour of dithiocarbamates and diselenocarbamates of nickel, palladium and platinum", .*Inorg. Chimi. Acta*, vol. 35, 1979, pp. 65-71.

[14] D.William, Jacobs, John and T. Pyle, "Spectrophotometric determination of palladium and platinum with dibenzyldithiooxamide", *Talanta*, vol. 9(9), Sept. 1962, pp. 761-767.

[15] Z. Marczenko and S. Kus, "Spectrophotometric determination of traces of platinum in palladium with dithizone after matrix precipitation as a compound with ammonia and iodide", *Anal. Chim. Acta*, vol. 196, 1987, pp. 317-322.

[16] Z. Marczenko, S. Kus and M. Mojski, "Extractive separation and spectrophotometric determination of palladium and platinum with dithizone in the presence of stannous chloride", *Talanta*, vol. 31(11), Nov. 1984, pp. 959-962.

[17] M. Ines Toral, P. Richter, N. Lara, M. Teresa Escudero and C. Soto, "Simultaneous Determination of Platinum and Palladium by Second Derivative Spectrophotometry Using 3-(2'-Thiazolylazo)-2, 6-Diaminopyridine as Chromophore Ligand", *Anal. Lett.*, vol. 33(1), 2000, pp. 93-109.

[18] M. Mojski and K. Kalinowski, "Extractive separation of platinum from macroamounts of palladium using triphenylphosphine oxide and its successive spectrophotometric determination by the stannous chloride method", *Microchem. J.*, vol. 25(4): 1980, pp. 507-513.

[19] E. Kavlentis, "Extractive spectrophotometric determination of palladium(II) and platinum(II) with 2-allylthiourea and thiocyanate in the presence of EDTA" , *Talanta*, vol. 44(4), 1997, pp. 571-576.

[20] E. Kavlentis, "Simultaneous extractive spectrophotometric determination of palladium(II)-platinum(II) or palladium(II)-gold(III) with benzyltriethyl-ammonium ion and iodide in the presence of EDTA", *Microchem. J.*, vol. 37(1), 1988, pp. 18-21.

[21] G.S. Manku, A.N. Bhat and B.D. Jain, "Spectrophotometric determination of osmium(IV), iridium(IV) and platinum(IV) and separation and determination of palladium(II) and ruthenium(III) in the presence of other platinum metals, with oximidobenzotetronic acid as reagent", *Talanta*, vol. 16(10), 1969, pp. 1421-1429.

[22] I. Vogel, A textbook of quantitative inorganic analysis, 5th ed., ELBS: London, 1985.

[23] L. Erdey, Gravimetric Analysis, Part II, Pergamon Press: Oxford, 1965.

[24] E. B. Sandell and O. Hiroshi, Photometric determination of traces of metals, John Wiley & Sons: New York, 1978.

[25] L.G. Sillen, "Some graphical methods for determing equilibrium constant II on Curve-fitting method for two-variables data", *Acta Chem* Scan, vol. 10, 1956, pp.186-202.

[26] P. Job, "Job plot", *Ann Chim*, vol. 9, 1928, pp. 113-203.

[27] D.D. Perin, Chemical Analysis-Masking and Demasking, vol. 33, 4th. ed. John Wiley & Sons: New York, 1999.

[28 B. S. Furniss, A. J. Hannaford, P. W. G. Smith and A. Tatchell, Vogel's textbook of Practical organic chemistry, Pearson Education: London, 2005.

[29] R. Anderson, Sample preparation and sample treatment and separation, John Wiley & Sons: New York, 1985.

[30] Ya. R. Bazel, T. A. Kulakova, Ya. I. Studenyak, R. Serbin, S. Rednik, V. Andruch, "Extraction of platinum with Astrafloxin FF from aqueous-organic solutions: Separative extraction spectrophotometric determination of platinum(II) and platinum(IV) species", *Journal of Analytical Chemistry*, vol. 67(6), 2012, pp. 519-526.

[31] J. Karthikeyan, P. Parameshwara and A. Shetty Nityananda, "Analytical properties of *p*-[*N*,*N*-bis(2-chloroethyl)amino] benzaldehyde thiosemicarbazone spectrophotometric determination of palladium(II) in alloys, catalysts, and complexes", *Environ. Mon. Assessment*, vol. 173(1-4), 2011, pp. 569-577.

VI. Acknowledgement

Authors are thankful to Delhi Technological University for providing financial assistance and laboratory facilities.

American International Journal of Research in Formal, Applied & Natural Sciences

Available online at http://www.iasir.net

ISSN (Print): 2328-3777, ISSN (Online): 2328-3785, ISSN (CD-ROM): 2328-3793

AIJRFANS is a refereed, indexed, peer-reviewed, multidisciplinary and open access journal published by International Association of Scientific Innovation and Research (IASIR), USA
(An Association Unifying the Sciences, Engineering, and Applied Research)

Spectrophotometric Determination of Trace Amounts of Samarium in Environmental Samples

Pushpa Ratre[1] and Devendra Kumar[2]
[1,2] Department of Applied Chemistry and Polymer Technology,
Delhi Technological University (Formerly Delhi College of Engineering),
Shahbad Daulatpur, Bawana Road, Delhi-10042, INDIA

Abstract: *Sm(III) forms two mixed-ligand complexes, a pink colour complex with 2-[(5-bromo-2-pyridylazo)]-5-diethyl-aminophenol (5-Br-PADAP) in the presence of p-tolunenes sulfonic acid (PTSA) at pH 7.0 and a red colour complex in the presence of triton X-100 or Polyethylene-di-isobutyl-glycol-ether (TX-100) and it is extractable with N-p-carboxyphenylbenzohydroxamic acid (PCBHA) in dichloromethane at pH 10.0. The optimum concentration ranges for the determination of Sm(III) are 0.1-3.5 and 0.05-3.0 μg mL^{-1} for the pink and red complexes, respectively. The proposed method has been successfully applied on the mafic rock reference samples, monazite sand and sea water of coastal region of Kerala in India. The average recovery of Sm(III) has been found to be 99.5 ± 0.1% with relative standard deviation (RSD) value ranging between 1.4-7.3%.*

Keywords*: Samarium (III); 5-Br-PADA; TX- 100; PTSA; N-p-carboxyphenylbenzohydroxamic acid*

I. Introduction

Rare earth elements are extremely important due to its applications in nuclear power activities, material science, catalysis, medicine, and life science. So, it is important to determine trace amounts of such element [1], [2]. These elements are widely distributed in low concentration in the Earth's crust. The vapors or dusts of these elements are highly toxic when inhaled. They tend to remain in the lungs, liver, spleen, and kidneys. Samarium is found along with other members of the rare-earth elements in many minerals, including monazite and bastnasite to the extent of 2.8% [3]. Samarium is used as a gasoline cracking catalyst and a polishing compound, as well as in the iron and steel industries to remove sulfur, carbon, or other electronegative elements[4].

Samarium is mainly used in drugs, electronic, glass, laser, electrical, nuclear and ceramics industries. Samarium is generally used in such applications as neutron absorber in nuclear reactors, quadramet (Sm 153 lexidronam) in the manufacture of drugs, doping calcium fluoride crystals in optical masers or lasers, carbon arc lighting in motion picture industry, etc. The oxide of samarium exhibits catalytic properties in the dehydration and dehydrogenation of ethyl alcohol [5]. $SmCo_5$ has been used in making new permanent magnet materials with the highest resistance to demagnetization of any known material[6]. These uses illustrate the importance of samarium and its compounds in the geological matrices.

In the proposed method, Samarium forms stable chelates with 2-[(5-bromo-2-pyridylazo)]-5-diethylaminophenol (5-Br-PADAP) [7]-[9] due to presence of the $–N-(CH_3)_2$ and halogen group in the presence of surfactant triton X-100 (TX-100) [10] and *p*-tolunenes sulfonic acid (PTSA) [11]. Hydroxamic acid and their derivatives are weak organic acids and have low toxicity. It has wide applications in quantitative determination of metal ions in the environment, organic, inorganic and pharmaceutical analysis [12], [13]. N-*p*-carboxyphenylbenzo-hydroxamic acid (PCBHA) has various applications in the field of pharmacology, toxicology and pathological areas [14]. This reagent is successfully utilized for the quantitative analysis of samarium ions in monazite sand and sea-water samples.

The spectrophotometric method is the most popular and cheaper technique for the quantative determination of lanthanide metal ions. A survey of literature reveals that various reagents have been employed for the determination of samarium (III). Soylak et al. [15] used a chrome azurol reagent under borax buffer of pH 7.5

and his method was sensitive but suffered from interferences of metal ions. Mathew et al. [16] and Dey et al. [17] developed a method with low molar absorbtivity, using a reagent 1-(2-pyridylazo)-2-naphthol (PAN) in presence of the surfactant. Gadzhieva et al. [18] developed a less sensitive method, using a 2-(2-hydroxy-3-sulfo-5-nitrophenylazo)-naphthalene-1,8-dihydroxy-3,6-disulfonate in the presence of surfactant. Dik et al. [19] developed a less sensitive method in hydrochloric Acid Solution. Agrawal et al. [20] developed a method in narrow pH range, using a N-phenylbenzohydroxamic acid and xylenol orange as reagent for the separation of lanthanoid element. Alaa et al. [21] developed a method with low sensitivity, using a pyrimidine azo derivatives in micelar medium. Mohamed et al. [22] developed a less sensitive method, using a 8-hydroxyquinoline-5-sulfonic acid as reagent which suffered from interference of rare-earth element. Shah et al. [23] developed a method with low molar absorbtivity, using a 4,5,dihydroxy-3-phenylazo-2,7-naphthalene disulphonic acid, disodium salt as reagent at narrow pH range.

Lanthanide elements being hard bases tend to form chemical bonds with atoms belonging to the hard acid group. For example, oxygen and lanthanide element tend to form Ln-O bonds. The most common coordination number of lanthanide complex is 8 or 9 due to their large ionic radius [24]. Samarium (III) ions form covalent polar bond with ligands having oxygen donor atoms such as 5-Br-PADAP, TX-100, PTSA and PCBHA reagents.

II. Experimental

A. Material and Methods

All chemicals used were procured from Central Drug House and Sigma Aldich. Millipore double distilled water was used for the preparation of all solutions.

a. Preparation of Substituted Hydroxamic Acid

PCBHA was synthesized by the reaction of equimolar concentration of *N*-p-carboxyphenylhydroxylamine and *N*-phenylbenzanilide and crystallizing it in absolute alcohol as reported in the literature [25].

A 4.7×10^{-3} mol L^{-1} (0.1%, w/v) solution of PCBHA were prepared in dichloromethane and employed for extraction of Sm(III)-5-Br-PADAP-TX-100 complex. The stock solutions 6.62×10^{-3} mol L^{-1} of rare earth ions was prepared in concentrated HCl and HNO_3 acids (1:1), respectively. The solutions were heated on a sand bath until the oxides was completely dissolved and diluted with water to the mark in volumetric flasks. The above stock solution was standardized by complexometric method of EDTA [26]. A 8.6×10^{-4} mol L^{-1} (0.03%, w/v) solution of 5-Br-PADAP in 95.0% ethanol was employed for color development. An aqueous solution of 1.54×10^{-3} mol L^{-1} (0.1%, w/v) of TX-100 and 5.14×10^{-2} mol L^{-1} (1%, w/v) solution of PTSA were used. Ammonia buffer solution of pH 8.0 to 14.0 were prepared by mixing a appropriate volume of NH_4Cl and NH_4OH in 100 ml volumetric flask and Phosphate buffer solution were also prepared by mixing a appropriate volume of 0.1m HCl or 0.1m NaOH into 0.1m disodium hydrogen phosphate and calibrated with digital pH meter (DB-1011) [26].

B. Apparatus

The absorption spectra of the solutions were recorded on double beam UV-Visible spectrophotometer 54440SS model in the range 300–800 nm using 10 mm quartz cell. A digital pH meter (DB-1011) was calibrated regularly with standard buffer solution of acid and base before use.

C. General Procedure

The pink colored Sm(III)-(PTSA)-(5-Br-PADAP) aqueous complex were prepared by standard solution containing (10-35) μg solution of Sm(III) was transferred into 10.0 ml volumetric flask. To the above solution, mix 1.0 mL (1%, PTSA) and 1.0 mL ethanolic solution of (0.03%, 5-Br-PADAP), solution and diluted to final volume upto 10.0 mL with phosphate buffer pH 7.0±0.2 solution and measured absorbance at 565.5 nm against the solvent in which it was prepared.

The red color Sm(III)-(TX-100)-(5-Br-PADAP) aqueous complex were prepared by standard solution containing (5.0-30) μg solution of Sm(III) was transferred into separtory funnel. Mix 0.5 mL (0.1%, TX-100) and 1.0 mL ethanolic solution of (0.03%, 5-Br-PADAP) solution and diluted to final volume upto 10.0 mL with ammonia buffer pH 10.0±0.2 solution then shaken it vigorously for 1 min with 5.0 mL of PCBHA solution in dichloromethane thereafter washed with 2×2 ml fresh dichloromethane. All extracts after drying over anhydrous sodium sulfate (≈2 gm) were transferred to a 10.0 mL volumetric flask and then made up to the mark with

dichloromethane. The absorbance of the complex was finally measured at 590 nm against the solvent in which it was prepared.

D. Sample Preparation and Sampling Method

a. Digestion of Monazite Sand Sample

A 2.0 g sample of monazite sand was dissolved in the ratio of 3:1:3 mL of HF, HCl, and HNO_3 in a glassy-carbon dish. The paste obtained was treated with 8.0 mL of HNO_3 at 50–60°C to the point of complete distillation of HF. The residue obtained was dissolved in water and transferred to a 100 mL volumetric flask; the solution was diluted to the mark with water. Take a portion of above samples and follow the above Procedure.

b. United State Geological Survey Mafic Rock Reference Samples (USGS)

The synthetic samples were prepared as per compositions of USGS mafic rock reference samples.

c. Sea Water Sample

The monazite sand and sea-water samples were collected from different site of coastal region of Kasargod and Mangalore of Kerala in summer season on the dated 16 April 2013 and 11 June 2013, respectively from India. The sea-water samples were filtered with a membrane filter (pore size 0.45 mm, Millipore) to remove dirt, sand and suspended matter. Take an aliquot of sea water sample, then put into ultrasonicater and leave it for 1h at 60°C, then follow the above procedure.

III. Results and Discussion

A. Absorption spectra

Effect of various surfactants and salt on the absorbance of Sm(III) complex was investigated at wavelength of (200-800) nm. Other surfactant such as Brij-35, cetylpyridinium chloride, sodium dodecyl sulfate, Tween-20 were tried, but it turbid the aqueous complex in the pH range of ammonia buffer solution of 8.0-11.0 and 6.0-8.0 of phosphate buffer.

The pink colored Sm(III)-PTSA-5-Br-PADAP aqueous complex and red coloured Sm(III)-TX-100-5-Br-PADAP-PCBHA organic complex show maximum absorbance at 565.5 nm and 590 nm, respectively with their corresponding blank and solvent and the same is discussed and shown in Table 1 and Fig. 1, respectively.

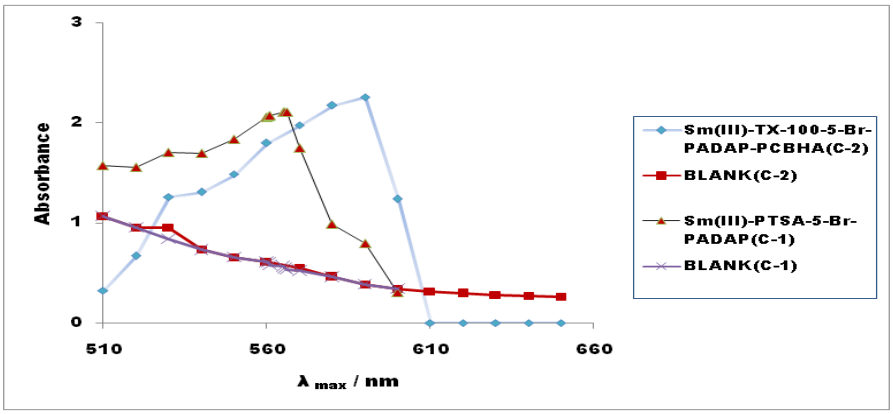

Figure 1 Absorption spectra of complex of Sm(III)-complex in aqueous(C-1) pH [7.0] and organic phase(C-2) pH [10], Sm(III) [7.2×10^{-6} mol L^{-1}]; PTSA [2.57×10^{-3} mol L^{-1}],TX-100 [1.5×10^{-4} mol L^{-1}]; 5-Br-PADAP [8.6×10^{-5} mol L^{-1}]; PCBHA [2.34×10^{-3} mol L^{-1}]

B. Choice of Extraction Solvent

The samarium (III) complex was extractable with many organic solvents such as chloroform, dichloromethane, toluene, benzene, n-butyl alcohol etc. Satisfactory results were obtained only with chloroform and dichloromethane. With other solvents, the molar absorptivity was found to be decreased i.e. $0.95\text{-}4.0\times10^{4}$ L mol^{-1} cm^{-1}. Since dichloromethane is less toxic than the chloroform. So it was chosen as solvent for extraction of Sm(III)-complex.

C. Effect of pH

The effect of different buffer solution on the formation of Sm(III)-PTSA-5-Br-PADAP aqueous complex and Sm(III)-TX-100-5-Br-PADAP-PCBHA organic complex was examined at 565.5 nm and 590.0 nm using buffer solutions of different pH i.e. 8.0-15.0 of ammonia buffer and phosphate buffer of 6.0-11.0. The best results were obtained between 10.0-14.0 pH of ammonia buffer and 7.0-8.5 pH of phosphate buffer as shown in Fig. 2. Moreover, other buffers of citrate, acetate and borax were also tried but satisfactorily result were not obtained.

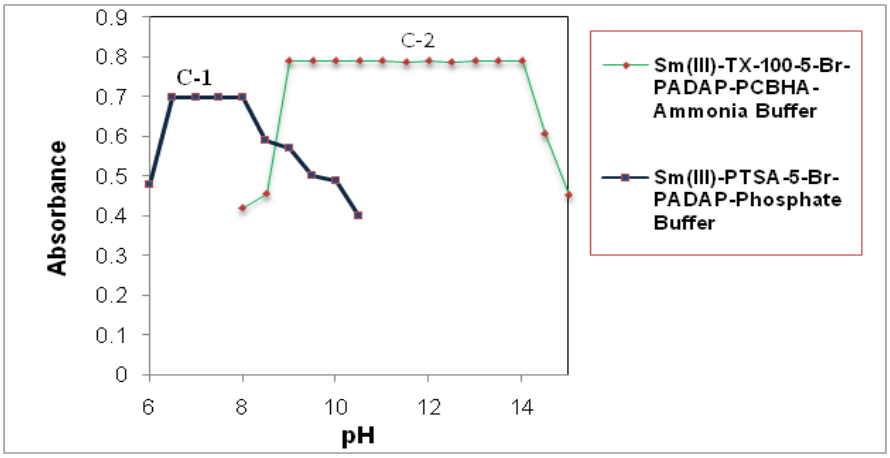

Figure 2 Effect of pH on the formation of Sm(III)-complex. C-1(Phosphate buffer) and C-2(Ammonia buffer), Sm(III) [2.86×10^{-6} mol L^{-1}]; PTSA [2.57×10^{-3} mol L^{-1}], TX-100 [1.5×10^{-4} mol L^{-1}]; 5-Br-PADAP [8.6×10^{-5} mol L^{-1}]; PCBHA [2.34×10^{-3} mol L^{-1}]

D. Effects of Reagents

For maximum color development of Sm(III)-(PTSA)-5-Br-PADAP aqueous complex, optimum concentration range of the various reagents are as follows: A (1.71-4.29) $\times 10^{-5}$ mol L^{-1} of 5-Br-PADAP in ethanol, (2.57-5.14) $\times10^{-3}$ mol L^{-1} aqueous solution of PTSA in distilled water. The Sm(III)-(TX-100)-5-Br-PADAP-PCBHA complex showed maximum color development in the concentration range of (7.6-10.0) $\times 10^{-5}$ mol L^{-1} of 5-Br-PADAP in ethanol and (1.4-3.0)$\times 10^{-4}$ mol L^{-1} aqueous solution of TX-100 and (2.1-2.6) $\times10^{-3}$ mol L^{-1} of PCBHA in dichloromethane.

E. Effect of Temeperature, Stability, Electrolyte and Dilution

The study on the variation of temperature for the formation of metal complexes showed no change in the absorbance of the Sm(III) complexes between 10 to 50ºC. Beyond this temperature, the absorbance of the complexes decreased. Hence, all extraction work was carried out at 30ºC. It was observed that the colour of the complexes were stable for 24h.

About 1.5 mol L^{-1} concentrations of KCl/ K_2SO_4 /NH_4Cl did not affect the absorbance and λ_{max} of the complex. The effect of variation in the volume of the aqueous phase, on the formation of the metal complexes was studied. No change in the absorbance and λ_{max} of the complex was observed while varying the volume ratio of the organic to aqueous phase from 2:1 to 1:5. Hence 1:1 organic solution was chosen for the entire work.

F. Composition of the Complexes

The composition of the mixed-ligand complexes of samarium were determined by the curve fitting methods as described in Sillen [27] and Job's continuous variation method [28]. A graph was plotted between log D (distribution ratio) of metal and [ligands]. The stoichiometric ratio of the metal to ligand in the complex was established to be 1:1:1 for [Sm(III): PTSA: 5-Br-PADAP] in aqueous phase.

The stoichiometric ratio of the metal to ligand in the organic complex was established to be 1:2:2:2 for [Sm(III): TX-100: 5-Br-PADAP: PCBHA] (Fig. 3).

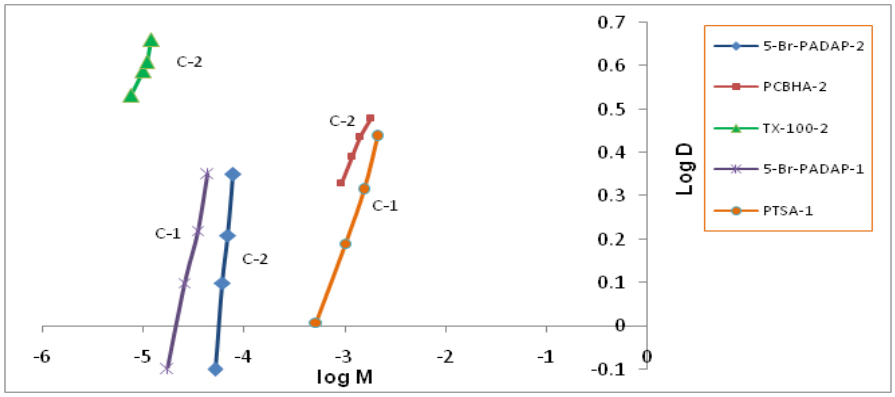

Figure 3 Curve fitting method for the determination of Sm(III) to PTSA/5-Br-PADAP(1:1:1) and 5-Br-PADAP/TX-100/ PCBHA(1:2:2:2) complex in dichloromethane.

The probable reaction mechanism is given below: (i)

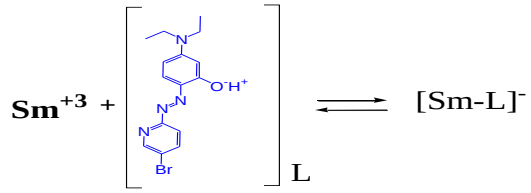

2- (5-Bromo-2-Pyridylazo) -5-Diethylaminophenol

$$[Sm\text{-}L]^- + [CH_3C_6H_4SO_3H]^+ \rightleftharpoons [Sm\text{-}L]^-[CH_3C_6H_4SO_3H]^+$$

p-Tolunenes sulfonic acid

(ii) $[Sm\text{-}(5\text{-}Br\text{-}PADAP)_2]^-$ + 2[TX-100] + 2$[PCBHA]^+$ ⇔ $\{[(TX\text{-}100)_2\ Sm(5\text{-}Br\text{-}PADAP)_2\ .(PCBHA)_2]Cl\}_0$ Subscript "0" here describes the organic phase.

G. Analytical Parameters

The Sm(III)-(PTSA)-(5-Br-PADAP) and Sm(III)-(TX-100)-(5-Br-PADAP)-PCBHA complex follow Beer's law up to (0.1-3.5) µg mL^{-1} in aqueous phase and (0.05-3.0) µg mL^{-1} in organic phase, respectively. The slope, intercept and correlation coefficient, detection limit of the method at (2σ) and sandall's sensitivity of Sm(III)-complex are calculated for the complexes and the same are listed in Table I. The precision of the method in terms of the relative standard deviation (n=10) for the determination of 2.5µg Sm(III) is ±0.052%.

Table I Spectrophotometric characteristics of Sm(III)-complex. Sm(III) [7.2×10^{-6} mol L^{-1}] ; TX-100 [1.5×10^{-4} mol L^{-1}]; PTSA [2.57×10^{-3} mol L^{-1}], 5-Br-PADAP [8.6×10^{-5} mol L^{-1}]; PCBHA [2.34×10^{-3} mol L^{-1}].

Sm(III)-complex	λ_{max}, nm	(ε), L mol^{-1} cm^{-1}	Beer's law, µg/mL	Detection limit ng/mL	Sandell's sensitivity (ng/cm^2)	Intercept / slope / correlation coefficient
Sm(III)-TX-100-5-Br-PADAP-PCBHA-Dichloromethane pH 10±0.2	590.0	1.42×10^5	0.05-3.0	21.0	10.50	0.094 /0.0006 / ±0.996
Sm(III)-PTSA-5-Br-PADAP (Aqueous complex) pH 7.0±0.2	565.5	1.27×10^5	0.1- 3.5	11.0	5.78	0.82/ 0.005 / ± 0.995

H. Effect of Foreign Ion

The variable amounts of foreign ions were introduced into a [7.2×10^{-6} mol L^{-1}] of Sm(III) complex. If there is some small change in the absorbance, then ± 2% tolerance limit for the ions can be considered. The methods are free from the interference of alkaline and alkaline earth metal and lanthanide group of metal ions. However, some transition metal ions such as Co(II), Ni(II), Cu(II), Pd(II) and Ru(III) were found to interfere with complexes which were effectively masked by the addition of EDTA prior to extraction and the same is shown in Table II.

Table II Tolerance limit (TL) of diverse ion in the determination of [7.2×10^{-6} mol L^{-1}] Sm(III)-complexes

Ions added	TL, mg 10 mL^{-1} aqueous phase[1]	TL, mg 10 mL^{-1} organic phase[2]	Relative error, %
Ru(III)	0.1**	0.25**	0.4
Co(II) ,Cu(II)	0.2*	0.34*	-1.9
Rh(III)	0.3	0.45	-1.2
Ni(II)	0.4*	0.6*	-0.9
Pd(II)	0.4**	0.2**	0.6
Th(IV)	0.5	0.25	-1.7
Pt(IV), Ce(IV), U(VI), Eu(III), Gd(III), Nd(III), Y(III), Yb(III), Fe(III)	0.6	0.55	-1.9-1.2
Mn(II)	0.07	0.14	1.2
V(V), Pr(III)	0.20	0.50	1.3
Nb(V), Ho(III),Tb(III),Tm(III)	0.50	0.10	-1.2
Bi(III), La(III)	0.60	0.50	0.9
Os(VIII)	0.80	0.60	1.1
Zr(IV)	1.25	2.0	1.5
Pb(II)	2.0	3.0	0.3
Zn(II)	20	60	1.4
Hg(II)	50	70	0.5
Ca(II)	80	100	-1.2
Mg(II), Cd(II)	100	100	-1.5
Phosphate	1.0	3.0	0.9
KSCN	10	20	0.3
Citrate	20	40	-1.3.
Oxalate	50	100	1.1
Bromide, Tartrate	160	170	-1.5
EDTA	1000	1000	0.9

1-Sm(III)-PTSA-5-Br-PADAP (Aqueous medium at pH [7.0±0.2]
2-Sm(III)-TX-100-5-Br-PADAP-PCBHA (Organic medium at pH[10.0±0.2]
*** Removed by 0.4 ml of 0.58% EDTA**
**** Masked with 1 ml, 1% aqueous SCN^- solution.**
Foreign ions interfere when they cause a change in the absorbance of the Sm(III)- complex by ≥ ± 2%.

I. Comparison with other methods

The analytical characteristics of some important spectrophotometric methods reported for the determination of Sm(III) reveal the superior part of the present method in terms of sensitivity and selectivity for the detection owing to the negligible interference from the lanthanide ions as listed in Table III.

J. Application of the methods

The methods are successfully applied on USGS mafic rock synthetic samples [29], monazite sand and sea water samples collected from costal region of Kerala in India. The validity of the methods were tested by using a reported method of Soylak et al. [15]. The average concentration of Sm(III) in different sites of costal region of Kerala state of India were found between 0.5 to 6.0 ppm with RSD value ranging between 1.9-2.8%. The average

recovery of Sm(III) were calculated to be 99.5 ± 0.1% with RSD value ranging between 1.4-7.3% as listed in Table IV and V.

IV. Conclusion

In the proposed method, a highly sensitive and selective spectrophotometric method is developed for the determination of trace amounts of Sm(III) in monazite sand and sea water in costal region of Kerala state of India, and in synthetically synthezied standared geological matrices samples. The surfactant, *p*-tolunenes sulfonic acid (PTSA) and triton-X-100 (TX-100) were used to increase the solubility and decrease the time of colour development of the complexes of samarium. An extacting agent N-*p*-carboxyphenylbenzohydroxamic acid (PCPBDA) are used due to its high organophilic character, having wide flexibility for the introduction of substituents, and widened acidity range for the formation of metal complexes. The applied methods are free from the interference of the lanthanoid group elements.

V. Acknowledgment

The authors are thankful to Delhi Technological University for providing financial assistence and Lab facilities.

Table III Comparative study of analytical potential of samarium(III) method.

Reagents	**Solvent/Acidity range**	**ϵ/L mol^{-1}cm^{-1} $\lambda_{max,}$ nm / Beer's law(µg/ml)**	**M:L**	**Remark**	**Ref**
Chrome azurols + Cetylpyridinium chloride	Aq / Borax buffer-pH, 7.5	1.4×10^5 / 505 / 0.05-2.0	NG	NPHR / II-Cr^{+3}, Fe^{+3} and Bi^{+3} etc	15
1-(2-pyridylazo)-2-naphthol+ cetyltrimethyl ammonium Bromide, TritonX-100, sodium dodecyl sulphate	Aq / Borax buffer-pH, 6.0-8.0 and ammonical buffer-pH, 8.0-10.0	5.8×10^4, 7.4×10^4, 5.7×10^4 / 545, 535, 540 / 1×10^{-6} - 3×10^{-5} mol L^{-1}	1:3	NPHR / Fe^{+3}, Cu^{+2}, Cd^{+2}, Ni^{+2}, Zn^{+2} and U^{+4} etc	16
Disodium 2-(2-Hydroxy-3-sulfonic-5-Nitrophenylazo) naphthalene-1,8-Dihydroxy-3,6-Disulfonate + CTMA	Aq / pH, 6.0	4.74×10^{-3} / 529 / 1.20-9.60	1:1:1	NPHR / II-Ca^{+2}, Cu^{+2} , Al^{+3} Zr^{+4}, Th^{+4}, Na_2HPO_4 · $12H_2O$, F^{-1} etc	18
N-phenylbenzohydroxamic acid +Xylenol orange	$CHCl_3$/ pH, 10.0	9.3×10^4 / 600 / 0.008-3.22	1:2:1	NPHR / II- Y^{+3}	20
Pyrimidine azo derivatives (Ra, Rb and Rc)+ CTMA or -CTMA	$CHCl_3$/ pH, 7.2, 7.7, 8.2	$(8.8\text{-}9.8)\times10^3$ and $3.16\text{-}3.40\times10^3$ / 595, 625, and 613 / (- CTMA)- 1.0–8.7, 1.3–9.4 and 1.2–8.1, (+CTMA) 0.5–3.9, 0.7–4.2 and 0.6–4.1	+ CTMA, 1:1 -CTMA, 1:2	NPHR / II-Cu^{+2} Zr^{+4}, Th^{+4}, Na_2HPO_4· $12H_2O$, F^{-1} etc	21
8-Hydroxyquinoline-5-sulfonic Acid	Aq / pH, 7.0	2.5×10^{-3} / 410 / 10- 100	1:1	NPHR / II- foreign ions interfere	22
4,5,Dihydroxy-3-phenylazo-2,7-naphthalenedisulphonic acid, disodium salt (Chromotrope 2R)	Aq / pH, 6.0-9.0	6.01×10^2 / 550 / NG	1:1	NG	23
(1) *p*-Tolunenes sulfonic acid + 5-Br-PADAP (2)TX-100 + 5-Br-PADAP+ N-*p*-carboxyphenylbenzohydroxamic acid	DCM / phosphate Buffer-pH=6.0-8.0. Ammonia Buffer pH= 8.0-11.0	Aq-1.27×10^5 at 565.5 / 0.1-3.5 Og-1.42×10^5at 590.0 / 0.05-3.0	1:1:1 and 1:2:2:2	II-Co^{+2}, Ni^{+2}, Cu^{+2}, Pd^{+2} and Ru^{+3} etc	PM

LIGENDS:

Aq : Aqueous solution, NG : Not Given, DCM : Dichloromethane, Ra : 5-(20-bromophenylazo)-6-hydroxy pyrimidine-2,4-dione, Rb : 5-(40-chlorophenylazo)-6-hydroxypyrimidine-2,4-dione, Rc : 5-(20,40-dimethylphenylazo)-6-hydroxypyrimidine-2,4-dione, -CTMA : Absence of cetyltrimethyl ammonium Bromide , +CTMA : Presence of cetyltrimethyl ammonium Bromide , 5-Br-PADAP : 2-[(5-bromo-2-pyridylazo)]-5-diethylaminophenol, (M:L) : (Metal: Ligand), NPHR : Narrow pH range, II : Ions interference, PM : Present method.

Table IV Concentration of samarium (III) in environmental samples using standared addition method.

S. No.	Sample	Sm (III) found by						
		present method [M^1] [ppm]			present method[M^2] [ppm]		Soylak et al.[15] Reported method [ppm]	
		Added	Actual[M^1]	M^1 [ppm ± RSD^a%]	Actual	[ppm ±RSD^a%]	Actual	[ppm ± RSD ^{a}%]
1.	**MS-1**	2.0	0.612	2.612 ± 2.6	0.613	2.613 ± 5.0	0.610	2.610 ± 5.2
2.	**MS-2**	2.0	5.410	7.410 ± 2.8	5.410	7.420 ± 1.0	5.400	7.400 ± 1.2
3.	**SW-1**	2.0	0.981	2.981 ± 2.0	0.984	2.984 ± 3.0	0.982	2.982 ± 5.3
4.	**SW-2**	2.0	1.200	3.200 ± 4.2	1.216	3.216 ± 1.1	1.212	3.212 ± 3.0

LIGENDS:
a : Five determination were made
MS-1 : 2Monozite sand samples from Kasargod from sea beaches of Kerala.
MS-2 : Monozite sand samples from Mangalore from sea beaches of Kerala.
SW-1 : Sea water samples from Kasargod from sea beaches of Kerala.
SW-2 : Sea water samples from Mangalore from sea beaches of Kerala.
M^1 : Sm(III)-PTSA-5-Br-PADAP complex (Method)
M^2 : Sm(III)-TX-100-5-Br-PADAP-PCBHA complex (Method)

Table V Concentration of samarium (III) in synthetic samples.

Samples	Synthetic composition of USGS mafic rock references samples (ppm)	M^1 [ppm ± RSD^a%]	M^2[ppm ± RSD^a%]
[W-2]	Nb, 5.0; Ni, 52.7; Mo, 2.7; Pb, 5.78; Zr, 75.5; Th, 1.82; U, 0.37; W, 0.196; V, 195.0; **Sm, 2.5**	2.47 ± 2.3	2.50 ± 2.6
[DNC-1]	Nb, 5.65; Ni, 437.9; Mo, 0.35; Pb, 9.23; Zr, 68.26; Th, 0.39; U, 0.17; W, 0.33; V, 147.5; **Sm; 2.5**	2.48 ± 2.5	2.50 ± 2.8
[BIR-1]	Nb, 5.59; Ni, 411.88; Mo, 6.68, Pb, 7.77; Zr, 45.54; Th, 0.24; W, 0.544; U, 0.247; W, 0.196; V, 777.7; **Sm, 2.5**	2.50 ± 1.9	2.50 ± 2.0

LIGENDS:
a : Five number of determinations
W-2, DNC-1, BIR-1 : Different composition of USGS Mafic Rock Samples
M^1 : Sm(III)-PTSA-5-Br-PADAP complex (Method)
M^2 : Sm(III)-TX-100-5-Br-PADAP-PCBHA complex (Method)

VI. References

[1] P. Hendersona, General Geochemical Properties and Abundances of the Rare Earth Elements, Amsterdam, Elsevier, 1984.
[2] C.P. Marshal and R W Fairbridge, Encyclopedia of Geochemistry, Kluwer Academic Publisher, Dordrecht. Boston, 1999.
[3] R. E. Kirk and D. F. Othmer, Encyclopedia of Chemical Technology, vol. 19, 1982, NewYork: Wiley, pp. 836-851.
[4] J. Emsley, Samarium, "Nature's Building Blocks: An A-Z Guide to the Elements", Oxford University Press, Oxford, England. UK, 2001.
[5] L. W. Fine and H. Beall, Chemistry for Engineers and Scientists. Philadelphia:Saunders, 1990.
[6] A. S. Kim, F. E. Camp and E. J. Dulis, IEEE Trans. Magnetics, vol. 26, 1990, pp.1936.
[7] C. R. Hammond, "The Elements, in Handbook of Chemistry and Physics", 81st ed, CRC press, 2004.
[8] S. Biswas, P. N. Pathak and S. B. Roy, "Development of an extractive spectrophotometric method for estimation of uranium in ore leach solutions using 2-ethylhexyl phosphonic acid-mono-2-ethylhexyl ester (PC88A) and tri-n-octyl phosphine oxide (TOPO) mixture as extractant and 2-(5-bromo-2-pyridylozo)-5-diethyl aminophenol (Br-PADAP) as chromophore", *Spectrochim Acta A Mol Biomol Spectrosc*., vol. 91, 2012, pp. 222-227.
[9] R. Salim and B. Shraydeh, "Spectrophotometric determination of cadmium(ll) using 2-(5bromo-2-pyridylazo)-5-diethylaminophenol", *Microchem. J.*, vol. 34, 1986, pp. 251-253.
[10] N.M. Modawe and M.A.Z.E. Hayeb, "H-Point standared addition method for simultaneous spectrophotometric determination of cobalt(II), nickel (II)", *Adv. Ana. Chem.*,vol. 3(1), 2013, pp.1-7.
[11] S. Padmanabha and V. Suryanarayana Rao, "spectrophotometric determination of trace copper in industrial waste after preconcentration with 4-Hydroxybenzaldeyde thiosemicarbazone in presence of micellar medium", *Water res. Develop.*, vol-1(2), 2011, pp. 63-66.

[12] Y. K. Agrawal, S. K. Menon and K. R. Patel, "Extraction and micro-determination of vanadium(V) in the environment with α-phenylstyrylacrylosubstituted hydroxamic acid and Aliquat 336 and inductively coupled plasma atomic emission spectrometry", *Microchim. Acta*, vol. 130, 1999, pp. 219-224.

[13] H. Jahangirian, J. Haron, S. Silong, N. A. Yusof, K. Shameli, S. Eissazadeh, R. R. Moghaddam, B. Mahdavi and M. Jafarzade, "Antibacterial effect of phenyl fatty hydroxamic acids synthesized from canola oil", *J. Medi. Plants Res.*, vol. 5(19), Sept. 2011, pp. 4826-4831.

[14] J. Jiang, A. T. Sahu, V. krchnak, A. jedinak, G. E. Sandusky, D. Sliva, "NAHA, a Noval Hydroxamic acid Derivatives, Inhibit growth and Angiogenesis of Breast cancer in vitro and in vivo", Mar 2012, pp. 29-31.

[15] M. Soylak and T. Orhan, "Spectrophotometric determination of samarium(III) with chrome azurol S in the presence of cetylpyridinium chloride", *Talanta*, vol. 53, Mar. 2000, pp. 125-129.

[16] A. V. Mathew, K. Kumar, I. M. Rao, "A. Satyanarayana and P. Shyamala, Spectrophotometric determination of neodymium(III), samarium(III) in micellar medium – An alternative to solvent extraction procedures", *Ind. J. chem. Techno.*, vol. 19, Sept. 2012, pp. 331-336.

[17] A .K. Dey and N. K. Munshi, "Spectrophotometric determination of lanthanides using 4-(2-Pyridylazo) resorcinol", *Microchim. Acta*, vol. 59, 1971, pp. 751-756.

[18] S. R. Gadzhieva, F. M. Chyragov and F. E. Guseinov, "Spectrophotometric study of the complexation of samarium(III) with disodium 2-(2-hydroxy-3-sulfo-5-nitrophenylazo)naphthalene-1,8-dihydroxy-3,6-disulfonate in the presence of cetyltrimethylammonium bromide", *J. Anal. Chem.*, vol. 60, Nov. 2005, pp. 819-821.

[19] T. A. Dik, N. N. Kostyuk and A. G. Trebnikov, "Spectrophotometric determination of Sm(III) content in hydrochloric acid solution", *J. Appl. Spectro.*, vol. 70, 2003, pp. 729-732.

[20] Y. K. Agrawal and P. T. Thomaskutty, "Separation and microdetermination of rare earth metals with N-phenylbenzohydroxamic acid and xylenol orange", *J. Radioanal. Nu. Chem.*, vol. 116, April 1987, 365-374.

[21] S. Alaa and A. S. Ibrahim, "Complexation and spectrophotometric study of samarium(III) using pyrimidine azo derivatives in the presence of cetyltrimethyl ammonium bromide", *Anal. Lett.*, vol. 43, Dec. 2010, pp. 2598-2608.

[22] Mohamed, M. T. Hafezand and M. Zaki, "Application of 8-hydroxyquinoline sulfonic Acid in the spectrophotometric determination of Some lanthanides", *Microchem. J.*, vol. 34, May 1986, 258-261.

[23] V. L. Shah and S. P. Sancal, "A spectrophotometric study of the chelates of chromotrope 2R with praseodymium, neodymium, samarium and europium", "*Microchem. j.*, vol. 14, Nov. 1969, pp. 261-270.

[24] C-H Huang, Rare Earths Coordination Chemistry-Fundamentals and Applications, Wiley-Blackwell, Oxford, 2010.

[25] H. Agarwal, O.P. Agarwal, R. Karnawat, I.K. Sharma and P.S. Verma, "Synthesis, characterisation and biocidal studies of some hydroxamic acids", *The Inter. J. of Appl. Bio. and Pharma. Techn.*, vol. I (3), Dec. 2010, 1293-1299.

[26] T. S. West, Complexometry with EDTA and Related Reagents, 3rd ed.**,** Broglia Press, London, 1969.

[27] L.G. Sillen, Some graphical methods for determining equilibrium constant II. On " curve-fitting" methods for two-variable data', *Acta Chem Scan*, vol. 10, 1956,186-202.

[28] P. Job, "Job plot", *Ann Chim*, vol. 9, 1928, pp. 113-203.

[29] F. J. Flanagan, United State of Geological Survey Bulletin 1623, Three USGS Mafic Rock Reference Samples, W-2, DNC-1, and BIR-1, US: Library of Congress Cataloging in Publication Data, 1976.

J. Mater. Environ. Sci. 4 (6) (2013) 828-831
ISSN : 2028-2508
CODEN: JMESCN

Synthesis of Chain Extended Lactic Acid/Polypropylene Glycol Co-polymer

Vimal Kumar, Anshu Dev, A.P. Gupta*
Department of Applied Chemistry and Polymer Technology,
Delhi College of Engineering, Faculty of Technology,
University of Delhi, New Delhi 110042

Received 2012, Revised 4 July 2013, Accepted 4 July 2013
* Corresponding Author: email: vimalkumar.7@gmail.com

Abstract
The synthesis of high-molecular-weight lactic acid based polymers by chain extension polymerization was investigated. A hydroxyl terminated telechelic prepolymer was synthesized and then it was chain extended to the high molecular weight polymer. All polymerizations were carried out in the melt, using tin octoate as catalyst. The products were characterized by titrametric methods, Dynamic mechanical analysis (DMA), FTIR and Viscometry. An increase in the molecular weight as well as storage modulus along with glass transition temperature (Tg) was observed.

Keywords: Lactic acid, Chain extended polymer, Dynamic mechanical analysis

Introduction
With growing environmental awareness, ecological concerns and new legislations, fully biodegradable materials, biocomposited [1] [2], and nanocomposites[3] of biodegradable materials are of prime interest. However fully biodegradable materials Lactic acid is an attractive monomer in the synthesis of biodegradable polymers, being obtained from renewable resource. In last few decades lactic acid have been studied extensively for a number of applications [4-6]. To have good mechanical strength PLA should possess higher molecular[7]. Direct polycondensation of lactic acid is a low cost process to produce PLA; however it does not give high-molecular-weight polymer because of difficulty of removal of water from the polymerization reaction[8]. Furthermore, during the polycondensation, the molecular weight of poly(lactic acid) is reduced by depolymerization and other side reactions at higher temperature where the lactide is formed. High molecular weight Poly(lactic acid) can also be produced by the ring opening polymerization of lactide, which is the dilactone of lactic acid [9-11] and synthesized from thermal cracking of low molecular weight PLA at higher temperature and low pressure. This process requires high energy and time. Chain coupling of low molecular weight PLA is a better alternative to obtained high molecular weight polymer [12-14]. In the present work, initially the lactic acid was condensation-polymerized to a low-molecular-weight prepolymer, which contains one kind of end group. In the second step, the molecular weight is raised by joining prepolymer chains together using difunctional substances, such as diisocyanates, as the chain extenders [14-16]. Resulting polymer was investigated by using various techniques.

Experimental
Material
Lactic acid was purchased from Merck 90% aqueous solution, ethylene glycol from Thomas Baker, tin octoate from Sigma Aldrich, chloroform from Thomas Baker was distilled over calcium chloride before used and MDI from BASF Chemicals was used as received.

Characterization
Viscosity of the polymers were determined using Ubbelohde viscometer using 2% solution in chloroform on thermostatically controlled water bath with accuracy of $\pm 0.1^{o}$ C
Dynamic mechanical analysis (DMA) was performed at Perkin Elmer DMA 8000 in single cantilever mode at 1 Hz of frequency and displacement of 0.05 mm at heating rate of 2^{o}K/min.
FTIR was performed on Nicolet 380 Attenuated Total Reflectance-Fourier transform infrared (ATR-FTIR) in reflectance mode using polymer bar.

Synthesis of Hydroxyl terminated poly (lactic acid) (PLAol)
Polymerization was carried out in 150 ml round bottom flask with stirrer and thermostatic controller oil bath. Water was removed from the lactic acid aqueous solution at 100^{o} C under reduced pressure for 2 hrs (Fig. 1). Lactic acid based telechelic prepolymer was synthesized using ethylene glycol as diol and tin octoate as catalyst at 200^{O} C under the continuous flow of nitrogen for 48 hrs. The hydroxyl value of the resulting polymer was determined as 4 by titrimetric method [17, 18].

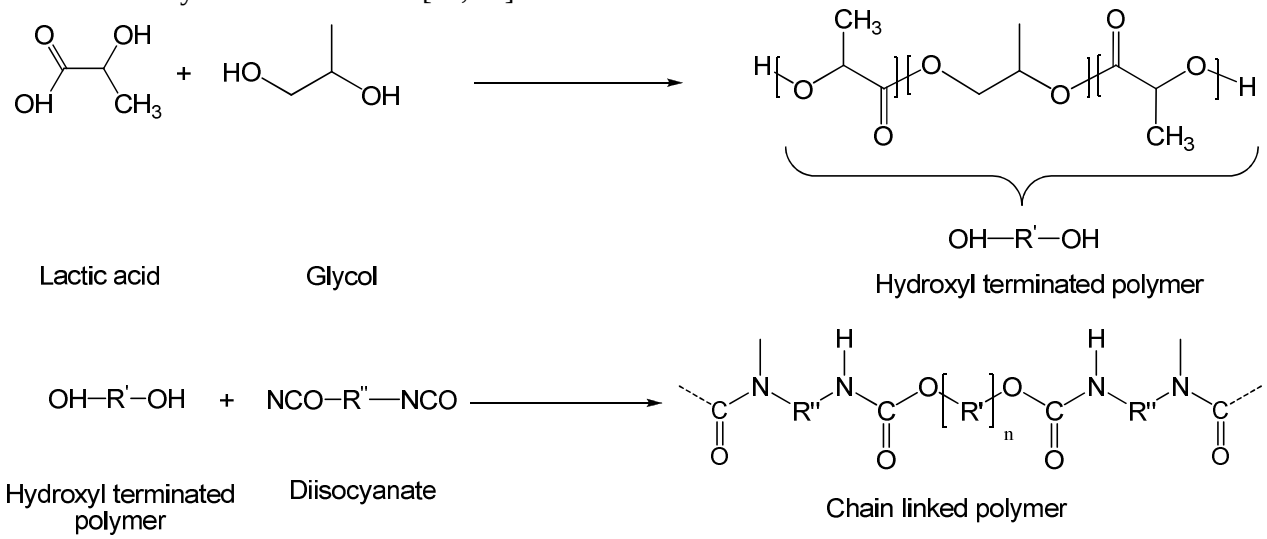

Figure 1 : Synthesis of chain extended poly(lactic acid)

Synthesis of poly (lactic acid) urethane (PLAU)
Polymerization of polyether ester urethane was carried out in 150 ml round bottom flask with stirrer (Fig. 1) and thermostatic controller over oil bath in melt under nitrogen blanket using PLAol with MDI and 20% (w/w of PALol) polypropylene glycol.

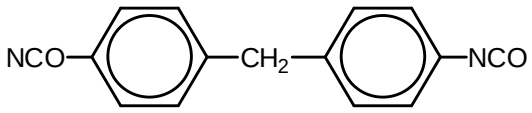

Figure 2: Methylen diphenyldiisocyanate (MDI)

Ratio of PLAol/diisocyanate was kept 1:1 (mole) to get linear thermoplastic polyester ether urethane. The amount of MDI was calculated on theoretical basis of hydroxyl number and isocyante content of MDI determined by titrimetric method (Fig. 2).

Result and Discussion

PLAol obtained was of low molecular weight as it possesses low viscosity, having lower Tg and lower strength. However PLAU obtained have higher Tg, higher strength and was yellowish in color.

Characterization

Viscosity of the PLAol and PLAU was obtained to be 1.188 and 1.582 respectively. The Intrinsic viscosity was evaluated using formula given in equation 1[18-20].

$$[\eta] = \frac{\sqrt{2\left(\frac{t}{t_0} - 1 - \ln\frac{t}{t_0}\right)}}{C} \qquad \text{……Equation 1}$$

Where t and t_0 is the flow time taken for polymer solution and solvent respectively and C is the concentration (g/cc) of solution.

Table 1 : Viscosity of PLAol and PLAU

	Relative Viscosity (ηrel)	Specific Viscosity (ηsp)	Reduced Viscosity (ηred)	Intrinsic Viscosity [η]
PLAol	1.188	0.188	0.094	0.088
PLAU	1.582	0.582	0.291	0.259

An increase in the viscosity of polymer, after chain linking, indicates the increase in the molecular weight of resulting polymer (Table 1). Since the [η] is directly proportional to the molecular weight of the polymer [15] by Mark Houwink equation,

$$[\eta] = k\overline{M}_v^a$$

……Equation 2

Where k and a are constants depends on solvent, polymer and conditions
Therefore

$$[\eta] \quad \alpha \quad \overline{M}_v$$

……Equation 3

FTIR results for PLAol shows characteristic peaks at 3495^{-1} (OH stretching) and 1745 cm^{-1} (C=O stretching), 1089 for -O- , methylene absorption (CH_2, CH_3) at 2971cm^{-1} (Fig. 3). FTIR of PLAU peak at 3495 cm^{-1} for –OH is replaced by Peak at 3350 cm^{-1} for -NH indicates the formation of polyurethane. However no peak was observed at 2300 cm^{-1} this indicates the complete conversion of diisocyante into urethane.

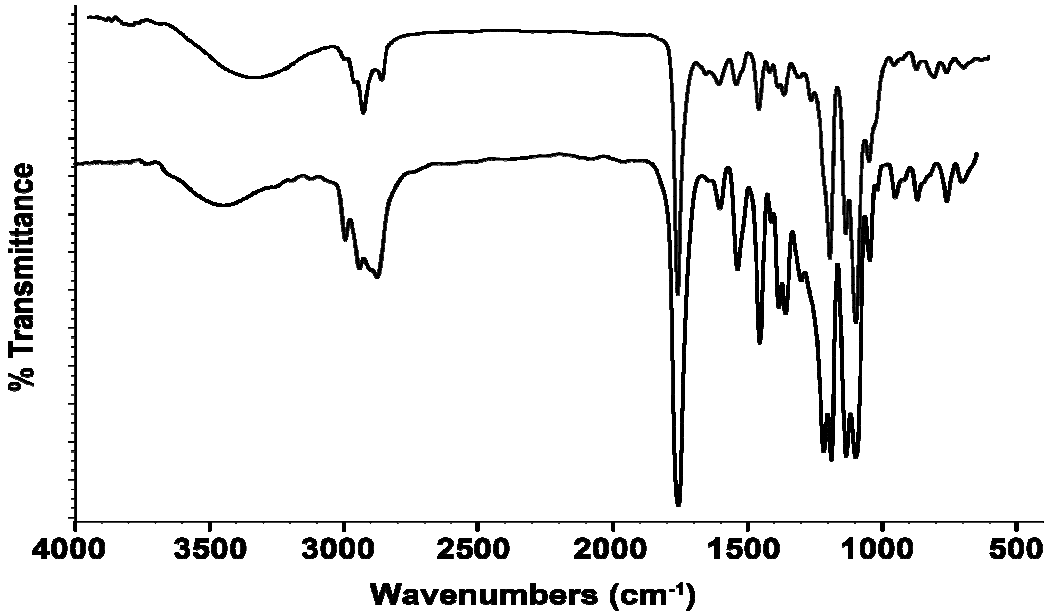

Figure 3 : FTIR spectra of PLAU and PLAol

Dynamic mechanical analysis is a powerful tool for the determination of Tg and thermo mechanical properties of the polymers. Samples for DMA were prepared by compression molding at 120°C.

Table 2: DMA results of PLAol and PLAU

	Tg	**Storage Modulus at -20°C (MPa)**	**Storage Modulus at 0°C (MPa)**
PLAol	34.18	480	417
PLAU	37.77	866	745

DMA results of chain extended polymer showed an increase in the glass transition temperature (Tg) along with the increase in storage modulus (figures 4 and 5). Tg was increased from 34.18 to 37.77° C and storage modulus increased from 480 MPa to 866 MPa at -20°C and 417 MPa to 7451 MPa at 0 °C (Table 2).

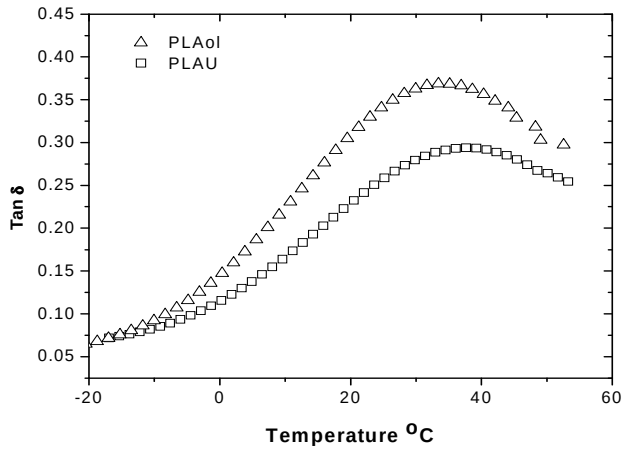

Figure 4 : Tan δ of PLAol and PLAU

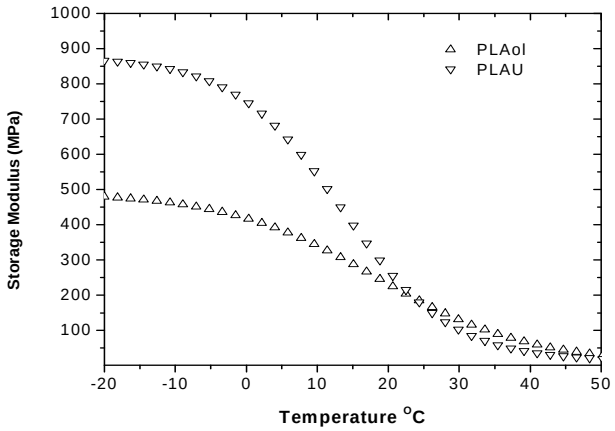

Figure 5 : Storage modulus of PLAol and PLAU

Conclusion

Chain coupling of PLA is an attractive method for the synthesis of high molecular weight PLA over other conventional lengthy methods. Chain coupling also offers the cost effectiveness, since it does not require sophisticated techniques and polymerization is possible a shorter time. Chain coupling of PLA result in increase in molecular weight along with higher glass transition temperature and storage modulus.

References

1. Bhaskar J., Haq S., Pandey A.K., Srivastava N. *J. Mater. Environ. Sci.*, 3 (2012) 605-612.
2. Singh V.K., Gope, P.C., Chauhan, S., and Bisht Deepak, S. *J. Mater. Environ. Sci.*, 3 (2012) 185-194.
3. Kumar V., Dev A., Gupta A.P. *Composites Part B: Engineering*, (2013) DOI: 10.1016/j.compositesb.2013.08.021
4. Gupta, A.P. and Kumar, V. *European Polymer Journal*, 43 (2007) 4053-4074.
5. Garlotta, D. *Journal of Polymers and the Environment*, 9 (2001) 63-84.
6. Mehta, R., Kumar, V., Bhunia, H., and Upadhyay, S. *Journal of Macromolecular Science, Part C: Polymer Reviews*, 45 (2005) 325-349.
7. Perego, G., Cella, G.D., and Bastioli, C. *Journal of Applied Polymer Science*, 59 (1996) 37-43.
8. Woo, S.I., Kim, B.O., Jun, H.S., and Chang, H.N. *Polymer Bulletin*, 35 (1995) 415-421.
9. Kricheldorf, H.R., Kreiser-Saunders, I., and Boettcher, C. *Polymer*, 36 (1995) 1253-1259.
10. Amass, W., Amass, A., and Tighe, B. *Polymer International*, 47 (1999) 89-144.
11. He, Y., Fan, Z., Wei, J., and Li, S. *Polymer Engineering and Science*, 46 (2006) 1583-1589.
12. Hiltunen, K., Seppala, J.V., and Harkonen, M. *Journal of Applied Polymer Science*, 63 (1997) 1091-1100.
13. Seppala, J.V., Helminen, A.O., and Korhonen, H. *Macromolecular Bioscience*, 4 (2004) 208-217.
14. Hiltunen, K., Seppala, J.V., and Harkonen, M. *Journal of Applied Polymer Science*, 64 (1997) 865-873.
15. Gupta, A.P. and Kumar, V. *Designed Monomers and Polymers*, 13 (2010) 65-72.
16. Gupta, A.P., Dev, A., and Kumar, V. *Journal of Polymers and the Environment*, 20 (2012) 514-518.
17. Hupburn, C., *Polyurethane Elastomers*. IInd ed. 1992, England: Elsevier Applied Scinece.
18. Jankauskaite, V., Macjauskas, G., and Lygaitis, R. *Material Science*, 14 (2008) 119.
19. Liu, C., Qian, Z., Gu, Y., Fan, L., Li, J., Chao, G., Jia, W., and Tu, M. *Materials Letters*, 60 (2006) 31-38.
20. Karayannidis, G.P., Achilias, D.S., Sideridou, I.D., and Bikiaris, D.N. *European Polymer Journal*, 41 (2005) 201-210.